Design, Fabrication, and Intelligent Optimisation of Electrospun Poly (-caprolactone) Nanofibrous Membranes for Tissue Engineering and Water Treatment Applications

YUZHUO WANG

Design, Fabrication, and Intelligent Optimisation of Electrospun Poly (ε-caprolactone) Nanofibrous Membranes for Tissue Engineering and Water Treatment Applications

Yuzhuo Wang

A Thesis presented for the degree of

Doctor of Philosophy

Department of Engineering

Durham University

United Kingdom

February 2026

Abstract

Tissue engineering and water treatment are two enduring technological frontiers with far-reaching implications for human health and environmental sustainability. The dual challenges of repairing damaged tissues and addressing water pollution demand advanced, multifunctional materials that are adaptable, efficient, and environmentally responsible. Electrospinning offers control over membrane morphology, porosity, and structure, making it particularly suitable for both applications. Among available materials, electrospun poly(ε-caprolactone) (PCL) has attracted increasing attention due to its processability, biocompatibility, and biodegradability. This study aims to elucidate the parameter–structure–performance relationships of electrospun PCL-based nanofibrous materials in the contexts of tissue engineering and oily water treatment. An image-based artificial intelligence (AI) workflow was also developed to enable predictive modelling of fibre diameter, thereby improving fabrication efficiency and reducing experimental workload. Additionally, membrane modification strategies were critically reviewed to provide practical guidance for optimising design.

For tissue engineering, electrospun PCL scaffolds were fabricated using polymers with varying molecular weights (MWs) under different solution concentrations and flow rates. Morphological features were assessed via scanning electron microscopy (SEM), wettability was evaluated by water contact angle (WCA) measurements, and biocompatibility was examined using L929 fibroblast cultures through MTT assays, SEM, and confocal fluorescence imaging. The MMW-25%-1.5 and HMW-20%-1.5 scaffolds exhibited optimal characteristics, including bead-free fibres (~470–490 nm), appropriate pore sizes (1.4–1.7 μm), and high porosity (>58%), which facilitated cell adhesion and proliferation. However, all scaffolds exhibited intrinsic hydrophobicity, which limited nutrient infiltration and cell adhesion. Additionally, an unexpected interaction between PCL and MTT reagents was observed, suggesting potential interference with the accuracy of the viability assay.

Incorporating biomass-derived hydrophilic polymers is indicated as a strategy to enhance scaffold performance.

For water treatment, sandwich-structured PCL/PMMA@PCL/PCL membranes were developed with PCL outer layers and a PMMA@PCL middle layer to enhance mechanical strength and separation efficiency. Ethanol treatment improved wettability via physical adsorption of hydroxyl groups, while cold-pressing reduced fibre diameter and increased membrane compactness through axial stretching. Compared to single-layer membranes, the multilayered structure showed improved mechanical robustness and achieved high oil rejection rates (~95%) in short-term filtration. While the flux recovery ratio (FRR) remained above 90%, it was limited by the inefficacy of deionised (DI) water rinsing in removing trapped oil. Long-term tests revealed a gradual decline in flux due to compaction and partial pore blockage, highlighting the need for improved antifouling and cleaning strategies.

To address the limitations of manual fibre diameter measurement, an image-based AI workflow was developed. The DiameterJ and Semiautomated Image Measurements of Polymers (SIMPoly) programmes were compared for SEM image processing, with DiameterJ selected for its superior accuracy and batch-processing capabilities. A dataset of 144 samples was generated and used to train an artificial neural network (ANN) model using four key electrospinning parameters: molecular weight, concentration, flow rate, and tip-to-collector distance. The ANN achieved high predictive accuracy ($R^2 > 0.97$, prediction error < 4%) and outperformed the response surface methodology (RSM) model, which showed limited generalisability (prediction error up to 28.57%). Sensitivity analysis via index of relative importance (IRI) and contour mapping identified molecular weight and solution concentration as the most influential factors, consistent with experimental observations.

In summary, this study provides a comprehensive investigation into the fabrication, characterisation, and intelligent optimisation of electrospun PCL-based nanofibrous materials. It establishes a unified framework linking processing parameters, structural features, and functional performance in both tissue engineering and water treatment. The integration of macro-scale experiments with data-driven modelling offers a scalable and transferable approach to intelligent material design, paving the way for next-generation fibrous membranes with enhanced multifunctionality and environmental sustainability.

Declaration

The work in this thesis is based on research carried out at the Department of Engineering, University of Durham, United Kingdom. The work was financially supported by the Chinese Scholarship Council (CSC)-Durham University Joint Scholarship. No part of this thesis has been submitted elsewhere for any other degree or qualification.

Some of the work presented in this thesis has been published in journals and conference proceedings as follows:

Publications

Published

1. Yuzhuo Wang (First Author), et al., Thermochemical conversion of biomass: Potential future prospects. *Renewable Sustainable Energy Rev.* 187 (2023) 113754. https://doi.org/10.1016/j.rser.2023.113754. **(IF=16.3, JCR/Q1, SCI)**
2. Yuzhuo Wang (First Author), et al., Fabrication and application of polycaprolactone-based composite scaffolds in tissue engineering: A review. *Mater Today Commun* 49 (2025) 113821. https://doi.org/10.1016/j.mtcomm.2025.113821. (**IF=4.5, JCR/Q2, SCI**, **Chapter 2)**
3. Yuzhuo Wang (First Author), et al., Fabrication and functionalisation of poly(ε-caprolactone)-based materials for water treatment: A comprehensive review. *J Environ Chem Eng* 14(1) 2026 120966. https://doi.org/10.1016/j.jece.2025.120966 (**IF=7.2, JCR/Q1, SCI**, **Chapter 3**)
4. Yuzhuo Wang (First Author), et al., Enhanced oil/water separation using electrospun sandwich-like fibrous membranes of PCL/PMMA@PCL/PCL. *Sep Purif Technol* 376 (2025) 134114. https://doi.org/10.1016/j.seppur.2025.134114. **(IF=9, JCR/Q1, SCI, Chapter 6)**
5. Yuzhuo Wang (First Author), et al., Integration of image processing and ANN modeling for prediction of electrospun PCL fibre diameters. *Mater Design* 260 (2025) 115180. https://doi.org/10.1016/j.matdes.2025.115180. **(IF=7.9, JCR/Q1, SCI**, **Chapter 7**)

To be Published

6. **Yuzhuo Wang (First Author)**, et al., In vitro studies of electrospun PCL nanofibrous scaffold for wound tissue engineering applications. (Under review of ***Polym Bull*****, Chapter 5**)

Conference

1. The 5th International Discussion Meeting on Chemistry and Technology of Combustion Application, Qingdao, China, 2025 (Oral presentation).
2. The 10th International Conference on Advances in Energy and Environment Research, Shanghai, China, 2025 (Poster Presentation).
3. Engineering PGR Research Conference, Durham, UK. 2025 (Poster Presentation).

Acknowledgment

Schopenhauer once said: “Man is always in pain, because his essence falls into the palm of his own hands.” Over time, I have come to reinterpret this not as a fate to lament, but as a truth that hardship is what forges resilience. My PhD journey, like the years before it, has been shaped by challenges—personal, academic, and cultural. These moments did not diminish me; instead, they taught me patience, courage, and the quiet strength to keep moving forward.

I am sincerely grateful to my primary supervisor, Dr. Lian Gan, for offering me the opportunity to pursue my PhD at Durham University and for standing beside me through difficult times. His guidance extended far beyond research discussions; in moments when I faltered, his understanding and encouragement helped me regain balance. His trust in my ability has been a steady force throughout this journey.

I owe deep thanks to Dr. Leteng Lin at Linnaeus University (Sweden) for his careful guidance and constructive feedback. His way of questioning and refining ideas challenged me to see my work from new angles. Our discussions often turned complex problems into clear, achievable steps, which made a lasting difference to my research. My gratitude also goes to Prof. Yingjie Li at Shandong University, my master’s supervisor, who laid the foundation for my academic path. His rigour and high expectations shaped my research approach, while his encouragement showed me the importance of persistence. Many of the skills and values I rely on today trace back to his teaching. I am also deeply grateful to Prof. Cuiping Wang at Shandong University of Science and Technology, who taught me during my undergraduate studies. Her continuous support and encouragement have played an essential role in my academic development.

I am also grateful to Dr. Richard Thompson, Associate Professor in the Department of Chemistry, for generously allowing me to use his laboratory facilities and for providing hands-on training. Our scientific discussions were both insightful and inspiring, and his support significantly broadened my

technical understanding and experimental capability. I am grateful to Prof. Charles Augarde, Prof. Claudio Balocco, and Ms. Louise Gascoigne for their kindness and practical help. In times of uncertainty, their support reminded me that I was not alone, and their efforts made my working environment warmer and more welcoming.

I am deeply grateful to my parents. Thank you for standing behind my decision to continue studying abroad, even when many of my peers chose to work and settle down. Your quiet support and understanding have been the foundation that has allowed me to pursue my goals without hesitation.

To my partner, future Dr. Yixin Li, I am thankful for your steady encouragement and belief in me, especially in moments when I struggled to believe in myself. Your presence brought balance to my life and made this journey far less lonely.

I look forward to the day we both finish our doctoral journeys and begin a new chapter together. To my friends, Dr. Kaixuan Zhou, Dr. Akmaral Karamergenova, Wen Xing, and Yujing Liu, I am glad we have shared this path. From exchanging ideas to simply listening when the days felt heavy, your friendship has been a source of strength and joy.

Lastly, I am grateful to the part of me that kept moving forward, kept learning, and allowed each challenge to shape me into a stronger person.

Dedicated to

Myself, Yuzhuo,

who has walked through challenges

and kept striving towards the light

Contents

List of Figures

List of tables

Nomenclature

a'	Traversal over all input variables
A	The effective area of membranes, cm^2
AA	Acetic acid
$a'b$	All connection paths from the input layer to the hidden layer
ACNF	Acetylated cellulose nanofibres
ACL	Anterior cruciate ligament
AI	Artificial intelligence
AgNPs	Silver nanoparticles
ANNs	artificial neural networks
ANOVA	Analysis of variance
Asp@lipo	Aspirin-loaded liposomes
aSWNTs	Amine-functionalized single-walled carbon nanotubes
ATCC	American Type Culture Collection
ATR	Attenuated total reflectance
AuNPs	Gold nanoparticles
AV	Aloe vera
b	The number of neurons in the hidden layer
BC	Bacterial cellulose
BCNC	Bacterial cellulose nanocrystal
BCP	Biphasic tricalcium phosphate
BP	Backpropagation
BSA	Bovine serum albumin
β-TCP	β-tricalcium phosphate

c	The neuron in the output layer, typically $c = 1$
C_f	The concentration of oil in the feeding, %
C_p	The concentration of oil in the permeation, %
CA	Cellulose acetate
CaAlg	Calcium alginate
CAD	Computer-aided design
CCD	Central Composite Design
CIMD	Cellulose-bearing imidazolium tosylate
CNC	Cellulose nanocrystal
C-nHA	Collagen-fixed nano-HA
CNT	Carbon nanotubes
COD	Chemical oxygen demand
C. officinalis	Calendula officinalis
COS	Chitooligosaccharides
CQDs	Carbon quantum dots
CS	Chitosan
CSNPs	Chitosan nanoparticles
δ	The thickness of wet membranes, cm
d	The fibre diameter of the membrane, nm
d_w	The density of water at room temperature, 1 g/cm^3
DAPI	4',6-diamidino-2-phenylindole
DC	Duck's feet collagen
DCM	Dichloromethane
DI	Deionized
DMAPS	Zwitterionic surfactant, [2-(Methacryloyloxy) ethyl] dimethyl-(3-sulfopropyl) ammonium hydroxide
DMEM	Dulbecco's modified Eagle medium
DMF	Dimethylformamide
ε	The volumetric porosity of the electrospun membranes, %

ECM	Extracellular matrix
EIPS	Evaporation-induced phase separation
E-jetting	Electrohydrodynamic jetting
EVOO	Extra virgin olive oil
FA	Formic acid
FBS	Fetal bovine serum
FDA	Food and Drug Administration
FDM	Fused deposition modelling
FDR	Flux decline rate
FEA	Finite element analysis
FRR	Flux recovery ratio
FTIR	Frontier Fourier Transform infrared spectroscopy
GA	Gum Arabic
GBM	Glioblastoma
g-C_3N_4	Graphitic carbon nitride
Gel	Gelatin
GelMA	Gelatin methacrylate
GIFT	General Image Fibre Tool
GO	Graphene oxide
GPC	Gel permeation chromatography
HA	Hydroxyapatite
HMW	High molecular weight
IRI	Index of relative importance
J	Pure water flux, LMH
J_1	Oil/water emulsion flux, LMH
J_2	Pure water flux in the second cycle, LMH
LMH	Membrane flux, L/(m^2×h)
LMW	Low molecular weight
LSCM	Laser scanning confocal microscope

MgO	Magnesium oxide
MLP	Multilayer perceptron
MMT	Montmorillonite
MMW	Medium molecular weight
MNPs	Magnetic nanoparticles
MOF	Metal-organic frameworks
MSE	Mean squared error
MSH	Melanocyte-stimulating hormone
MTT	3-(4,5-Dimethylthiazol-2-yl)-2,5-diphenyltetrazolium bromide
MW	Molecular weight
MWCNTs	Multiwall carbon nanotubes
n	The number of samples
NaF	Sodium fluoride
NIPS	Non-solvent-induced phase separation
OCP	Octacalcium phosphate
PANI	Polyaniline
PBS	Polybutylene succinate
PCL	Polycaprolactone
PCL-b-PTFOA	PCL-block-1H,1H,2H,2H-Perfluorooctyl acrylate (TFOA) copolymer
PCL-b-P4VP	Poly(ε-caprolactone)-b-poly(4-vinyl pyridine)
PCL-D	PCL blended with its low-molecular-weight oligomeric diol
PDLLA	Poly (D, L-lactide)
PE	Polyethylene
PEG	Polyethylene glycol
PEO	Polyethylene oxide
PES	Polyethersulfone
PEP	Peppermint essential oil
PHB	Poly-3-hydroxybutyrate
ph-LPSQ	phenyl polysilsesquioxane

PLA	Polylactic acid
PLGA	Poly (lactide-co-glycolide)
PLLA	Poly(L-lactide)
PMMA	Poly (methyl methacrylate)
PP	Polypropylene
PPy	Polypyrrole
PS	Polystyrene
PU	Polyurethane
PVA	Polyvinyl alcohol
PVDF	Polyvinylidene fluoride
PVP	Polyvinylpyrrolidone
PWF	Pure water fluxes
r	The average pore radius, nm
R	The percentage of oil rejection, %
R^2	Coefficient of determination
RSM	Response surface methodology
x	Coded values that normalise the corresponding variables
X	The actual value of the factor
X_{center}	The central (median) value
X_{high}	The maximum values of the factor
X_{low}	The minimum values of the factor
SA	Sodium alginate
SEM	Scanning electron microscope
SF	Silk fibroin
SIMPoly	Semiautomated Image Measurements of Polymers
SKL	Sulfonated kraft lignin
SMP	silk microparticles
SrHA	Strontium-doped HA
T_c	Crystallisation temperature, °C

T_m	melting temperature, °C
T_g	Glass transition temperature, °C
TCH	Tetracycline hydrochloride
TIPS	Thermally-induced phase separation
TNBC	Triple-negative breast cancer
Val fail	Validation failure count
VIPS	Vapour-induced phase separation
VOCs	Volatile organic compounds
W_d	The weight of the dry membranes, g
W_w	The weight of the wet membranes, g
WCA	Water contact angle
WHO	World Health Organization
WS NP	Walnut shells nanoparticles
β-TCP	β-tricalcium phosphate
PVDF	Polyvinylidene fluoride
ZnO	Zinc oxide
y_i	Actual values
$\hat{y}_i$	Predicted outputs of the actual values
$\bar{y}_i$	The mean values of the actual values
5-Fu	5-fluorouracil

CHAPTER 1

1 Introduction

1.1 Investigation background

Polymer-based membranes, owing to their tunable composition, structure, and functionality, play critical roles in a wide range of biological and environmental processes and find extensive applications in biomedical engineering (particularly in tissue engineering) and environmental engineering (notably in water purification and wastewater treatment). In tissue engineering, membranes are often used as scaffolds that mimic the extracellular matrix (ECM), promoting cell adhesion, proliferation, and differentiation for tissue regeneration. In environmental applications, membranes serve as separation media that efficiently remove contaminants from water through filtration, adsorption, or catalytic degradation.

Tissue engineering and water treatment are two enduring technological frontiers with far-reaching implications for human health and environmental sustainability. On one hand, tissue engineering addresses the pressing need for the repair and regeneration of damaged tissues and organs because the damage to tissues often leads to severe pain, functional impairment, disability, and even death. On the other hand, water pollution and freshwater scarcity have emerged as global crises, intensified by rapid industrialisation, urban expansion, and population growth. The World Health Organisation (WHO) reports that over 80 countries are experiencing water shortages, with nearly 25% of the global population lacking reliable access to safe drinking water [1]. These parallel challenges call for advanced, multifunctional materials and technologies that are adaptable, efficient, and environmentally sustainable.

1.2 Tissue engineering: Clinical needs and material strategies

Tissue engineering aims to isolate and expand seed cells from living tissues, culture them on artificial scaffolds to form cell-material complexes, and subsequently implant them into the body. Within the body, the cells proliferate and differentiate while the scaffold gradually degrades, ultimately creating new tissue to achieve functional repair and reconstruction [2]. Damage to tissues such as skin, bone, nerves, blood vessels, and internal organs often leads to severe pain, functional impairment, disability, and even death due to the limited regenerative capacity of adult tissues. According to WHO statistics, tissue damage contributed to over 56.7% of fatalities in the 2023 fuel depot explosion in Armenia [3]. Similarly, fractures have become a major global health issue, resulting in high morbidity, mortality, and socioeconomic burden. Projections indicate a 27% increase in the annual cost of fragility fractures by 2030 across European countries, including Germany, France, the UK, Italy, Spain, and Sweden [4].

Tissue engineering offers a promising solution by mimicking the structure and function of the ECM using biodegradable, biocompatible, nontoxic, and porous scaffolds with adequate mechanical properties. To this end, electrospun nanofibrous membranes have been widely investigated as artificial ECMs. These scaffolds provide not only structural support but also micro- and nanoscale cues for cellular processes, including migration, adhesion, proliferation, and differentiation [5]. Their simple production process, tunable architecture, and morphological similarity to native ECM make them attractive candidates for regenerating a wide range of tissues.

1.3 Water pollution and the demand for advanced treatment materials

Water pollution and the scarcity of clean water are pressing global issues. Industrial effluents, agricultural runoff, domestic sewage, and medical wastewater introduce a wide range of pollutants, including oils, fats, proteins, volatile organic compounds (VOCs), heavy metals, acids, alkalis, and pathogenic microorganisms [6]. Among these, oily wastewater poses particularly severe environmental and economic risks. For example, the Deepwater Horizon spill released 779 million litres of crude oil into the ocean, contaminating over 3200 km^2 of marine ecosystems [7]. Once

released, oil undergoes a series of complex transformations, such as evaporation, diffusion, emulsification, dissolution, and microbial degradation, all of which contribute to long-lasting ecological damage. Traditional separation methods, such as skimming, flotation, and ultrasonic techniques, suffer from high energy consumption, low efficiency, and difficulty in separating emulsified oil/water systems [8]. These limitations have intensified the search for high-performance water treatment materials that are both energy-efficient and environmentally friendly. Membranes capable of selective oil/water separation and multifunctional performance are particularly desirable.

1.4 Electrospinning technology for nanofibrous membranes

Various fabrication techniques have been developed to produce polymer-based membranes with tailored structures and functionalities for diverse applications. Common approaches include phase separation, freeze-drying, electrospinning, and 3D printing. Each technique provides a unique way to control membrane morphology, porosity, and surface characteristics, enabling a flexible design tailored to the target application. For instance, phase separation can generate interconnected porous structures through thermodynamic instability of polymer solutions [9], while freeze-drying preserves the hierarchical porosity of polymer suspensions during solvent sublimation, producing lightweight, sponge-like scaffolds [10]. 3D printing enables precise control over macroscopic geometry and pore architecture, facilitating the fabrication of complex, customized scaffolds for biomedical and filtration purposes [11].

Among these methods, electrospinning has attracted extensive attention owing to its ability to produce nanoscale fibres with tunable morphology and composition continuously. The process uses a high electric field to draw a polymer solution or melt into ultrafine fibres, which are then collected into nonwoven membranes. The resulting nanofibrous structures feature high surface-area-to-volume ratios, interconnected pores, and adaptable chemical functionality. Such characteristics allow electrospun membranes to bridge the needs of both tissue engineering and water treatment, where the former requires biocompatible and cell-adhesive architectures that mimic the ECM, and the latter benefits from the large surface area and controlled wettability for efficient separation and adsorption processes [12]. The properties of electrospun fibres can be modulated by various factors, including: (a) polymer solution properties (e.g., polymer type, molecular weight, solvent system, solution

concentration, viscosity, conductivity, surface tension, dielectric constant); (b) processing parameters (e.g., applied voltage, spinneret-to-collector distance, flow rate, spinneret configuration); and (c) ambient environmental conditions (e.g., temperature, humidity) [13].

To mimic the structural and biological functions of the natural ECMs, electrospun nanofibrous membranes have been widely investigated as artificial scaffolds for tissue engineering [14]. These scaffolds not only provide mechanical support but also deliver biomimetic topographical and chemical cues that regulate cellular processes such as migration, adhesion, proliferation, and differentiation, which are key to facilitating tissue repair and regeneration. The technique offers significant advantages in terms of fabrication flexibility, enabling the creation of tunable scaffold shapes, sizes, and architectures that meet the diverse requirements of different tissue types. Figure 1. 1 illustrates the role of electrospun membranes in the wound-healing process, a representative application in tissue engineering [15].

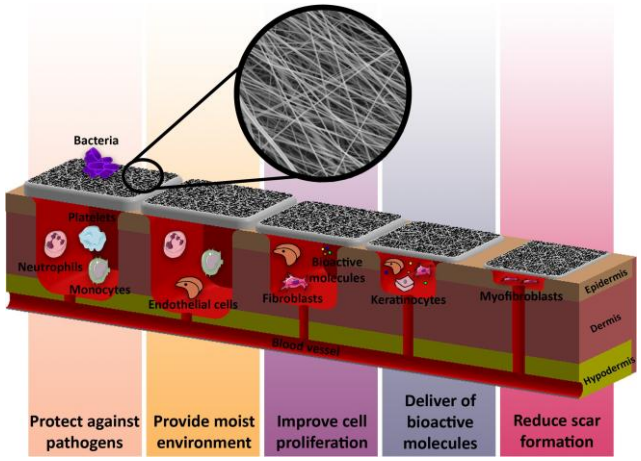

Figure 1. 1: The process that electrospun membranes play during wound healing (an essential part of tissue engineering) (Reproduced with permission from [15]. Copyright 2018 Elsevier).

A variety of natural polymers (e.g., chitosan (CS), collagen, gelatin (Gel), silk fibroin (SF), zein) and synthetic polymers (e.g., polycaprolactone (PCL), poly(lactic-co-glycolic) acid (PLGA), poly(glycolic acid) (PGA), polyurethane (PU)) have been electrospun to form nanofibrous scaffolds [16, 17]. Blending natural and synthetic polymers helps combine the bioactivity and biocompatibility of the former with the mechanical strength and durability of the latter [18]. Furthermore, functional inorganic additives such as metal oxides [19], phosphate-based compounds (e.g., hydroxyapatite (HA), calcium phosphate) [20], carbon nanotubes (CNTs) [21], and graphene [22] have been incorporated to enhance mechanical properties, electrical conductivity, and biological performance.

Advanced electrospun scaffolds are therefore at the forefront of current and future biomedical material research.

In the field of oily water treatment, electrospun nanofibrous materials are commonly used as adsorbents or separation membranes. As adsorbents, they efficiently remove heavy metals, dyes, and organic contaminants via physical adsorption and chemical interaction mechanisms [23]. Separation membranes, such as ultrafiltration, microfiltration, nanofiltration, and osmosis, enable selective separation by modulating pore size and surface wettability, often delivering high efficiency and strong antifouling performance [24]. The working principles of typical water treatment membranes are summarised in Figure 1. 2 [25]. Recently, electrospun membranes have been increasingly applied for oil/water separation, due to their tunable surface wettability and hierarchical porous structure [26]. Membranes with hydrophobic/oleophilic or hydrophilic/oleophobic surface properties can selectively allow oil or water to permeate, achieving efficient oil/water separation. Similar to their use in tissue engineering, membranes for environmental applications are typically fabricated from natural or synthetic polymers and can be functionalized with additives tailored to specific treatment needs. This compositional and structural flexibility allows for the design of high-performance membranes for targeted pollutant removal in complex wastewater systems.

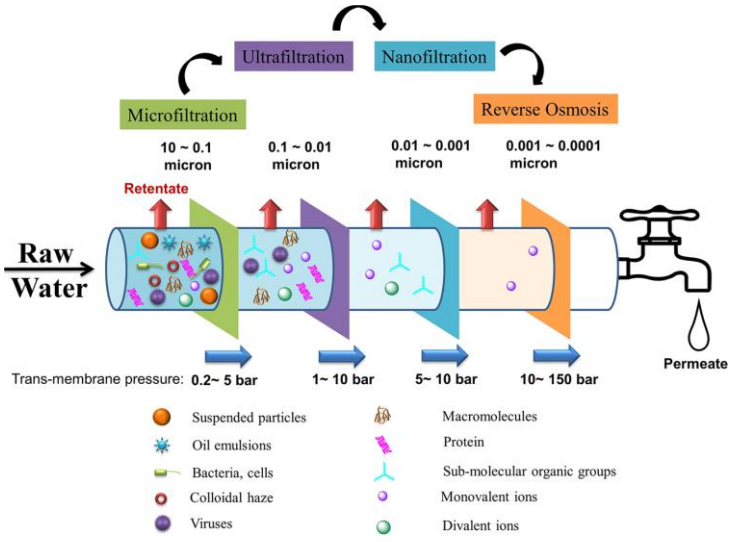

Figure 1. 2: Basic mechanisms of commonly used water treatment membranes (Reproduced with permission from [25]. Copyright 2017 Elsevier).

Overall, the combination of high surface area, interconnected porosity, proper mechanical strength, and tunable chemistry endows electrospun membranes with remarkable versatility. These structural

features enable efficient mass transfer and selective permeability, which are essential for water purification, while simultaneously providing a 3D biomimetic microenvironment that promotes cell adhesion, proliferation, and tissue regeneration in tissue engineering applications. Consequently, electrospinning serves as a unifying platform that bridges the structural and functional requirements of both biomedical and environmental membranes.

1.5 PCL in biomedical and environmental applications

The selection of appropriate polymers is crucial for creating nanofibrous membranes with desired topographical and functional characteristics. PCL, a synthetic aliphatic polyester, has been widely employed in electrospun scaffolds for tissue engineering owing to its excellent biocompatibility, good mechanical strength, and processability [26]. Although PCL undergoes hydrolytic degradation under physiological conditions, making it suitable for temporary implants, its relatively slow degradation rate is advantageous for applications requiring long-term structural support. Since the 1970s, PCL has been extensively studied in both in vitro and in vivo settings for wound healing and regenerative medicine, demonstrating consistent performance across various biomedical applications [27]. Beyond biomedical use, PCL is also an attractive candidate for the fabrication of filtration membranes in water treatment, owing to its biodegradability, biocompatibility, and environmental safety [28, 29]. Its compatibility with multiple fabrication methods, including electrospinning, phase separation, and 3D printing, enables the development of a broad range of PCL-based materials with tunable properties for various environmental applications [30]. To overcome limitations related to hydrophobicity or mechanical rigidity, recent research has focused on forming PCL-based composites by blending with natural polymers or incorporating functional additives, which result in multifunctional membranes with improved application-specific performance [31].

1.6 Structure–function optimisation via image analysis and machine learning

In both tissue engineering and water treatment, the morphology of electrospun nanofibrous membranes, especially fibre diameter, plays a critical role in determining pore size, porosity, mechanical strength, and overall functional performance [32]. Precise and efficient morphological

characterisation is therefore essential for understanding structure–property relationships and optimising fabrication parameters. Traditionally, fibre diameter analysis has relied on manual measurements from SEM images using basic tools like the line function in ImageJ/Fiji, followed by standard statistical processing [33]. However, such methods suffer from limitations including subjective bias, low sampling efficiency, and time-consuming workflows [34]. To address these issues, several automated image processing tools have been developed to improve speed and reproducibility. Examples include DiameterJ, an open-access ImageJ plugin [35]; SIMPoly, a MATLAB-based programme for semiautomated fibre measurement [36]; and the General Image Fibre Tool (GIFT) [37]. These tools enable the rapid, high-throughput extraction of fibre diameter distributions from SEM images, facilitating more robust quantitative analysis.

Nonetheless, due to the multivariate and nonlinear nature of electrospinning, it remains challenging to predict fibre morphology directly from process parameters. Traditional experimental design often requires extensive, time-consuming trial-and-error iterations to explore the influence of different variables [38, 39]. To overcome this limitation, artificial neural networks (ANNs) have been widely adopted as powerful machine learning models capable of learning complex input–output relationships in a data-driven manner [40]. ANNs serve as black-box predictors that map multiple input variables, such as polymer concentration, flow rate, voltage, and ambient conditions, to continuous outputs, such as fibre diameter. Compared with conventional regression or factorial designs, ANN models can handle large, nonlinear, and noisy datasets with high accuracy and generalisability. Their application significantly reduces experimental workload, material consumption, and optimisation time [41]. The integration of automated image-processing-based fibre characterisation with ANN modelling offers a promising framework for intelligent optimisation of electrospinning parameters. Such data-driven approaches will play an increasingly vital role in the design and production of high-performance nanofibrous membranes for both biomedical and environmental applications.

1.7 Motivation and objectives

PCL is a promising material for biomedical and environmental applications due to its biodegradability, biocompatibility, and ecological safety. However, the relationships between

electrospinning parameters and scaffold morphology are complex and often require extensive experimental trials to clarify. In addition, a comprehensive synthesis of the latest developments in the fabrication and functionalisation of PCL-based materials for tissue engineering and water treatment remains absent. To address these gaps, this study aims to elucidate the parameter–structure–performance relationships of electrospun PCL nanofibrous materials in both tissue engineering and water treatment contexts. It further explores an image-based artificial intelligence workflow to enable predictive modelling of fibre diameters, thereby improving process efficiency and reducing experimental workload. A comprehensive review of membrane modification strategies is also undertaken to provide practical guidance for material design and performance optimisation. The research objectives are as follows:

- **Objective 1: To conduct a comprehensive review of membrane modification strategies to provide practical guidance for material design and performance optimisation.**

  This objective aims to conduct a comparative review of recent developments in PCL-based composites for both tissue engineering and water treatment. For tissue engineering, the review focuses on how fabrication techniques and material modifications influence the structure, mechanical properties, and bioactivity of scaffolds across various target tissues. It also considers broader aspects such as clinical translation, scalable manufacturing, and the integration of computational tools as future directions. For water treatment, the review examines PCL-based applications in adsorption, membrane separation, and photocatalysis, with a particular emphasis on how fabrication methods, such as electrospinning, freeze-drying, phase separation, and 3D printing, impact material properties and treatment performance. Furthermore, it highlights the potential of multifunctional integration and the synergistic use of high-performance computing, automation, and machine learning as promising approaches for advancing next-generation PCL-based materials.

- **Objective 2: To elucidate the parameter–structure-performance relationship in electrospun PCL scaffolds for tissue engineering applications.**

  This objective aims to systematically examine how variations in electrospinning parameters, such as PCL molecular weight, solution concentration, and flow rate, influence the resulting scaffold morphology, including fibre diameter, porosity, and pore size. A particular focus is on the

molecular weight variability of commercial PCL, with gel permeation chromatography (GPC) used to assess deviations between nominal and actual molecular weights and their implications for reproducibility. Furthermore, this objective includes identifying potential interferences between PCL materials and commonly used viability assays (e.g., MTT). Ultimately, the goal is to enable rational design of biocompatible scaffolds that support enhanced fibroblast adhesion, proliferation, and spreading.

- **Objective 3: To design and fabricate multilayer electrospun PCL membranes for high-performance oily water separation.**

  This objective focuses on developing a novel sandwich-structured membrane architecture in which hydrophobic PCL outer layers encapsulate a middle layer comprising a PCL/PMMA blend. The influence of post-processing treatments, including mechanical compression and ethanol immersion, on membrane integration, flexibility, wettability, and mechanical robustness will be thoroughly investigated. Performance testing under pressurised crossflow conditions will be conducted to assess water flux, fouling resistance, and oil rejection efficiency. Structural and surface characterisations (e.g., hydrophilicity, surface morphology, and mechanical properties) will be used to establish quantitative structure–function correlations, aiming to optimise membrane design for the filtration of industrially relevant oily wastewater.

- **Objective 4: To develop an image-based artificial intelligence workflow for predictive modelling of electrospun fibre diameters.**

  This objective proposes an integrated approach combining automated SEM image processing with ANN to enable intelligent prediction and control over fibre morphology. Specifically, open-source image processing tools, such as DiameterJ and SIMPoly, will be used to generate large datasets of fibre diameter measurements, which will serve as input to ANN regression models. ANN models will be trained to predict fibre diameter based on electrospinning parameters, providing insights into the relative importance of key variables through parametric analysis and visual interpretation (e.g., IRI analysis and contour plots). The broader aim is to establish a generalisable, data-driven framework for morphological prediction and process optimisation applicable to a wide range of electrospun materials.

1.8 Thesis outline

The organisation of this thesis is as follows:

- **Chapters 2 and 3: Literature review (Addressing objective 1)**

  These two sections provide a comprehensive overview of recent advances in PCL-based nanofibrous materials for tissue engineering and water treatment. It highlights the current state of the art, identifies existing challenges, and outlines future research directions to enhance their practical applications.

- **Chapter 4: General materials and methods**

  This section introduces the general materials and methods employed throughout the thesis, including protocols for scaffold and membrane fabrication, cell culture, and oil/water separation, as well as characterisation techniques and computational principles of image analysis and ANN modelling.

- **Chapter 5: Electrospun PCL scaffolds for tissue engineering (Addressing Objective 2)**

  This section investigates the structure–property relationships of electrospun PCL scaffolds, focusing on how fabrication parameters influence nanofibre morphology and cellular responses.

  Original Contribution: A systematic elucidation of the correlation between processing parameters and scaffold morphology is presented.

- **Chapter 6: Multilayer PCL-based membranes for oily water treatment (Addressing Objective 3)**

  This section presents a detailed study on the design, fabrication, and performance evaluation of PCL-based multilayer membranes for oily wastewater separation. The effects of post-treatment processes such as ethanol immersion and mechanical compression are also investigated.

  Original Contribution: Significant improvements in wettability, antifouling performance, mechanical robustness, and oil/water separation efficiency are demonstrated through membrane design innovation and structural optimisation.

- **Chapter 7: Integrated image processing-ANN modelling for electrospun fibre prediction (Addressing Objective 4)**

  This section describes the development of an integrated, data-driven workflow that combines automated image processing with ANN modelling to predict fibre diameter under diverse electrospinning conditions.

  Original Contribution: A methodological innovation is proposed that enables high-throughput, accurate morphological prediction while substantially reducing experimental workload and material usage, which is scalable and transferable across various electrospun membrane systems.

- **Chapter 8: Conclusions and perspectives**

  This section summarises the thesis's significant findings and outlines potential future research directions and application pathways.

CHAPTER 2

2 Literature review of PCL-based composite scaffolds in tissue engineering

Abstract

PCL is a widely used biodegradable polymer in tissue engineering due to its excellent biocompatibility, processability, and mechanical tunability. However, its clinical translation is limited by inherent drawbacks, including hydrophobicity, low bioactivity, and slow degradation. This review aims to provide a comprehensive and critical evaluation of PCL-based scaffolds, focusing on fabrication strategies, composite modifications, and their performance across diverse tissue engineering applications. Four primary fabrication techniques, including electrospinning, 3D printing, freeze-drying, and phase separation, are systematically compared with respect to structural characteristics, mechanical performance, scalability, and biological functionality. Various material modifications involving natural polymers (e.g., gelatine (Gel), chitosan (CS), collagen), synthetic polymers (e.g., Poly(lactic acid) (PLA), Poly(lactic-co-glycolic acid) (PLGA), Polyethylene glycol (PEG)), and inorganic or conductive additives (e.g., Hydroxyapatite (HA), metal oxides, carbon nanomaterials) are discussed for their roles in enhancing scaffold bioactivity, degradation rate, and tissue-specific functionality. Application-specific insights are provided on PCL-based scaffolds for bone and skin tissue regeneration. The review also highlights recent advances in intelligent scaffold design using computational modelling and artificial intelligence, and assesses sustainability, sterilisation, and regulatory challenges for clinical translation. Despite current limitations, PCL-based scaffolds show great promise for personalised and functional tissue regeneration.

2.1 Introduction

Tissue damage can be life-threatening due to its potential to impair vital organs (e.g., brain, lungs, heart, liver), cause severe haemorrhage (e.g., liver or spleen rupture), and trigger fatal complications such as infection and multi-organ failure. It also disrupts critical regulatory systems, including the immune, nervous, and endocrine networks. For instance, in severe burn injuries, mortality is primarily attributed to fluid loss and infection following extensive tissue necrosis. According to the WHO, the mortality rate exceeded 56.7% in the 2023 fuel depot explosion in Armenia [3]. Fractures similarly represent a primary global health concern, with high rates of morbidity, mortality, and socioeconomic impact. WHO projections indicate a 27% increase in the annual cost of fragility fractures by 2030 across several European countries, including Germany, France, the UK, Italy, Spain, and Sweden [4]. Tissue engineering has emerged as a vital strategy to address these challenges by promoting the repair and regeneration of damaged or non-regenerative tissues. Integrating principles from cell biology, materials science, and engineering, it aims to construct functional tissue substitutes.

PCL, introduced into biomedical use in the 1970s, remains widely applied with good processability, biocompatibility, and biodegradability [42]. However, its hydrophobicity and relatively high cost limit its further application. Current efforts focus on modifying PCL with hydrophilic or low-cost additives to improve cell interactions and reduce material cost, while maintaining mechanical and structural integrity [7]. To enhance their biological performance, natural polymers such as cellulose and its derivatives [43], Gel [16], collagen [44], and CS [45] are often incorporated into electrospun PCL matrices. These combinations improve bioactivity and nutrient permeability compared to pure PCL, while retaining greater mechanical strength than scaffolds composed solely of natural materials. In parallel, PCL is frequently blended with synthetic polymers, including PLGA [17], PLA [46], PEG [47], and polyvinyl alcohol (PVA) [48], to modulate degradation rates and further tune scaffold properties. Additionally, functional inorganic components such as metal oxides [19], phosphate-based compounds (e.g., HA, calcium phosphate) [20], carbon nanotube (CNT) [21], and graphene [22] are increasingly employed to enhance mechanical strength and electrical conductivity. Owing to these functional improvements, PCL-based scaffolds have been widely applied in bone, skin, nerve, dental, cartilage, and vascular tissue engineering.

Tissue engineering provides a practical approach to tissue repair by replicating the structure and function of the ECM with synthetic biomaterials [42]. Scaffolds, as their central element, are typically fabricated using techniques such as electrospinning, 3D printing, freeze-drying, or phase separation. Each method yields distinct structural outcomes: electrospinning produces nanofibrous networks [49], 3D printing enables precise control over architecture [50], freeze-drying forms soft porous matrices [51], and phase separation produces foam-like structures [52]. Their performance depends on a careful balance of degradability, biocompatibility, bioactivity, mechanical strength, and cost. Publication trends from the Web of Science (Figure 2. 1a) indicate steady growth in electrospinning and a sharp rise in 3D printing, while freeze-drying and phase separation remain less explored areas. Similar patterns are evident in studies on PCL-based scaffolds (Figure 2. 1b), where electrospinning and 3D printing are the predominant methods. Despite extensive research on PCL-based scaffolds, key knowledge gaps persist, particularly in systematically comparing fabrication techniques and developing targeted modification strategies to optimise scaffold performance for specific applications.

Therefore, a systematic review is warranted to clarify how different fabrication methods and material modifications influence the structural, mechanical, and biological performance of PCL-based scaffolds. Such insight is crucial for guiding the selection of application-specific materials, processing strategies, and functionalization approaches in tissue engineering. Such insight is essential for guiding the selection of application-specific materials, processing strategies, and functionalization approaches in tissue engineering. This section addresses these needs by critically evaluating four representative fabrication techniques (electrospinning, 3D printing, freeze-drying, and phase separation) with a focus on their underlying principles, advantages, limitations, and the properties of the resulting scaffolds. Comparative analyses are conducted to assess the suitability of each fabrication method and its associated functional additives for bone and skin tissue engineering applications. Furthermore, interdisciplinary considerations, such as clinical translation challenges, the integration of computational modelling and artificial intelligence into scaffold design, and the sustainability and scalability of production methods, are discussed.

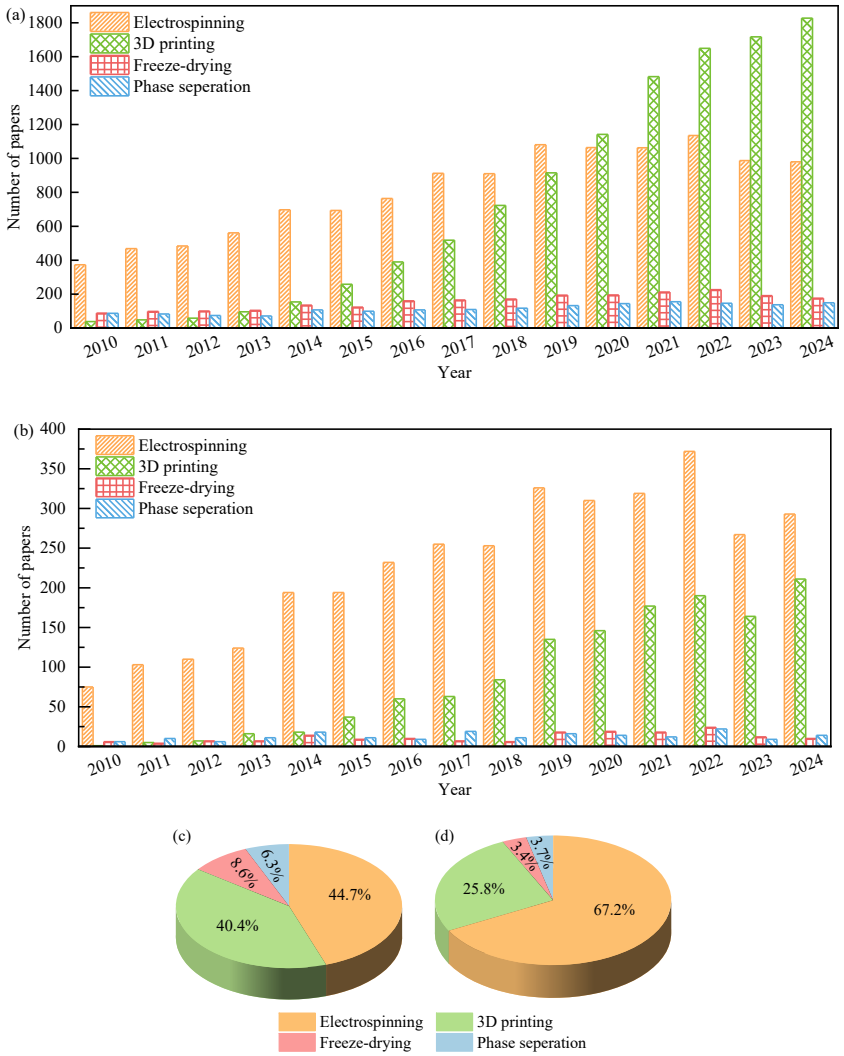

Figure 2. 1: Publication trends (2010–2024) and percentage distribution of total and PCL-based scaffolds (a–d), fabricated by four methods—electrospinning, 3D printing, freeze-drying, and phase separation—based on Web of Science data.

2.2 Fabrication methods of PCL-based scaffolds for tissue engineering

2.2.1 Electrospinning

Electrospinning offers a cost-effective, scalable approach to fabricating fibrous scaffolds with controllable morphology. Its fundamental setup and working principle are illustrated in Figure 2. 2a and b. Detailed composition and working principle of electrospinning are provided in Section 4.2. Electrospun membranes feature high surface area, porosity, and adjustable microstructure [53]. Fibre characteristics are primarily influenced by (a) polymer solution properties (e.g., molecular weight,

concentration, viscosity, conductivity), (b) process parameters (e.g., voltage, collector distance, flow rate), and (c) environmental conditions (e.g., temperature, humidity) [54]. This method enables the generation of nano- to microscale fibres that closely resemble the architecture of native ECM. However, the hydrophobic nature of PCL limits cell adhesion and nutrient diffusion. To address this, various composite strategies have been developed to improve the biofunctionality of PCL-based electrospun scaffolds. For example, Surucu et al. [55] fabricated core–shell PCL/CS scaffolds (see Figure 2. 2c-g), which exhibited an increased average pore size (3.17 ± 0.65 µm for PCL/CS vs. 1.08 ± 0.49 µm for PCL), reduced water contact angle (78.2 ± 2.5 ° for PCL/CS vs. 114.0 ± 3.2 ° for PCL), and improved cell adhesion compared to commercial controls. Although most mammalian cells range from 10 to 30 µm in diameter, electrospun nanofibrous scaffolds typically possess smaller pore sizes that primarily promote cell attachment and surface proliferation rather than deep cell infiltration. Additionally, the soft, flexible nature of electrospun membranes makes them particularly suitable for regenerating delicate tissues, such as skin, blood vessels, and nerves, where conformability and mechanical compliance are crucial.

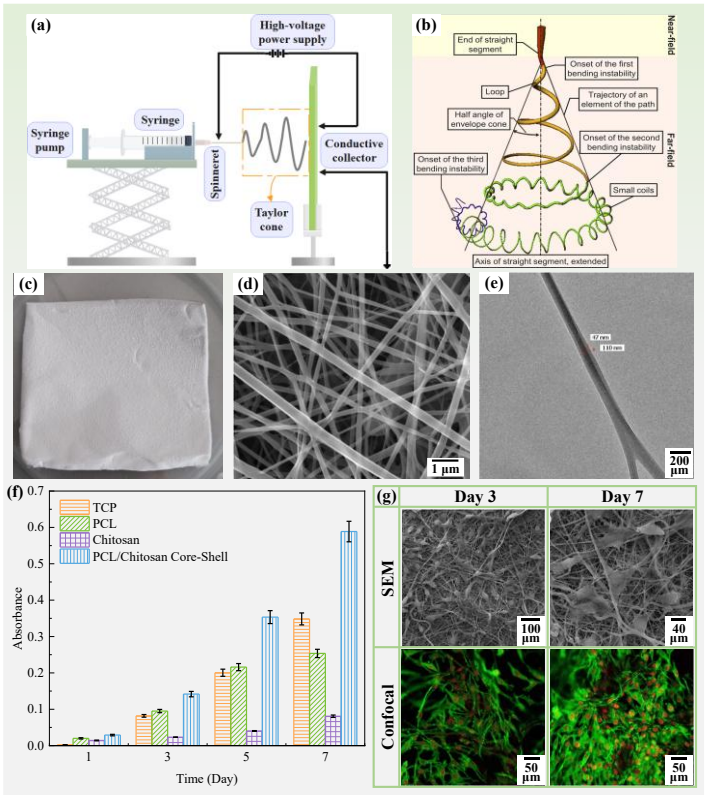

Figure 2. 2: Basic setup (a) and jet evolution (b) of electrospinning (Reproduced with permission from [53]. Copyright 2019 American Chemical Society). (c–g) morphological and biological characterisation of PCL/CS core–shell scaffolds: macrostructure (c), SEM (d), TEM (e), MTT

absorbance (f), and SEM/confocal images on days 3 and 7 (g) (Reproduced with permission from [55]. Copyright 2016 Elsevier).

2.2.2 3D printing

3D printing has become a key technology in tissue engineering, enabling the fabrication of scaffolds with well-defined, interconnected porous structures that support cell infiltration, proliferation, and nutrient transport [11]. Through computer-aided design (CAD) and layer-by-layer deposition, this technique offers precise structural control, making it ideal for personalised and anatomically specific applications. Common 3D printing methods include fused deposition modelling (FDM), direct powder extrusion, and electrohydrodynamic jetting (E-jetting). Although resolution is generally lower than that of electrospinning, which can achieve nano- to microscale features, 3D printing excels at producing larger, structurally complex constructs. PCL is widely used in 3D-printed scaffolds due to its biocompatibility, biodegradability, low melting point (~60 °C), and suitable rheological properties [56]. To further enhance functionality, it is often combined with metallic particles, inorganic fillers (e.g., HA), or other polymers, thereby improving mechanical performance, conductivity, and application-specific properties [50]. With their high structural fidelity and mechanical robustness, 3D-printed PCL-based scaffolds are well-suited for various tissue engineering applications, particularly for bone regeneration (Figure 2. 3a) [57]. The overall SEM morphology of 3D-printed scaffolds is consistent with that shown in Figure 2. 3b [58].

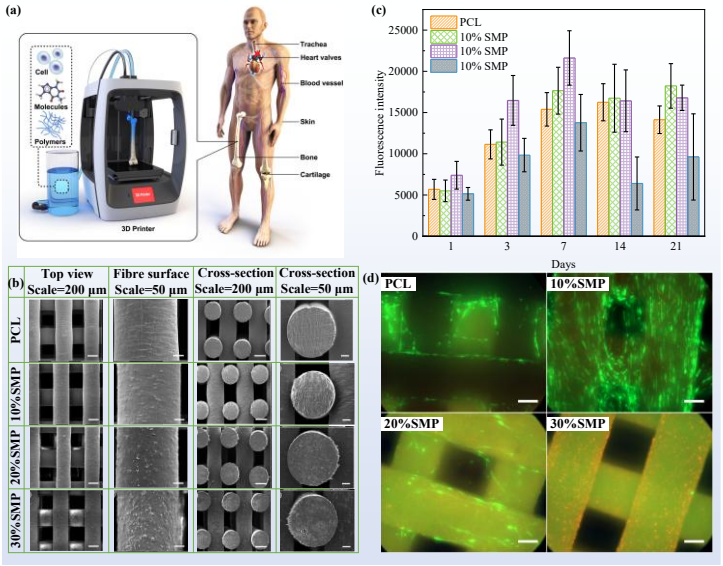

Figure 2. 3: Applications of 3D-printed scaffolds (a) (Adapted from [57]. Licensed under CC BY 4.0). (b–d) characterisation of PCL/SMP scaffolds: SEM images (b), fluorescence intensity (c), and cell metabolic activity (d) on days 1, 3, 7, 14, and 21 (scale bar: 100 μm) (Adapted from [58].

Licensed under CC BY 4.0).

2.2.3 Freeze-drying

Freeze-drying, also known as lyophilisation, is a standard method for fabricating porous scaffolds by removing solvents (e.g., 1,4-dioxane, acetic acid, and formic acid) through sublimation [10]. The process relies on solvent crystallisation templating, in which solvent crystals formed during the freezing of polymer solutions act as pore-forming agents. It typically involves three steps: (i) freezing the polymer solution to induce solvent crystallisation, (ii) reducing pressure to sublimate the frozen solvent, and (iii) yielding a porous scaffold after drying. Pore morphology is mainly governed by freezing temperature and cooling rate; lower temperatures and slower rates generally produce larger pores. Freeze-drying is valued in tissue engineering for its ability to deliver highly porous structures that support cell infiltration and nutrient transport. However, it also has notable limitations, including scaffold shrinkage, poor reproducibility, and low mechanical strength due to irregular pore formation. To overcome these issues, freeze-drying is often combined with techniques such as electrospinning [59] or 3D printing [60] to enhance structural and functional performance. As a representative example, Figure 2. 4a and d illustrate the fabrication process and SEM morphology of freeze-dried porous PCL/CS scaffolds, respectively [61].

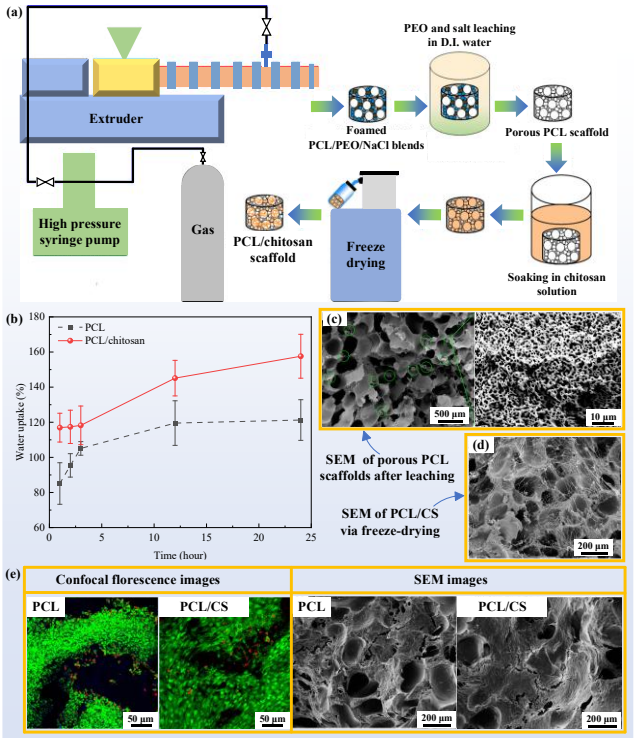

Figure 2. 4: Preparation of PCL/CS scaffolds by freeze-drying (a); water uptake of porous PCL

scaffolds with and without CS (b); SEM images of porous PCL (c) and PCL/CSNF scaffolds (d); and confocal fluorescence and SEM of 3T3 cells on PCL and PCL/CS scaffolds after 7 days (e) (green = live cells, red = dead cells) (Reproduced with permission from [61]. Copyright 2014 American Chemical Society).

2.2.4 Phase separation

Phase separation techniques can be broadly classified into four types: non-solvent-induced phase separation (NIPS), thermally induced phase separation (TIPS), vapour-induced phase separation (VIPS), and evaporation-induced phase separation (EIPS). Their fabrication principles are illustrated in Figure 2. 5a-d, while Figure 2. 5e presents the typical morphology of phase-separated scaffolds, using PCL/graphene as a representative example. NIPS forms a three-dimensional polymer network through solvent/non-solvent exchange [62]. Typically, the polymer solution is cast into a film, immersed in a non-solvent bath, and undergoes phase separation via solvent exchange, yielding a microporous membrane. This method is often combined with particulate leaching, using porogens such as salt crystals or wax beads, to enhance pore interconnectivity. In TIPS, polymers are dissolved in high-boiling-point, low-volatility solvents at elevated temperatures; upon cooling, phase separation and scaffold formation occur [63]. VIPS involves exposing the polymer solution to a humid atmosphere, where water vapour diffuses into the solution, inducing phase separation at the vapour–liquid interface [64]. EIPS, by contrast, relies on controlled solvent evaporation after casting the solution onto a substrate to form thin, porous films [65]. Scaffolds produced via phase separation typically exhibit interconnected porosity, which promotes cell adhesion, migration, and tissue ingrowth. However, the method is limited by poor morphological reproducibility and high sensitivity to processing parameters such as solvent type and temperature. Achieving structural consistency can be challenging, and residual solvents may introduce cytotoxicity. Furthermore, the resulting loose microstructure typically leads to poor mechanical strength.

In summary, electrospinning, 3D printing, freeze-drying, and phase separation each offer distinct structural and functional advantages for tissue engineering but also face limitations in scalability, reproducibility, and environmental sustainability. While the fundamental fabrication principles of these methods remain the same, their practical requirements and performance outcomes vary considerably across application domains. Their adaptation to water treatment is further discussed in Section 3.

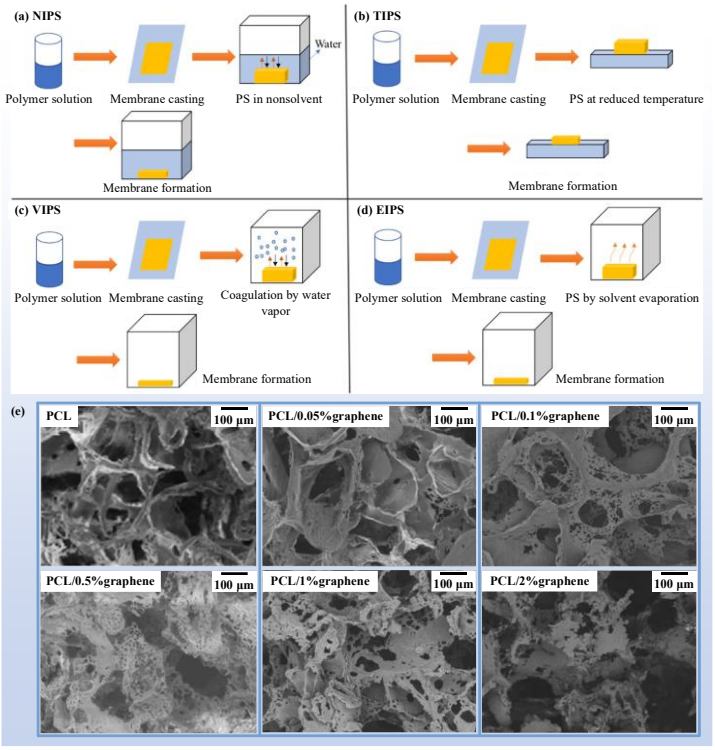

Figure 2. 5: Schematics of four phase separation techniques (a–d): NIPS, TIPS, VIPS, and EIPS (Reproduced with permission from [9]. Copyright 2022 Elsevier). (e) SEM of PCL/graphene scaffolds by EIPS (e) (Reproduced with permission from [66]. Copyright 2020 Elsevier).

2.3 Applications of PCL-based composite scaffolds in bone tissue engineering

Electrospun PCL-based scaffolds have been widely investigated for bone repair due to their biocompatibility and processability. However, the intrinsic hydrophobicity and limited bioactivity of pristine PCL hinder cell adhesion, proliferation, and osteogenic differentiation. To address these limitations, various functional additives have been incorporated to enhance both biological performance and mechanical strength. Lecithin, gold nanoparticles (AuNPs) [67], and cellulose nanocrystal (CNC) [68] have been shown to improve hydrophilicity and support cell proliferation. In particular, lecithin significantly promoted cell adhesion and upregulated osteogenic markers in mesenchymal stem cells [69]. Graphene oxide (GO) [70] provided a bioactive and conductive surface, further enhancing stem cell differentiation. Inorganic components such as HA [71], octacalcium phosphate (OCP) [72], and zinc oxide (ZnO) [73] have improved mineralisation capacity, antibacterial activity, and degradation control. Reinforcement with amine-functionalised carbon nanotubes (aSWCNTs) [74] or polypyrrole nanoparticles (PPy-NPs) [75] not only increased

conductivity and mechanical properties but also enhanced osteogenesis under electrical stimulation. Magnesium oxide (MgO) [76] further contributed to mechanical strengthening and early-stage mineral deposition. Collectively, these electrospun composites have demonstrated strong potential in promoting adhesion, proliferation, and osteogenic differentiation, making them promising for bone tissue engineering.

In contrast to electrospinning, which is better suited for flexible and superficial applications (e.g., skin tissue; see Section 2.4), 3D printing is more applicable to bone repair due to its ability to fabricate rigid, anatomically tailored scaffolds with interconnected porosity. Bone tissue requires structural stability and spatial organisation to support vascularisation, mineralisation, and mechanical loading. 3D printing provides precise control over architecture, pore size, and geometry, allowing for the design of biomimetic scaffolds that conform to complex defect sites. PCL-based composites printed via 3D techniques have incorporated HA [77], collagen-fixed nano-HA (C-nHA) [78], strontium-doped HA (SrHA) [79], and calcium silicate [80] to enhance mineralisation, mechanical integrity, and osteoinduction. For instance, Liu et al. [79] showed that PCL/SrHA scaffolds significantly promoted new bone formation in rat cranial defects compared to pristine PCL. Magnesium-based additives (e.g., Mg nanoparticles and MgO) have further improved degradation rates and angiogenic potential, thereby accelerating bone regeneration. Dong et al. [81] demonstrated that Mg/PCL composites (3 wt.% Mg) enhanced biocompatibility and osteogenesis in vivo. Biopolymer incorporations, such as Gel [103], SF [73], bacterial cellulose (BC) [104], and PLA [105], have enhanced hydrophilicity, compressive strength, and cell adhesion. Vyas et al. [58] reported that adding 10 wt.% silk microparticles (SMP) to PCL scaffolds enhanced mechanical performance and supported osteogenic differentiation of adipose-derived stem cells (Figure 2. 3b-d). Additional modifications, such as PEG-induced micropore modulation [85], gradient architecture design [86], electrospinning/3D printing hybrids [82], and collagen immobilisation via NaOH surface activation [78], have further improved cell–material interactions. These modifications also promoted cell adhesion, proliferation, and osteogenic differentiation, highlighting their promise as effective candidates for bone tissue engineering. Finally, integration of functional agents, such as graphene [87], silver nanoparticles (AgNPs) [88], and polyaniline (PANI) [89], has endowed scaffolds with electrical responsiveness, immunomodulatory effects, and antibacterial properties. Controlled

delivery systems, including aspirin-loaded liposomes (Asp@lipo) [90], have also shown promise in promoting bone regeneration in defect models. In summary, 3D-printed PCL-based composite scaffolds have achieved synergistic optimisation of mechanical and biological properties through multi-scale structural design and multifunctional integration, highlighting their promising potential for clinical translation in bone tissue engineering.

Freeze-dried PCL-based scaffolds have also shown promise in bone tissue engineering. Incorporating phosphorylated PCL with magnetic nanoparticles (MNPs) significantly improved osteoconductivity and osteoinductivity by mimicking the native bone environment, promoting calcium deposition, and upregulating osteogenic gene expression [91]. PCL/Gel/berberine scaffolds fabricated via freeze-drying demonstrated effective bone repair in a rat cranial defect model, with berberine enhancing scaffold degradability and promoting cell proliferation and osteogenesis [92]. In another approach, wet-spun PCL scaffolds combined with fibrinogen were freeze-dried into 3D composite structures that improved Saos-2 cell adhesion, spatial distribution, mechanical strength, and intercellular connectivity [93]. These results suggest that multi-component synergy, achieved through rational composition design and freeze-drying fabrication, offers an effective strategy to enhance the structural and functional performance of PCL-based scaffolds for bone regeneration.

Phase separation techniques have also been applied to develop porous PCL-based scaffolds with well-connected pore networks for bone tissue engineering. TIPS and NIPS are often used in combination with particle leaching (e.g., salt leaching) to construct macro–microporous architectures [94], enabling cell infiltration, nutrient diffusion, and tissue ingrowth. Incorporation of natural components such as Gel [94], zein [95], starch [96], and duck's feet collagen (DC) [97] has improved hydrophilicity, degradation rates, and osteoinductive properties. Inorganic additives, including graphene [66], biphasic tricalcium phosphate (BCP) [98], HA [99], and bioactive glass [100], have enhanced mechanical strength and mineralisation. For example, PCL scaffolds fabricated via NIPS with DC and particle leaching exhibited a biomimetic hierarchical structure, increased mineralisation, and upregulated osteogenic gene expression [97]. Similarly, PCL/graphene scaffolds prepared by phase separation achieved porosity above 85%, improved compressive strength and wettability, and supported cell adhesion and nutrient transport (Figure 2. 5e) [66]. Typically, PCL-based composite scaffolds produced via phase separation exhibit porosity in the 70-90% range, structural tunability,

functional integration, and excellent biological performance, including support for cell adhesion, proliferation, and osteogenic differentiation, providing a promising pathway for developing high-performance biomimetic bone substitutes in regenerative medicine.

In general, scaffold porosity is dictated by the fabrication method, following the trend: freeze-drying > phase separation ≈ 3D printing > electrospinning, while mechanical strength follows the order: 3D printing > electrospinning > freeze-drying ≈ phase separation. The performance of PCL-based scaffolds for bone regeneration is strongly dictated by fabrication method and composite formulation. 3D-printed scaffolds consistently exhibit the highest mechanical strength (often exceeding 50 MPa) and structural precision, making them most suitable for load-bearing applications, although their porosity is relatively limited. Electrospun scaffolds are mechanically weaker (1–15 MPa) but provide ECM-like fibrous networks that favour surface cell adhesion while restricting deep tissue infiltration. Freeze-dried and phase-separated scaffolds achieve high porosity (70–90%), which promotes vascularisation and nutrient transport, but they suffer from low mechanical strength (typically <5 MPa) and poor reproducibility. Overall, bone regeneration benefits most from scaffolds that balance porosity with mechanical integrity: 3D printing ensures structural reliability, while freeze-drying and phase separation offer biologically favourable microenvironments that require reinforcement to overcome their mechanical shortcomings. Mechanical performance can be further enhanced by incorporating inorganic additives such as HA (e.g., SrHA, C-nHA, nano-HA/PCL), metal/metal oxides (e.g., Mg, ZnO, AuNPs), nanoparticles (e.g., MNPs, SMP, nanoclay), graphene, and calcium silicate, which collectively improve stiffness, bioactivity, and load-bearing capacity. Hydrophilicity, cell adhesion, and osteogenic potential are primarily enhanced by blending natural polymers, such as Gel, collagen, CNCs, zein, and lecithin, thereby increasing wettability and promoting osteogenic differentiation.

Each fabrication method offers distinct advantages. Electrospinning produces biomimetic fibres suitable for superficial or non-load-bearing defects [82]. Freeze-drying and phase separation yield highly porous structures that are beneficial for vascularisation but are limited by poor strength [60]. In contrast, 3D printing enables the fabrication of rigid, anatomically tailored scaffolds with excellent stability. However, it is constrained by high equipment cost, operational complexity, and limited resolution in reproducing nanoscale ECM-like features [50, 82]. To address the limitations of

individual methods, hybrid approaches have emerged, particularly combining 3D printing with electrospinning, to integrate the mechanical robustness of printed frameworks with the biological advantages of nanofibres, enabling multi-scale, functionally graded scaffolds tailored for complex bone regeneration [101].

2.4 Applications of PCL-based composite scaffolds in skin tissue engineering

In tissue engineering, PCL-based scaffolds have been widely applied for skin wound healing. Electrospinning and freeze-drying are commonly used fabrication techniques, as both can generate scaffolds with the softness, flexibility, and resilience required for skin tissue repair. To improve hydrophobicity, natural polymers have been extensively incorporated with PCL to enhance both structural and biological properties. Blending PCL with cellulose, CS, Gel, SF, or collagen has been shown to improve hydrophilicity and promote cellular attachment [102]. For example, Chandika et al. [103] developed electrospun PCL/fish collagen scaffolds functionalised with chitooligosaccharides (COS), which improved hydrophilicity and significantly accelerated wound healing in vivo by promoting re-epithelialisation and dermal tissue maturation (Figure 2. 6). Reinforcement with CNCs and GO has also enhanced mechanical strength and electrical conductivity while providing a more biomimetic environment conducive to cell proliferation and migration [104, 105].

Plant-derived components have further enhanced the scaffold's biofunctionality. The incorporation of peppermint essential oil (PEP) into PCL-based scaffolds imparted inherent antibacterial activity, providing an antibiotic-free strategy for wound-dressing applications [106]. Composite scaffolds combining PCL with zein and gum Arabic (GA) have been designed to mimic the ECM architecture better while improving biocompatibility and mechanical performance [107]. Baghersad et al. [108] integrated aloe vera (AV) and tetracycline hydrochloride (TCH) into PCL/Gel electrospun scaffolds, confirming AV incorporation via FTIR analysis of glycosidic bond peaks at 1050–1090 cm^{-1}. These scaffolds exhibited excellent hydrophilicity (WCA < 40 °) and supported high fibroblast viability (81% at 72 hours). In vivo studies further demonstrated significantly enhanced wound closure compared to control groups. Collectively, both in vitro and in vivo results support the potential of

multifunctional PCL-based composite scaffolds to accelerate epidermal regeneration, promote angiogenesis, and reduce inflammation. Electrospun scaffolds, in particular, are well-suited for superficial wound applications due to their nanofibrous structure, which promotes cell adhesion, proliferation, and migration. These properties make them ideal candidates for use in epidermal repair, haemostasis, and infection control in skin tissue engineering.

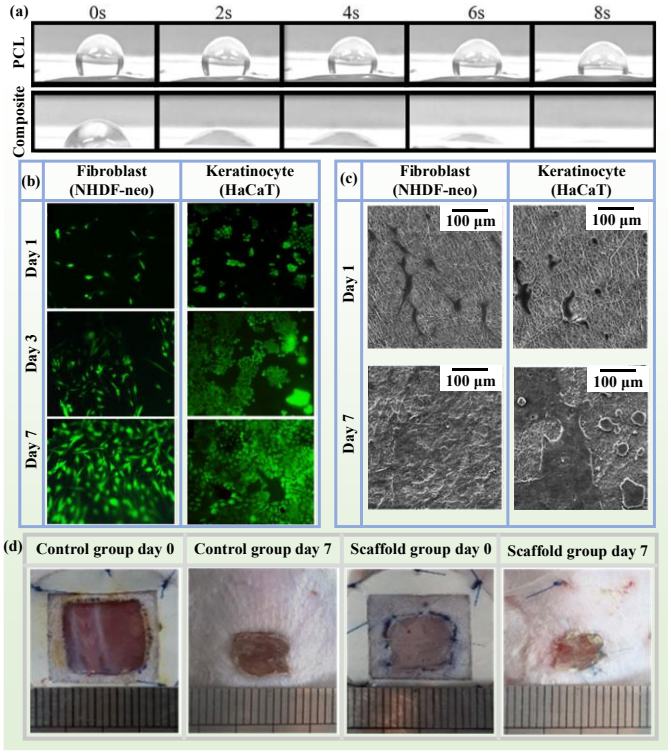

Figure 2. 6: WCA of PCL and composite scaffolds (a); fluorescence (b) and SEM (c) of NHDF-neo and HaCaT cells on composite scaffolds; and wound-healing performance vs control (Tegaderm) at 7 days (d). Composite mats: PCL/collagen/COS, with fish collagen:PCL = 9:1 (Reproduced with permission from [103]. Copyright 2021 Elsevier).

Freeze-drying is also an effective method for fabricating PCL-based scaffolds that aim to enhance wound healing. Incorporating synthetic polymers (e.g., Poly(L-lactide) (PLLA), PEG) [110], natural biopolymers (e.g., zein, CS, Gel) [111], or therapeutic agents [112] into PCL enables the production of structurally uniform, highly porous, and interconnected scaffolds via freeze-drying. These composite systems exhibit improved hydrophilicity, antibacterial activity, and overall biofunctionality. For example, Hakim et al. [113] developed PCL scaffolds blended with extra-virgin olive oil (EVOO), observing an inverse relationship between pore size and EVOO content (0–7 wt.%), while maintaining non-cytotoxicity and antibacterial properties that support cell growth. In another study, Jing et al. [61] fabricated PCL/CS scaffolds with 78% porosity using a combined approach of

extrusion foaming, porogen leaching (PEO/NaCl), and freeze-drying. The addition of CS nanofibres modestly increased the compressive modulus and significantly enhanced water uptake by 35% compared to pure PCL scaffolds. Confocal microscopy and SEM analysis revealed spindle-shaped cell morphology and increased proliferation on composite scaffolds, in contrast to the limited cell activity observed on pristine PCL (see Figure 2. 4e).

Unlike bone repair, skin regeneration relies more on hydrophilicity, biological activity, and degradability than on high mechanical strength. Electrospun scaffolds typically exhibit tensile strengths of 3–10 MPa and feature fibrous architectures that support epithelialization and facilitate rapid wound closure. Freeze-dried scaffolds achieve higher porosity (>80%) and interconnected networks that enable cell infiltration and vascularisation, though their compressive strength usually remains modest (2–5 MPa). An exception is PCL/Zein scaffolds, which reached compressive strengths of ~10 MPa, showing that specific composite formulations can partially offset the mechanical limitations of freeze-drying. Functional enhancements are mainly introduced through natural and plant-derived additives. Gel, collagen, CS, and SF consistently improve wettability and fibroblast adhesion, while AV, PEP, GA, and calendula extracts provide antibacterial, anti-inflammatory, or pro-healing functions. Reinforcement with GO, CNC, or WS NPs further improves tensile properties and promotes cell proliferation. In terms of degradation behaviour, skin scaffolds are generally designed for relatively rapid resorption over weeks, aligning with wound healing timelines and contrasting with the slower degradation rates required for bone scaffolds.

Electrospun scaffolds tend to exhibit higher mechanical strength due to dense fibre packing and reduced porosity, making them suitable for superficial wound healing by supporting epithelialisation and cell migration. Freeze-dried scaffolds, by contrast, generate highly porous sponge-like structures. While mechanically weaker, they are better suited for full-thickness wounds, enabling cell embedding, sustained release of growth factors, and vascularised tissue regeneration. In summary, electrospinning and freeze-drying offer complementary advantages: electrospun scaffolds are ideal for rapid re-epithelialisation and superficial repair. In contrast, freeze-dried scaffolds are better suited for complex, deep-seated tissue defects. The specific biological and mechanical requirements of the target wound should therefore guide the selection of the fabrication method.

2.5 Interdisciplinary integration of computational modelling and machine learning

With the development of digital manufacturing and intelligent design technologies, computational modelling and ML have increasingly contributed to the advancement of tissue engineering, offering broad application potential in biomaterial design, scaffold fabrication, cell modelling, bioprinting, and personalised regenerative therapies by addressing limitations inherent in conventional approaches [114]. Finite element analysis (FEA) is widely employed to evaluate stress distribution and mechanical performance, providing a robust mechanical basis for tailoring scaffold architecture to the functional demands of bone tissue engineering [115]. AI algorithms significantly reduce computational costs, enabling rapid prediction of mechanical properties and streamlining both design and experimental validation. ANN-based models have proven effective in optimising electrospinning and 3D bioprinting parameters and material compositions, and in controlling scaffold morphology, thereby improving biocompatibility and fabrication reproducibility [116]. In addition, ML algorithms can integrate patient-specific clinical data to assist in the design of personalised scaffolds and regeneration protocols, thereby improving therapeutic precision and efficacy [117]. ML facilitates the modelling of cellular behaviour and tissue development by elucidating complex interactions between cell proliferation, microenvironmental cues, and growth dynamics [118]. Deep learning, a subfield of ML, has demonstrated exceptional capabilities in analysing cell images, identifying cell types, and predicting cell behaviour, which are critical for optimising tissue engineering strategies [119].

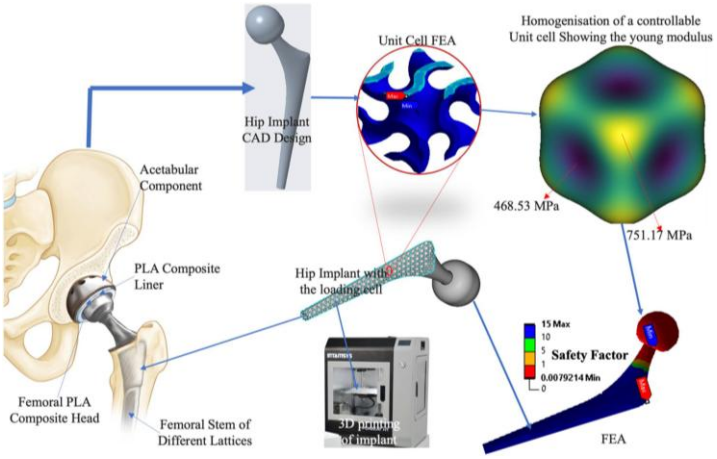

Figure 2. 7: Modelling process with FDM for loading biochemical signals on bone implant scaffolds (Adapted from [121]. licensed under CC BY 4.0).

More recently, the integration of FEA with AI, particularly ANNs, has improved simulation efficiency and accelerated design iterations [120]. For example, a combined FEA–ANN framework was used to design scaffolds with gradient porosity, successfully predicting cell infiltration capacity and guiding the fabrication process to meet both biological and mechanical requirements [116, 121]. Additionally, AI-assisted lattice design has enabled the 3D printing of biomimetic scaffolds that replicate the mechanical characteristics of native bone while addressing patient-specific anatomical needs (Figure 2. 7) [121]. These constructs demonstrated enhanced load-bearing performance and supported robust cell proliferation in vitro.

Despite its promising outlook, the integration of ML into tissue engineering remains in its early stages. Continued innovation and interdisciplinary collaboration are expected to unlock more advanced applications. Overall, integration of computational modelling and AI, with their predictive power, optimisation capability, and support for personalisation, is increasingly recognised as an enabling technology for improving scaffold design, process efficiency, and clinical relevance in tissue engineering.

2.6 Evaluation of different fabrication approaches

In tissue engineering, electrospinning, 3D printing, freeze-drying, and phase separation are widely employed for the fabrication of PCL-based scaffolds, each with distinct profiles in flexibility, mechanical strength, porosity, reproducibility, environmental sustainability, and cost-effectiveness. Electrospinning offers high flexibility and biomimetic nanofibrous morphologies with relatively low equipment requirements; however, its low porosity and poor reproducibility are limiting factors. 3D printing consumes minimal solvents yet requires higher energy and initial equipment investment; however, it provides excellent reproducibility, process cleanliness, and strong potential for scalable, patient-specific scaffold production [122]. Freeze-drying produces highly porous, sponge-like structures that are favourable for vascularisation and deep tissue infiltration; however, the method is energy-intensive and costly, and it yields weak mechanical properties [123]. Phase separation can produce hierarchical pore architectures with balanced mechanical and biological features, but it relies on toxic organic solvents, suffers from low reproducibility, and offers poor mechanical stability [124].

Material costs among the four methods are generally comparable; however, 3D printing becomes

more economical at scale due to its high throughput and automation [122]. Thus, electrospinning is well-suited for early-stage research and applications, such as skin repair or nerve guidance. Freeze-drying and phase separation remain essential for soft tissues that require high porosity, while 3D printing is best suited for bone regeneration and load-bearing defects. Future strategies are expected to integrate multiple techniques, for example, combining 3D printing with electrospinning, to merge architectural precision with ECM-mimetic features. In parallel, greener fabrication approaches, such as the use of low-toxicity solvents and solvent recovery systems, will be crucial in improving environmental sustainability.

According to current knowledge, Figure 2. 8 presents a radar chart comparing six key performance indicators (mechanical strength, porosity, flexibility, reproducibility, environmental sustainability, and industrial-scale cost-effectiveness) for materials fabricated by electrospinning, phase separation, 3D printing, and freeze-drying. This visualisation provides an intuitive overview of the relative strengths and limitations of each fabrication method in tissue engineering applications.

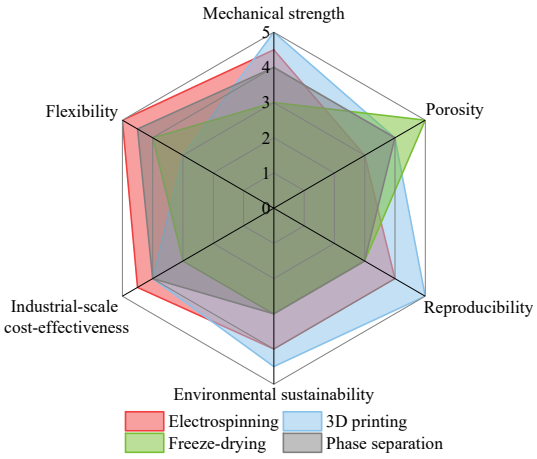

Figure 2. 8: Radar chart comparing six key performance indicators, including mechanical strength, porosity, flexibility, reproducibility, environmental sustainability, and industrial-scale cost-effectiveness, of scaffolds fabricated using electrospinning, 3D printing, freeze-drying, and phase separation.

2.7 Conclusions

This section provides a comprehensive and critical overview of PCL-based scaffolds for tissue engineering, with an emphasis on fabrication strategies, material modifications, and performance in application-specific contexts. Four primary fabrication techniques (electrospinning, 3D printing, freeze-drying, and phase separation) are compared based on structural features, processing flexibility,

mechanical properties, and biological functionality. Electrospinning offers the most balanced performance and enables the generation of nanofibrous scaffolds that closely mimic the ECM, making it particularly well-suited for soft tissues such as skin. In contrast, 3D printing offers superior structural precision and customizability, making it ideal for load-bearing applications. Freeze-drying and phase-separation techniques enable the generation of highly porous scaffolds with interconnected channels; however, challenges with reproducibility and mechanical stability limit their standalone use. These challenges have increasingly been addressed through hybrid fabrication approaches that integrate the strengths of multiple techniques.

In terms of material composition, pure PCL is limited by its hydrophobicity, low bioactivity, and slow degradation rate. To address these issues, natural polymers such as Gel, CS, collagen, and SF, as well as synthetic polymers including PLA, PLGA, PEG, and PVA, have been incorporated to enhance biocompatibility, degradation kinetics, and cellular interactions. Inorganic and conductive additives, such as HA, metal oxides, CNTs, and graphene, have been introduced to improve mechanical properties, modulate electrical conductivity, and promote lineage-specific differentiation, including osteogenesis, neurogenesis, and angiogenesis. Ultimately, the performance of PCL-based scaffolds depends on the interplay between fabrication technique and composite formulation. A tailored combination of structural design and material modification is crucial to meet the specific biological and mechanical requirements of various tissue engineering applications.

CHAPTER 3

3 Literature review of PCL-based composite scaffolds in water treatment

Abstract

PCL-based materials have attracted increasing attention in water treatment due to their biodegradability, tunable structure, and compatibility with various functional modifications. This section systematically summarises recent progress in the development and application of PCL-based composite materials across four central treatment mechanisms: adsorption, membrane separation, and photocatalytic degradation. Emphasis is placed on how different fabrication methods, including electrospinning, phase separation, freeze-drying, and 3D printing, affect membrane morphology, surface functionality, and pollutant removal performance. Strategies to enhance the adsorption and separation efficiency of PCL-based membranes are discussed, focusing on polymer blending, incorporation of nanofillers (e.g., GO, metal oxides), and structural design innovations. The review also highlights multifunctional systems integrating photocatalysis with separation or adsorption. Despite promising laboratory results, challenges persist in terms of mechanical durability, regeneration, scalability, and performance under real-world wastewater conditions. This section provides a comprehensive overview of the state of the art in PCL-based water treatment materials, outlining future research directions to advance their practical applications.

3.1 Introduction

Water pollution and freshwater scarcity have become pressing global challenges, intensified by rapid industrialisation, urban expansion, and population growth. Access to clean water is essential for

human health and sustainable development. However, more than 80 countries are already experiencing water shortages, and nearly 25% of the global population lacks reliable access to safe freshwater sources [1]. As global water scarcity grows, wastewater reclamation and reuse have emerged as essential strategies to supplement conventional water resources. Wastewater contains diverse pollutants originating from domestic, industrial, and agricultural activities. Organic contaminants such as oils, fats, proteins, volatile organic compounds (VOCs), and petroleum derivatives mainly arise from domestic sewage, food processing, and petrochemical industries [22]. Inorganic pollutants, including heavy metals, acids, alkalis, and suspended solids, are associated with manufacturing, mining, and construction. Agricultural runoff and livestock operations introduce excess nitrogen and phosphorus, causing eutrophication and ecosystem degradation [126], while pesticides and pharmaceuticals further contaminate surface and groundwater [6]. Moreover, pathogenic microorganisms from domestic, medical, and aquaculture wastewater threaten both public health and aquatic life [125]. The complex composition and environmental persistence of these pollutants highlight the necessity for effective and adaptable water treatment strategies.

Currently, several treatment approaches are widely employed to address these challenges, including adsorption, membrane separation, photocatalysis, and biological degradation. Adsorbents are used to remove heavy metals, dyes, and organic molecules through physical and chemical interactions [6]. Membrane-based methods, such as ultrafiltration, microfiltration, nanofiltration, and forward osmosis, achieve selective separation by tuning pore size and surface hydrophilicity, often offering high separation efficiency and good antifouling performance [23]. Photocatalytic processes, especially those utilising TiO_2 or ZnO, facilitate the breakdown of organic contaminants under light irradiation [127]. As illustrated in Figure 3. 1a, interest in research on adsorption, membrane filtration, and photocatalysis has steadily grown over the past decade. To improve the functionality of these materials, various fabrication techniques have been developed, including electrospinning [128], phase separation [129], freeze-drying [130], and 3D printing [131]. These methods enable control over microstructure and surface properties, allowing materials to be tailored to specific treatment needs. Over the past decade, research on electrospun membranes has dominated the field, representing approximately 65% of relevant publications. In comparison, studies on phase separation, freeze-drying, and 3D printing have also grown steadily, accounting for 14.2%, 12.4%, and 8.4%,

respectively (Figure 3. 1b).

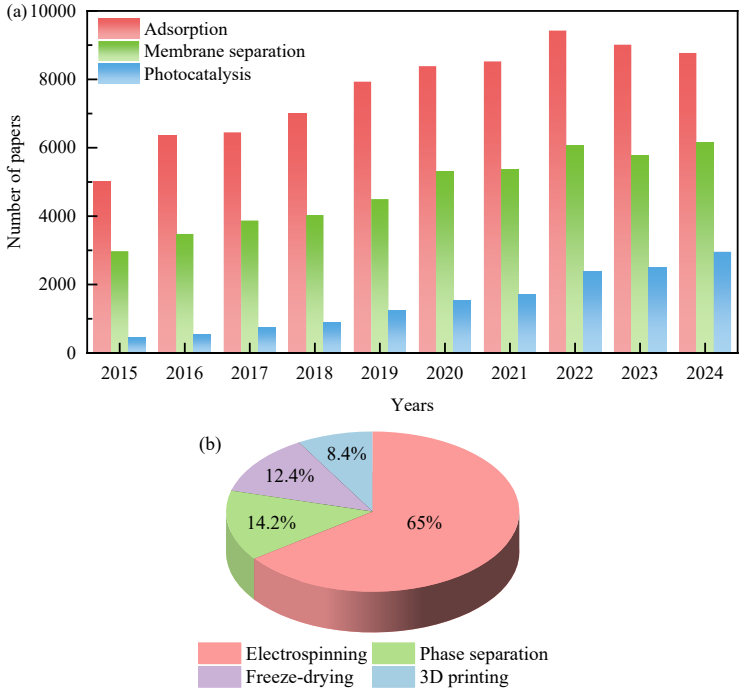

Figure 3. 1: (a) Number of publications on adsorbents, filtration membranes, and photocatalytic materials for water treatment (Web of Science data); (b) proportion of studies on membranes fabricated by electrospinning, phase separation, freeze-drying, and 3D printing for water treatment over the past decade.

The processability of PCL across multiple fabrication routes makes it suitable for developing a range of functional water-treatment materials [29, 30]. Recent studies have focused on enhancing the properties of PCL-based composites by incorporating nanoparticles, natural polymers, and photocatalysts to improve pollutant removal, mechanical stability, and long-term durability. These composite systems combine the advantages of each component, resulting in improved performance and multifunctionality [30, 31]. For instance, incorporating natural polymers, such as CS or cellulose, into PCL matrices enhances hydrophilicity and mechanical strength, thereby improving membrane separation efficiency and resistance to fouling [130]. Similarly, embedding TiO_2 or ZnO photocatalysts enhances their dispersion and reactive surface area, promoting more effective degradation of organic pollutants [127].

Despite growing interest, a comprehensive synthesis of the latest developments in the fabrication and functionalisation of PCL-based materials for water treatment remains absent. To bridge this gap, this section systematically examines recent progress in the use of PCL-based composites across adsorption, membrane separation, and photocatalytic degradation. It also evaluates the impact of

diverse fabrication techniques, mainly including electrospinning, phase separation, freeze-drying, and 3D printing, on the physicochemical properties and water treatment efficiency of these materials. By offering a comparative analysis of structural design strategies and their application outcomes, this section aims to provide a knowledge base for future material innovation and system integration, ultimately promoting the translation of PCL-based composites into scalable, sustainable solutions for practical water pollution challenges.

3.2 Functional applications of PCL-based materials in water treatment

3.2.1 Functionalized PCL composites for selective adsorption

The adsorption performance of PCL-based materials in aqueous environments is primarily determined by their porous structures and surface functionalities. Depending on their functionalisation and composite design, these materials have been applied for the removal of various water contaminants, including oils, organic dyes, heavy metal ions, and emerging pollutants such as pharmaceuticals. Fabrication techniques such as electrospinning and phase separation produce materials with high specific surface areas and interconnected porosity, promoting the physical capture of pollutants from aqueous media [29]. Chemical adsorption can be further enhanced by functionalizing the surface with carboxyl, amino, or other reactive groups [132] or by incorporating high-affinity components such as CS, GO, and metal-organic frameworks (MOFs) [133, 134]. Additional mechanisms, including electrostatic interactions, coordination complexation, hydrophobic effects, and π–π stacking, contribute to improved adsorption selectivity and capacity [133, 135].

3.2.2 PCL-based membranes for selective separation

The separation efficiency of PCL-based membranes is governed by their selective permeability and surface characteristics, enabling the removal of pollutants via size-exclusion and interfacial interactions. Due to its excellent film-forming properties and mechanical stability, PCL serves as an effective matrix for fabricating micro- and nanostructured membranes, particularly via electrospinning and phase separation. These membranes act as physical barriers to contaminants such

as dyes, microorganisms, and colloids, primarily via molecular sieving [136]. Incorporation of hydrophilic modifiers improves surface wettability, reduces fouling, and enhances both water flux and antifouling performance [137]. In nanofiltration and ultrafiltration systems, removal of heavy metals and organic pollutants is further facilitated by electrostatic repulsion and hydrophilic–hydrophobic interactions [138].

3.2.3 PCL-supported photocatalytic membranes for advanced oxidation

Photocatalytic degradation has emerged as a promising strategy for water treatment. Commonly used photocatalysts include metal oxides (e.g., TiO_2, ZnO, Fe_3O_4) and organic semiconductors (e.g., graphitic carbon nitride (g-C_3N_4), carbon quantum dots (CQDs)) [139]. Upon light irradiation, the embedded photocatalysts generate electron–hole pairs, which react with water and oxygen to form reactive oxygen species (ROS) such as ·OH and $\cdot O_2^-$. These ROS rapidly oxidise and decompose organic pollutants, such as antibiotics, pesticides, and dyes, into non-toxic end products, including CO_2 and H_2O [140]. The PCL matrix provides mechanical stability and a large surface area, facilitating the exposure of active sites and enhancing overall photocatalytic efficiency. Furthermore, the photocatalytic process supports material regeneration and self-cleaning under light, eliminating the need for additional chemical or physical regeneration steps [141]. The porous nature of PCL-based photocatalytic membranes also enables simultaneous adsorption and filtration, imparting multifunctionality to these systems [142, 143].

3.3 Functional optimisation of PCL-based composites for water treatment

Fabrication methods introduced in Section 2.2, including electrospinning, 3D printing, freeze-drying, and phase separation, are also widely applied in the design of PCL-based materials for water treatment. Unlike their roles in tissue engineering, where emphasis is placed on biomimicry, porosity, and cell–material interactions, the requirements in water treatment are centred on stability, reusability, and pollutant removal efficiency. Accordingly, the same techniques exhibit different strengths and limitations when translated into this context.

3.3.1 Optimisation strategies for PCL-based adsorbents

The inherent hydrophobicity of PCL and limited surface functionality constrain performance in adsorption and complex separation scenarios. To address these limitations, two primary strategies have been explored: material modification and structural design. Material modifications involve polymer blending and the integration of functional additives. For instance, blending electrospun PCL adsorbents with PLLA [144] or polyvinylpyrrolidone (PVP) [145] improves mechanical strength and adsorption efficiency, while nanofillers such as GO [146], Fe_3O_4 [147], SiO_2 aerogels [148], and activated carbon [149] introduce properties like magnetic responsiveness, hierarchical porosity, and enhanced hydrophilicity. GO facilitates adsorption through π–π interactions, and Fe_3O_4 enables magnetic separation. Additional examples include phenyl polysilsesquioxane (ph-LPSQ) for improved chemical resistance [150] and perfluorooctyl acrylate (TFOA) copolymer (PCL-b-PTFOA) copolymers for enhanced mechanical performance and self-cleaning capability [151].

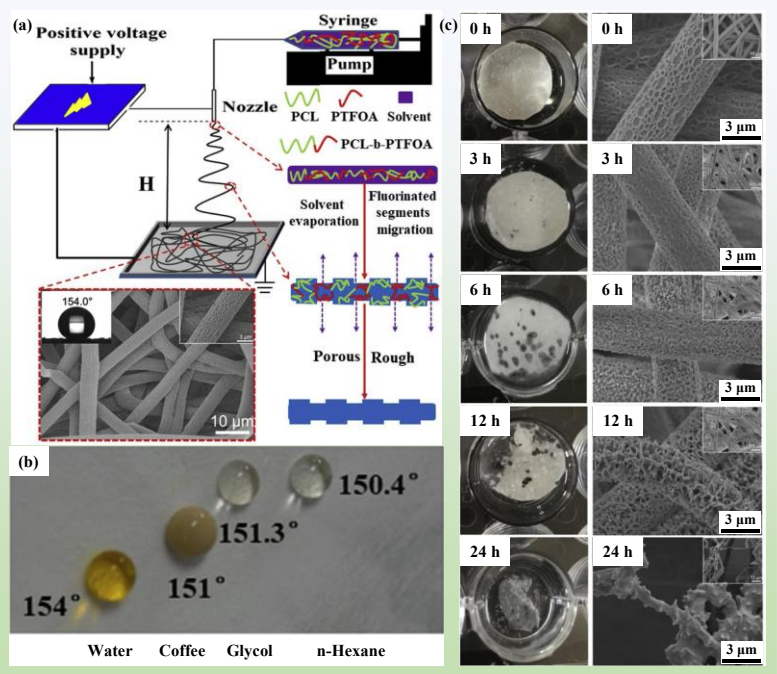

Figure 3. 2: (a) Schematic of electrospun PCL-b-PTFOA nanofibre membrane; (b) droplet behaviour on the membrane surface; (c) biodegradation progression shown by photographs and SEM images at different time intervals (Reproduced with permission from [151]. Copyright 2020 Elsevier).

Electrospun PCL-b-PTFOA membranes exhibit increased elongation at break (from 152.97% to 678.15%) and tensile strength (from 4.11 to 5.78 MPa), as well as superior degradability, antifouling properties, and self-cleaning performance (Figure 3. 2). These modifications have led to membranes

capable of achieving separation efficiencies above 99%, with high durability under harsh pH and temperature conditions. Structural designs further boost separation performance. Hierarchical architectures created by alternating electrospinning and electrospraying mimic lotus-leaf surfaces, resulting in superhydrophobicity and enhanced oil/water separation (Figure 3. 3) [152]. These structures increase roughness and air-pocket capacity, leading to superhydrophobicity (WCA > 150 °) and high oil sorption (30–50 g/g), while maintaining >99.9% separation efficiency for oils such as n-hexane and wax oil [28, 153]. Layered PCL/GO membranes and porous composite structures demonstrate similarly high performance, achieving 99.94% hexane/water separation and 35.8 g/g adsorption capacity [154].

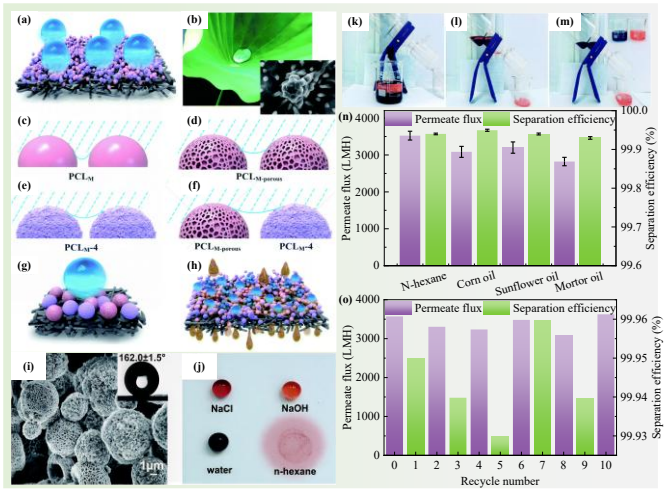

Figure 3. 3: (a) PCL composite membrane; (b) natural lotus leaf structure; (c) PCL microspheres; (d) porous PCL microspheres; (e) PCLM-4 membrane; (f) comparison between porous microspheres and PCLM-4; (h) schematic of the oil/water separation mechanism; (i) SEM and (j) wettability of the PCL composite membrane; (k–m) separation of n-hexane (red)/water (blue) mixtures; (n) permeate flux and separation efficiency; (o) performance comparison after 1 and 10 cycles (Reproduced with permission from [152]. Copyright 2019 Royal Society of Chemistry).

Phase separation techniques offer an effective route to fabricate multiscale porous adsorbents, supporting additive dispersion and rapid contaminant uptake. Mechanical reinforcement is achieved by embedding electrospun poly (methyl methacrylate) (PMMA) fibres [155] or by incorporating nanofillers such as multiwall carbon nanotubes (MWCNTs) [156], significantly improving Young's modulus and yield stress. Functionally, PCL-based adsorbents combined with MOFs [157], clay minerals [29], or metal oxides [158] exhibit strong selectivity and reusability. Amine-functionalized MOFs mixed with PCL adsorbents exhibited uniform porosity and high adsorption capacities for methyl orange (309 mg/g) and methylene blue (208 mg/g), with stable performance over 10

adsorption–desorption cycles (Figure 3. 4) [157]. NIPS-fabricated PCL composites incorporating degradable PCL-D and Laponite demonstrated improved porosity, antifouling behaviour, and mechanical robustness. These membranes achieved adsorption capacities of ~84.9 mg/g for Pb^{2+}, ~90.6 mg/g for Cd^{2+}, ~45 mg/g for methylene blue, and ~57 mg/g for neutral red, along with a 36–40% salt rejection rate and ~82% flux recovery after five cycles [29].

3.3.2 Performance enhancement of PCL-based filtration membranes

Over the past decades, membrane separation has attracted growing interest in wastewater treatment. PCL-based filtration membranes have shown strong potential for the efficient removal of oils, dyes, salts, and emerging contaminants, benefiting from tunable microstructures, hydrophilic surface modifications, and the incorporation of diverse nanomaterials. Effective membranes require pore sizes small enough to retain pollutants yet sufficiently large to allow water transport. Among the available fabrication methods, electrospinning [128] and phase separation, particularly NIPS and EIPS [129], are the most extensively studied for producing PCL-based membranes with tailored porosity, surface energy, and antifouling properties. Performance enhancements have been achieved through the addition of biopolymers, metal oxides, and functional nanomaterials.

By introducing hydrophilic polymers [159], surfactants [160], or biomimetic modifiers [161], electrospun PCL membranes can attain superhydrophilic and underwater superoleophobic properties, allowing gravity-driven emulsion separation with efficiencies above 97% and high flux recovery across multiple cycles. PCL/sulfonated kraft lignin (SKL) membranes exhibited superhydrophilicity (WCA = 0 °) and oil contact angles exceeding 150 °, enabling gravity-based separation without external pressure [159]. These membranes achieved pure water fluxes of 800–900 L/(m^2×h) (LMH) and emulsion fluxes of 170–480 LMH, with over 98% flux recovery after 10 cycles. Mussel-inspired surface treatments using tannic acid and silane coupling agents improved reusability and antifouling performance, maintaining > 99% separation efficiency after 20 cycles [161]. Integration of CS into PCL generated a nanofibre–nanonetwork architecture that enhanced water affinity and pollutant retention. The resulting CS@PCL membranes successfully separated immiscible oil/water mixtures, oil-in-water, and water-in-oil emulsions, with efficiencies of 94.6%, 99.9%, and 94.5%, respectively [162]. The separation mechanism is shown in Figure 3. 5. Sustainable additives such as cellulose

nanofibres (CNFs) [163] and bio-derived activated carbon [149] have also been employed to improve both pollutant removal and environmental compatibility, demonstrating the adaptability of electrospun membranes for diverse treatment needs.

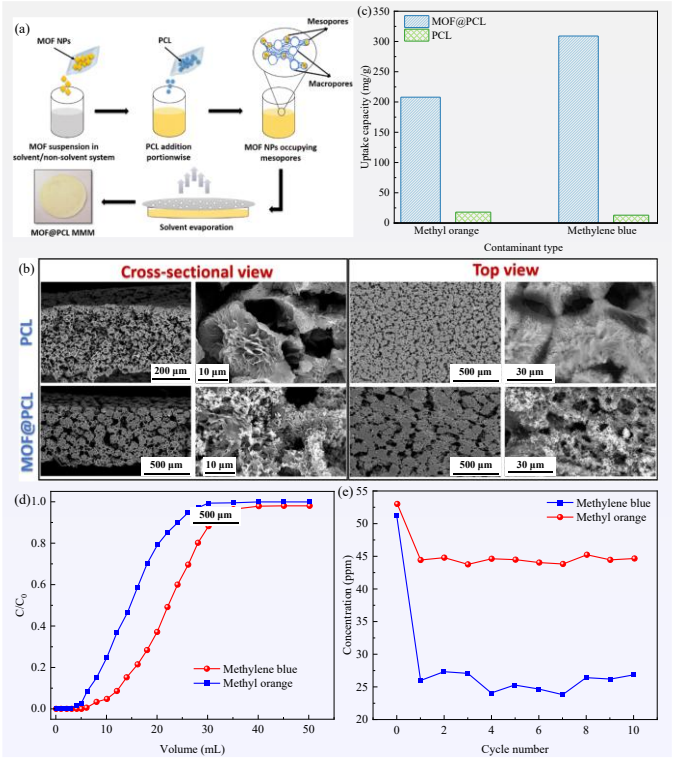

Figure 3. 4: (a) Preparation of MOF@PCL composite membrane; (b) SEM of pristine PCL and 5 wt.% MOF@PCL; (c) maximum adsorption capacities; (d) breakthrough curves; (e) recyclability of PCL and 5 wt.% MOF@PCL membranes for Methyl Orange and Methylene Blue (the first point in (e) indicates the concentration of the stock solution before filtration) (Reproduced with permission from [157]. Copyright 2023 Royal Society of Chemistry).

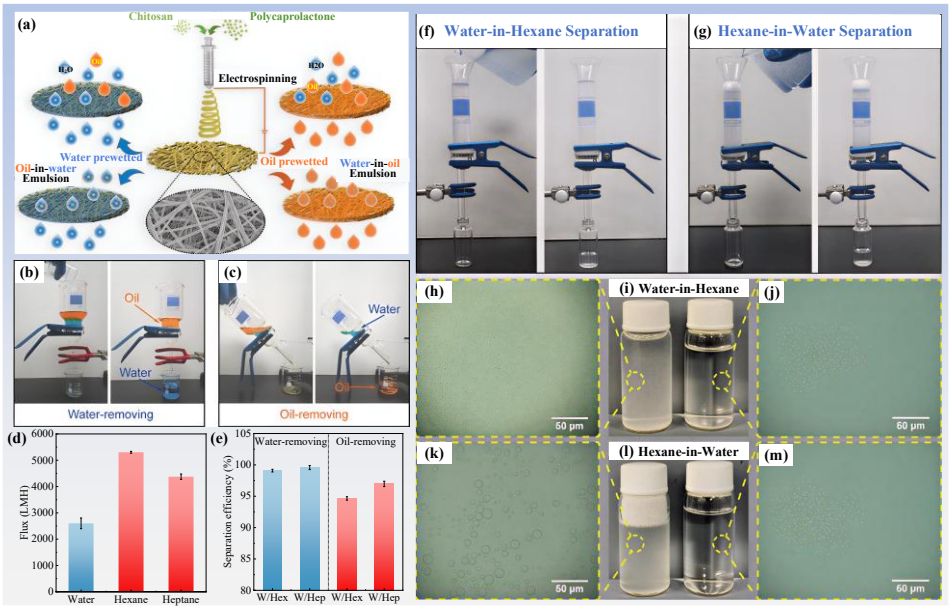

Figure 3. 5: (a) Schematic of the separation mechanism in CS@PCL super-amphiphilic membranes;

(b, c) setups for water and oil removal; (d) liquid flux and (e) oil/water separation efficiency; (f, g) setups for water-in-hexane and hexane-in-water emulsions; (h–m) visual comparison of emulsions before and after separation (Reproduced with permission from [162]. Copyright 2021 American Chemical Society).

In parallel, phase separation techniques (NIPS and EIPS) provide reliable methods for fabricating PCL membranes with controllable pore structures and effective pollutant removal. NIPS enables pore formation through solvent–nonsolvent exchange, which can be tuned by polymer blending (e.g., polybutylene succinate (PBS) [164], SKL [165]), solvent selection [166], and nanofiller incorporation (TiO_2 [167], GO [168], MXene ($Ti_3C_2(OH)_2$) [169]). These strategies enhance porosity, hydrophilicity, and fouling resistance, leading to increased pure water flux, improved dye or heavy metal removal, and enhanced flux recovery under pressure-driven conditions. SKL/PCL membranes prepared using acetic acid showed improved hydrophilicity (WCA reduced from 72 ° to 56 °), stable water flux (~45 LMH at 0.276 MPa), and low flux decline (< 7%), with recovery rate over 98% (Figure 3. 6) [165]. Incorporating 4 wt.% MXene into PCL reduced WCA to 50.3 ± 1.7 ° and increased water permeance to 5.99 LMH, approximately four times higher than neat PCL (1.43 LMH) at 1 wt.% MXene. Composite membranes rejected 98.92% of crystal violet dye, while also showing enhanced tensile strength and biodegradability (Figure 3. 7) [169].

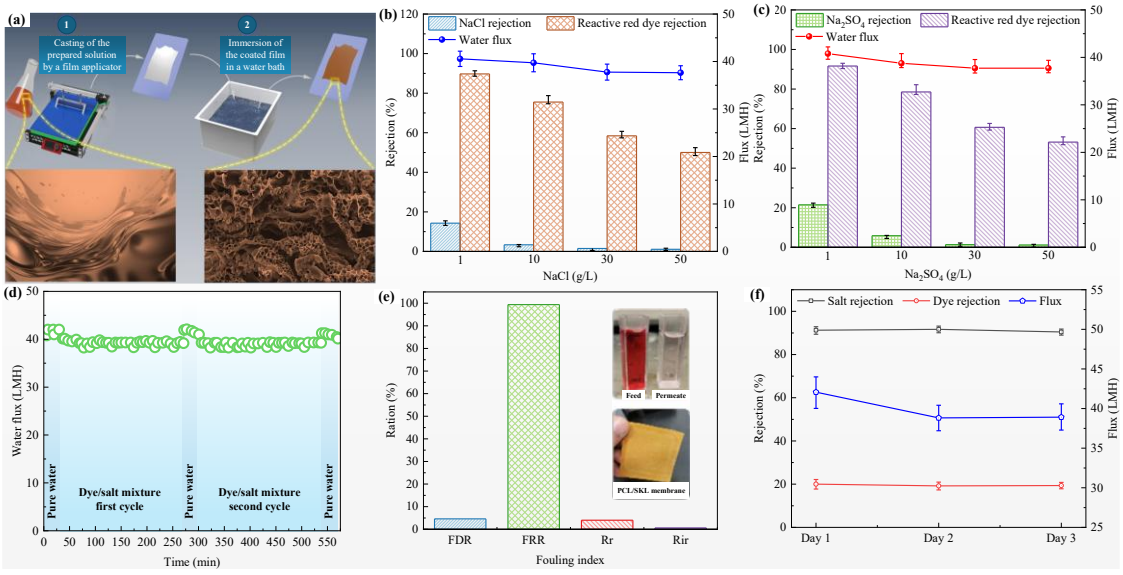

Figure 3. 6: (a) Schematic of PCL/SKL membrane fabrication; removal performance of 9 wt.% PCL/SKL membrane for (b) reactive red dye/NaCl and (c) reactive red dye/Na_2SO_4 mixtures; (d) water flux and (e) antifouling performance during treatment of the Na_2SO_4-containing mixture; (f) long-term operational stability (Adapted from [165]. Licensed under CC BY 4.0).

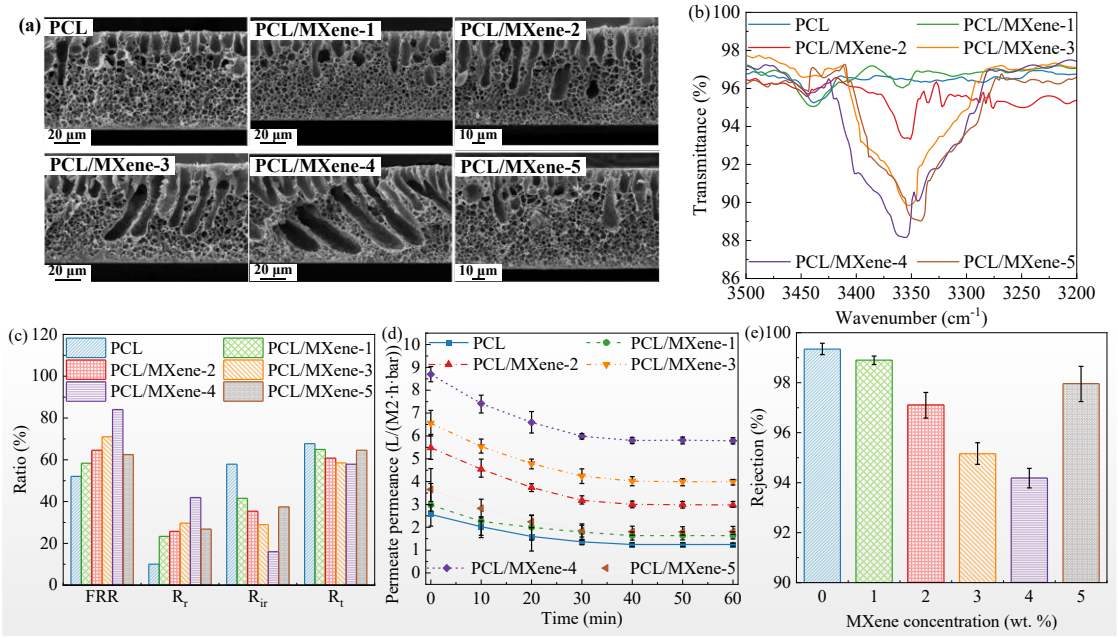

Figure 3. 7: (a) Cross-sectional SEM of PCL/MXene membranes; (b) ATR-FTIR spectra (3200–3500 cm^{-1}); (c) antifouling performance; (d) permeate flux over filtration time; (e) rejection efficiency toward crystal violet dye (Reproduced with permission from [169]. Copyright 2021 Elsevier).

EIPS, in contrast, relies on solvent evaporation to control pore morphology, allowing the formation of dense, sponge-like, or hollow structures. The use of block copolymers [170] or inorganic fillers such as ZnO [171], Ag–MMT (Montmorillonite) [172], and GO–CuO [173] further strengthens mechanical properties and imparts functionalities such as antibacterial activity, contaminant selectivity, and ion removal. ZnO-filled membranes exhibited improved elastic modulus and removal efficiency for nitrate and cadmium, while Ag–MMT incorporation enhanced hydrophilicity, antimicrobial activity, and the removal of heavy metals and anions. Post-treatment of poly(ε-caprolactone)-b-poly(4-vinyl pyridine) (PCL-b-P4VP) membranes with NaOH altered their cross-sectional morphology from dense to hollow and increased surface hydrophilicity (Figure 3. 8) [170]. Even without such modifications, these membranes achieved high electrodialysis desalination performance, with a current efficiency of 97.7% at 11.32 mA/cm² over six cycles. However, the reproducibility of phase-separated membranes may be affected by variations in coagulation conditions such as temperature and humidity. Additionally, reliance on toxic solvents and the need for extensive post-treatment steps pose challenges for large-scale manufacturing and environmental sustainability.

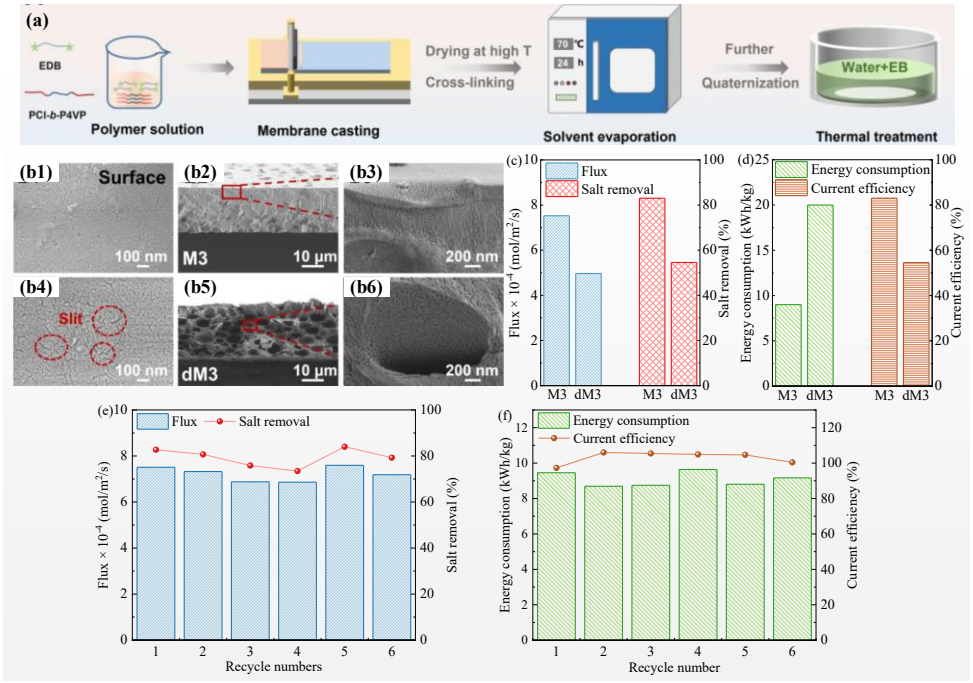

Figure 3. 8: (a) Schematic of membrane fabrication by EIPS; (b) SEM of membrane surfaces and cross-sections: M3 (b1–b3) and dM3 (b4–b6); (c) salt flux and removal efficiency; (d) energy consumption and current efficiency; (e, f) operational stability over six cycles (M3 and dM3 represent PCL-b-P4VP membranes without and with NaOH treatment, respectively) (Reproduced with permission from [170]. Copyright 2024 Elsevier).

3.3.3 Photocatalyst integration in PCL-based composite membranes

Photocatalytic degradation is a significant application of PCL-based composite membranes, utilising the polymer's flexibility and biodegradability as a support matrix for metal oxide catalysts. Incorporation of photocatalysts such as TiO_2, ZnO, Fe_3O_4, $MnWO_4$, and WO_3 can enhance membrane hydrophilicity, mechanical stability, and reusability, while enabling UV- and visible-light-driven degradation of organic pollutants.

The large surface area and high porosity of electrospun membranes facilitate efficient light absorption and pollutant contact, enabling high photocatalytic efficiency under both UV and visible light. Electrospun TiO_2-loaded membranes have achieved over 96% degradation of Rhodamine B (RhB) under visible light [174]. Composites combining PCL with CS [175], PU [176], or polyhydroxybutyrate (PHB) [177] offer adsorption capability and mechanical reinforcement, allowing near-complete removal of dyes such as Acid Orange 7 and RhB. Further enhancements have been achieved through coaxial fibre designs [177], Janus structures [178], and layered hybrids with rectorite [179] and Fe_3O_4 [177], which contribute to stable photocatalytic performance and separation

efficiencies exceeding 99% across multiple reuse cycles. However, their broader practical applicability is constrained by limited structural stability under hydraulic pressure and prolonged irradiation, as well as by difficulties in achieving scalable, reproducible fabrication.

NIPS and freeze-drying offer complementary benefits for the fabrication of photocatalytic membranes. By carefully controlling solvent–non-solvent exchange and incorporating photocatalysts, NIPS membranes exhibit enhanced pore interconnectivity and dye rejection, along with UV-triggered self-cleaning. Freeze-drying, though less commonly used, enables the formation of highly porous 3D scaffolds that serve dual roles in adsorption and photocatalysis. These techniques facilitate the incorporation of TiO_2 [180], ZnO [181], or $MnWO_4$ [182] into bulk PCL matrices with well-defined porous structures, enabling high flux, mechanical strength, and dye removal efficiency. NIPS-derived CA/PCL membranes doped with TiO_2 or ZnO achieved over 95% rejection of various dyes and exhibited UV-triggered self-cleaning [180, 181]. Freeze-dried PCL/poly (D, L-lactide) (PDLLA) membranes loaded with Fe_3O_4@WO_3 demonstrated dual-functionality, combining >99% oil–water separation with 90% RhB degradation under visible light (Figure 3. 9) [183]. Nevertheless, NIPS-derived membranes typically exhibit lower photocatalytic efficiency than electrospun counterparts due to limited surface exposure of active sites. Freeze-dried membranes, while highly porous, often suffer from inferior mechanical strength and limited process control, making them more suitable as support layers or for batch-mode applications rather than as standalone systems.

To enhance responsiveness under visible light, PCL membranes have also been combined with advanced semiconductors such as CQDs [184], g-C_3N_4 [185], and PANI [143]. These additives improve charge separation and extend the light absorption spectrum, thereby increasing photocatalytic efficiency. For example, CQD/g-C_3N_4 composites enabled 96.88% degradation of Aflatoxin B_1 within 30 minutes [184]. Electrospun membranes integrating TiO_2/g-C_3N_4 heterojunctions [185] or GO/PANI [143] have shown stable photocatalytic performance with good reusability. Yu et al. [142] developed a multifunctional tri-mode membrane by integrating GO/PANI particles onto electrospun PCL substrates (Figure 3. 10a), enabling solar-driven evaporation, photocatalytic degradation, and electrically driven cross-flow filtration. In solar mode, the membrane absorbed 97.44% solar energy and achieved a 1.47 kg/m^2/h evaporation rate (Figure 3. 10d–e). In photocatalytic mode, it removed 93.22% of the organic dyes under 1 kW/m^2 of solar irradiation over

12 hours (Figure 3. 10f–g). In crossflow filtration mode, it reached 99% dye rejection with stable flux > 40 LMH (Figure 3. 10h). Such tri-mode membranes highlight the potential of PCL-based platforms to serve as integrated, high-efficiency systems for water purification.

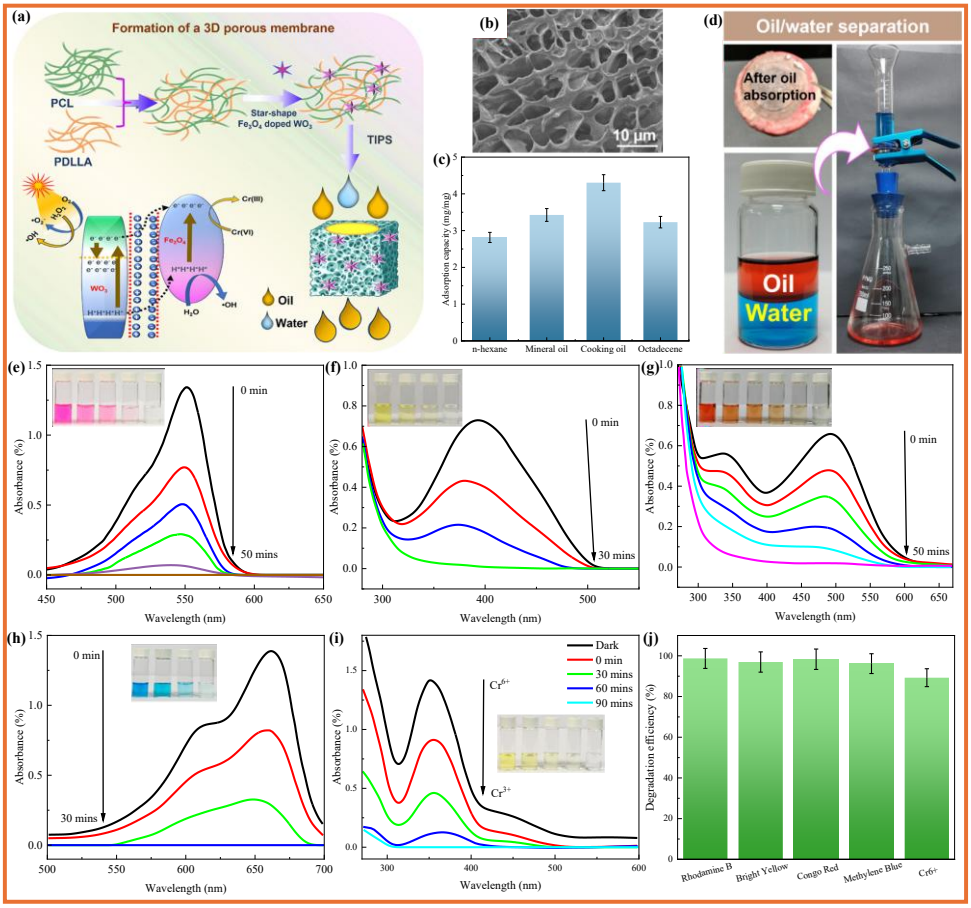

Figure 3. 9: (a) Photocatalytic mechanism of the PCL/PDLLA/Fe_3O_4@WO_3 membrane; (b) SEM of the membrane; (c) oil–water separation through oil adsorption; (d) oil absorption capacity; (e–i) UV–vis spectra of RhB, Bright Yellow, Congo Red, and Methylene Blue before/after treatment; (j) degradation efficiencies of the corresponding dyes (Reproduced with permission from [183]. Copyright 2024 Elsevier).

3.4 Stability, reusability, and environmental impacts

Adsorption is valued for its simplicity and versatility; however, its limited capacity and challenges in regenerating spent materials restrict its long-term use [186]. For example, MOF@PCL mixed-matrix membranes fabricated via EIPS maintained dye removal over 10 cycles, but their durability remained suboptimal [157]. Desorption regeneration is particularly problematic, as the use of strong acids, alkalis, or organic solvents often leads to membrane degradation and a decline in performance, thereby limiting practical recyclability. Membrane separation offers high selectivity and effluent quality, and has been widely applied in industry; however, fouling and pore clogging induce flux

decline and compromise operational longevity [159]. Enhancing antifouling performance and developing efficient cleaning strategies are therefore essential. Photocatalysis enables the complete degradation of pollutants under irradiation and is considered environmentally favourable, but its application is constrained by limited light responsiveness, catalyst instability, and poor recyclability. Catalyst leaching, nanoparticle aggregation, and degradation of PCL supports under prolonged irradiation further hinder stability and scalability.

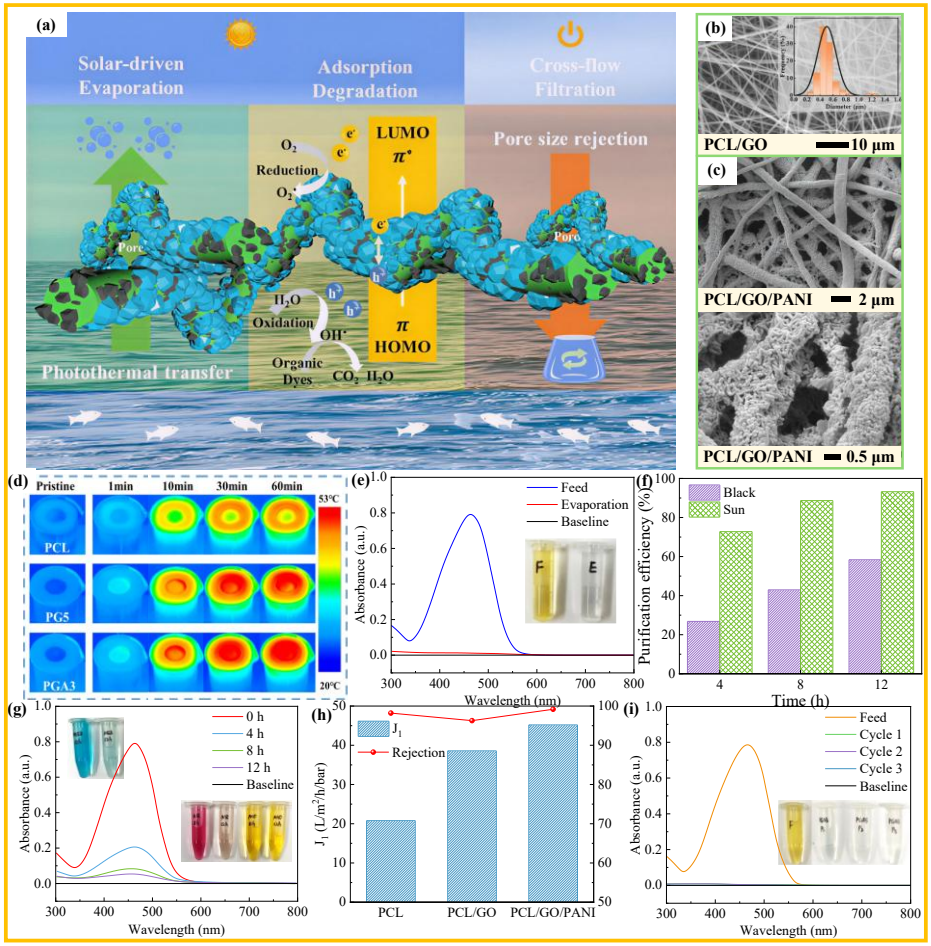

Figure 3. 10: (a) Tri-mode wastewater recycling mechanism; SEM of (b) PCL/GO and (c) PCL/GO/PANI membranes; (d) infrared images of solar evaporation; (e) UV spectra of feed and evaporated solutions; (f) purification efficiency under dark and solar conditions; (g) UV spectra under solar irradiation; (h) foulant flux and rejection under cross-flow mode; (i) UV spectra of permeate over three filtration cycles (Adapted from [143]. Licensed under CC BY 4.0).

Although PCL is biodegradable and generally low-toxic, its large-scale use still raises environmental concerns. Solvent-based fabrication can release volatile organic compounds and generate large volumes of contaminated wastewater [187]. The membrane industry alone produces over 50 billion litres of solvent-contaminated wastewater annually, accounting for more than 95% of its total waste output [188]. At the same time, energy-intensive operations such as UV/visible-light photocatalysis

increase the carbon footprint [189]. Enhancing material durability and resistance to fouling helps extend service life, reduce replacement, cleaning, and energy consumption, thereby lowering the lifecycle footprint. Conversely, harsh chemical cleaning and repeated regeneration generate concentrated waste streams, while leaching of active additives (e.g., TiO_2, ZnO, CNTs) introduces nanotoxicity risks [190]. Moreover, mechanical abrasion or UV exposure may fragment PCL into microplastics that persist temporarily in aquatic environments and pose ecological risks [191].

To mitigate these issues, lifecycle assessment should be integrated into design, operation, and disposal stages. Green fabrication strategies, including the use of sustainable solvents (e.g., formic or acetic acid) and solvent-free processes (e.g., 3D printing), are recommended. Incorporating solar-light-responsive photocatalysts and strengthening evaluations of reusability, degradation byproducts, and system-level toxicity will be essential to ensure environmental safety and energy efficiency [192]. Robust waste management practices and regulatory frameworks are likewise required to minimise the ecological burdens of large-scale implementation.

Based on current understanding, Figure 3. 11 presents a radar chart comparing five key performance indicators (stability, reusability, environmental sustainability, industrial translation potential, and carbon footprint) across adsorption, membrane separation, and photocatalysis approaches. Membrane separation has seen broader adoption but is hindered by solvent use and the potential for microplastic generation. Adsorption suffers from inefficient regeneration and reliance on solvents, limiting its sustainability. Photocatalytic systems are currently constrained by catalyst leaching, aggregation, and PCL degradation, which limit their performance and scalability.

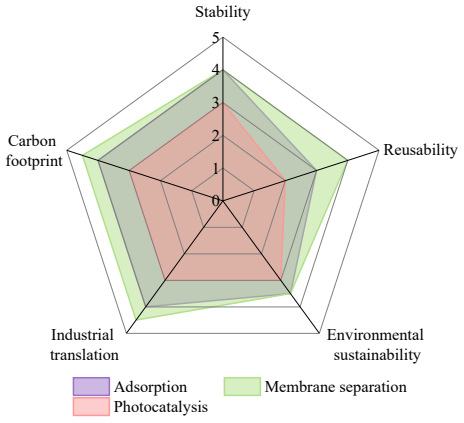

Figure 3. 11: Radar chart comparing adsorption, membrane separation, and photocatalysis based on five performance indicators, including stability, reusability, environmental sustainability, industrial translation, and carbon footprint.

3.5 Multifunctional integration and machine learning for industrial translation

A key direction for advancing PCL-based water treatment is to integrate multiple functions, adsorption, separation, photocatalysis, and biodegradation, within a unified system to address the complex composition of wastewater. For example, a tri-modal membrane successfully combined solar evaporation, photocatalytic degradation, and electrically assisted filtration within a single substrate [143]. Emerging designs, such as Janus membranes and multilayered architectures, further enhance functionality by introducing intelligent features, including self-cleaning, pH responsiveness, and in-situ regeneration.

Most existing studies have been conducted under controlled laboratory conditions, typically focusing on single-component systems such as RhB, methylene blue, or crude oil. These simplified scenarios fail to reflect the complexity of actual municipal or industrial wastewater, which often contains a broad range of interacting contaminants, including pharmaceutical residues, fluctuating pH levels, high salinity, and biofouling agents. To bridge the gap between laboratory research and practical application, pilot-scale investigations under real-world conditions are urgently needed. Additionally, the development of standardised performance evaluation protocols is essential for enabling meaningful comparisons and guiding future material optimisation.

The integration of digital technologies represents a transformative opportunity. High-performance computing (HPC), automation, and ML can accelerate material discovery and application [193]. High-throughput screening (HTS) and robotic platforms facilitate rapid synthesis and testing, while ML models can identify structure–performance relationships and optimise fabrication parameters. For example, physics-informed ML frameworks have successfully screened 2D materials for the removal of per- and polyfluoroalkyl substances (PFAS). They may be adapted to predict PCL membrane performance in heavy metal remediation [194]. Toolkits such as Materials Simulation Toolkit for Machine learning (MAST-ML) help lower the entry barrier for deploying predictive models [195]. Ensuring data quality, model interpretability, and reproducibility remains essential. The convergence of ML with sensor networks and Internet of Things (IoT) infrastructure will enable real-time, responsive treatment systems tailored to dynamic environmental conditions [196].

Ultimately, the synergistic deployment of HPC, automation, and ML offers a promising pathway for scaling up PCL-based technologies, ensuring their robustness and sustainability in next-generation water treatment.

3.6 Conclusions

PCL-based materials offer a versatile and sustainable platform for water treatment, integrating biodegradability, structural tunability, and compatibility with various functional components. Advances in fabrication techniques, such as electrospinning, NIPS, EIPS, freeze-drying, and 3D printing, have enabled the development of PCL-based materials with tailored porosity, wettability, and mechanical properties. Through material modifications and structural design, significant progress has been made in enhancing adsorption capacity, improving separation efficiency, and increasing photocatalytic activity.

However, several limitations still hinder the development of large-scale applications. These include limited long-term stability under hydraulic stress and irradiation, insufficient data on reusability and pollutant desorption, and reliance on toxic solvents or energy-intensive processing. Additionally, most studies are confined to single-contaminant systems under ideal laboratory conditions, lacking validation in real wastewater scenarios. To overcome these challenges, integrating digital technologies, such as HTS, ML, and IoT-enabled monitoring, offers significant potential to accelerate the design, optimisation, and implementation of PCL-based water treatment systems. When combined with advances in green fabrication techniques and comprehensive lifecycle sustainability assessments, these approaches can facilitate the transition of PCL-based composites from laboratory-scale prototypes to scalable, multifunctional platforms for sustainable water purification.

CHAPTER 4

4 General materials and methods

4.1 Experiment with raw materials

4.1.1 Raw materials in cell culture experiments

Three PCL samples purchased from Sigma-Aldrich (UK) with different average MW were used. The measured values and designations were 38600 g/mol (Low molecular weight, LMW), 83700 g/mol (Medium molecular weight, MMW), and 96700 g/mol (High molecular weight, HMW). Acetic acid (AA) and formic acid (FA) were also purchased from Sigma-Aldrich (UK) as solvents for fabricating PCL scaffolds. Phosphate Buffer Saline (PBS) and Dulbecco's Modified Eagle Medium (DMEM) were obtained from Thermo Fisher Scientific (UK). Penicillin, fetal bovine serum (FBS), ethanol (70%), trypsin, bovine serum albumin (BSA), 4',6-diamidino-2-phenylindole (DAPI), isopropanol, and 3-(4,5-dimethylthiazol-2-yl)-2,5-diphenyltetrazolium bromide (MTT) were purchased from Sigma-Aldrich (UK). The Phalloidin-iFluor 488 reagent (ab176753) was obtained from Abcam (UK). NCTC clone 929 (L929) was obtained from the American Type Culture Collection (USA).

4.1.2 Raw materials in oily water filtration experiments

The PCL (sample in MMW) and PMMA (average MW of 120,000 g/mol) were purchased from Sigma-Aldrich (UK). Acetic acid and formic acid were also obtained from Sigma-Aldrich (UK) as solvents for fabricating the PCL membranes for the top and bottom layers. Dimethylformamide (DMF) and dichloromethane (DCM) were obtained from Thermo Fisher Scientific (UK) and used as solvents for PMMA and PCL in the middle layer, respectively. n-hexadecane (purity >95%), ethanol

(100%), the zwitterionic surfactant [2-(Methacryloyloxy) ethyl] dimethyl-(3-sulfopropyl) ammonium hydroxide (DMAPS), and Coumarin 6 dye were also ordered from Sigma-Aldrich (UK).

4.2 Electrospinning of PCL-based materials

Before electrospinning, the prepared solution was loaded into syringes fitted with 26 G spinnerets (inner diameter of 0.25 mm). A high-voltage source (Series ES, Gamma High Voltage, USA) connected to a low-voltage safety switch unit was used to supply the electrospinning voltage of 15 kV. The jets were ejected from the tips of spinnerets towards a vertical collector (15 cm × 15 cm). The KDS 100 Legacy Single Syringe Infusion Pump (KD Scientific, USA) fed solutions in syringes to the spinneret tips at different flow rates. All the fibrous membranes were collected on aluminium foils and peeled off after drying overnight at ambient temperature.

4.3 Cell culture experiments

Cell culture experiments were performed to evaluate the biocompatibility and cell–scaffold interactions of PCL electrospun nanofibrous membranes using L929 fibroblast cells. Figure 4. 1 illustrates the process of cell thawing and subculture. Briefly, cryovials were removed from liquid nitrogen and immediately placed in a 37 °C water bath for rapid and uniform thawing to minimise thermal shock and cell damage. Once the ice had melted entirely, the cell suspension was transferred into a centrifuge tube containing pre-warmed complete DMEM to dilute the cryoprotectant (dimethyl sulfoxide, DMSO).

The mixture was then centrifuged to remove DMSO, after which the supernatant was discarded, and the cell pellet was resuspended in fresh pre-warmed medium. The recovered cells were subsequently transferred into culture flasks and placed in a CO_2 incubator (37 °C, 5% CO_2, 95% relative humidity) for recovery and proliferation. Once the cells reached approximately 80–90% confluence, they were subcultured into new flasks for further expansion. These steps ensured that healthy, metabolically active cells were obtained for the subsequent scaffold-seeding experiments.

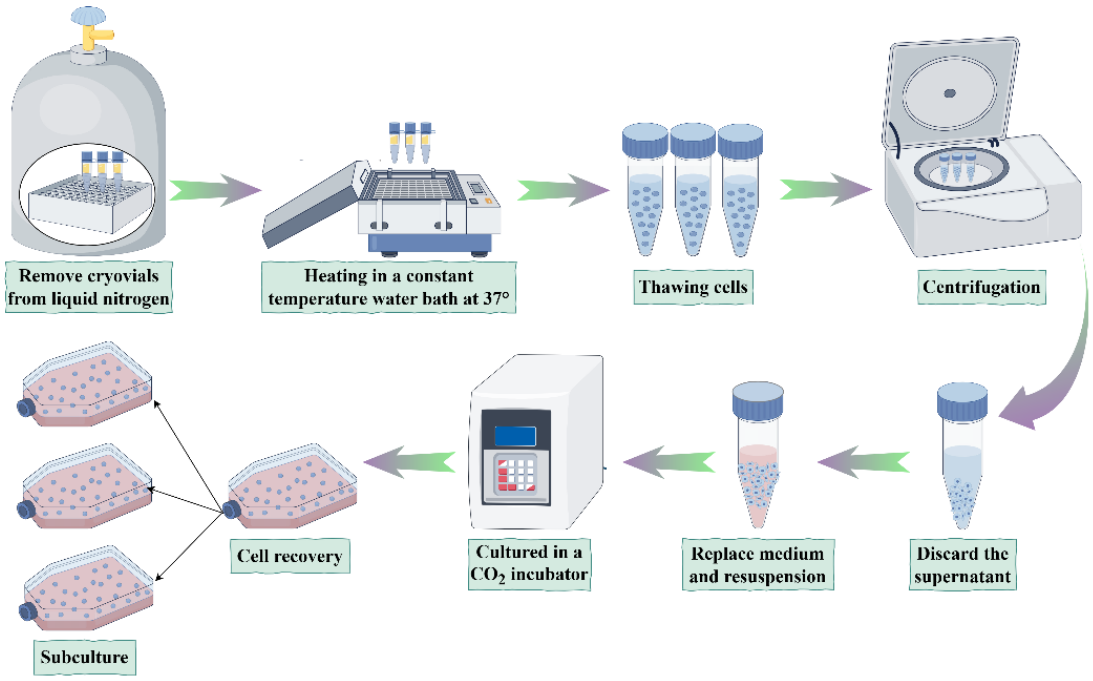

Figure 4. 1: The process of cell thawing and subculture.

The culture process of L929 cells on PCL electrospun nanofibrous scaffolds is shown in Figure 4. 2. Before cell seeding, the electrospun PCL mats were cut into 16 mm-diameter discs (well diameter of 24-well plates), and the peripheral regions were trimmed to ensure uniform thickness and consistent fibre morphology across all samples. To ensure sterility, the scaffolds were immersed in 70% ethanol for 30 min under aseptic conditions, followed by three rinses with pre-warmed phosphate-buffered saline (PBS) to remove residual ethanol and restore physiological osmotic balance. L929 cells were maintained in DMEM supplemented with 10% FBS and 1% penicillin–streptomycin (Pen-Strep), which provides essential nutrients and prevents bacterial contamination.

For seeding, a cell suspension (2×10^4 cells/mL) was carefully dispensed onto each scaffold placed in 24-well culture plates. The plates were then incubated in DMEM media at 37 °C in a humidified atmosphere with 5% CO_2, which supports optimal cell adhesion and proliferation on the nanofibrous matrix. The culture medium was replenished every two days to sustain nutrient levels and remove metabolic byproducts. The 2D control group was prepared under identical conditions, except that tissue-culture polystyrene (TCP) plates were used instead of PCL scaffolds. This allowed for a direct comparison between conventional 2D culture and the 3D nanofibrous environment provided by the electrospun scaffolds. The cell culture experiments were conducted with technical assistance from Dr. Ross Carnachan (formerly affiliated with the Department of Engineering, Durham University).

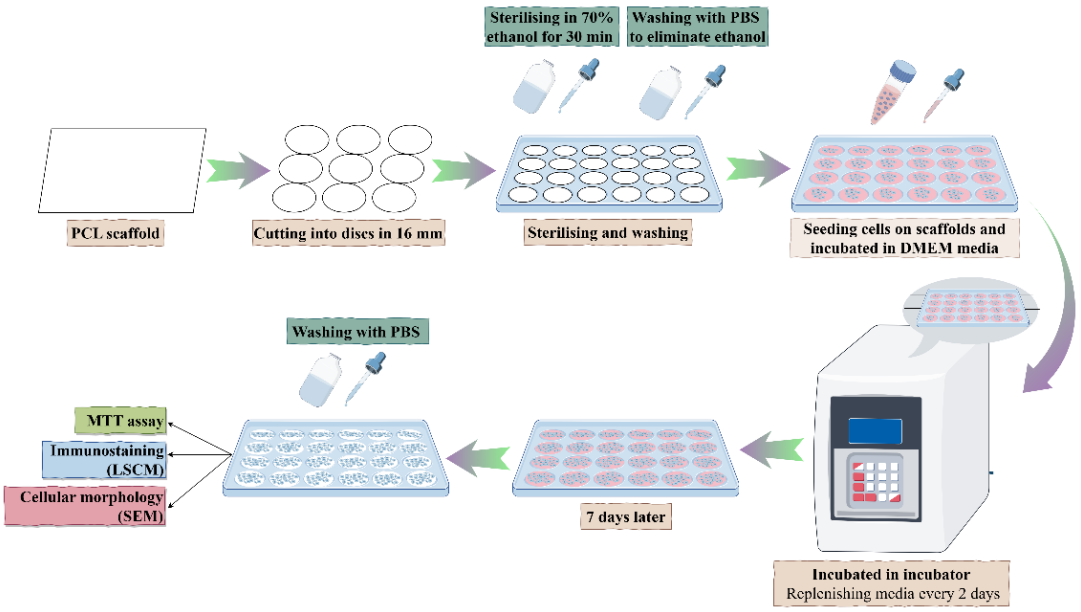

Figure 4. 2: The culture process of L929 cells on PCL electrospun nanofibrous scaffolds.

4.4 Oil/water emulsion preparation and filtration

4.4.1 Emulsion Preparation

A fresh and stable oil/water emulsion was prepared before each filtration experiment to ensure reproducibility of results, as shown in Figure 4. 3. The oil phase (n-hexadecane) was dyed using Coumarin 6 (5 mg dye per g of oil) to enhance visual observation during filtration. As the dye tends to bleach over time, the coloured n-hexadecane should be freshly prepared before each filtration experiment. The mixture was ultrasonicated for 10 min to achieve uniform dye dispersion, then filtered through Millipore paper to remove undissolved residues.

Separately, 1 g of zwitterionic surfactant (DMAPS) was dissolved in 1 L of DI water using a laboratory high-shear mixer operating at 15,000 rpm for 4 min, ensuring complete dissolution. The coloured oil was subsequently added to the surfactant-containing aqueous phase and further emulsified at 15,000 rpm for 10 min to obtain a uniform, stable emulsion. The resulting emulsion exhibited a narrow and approximately normal distribution of oil droplet sizes, providing a reproducible model system for membrane filtration. Although the emulsion remained stable over several hours under quiescent conditions, it was used immediately after preparation to minimise gradual phase separation and dye oxidation during storage.

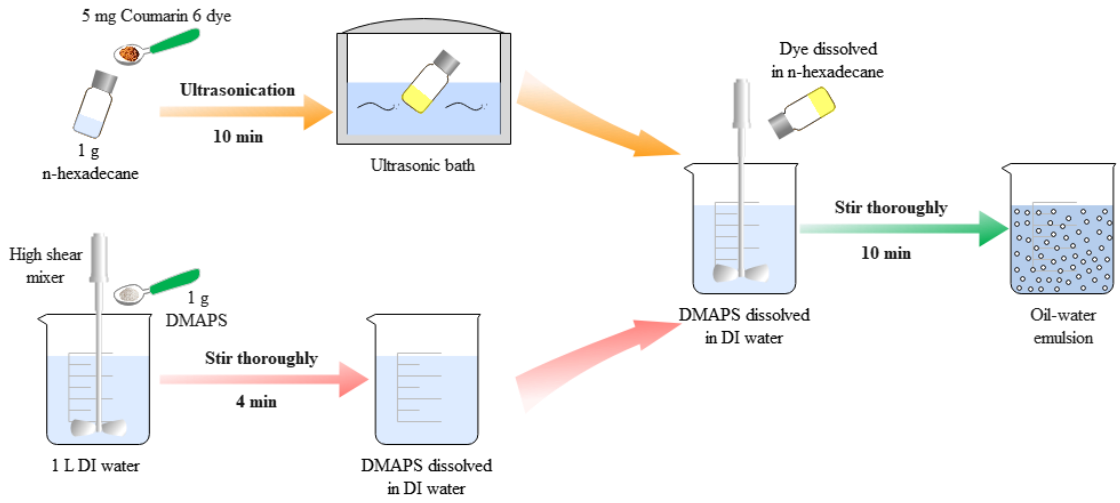

Figure 4. 3: Preparation process of oil/water emulsion.

4.4.2 Filtration experiments

Oil/water separation experiments were conducted using a pressurised crossflow filtration rig as illustrated in Figure 4. 4. This configuration allows for continuous tangential flow over the membrane surface, reducing fouling and providing more representative conditions than conventional dead-end setups. Prior to testing, cold-pressed membrane samples (7.5 cm × 5.0 cm) were immersed in 100% ethanol for 1 hour to thoroughly wet and degas, then rinsed with DI water to remove residual ethanol. Each membrane was mounted at the centre of the filtration cell, fully covering the effective filtration area (7 cm × 4.5 cm, 31.5 cm^2). The cell was then sealed with six sets of bolts and connected to the crossflow circuit using flexible tubing.

During operation, the oil/water emulsion was circulated across the membrane surface under a feed pressure of 0.5 MPa, a value determined to provide stable flow and measurable permeate flux without causing mechanical deformation of the membrane. The permeate was continuously collected on an electronic balance (ME4002, Mettler Toledo, USA), with mass data automatically recorded every 30 seconds for flux calculations. Oil droplets larger than the membrane pores were retained on the feed side, forming a concentrated retentate, while water permeated through, demonstrating effective oil/water separation.

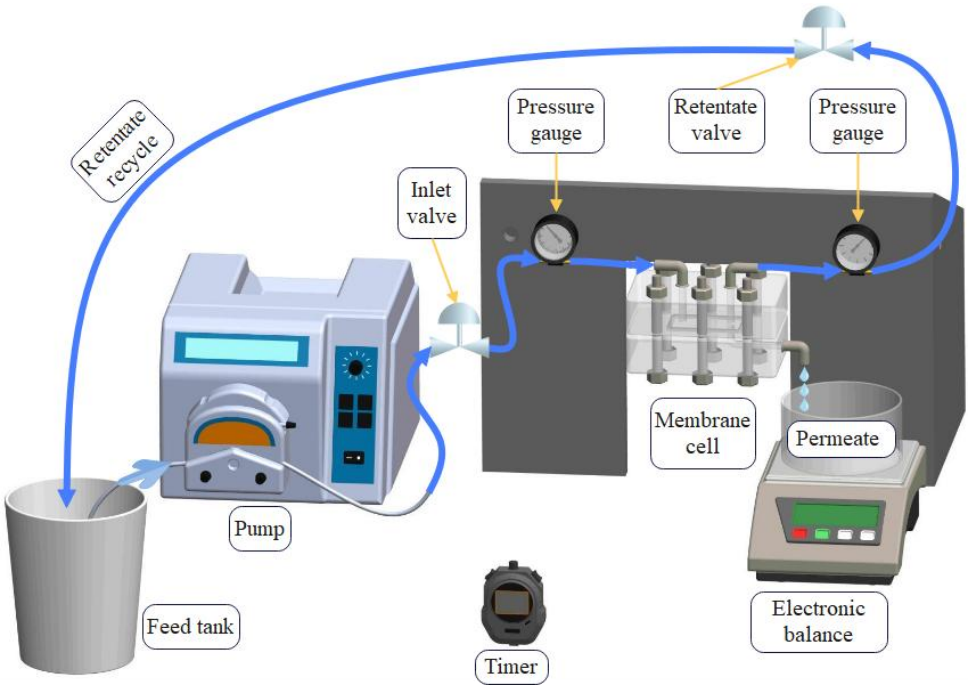

Figure 4. 4: The Schematic 3D diagram of the crossflow filtration unit.

4.5 Common characteristics analysis in cell culture and water treatment

4.5.1 Viscosity

Solutions' viscosity was measured using a rotational rheometer (Pro Rotational Rheometer, KINEXUS, UK). A CP4/40 SR5862 cone-plate geometry was employed, and the shear rate was set at 100 s^{-1} for all measurements.

4.5.2 Morphology analysis

The morphology of the PCL-based composite electrospun nanofibre materials was examined using an SEM (Zeiss Evo 10, Carl Zeiss Microscopy Ltd., Germany) operated at an accelerating voltage of 12 kV. Before imaging, the membranes were coated with a 17 nm gold layer to enhance surface conductivity and minimise charging effects. The fibre diameters, pore sizes, and porosity of the scaffolds were measured in SEM images using ImageJ. Average values and standard deviations were calculated based on the measurement results.

The thickness of the electrospun membranes used for mechanical testing was typically 80–200 μm,

depending on the electrospinning duration. The thickness was measured using a high-precision calliper (CCMA-M, TESA Technology, Switzerland) with a precision of up to 0.001 inch (25.4 μm). A microscope was first used to measure membrane thickness. It turned out rather challenging to prepare cross-sectional samples by scissor-cutting. The resulting compression from scissors would collapse the cross-section into a narrow line, leading to an underestimation of thickness. To preserve this, cryo-fracturing was then tried by rapidly freezing the membranes with liquid nitrogen. However, the resulting cross-sections from cryo-fracturing were often irregular or distorted, making it difficult to achieve a focused field with sufficient depth for reliable measurements under the microscope. Given these limitations, the high-precision calliper was ultimately adopted, as it is simple yet provides adequate accuracy for samples of this thickness range. To minimise compression effects during measurement, only a moderate contact force was applied when using the calliper. Thickness measurements were performed at three different positions on each membrane, and the mean value was recorded. The triplicate measurements showed a variation of ± 5%, confirming that the calliper resolution provided adequate precision for comparative analysis.

The volumetric porosity of the electrospun membranes was also determined. Membranes (7.5 cm × 5 cm), after ethanol treatment, were immersed in DI water for 24 hours. Lint-free wipes gently absorbed excess surface water, and the weight of the wet membranes was measured by a high-precision electronic balance (XS104, Mettler-Toledo International Inc., Switzerland). The wet membranes were then dried in a vacuum oven at 40 °C for 24 hours, and the dry weight was measured. The volumetric porosity (ε) of the electrospun membranes was calculated by the following Eq. (1) [197]:

$$\varepsilon = \frac{W_w - W_d}{d_w \times A \times \delta} \times 100 \quad (1)$$

where ε is the volumetric porosity of the electrospun membranes (%); W_w and W_d are the weight of the wet and dry membranes (g), respectively; A is the effective area of membranes (cm^2); δ is the thickness of wet membranes (cm); and d_w is the density of water at room temperature (1 g/cm^3).

The average pore radius (r, nm) of the membranes was calculated based on the Guerout-Elford-Ferry equation as illustrated in Eq. (2) [159]:

$$r = \sqrt{\frac{\pi}{4}} \times \left(\frac{\pi}{2\log\left(\frac{1}{\varepsilon}\right)} \right) \times d \tag{2}$$

where d is the fibre diameter of the membrane.

4.5.3 Hydrophilicity

The surface wettability of electrospun membranes was evaluated by measuring the WCA, as it plays a crucial role in determining interfacial interactions in both biomedical and environmental applications. In tissue engineering, an appropriate level of hydrophilicity promotes nutrient penetration and facilitates cell adhesion, proliferation, and differentiation on the scaffold surface. In water treatment, hydrophilic surfaces help form a hydration layer that suppresses the adhesion of oils and contaminants, thereby enhancing antifouling performance and maintaining water permeability.

The WCA was measured using a sessile drop instrument (Model 260 Goniometer/Tensiometer, ramé-hart Instrument Co., USA). A 15 µL droplet of DI water was dispensed onto the membrane surface using a manual micropipette (F151305, Scientific Laboratory Supplies Ltd., UK). The evolution of the droplet was recorded using uEye Cockpit software, and the static contact angle (θ) was analysed by ImageJ software. Each membrane sample was measured three times, with average values and standard deviations calculated. A smaller WCA (< 90 °) corresponds to higher surface energy and improved hydrophilicity, facilitating nutrient penetration and cell growth in tissue engineering and enhancing antifouling and water permeability in water treatment. Conversely, a larger WCA (> 90 °) indicates a hydrophobic surface with lower water affinity.

4.6 Specific analysis in cell culture experiments

4.6.1 MTT cell proliferation assay

The MTT method was used to measure absorbance and determine cell viability after 1, 3, and 7 days. The stale media was discarded, and then 400 µl of fresh media and 100 µl of MTT solution were added to each well. After 3 hours of incubating, the mixed solution was carefully removed, leaving the purple crystals behind. Then, 500 µl of isopropanol was added to each well and shaken for 30

minutes to dissolve all formazan crystals. 100 μL of dissolved purple solution was transferred from each well to a 96-well plate. The absorbance values were measured at 570 nm in a microplate reader (Synergy™ H4 Hybrid, Thermos Fisher Scientific, UK). Cell viability was compared between the 3D and 2D control groups. Each test was replicated 3 times.

4.6.2 Immunostaining

To estimate cell adhesion and proliferation on/in the scaffolds, Laser Scanning Confocal Microscopy (LSCM) was performed on the 3rd and 7th days of the culture period. After discarding the media, the samples were washed with PBS and fixed in 4% paraformaldehyde overnight at 2 °C in the fridge. Then, the samples were washed twice in PBS, incubated in permeabilisation solution (0.1% w/v Triton X-100 in PBS) and blocking buffer (1% BSA and 0.1% w/v Triton X-100 in PBS) for 60 minutes. Next, the samples were incubated with the Phalloidin-iFluor 488 Reagent (ab176753) at 1/1000 for 3 hours. Labelled constructs were washed and counter-stained with DAPI (1/1000 dilution in blocking buffer) for 3 hours. Finally, the samples were mounted onto slides and analysed using the LSCM (Zeiss 800 LSCM, Carl Zeiss Microscopy Ltd, Germany).

4.6.3 Cellular morphology

After 3 and 7 days of cell culture, SEM was used to survey cell adhesion and proliferation on/in the PCL scaffolds. The samples were removed from the incubator, and the media in each well was discarded. Each scaffold was rinsed with PBS 3 times to remove nonadherent cells, then fixed in 4% formalin solution overnight at 4 °C for cell growth imaging. The constructs were washed in PBS and dehydrated with graded ethanol concentrations (30, 50, 70, 80, 90, and 100%). The ethanol was then replaced with t-butanol and stored at 2 °C until t-butanol solidifies. After that, the constructs were stored in dry ice overnight, then freeze-dried for 24 hours. Finally, the samples were sputter-coated with gold (thickness 15 nm) and observed through SEM, as mentioned in Section 4.5.2.

4.7 Specific analysis in oily water filtration experiments

4.7.1 Combined FTIR-DSC analysis

The chemical composition of samples was analysed using a PerkinElmer Frontier Fourier Transform

infrared spectroscopy (FTIR) spectrometer equipped with a Specac Quest attenuated total reflectance (ATR) accessory featuring an extended-range diamond puck. Each sample was scanned in the mid-infrared range from 4000 to 400 cm^{-1} at a resolution of 4 cm^{-1}. Thermal behaviour was analysed using a PerkinElmer DSC 8500 differential scanning calorimeter operated under a helium purge atmosphere (CP grade, 20 mL/min). Both heating and cooling were conducted at 10 °C/min over the temperature range from −80 to 250 °C. The combined FTIR and DSC analysis was employed to assess potential interactions or compatibility between PCL and PMMA in the fabricated membrane samples.

4.7.2 Mechanical properties

The mechanical properties of electrospun membranes were analysed using a universal testing machine (ElectroForce® 3200 Series III Test Instrument, TA Instruments, USA) at a crosshead speed of 0.05 mm/s. Dog-bone-shaped specimens in the size of 6 × 15 mm were prepared for testing. Stress-strain curves were obtained, from which the elongation at break, tensile strength, and Young's modulus of fabricated membranes were determined.

4.7.3 Dynamic light scattering

All oil–water emulsion samples were characterised for droplet size distribution using dynamic light scattering (DLS, Malvern Instruments, UK). Approximately 5 mL of each emulsion was drawn into a syringe and carefully transferred into a folded capillary zeta cell, ensuring complete filling without air bubbles. The cell was then inserted into the instrument. Measurements were performed in automatic mode, with three consecutive runs of 120 seconds per sample. The average droplet size was used as an indicator of the dispersion state and emulsion stability.

4.7.4 Pure water filtration test

The pure water fluxes (PWF) were measured in real-time at a pressure of 0.5 MPa and calculated using Eq. (3) [169]:

$$J = \frac{V}{T \times A} \tag{3}$$

where J is the flux of pure water (L/m^2/h, LMH); V is the real-time volume (L); T is real-time (h);

and A is the effective area of membranes (fixed at 0.00315 m^2 in this work)

4.7.5 Oil/water emulsion separation test

The performance of the membranes for oil/water emulsion separation was tested by short-term multicycle filtration experiments following the procedure: (1) PWF (J) was first measured for 15 minutes; (2) the pure water was replaced with oil/water emulsion, and emulsion filtration was conducted for 15 minutes with the flux of oil/water emulsion (J_1) calculated; (3) the fouled membrane was then rinsed with DI water to remove the cake layer. This sequence was considered as one filtration cycle. In the second cycle, pure water was filtered again, and the resulting flux was recorded as J_2. Each filtration test was conducted for 3 consecutive cycles and repeated 3 times. The flux decline rate (FDR) and flux recover rate (FRR) were calculated using Eqs. (4) and (5), respectively [159]:

$$FDR = \left(1 - \frac{J_1}{J}\right) \times 100 \tag{4}$$

$$FRR = \left(\frac{J_2}{J}\right) \times 100 \tag{5}$$

The percentage of oil rejection was calculated based on Eq. (6) [198]:

$$R = \left(1 - \frac{C_p}{C_f}\right) \times 100 \tag{6}$$

where R is the percentage of oil rejection (%); C_p and C_f are the concentration of oil in the permeation and feeding (%), respectively.

The oil/water emulsion separation performance was also evaluated through long-term filtration experiments: distilled water was filtered for 15 minutes, then the oil/water emulsion for 60 minutes, and finally distilled water for another 15 minutes. The same parameters were calculated using Eqs. (4-6).

4.8 Integration of image processing and ANN modelling

An integrated, data-driven workflow combining automated image processing with ANN modelling

was developed to enable high-throughput, accurate prediction of fibre morphology across diverse electrospinning conditions. This approach significantly reduced experimental workload and material consumption. The overall workflow is illustrated in Figure 4. 5. Initially, image processing was performed to extract fibre-diameter data from SEM images obtained under systematically varied fabrication parameters. The extracted data were then used to train and validate an ANN model capable of predicting fibre diameters for unseen parameter combinations. This integrated strategy not only facilitates the design and optimisation of electrospun PCL fibres but also provides a generalisable framework for morphological prediction in a wide range of fibrous material systems.

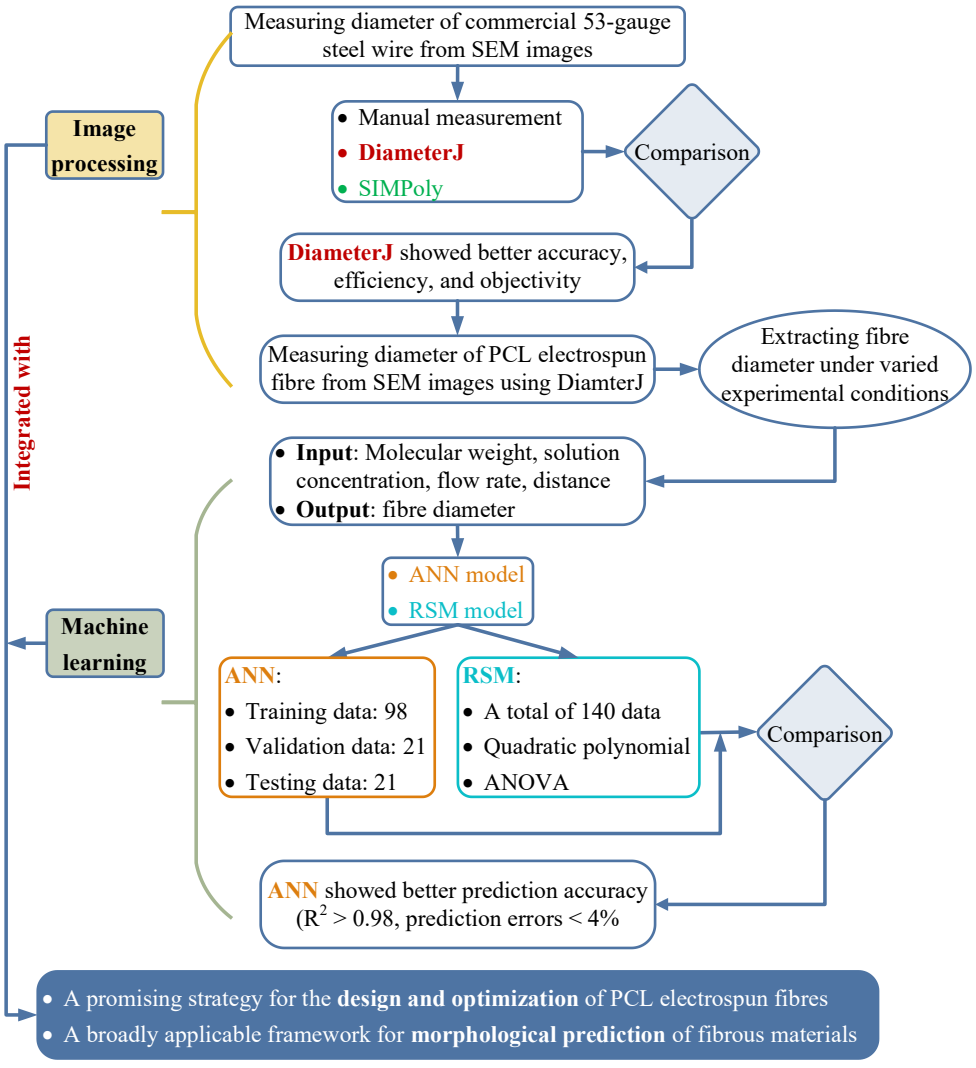

Figure 4. 5: The workflow of the integrated image processing-ANN model for prediction and analysis of fibre diameter of electrospun PCL membranes.

Electrospun membranes were characterised using SEM to assess their morphological features. To benchmark the accuracy and consistency of fibre diameter measurements, three approaches were

compared: two automated image-processing programmes, namely DiameterJ (a plugin in ImageJ/Fiji) [35] and SIMPoly (a programme in MATLAB) [36], which automatically identify and measure fibre diameters from SEM micrographs, and a manual measurement method using the Line tool in ImageJ/Fiji, where individual fibres are selected and measured manually one by one. An SEM image of commercial 53-gauge steel wire with a known diameter of 16.7 ± 0.1 μm was used as a reference, as shown in Figure 4. 6.

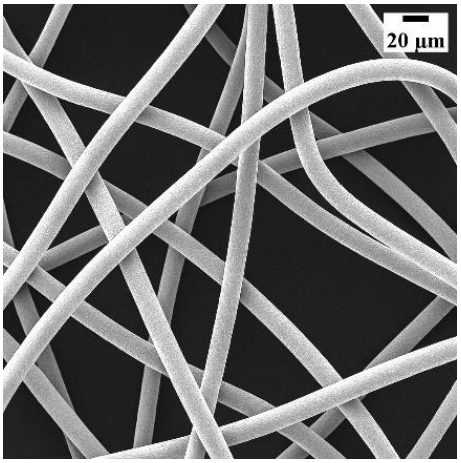

Figure 4. 6: The SEM image of 53-gauge steel wire.

4.8.1 DiameterJ plugin and SIMPoly programme

The SEM image of the 53-gauge steel wire was analysed using both the DiameterJ plugin and the SIMPoly programme to evaluate the accuracy and consistency of automated fibre diameter measurements. The algorithmic workflow of DiameterJ is illustrated in Figure 4. 7. DiameterJ analyses the segmented SEM image through a sequence of centreline tracing, intersection removal, and iterative correction steps to compute fibre diameter, orientation, intersection density, and mesh hole characteristics. In contrast, Figure 4. 8 illustrates the SIMPoly workflow, where SEM images are processed sequentially via histogram equalisation, morphological reconstruction, global thresholding, and Canny edge detection, followed by noise removal and edge refinement to obtain a binary image. The programme then traces the fibre centrelines and automatically generates the diameter distribution.

While both tools perform automatic diameter extraction from SEM images, they differ substantially in their implementation platforms, image segmentation strategies, and workflow flexibility, as summarised below.

i) Operating platform and image segmentation strategy. DiameterJ is implemented as a plugin for ImageJ/Fiji. For each SEM image, multiple built-in thresholding algorithms (e.g., Default, Mean, Otsu, Triangle, Li) are automatically applied to produce a series of binary segmentations. Users then visually inspect the results and select the segmentation that best distinguishes fibres from the background for subsequent analysis. This approach ensures robust adaptability across images with varying brightness or contrast. In contrast, SIMPoly is a MATLAB-based script that executes a fixed sequence of image-processing operations, including contrast enhancement through contrast-limited adaptive histogram equalisation, morphological reconstruction, global thresholding, and edge refinement. The entire segmentation process is automated and consistent across samples, but lacks user control for adaptive selection.

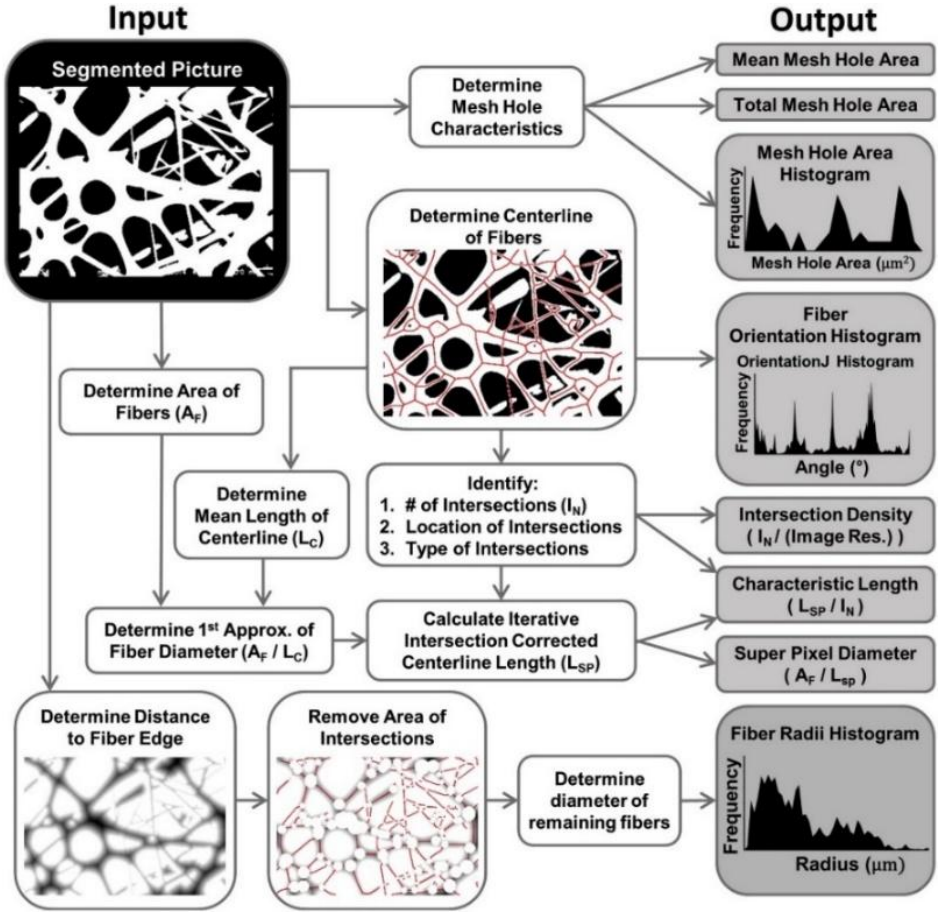

Figure 4. 7: Workflow diagram of the DiameterJ fibre analysis algorithm (Reproduced with permission from [35]. Copyright 2015 Elsevier).

ii) Diameter extraction method. DiameterJ provides two built-in algorithms for fibre diameter estimation: the Super-Pixel method, which computes the mean diameter by dividing the total fibre area by the total centreline length, and the Histogram method, which overlays the fibre skeleton on

the Euclidean distance map to calculate per-pixel radii, followed by Gaussian fitting. SIMPoly, on the other hand, performs skeletonisation using axial thinning and computes local diameters via distance transforms applied to the skeleton pixels. A histogram is then constructed from doubled skeleton distances, and a single Gaussian peak is fitted to obtain the average fibre diameter. Additionally, SIMPoly generates a colour-coded diameter map that visualises the spatial variation in fibre size.

iii) Workflow control and analytical throughput. DiameterJ offers user interaction in segmentation selection and provides additional structural metrics such as fibre orientation, pore size, and porosity. It also supports batch processing, enabling high-throughput analysis of large image datasets. In contrast, SIMPoly follows a rigid, one-image-at-a-time workflow, offering full automation but lower flexibility and throughput. In summary, DiameterJ provides greater flexibility and structural analysis options through a semi-automated, user-guided workflow. In contrast, SIMPoly delivers a fully automated but more rigid image-processing sequence suitable for single-image analysis.

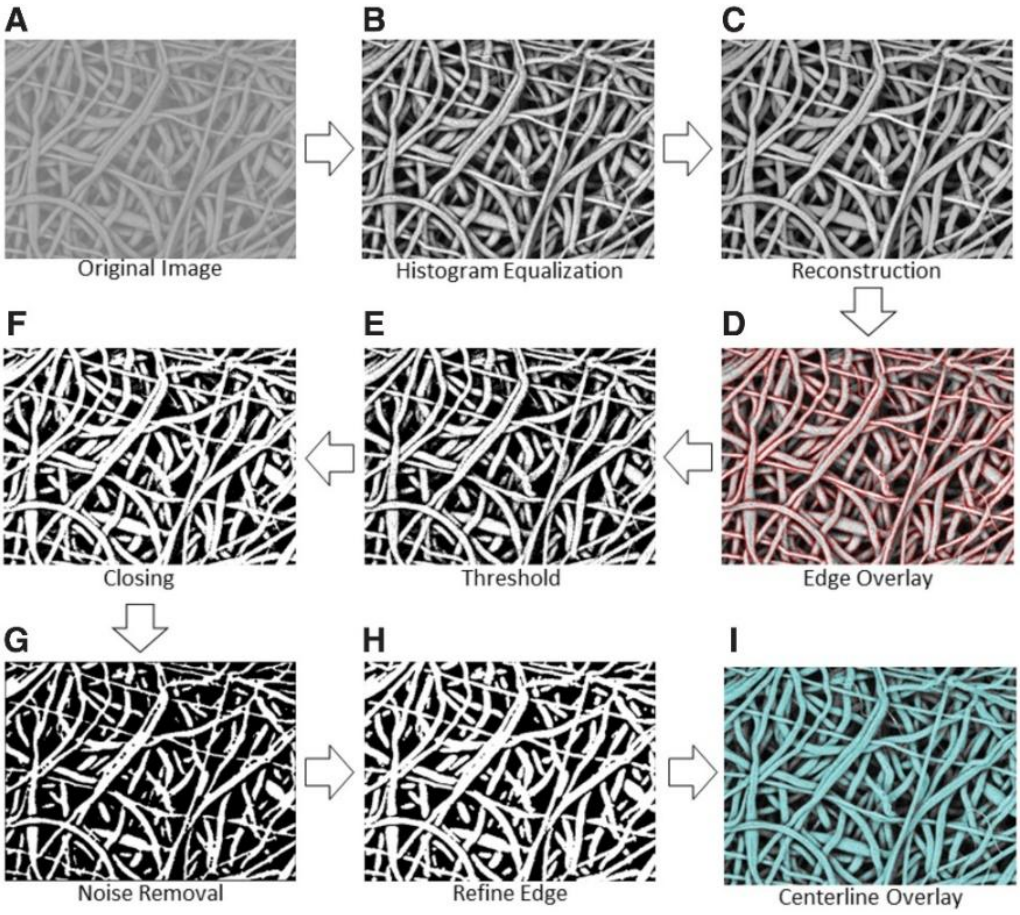

Figure 4. 8: Workflow diagram of the SIMPoly fibre analysis algorithm (Adapted from [36]. Licensed under CC BY 4.0).

4.8.2 Manual measure using the line tool

The Line tool in ImageJ/Fiji software was used to manually measure fibre diameters in an SEM image of 53-gauge steel wire. After calibrating the scale bar, lines were drawn across the fibre cross-sections using the Line tool (see Figure 7. 2a), with efforts made to ensure perpendicularity to the filament axis. All measured segments were recorded using the ROI Manager, and their lengths were taken as the corresponding fibre diameters. 150 filament segments were randomly selected and measured to calculate the average fibre diameter. The manually measured results were compared with those obtained using the DiameterJ plugin and the SIMPoly programme to assess consistency and accuracy across different analysis methods.

4.8.3 ANN model

An ANN was employed to establish a quantitative relationship between electrospinning parameters and the resulting fibre diameter. The detailed construction, training, and validation procedures of the ANN are presented in Section 7.2.

The multilayer perceptron (MLP) is the most fundamental and widely used neural network architecture in ANN models [199]. An MLP consists of an input layer, one or more hidden layers, and an output layer, responsible for receiving original feature inputs, extracting and transforming features, and generating prediction outputs, respectively [200]. The network operates in a feedforward manner, where the output of one layer serves as the input to the next layer, continuing sequentially until the final output is obtained. To enable nonlinear mapping and prevent gradient vanishing, activation functions such as Sigmoid, Tanh, or ReLU are commonly applied in the hidden layers. The backpropagation (BP) algorithm is a widely used and effective nonlinear statistical method for calculating the weights and biases of neurons [201]. During the learning process, the BP algorithm iteratively updates the weights and biases based on the difference between the predicted and actual values until the optimal performance is achieved [202].

A MATLAB-based MLP network (Neural Network Toolbox) was independently constructed and trained. The network comprised an input layer, a single hidden layer with 10 neurons, and an output layer, and was trained using the BP algorithm with the Levenberg–Marquardt optimisation method.

An adaptive learning rate and early-stopping strategy were introduced to enhance convergence and prevent overfitting. Four electrospinning parameters, including polymer molecular weight, solution concentration, feed flow rate, and tip-to-collector distance, served as input variables, while the experimentally obtained average fibre diameter was set as the output variable. The dataset was randomly divided into training (70%), validation (15%), and testing (15%) subsets to ensure generalisability. The training was repeated with different random initialisations to confirm stability, and model performance was assessed using the mean squared error (MSE) and coefficient of determination (R^2). A schematic of the ANN architecture (Figure 7. 1) and its mathematical formulation (Eqs. (7–8)) are provided in Section 7.2. Overall, the ANN serves as a predictive tool to capture nonlinear correlations among the electrospinning parameters and to guide process optimisation.

CHAPTER 5

5 Electrospun PCL scaffolds for tissue engineering

Abstract

Electrospun PCL nanofibrous scaffolds closely mimic the ECM, offering significant potential for tissue engineering. However, precise morphological control remains essential. In this section, scaffold morphology was systematically optimised by adjusting molecular weight, solution concentration, and flow rate during electrospinning. Bead-free fibres with suitable pore sizes and porosity were achieved using medium- and high-MW PCL. In vitro assays with L929 fibroblasts confirmed enhanced cell adhesion, proliferation, and spreading on the optimised scaffolds. Notably, an unexpected interaction between PCL and MTT assay reagents was observed, suggesting potential artefacts in standard viability measurements. Although the morphological features were improved, the intrinsic hydrophobicity remained a limitation, highlighting the need for surface modification or blending with biomass-derived polymers to enhance hydrophilicity and biocompatibility, thereby supporting broader applications in regenerative medicine.

5.1 Introduction

The development of electrospun nanofibrous scaffolds has revolutionised tissue engineering by enabling the fabrication of biomimetic structures that closely resemble the ECM. Their high porosity and interconnected nanofibre networks provide favourable environments for cell attachment, proliferation, and nutrient exchange. Among various polymers, PCL is one of the most widely used synthetic materials due to its biocompatibility, mechanical robustness, and slow hydrolytic

degradation under physiological conditions, which make it suitable for long-term implantation and regenerative applications [203].

Polymer molecular weight (MW) plays a key role in influencing electrospinning behaviour and membrane morphology. Gel permeation chromatography (GPC) analysis is strongly recommended before electrospinning to verify the actual MW of commercial PCL polymers, yet it is frequently overlooked. Significant discrepancies were observed between the labelled and measured MW values of purchased PCL batches. For example, a batch produced in 2014 and labelled as M_w of 80,000 g/mol was found to have degraded to 38600 g/mol, likely due to long-term humid air exposure. Even two recent batches from 2021, both labelled as 80,000 g/mol, showed measured M_w values of 83700 and 96700 g/mol, respectively. Such deviations are critical, as MW governs the viscosity, chain entanglement density, and surface tension of polymer solutions, thereby affecting Taylor cone formation, jet stability, and ultimately fibre morphology during electrospinning.

Despite its fundamental importance, the influence of PCL molecular weight on scaffold microstructure and resulting biological performance has limited systematic investigation. Furthermore, while many studies have attempted to improve PCL's biocompatibility through polymer blending, copolymerisation, or surface functionalization as summarised in Section 2, these composite modifications introduce additional variables that obscure the intrinsic structure–property relationships. Therefore, in this section, pure PCL was deliberately chosen as a model system to provide a clear and quantitative understanding of how molecular weight, solution concentration, and feed flow rate affect electrospinning behaviour and scaffold properties.

The fabricated nanofibrous scaffolds were characterised using SEM to analyse morphology (fibre diameter, pore size, and porosity). The solution viscosity was measured to determine its dependence on both MW and concentration, and WCA was used to evaluate surface wettability and assess scaffold hydrophilicity. To elucidate cell–scaffold interactions, L929 fibroblasts were cultured on PCL scaffolds, with TCP as a 2D control. Cell viability, attachment, and morphology were assessed using MTT assays, LSCM, and SEM. This systematic investigation aims to elucidate the fundamental relationships among PCL molecular weight, electrospinning parameters, and scaffold architecture, thereby establishing a reproducible baseline for the rational design and optimisation of PCL-based composite or surface-modified scaffolds in future tissue engineering applications.

5.2 Preparation of electrospun scaffolds

A schematic diagram of the electrospinning setup is shown in Figure 5. 1, and the experimental design for PCL solution preparation is summarised in Table 5. 1. For low molecular weight (LMW) PCL, solutions were prepared at concentrations of 20%, 30%, and 40% w/v. For medium (MMW) and high molecular weight (HMW) PCL, solutions were prepared at 15%, 20%, 25%, and 30% w/v. To obtain homogeneous solutions, PCL particles were dissolved in a solvent mixture of acetic acid and formic acid (AA/FA, 3:1 v/v) and stirred overnight using a magnetic stirrer (Thermo Cimarec Stirring Hotplate SP131635, The Lab World Group, USA). Electrospinning was performed under ambient atmospheric conditions. Each solution was loaded into a 5 mL plastic syringe equipped with a metallic spinneret (inner diameter: 0.25 mm). A high-voltage power supply (Series ES, Gamma High Voltage, USA) integrated with a safety switch unit applied 15 kV during electrospinning.

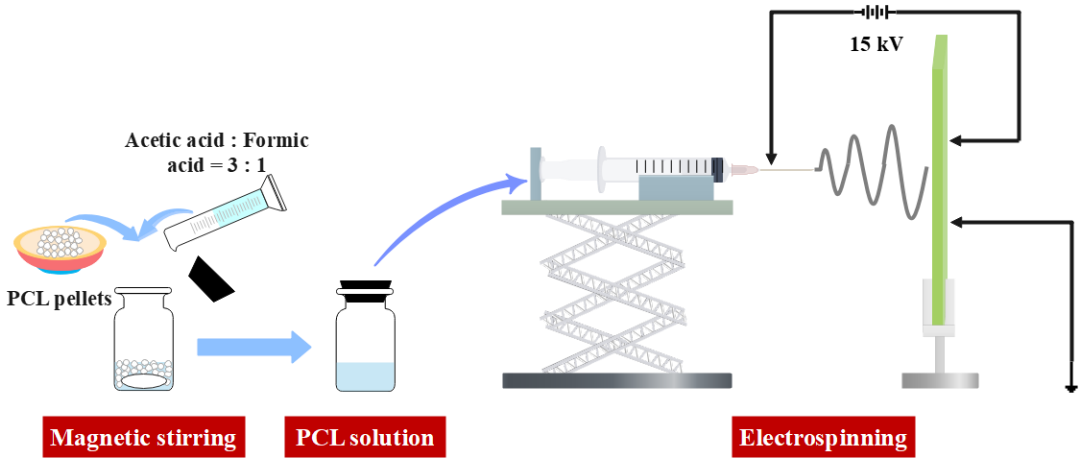

Figure 5. 1: Schematic diagram of the electrospinning setup for the fabrication of PCL nanofibrous scaffolds.

The polymer jet was directed from the spinneret tip toward a vertically mounted copper collector (15 cm × 15 cm) covered with aluminium foil, located 15 cm from the tip, a typical distance that allows sufficient solvent evaporation before fibre deposition. The PCL solution was delivered using a KDS 100 Legacy Single Syringe Infusion Pump (KD Scientific, USA) at controlled flow rates of 0.8, 1.5, or 2.3 mL/h. Following electrospinning, the resulting PCL nanofibre scaffolds were carefully removed from the foil and air-dried overnight at room temperature. For clarity, samples were labelled by molecular weight, solution concentration, and flow rate. For example, "LMW-20%-1.5" refers to a scaffold fabricated from a 20% w/v LMW solution at a flow rate of 1.5 mL/h.

Table 5. 1: Experimental design summary for the preparation of PCL solutions with varying MWs, concentrations, and flow rates.

Molecular weight (g/mol)	Solution concentration (% w/v)	Flow rate (ml/h)
38600	20	1.5
	30	1.5
	40	1.5
83700	15	1.5
	20	1.5
	25	0.7
	25	1.5
	25	2.3
	30	1.5
96700	15	1.5
	20	0.7
	20	1.5
	20	2.3
	25	1.5
	30	1.5

5.3 Results and discussion

5.3.1 Viscosity

As shown in Figure 5. 2, the viscosity of the PCL solutions increased with both polymer concentration and molecular weight. This trend is expected because higher-molecular-weight polymers contain longer chain segments that become more easily entangled as the solution concentration increases. At lower concentrations (e.g., MMW-15%), the chains were only weakly entangled. When the concentration increased to 25%, the chains overlapped and formed a transient network that resisted shear deformation, leading to a sharp increase in viscosity. The difference between MMW-15% (0.190 ± 0.011 Pa·s) and MMW-25% (1.058 ± 0.065 Pa·s) clearly illustrated

this transition, while HMW-25% reached the highest viscosity (~ 2.24 Pa·s), reflecting its greater chain length and entanglement density.

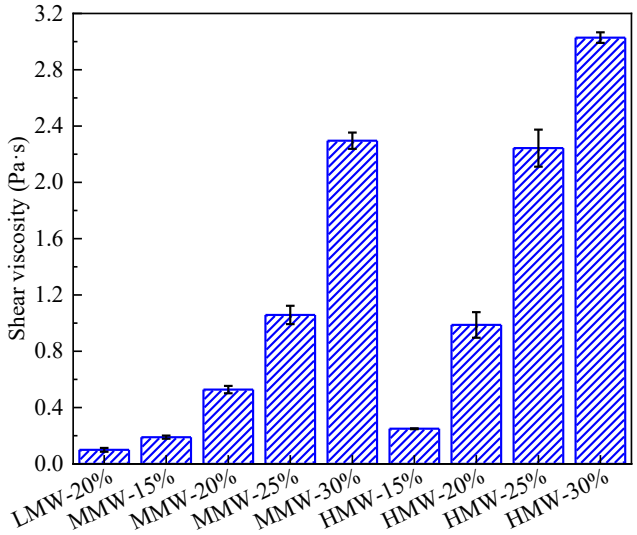

Figure 5. 2: Influence of molecular weight and solution concentration on viscosity of PCL solutions measured at 25 °C and a shear rate of 100 s^{-1}.

Although only one LMW sample was tested due to material limitations, the data still showed a coherent trend that supported the general relationship among molecular weight, concentration, and viscosity. Similar observations have been reported in previous studies on electrospinning-grade PCL solutions [204, 205]. These results also explain the subsequent fibre morphologies presented in Section 5.3.2. Solutions with very low viscosity (such as LMW-20% and MMW-15%) tend to produce unstable jets and bead formation, whereas the more viscous formulations (MMW-25% and HMW-25%) provide better jet stability and continuous fibre formation.

The viscosity values in Figure 5. 2 define a practical processing window for the present work, that is, below approximately 0.5 Pa·s, the solution is too fluid for stable spinning. In contrast, beyond about 2 Pa·s, the jet becomes difficult to stretch, potentially resulting in thicker fibres. The selected MMW-25% and HMW-20% samples, therefore, represent a balanced condition that ensures continuous fibre formation and good structural uniformity, as confirmed in the following section on scaffold morphology.

5.3.2 Morphology of nanofibre scaffolds

Figure 5. 3-Figure 5. 5 collectively illustrate how the molecular weight and concentration of PCL solutions determine the morphology, uniformity, and structural parameters of the electrospun

scaffolds. Under identical spinning conditions (1.5 mL/h flow rate, fixed voltage, and temperature), the micrographs in Figure 5. 3 revealed a gradual transition from bead-dominated structures to smooth and continuous fibre networks as the viscosity of the precursor solutions increased. At low viscosities, particularly in LMW and low-concentration solutions, insufficient polymer chain entanglement led to unstable jet formation and droplet ejection rather than continuous fibre spinning. This phenomenon, known as electrospray, produces bead-like or droplet morphologies that disrupt scaffold continuity [206]. As polymer concentration and MW increase, the enhanced chain overlap and viscoelasticity stabilise the jet, allowing smooth elongation of the polymer stream and uniform fibre deposition [207]. This morphological evolution directly mirrors the rheological behaviour described in Figure 5. 2 and reflects the crucial role of chain entanglement in sustaining a stable polymer jet during electrospinning.

For low-viscosity LMW solutions, the jet lacked sufficient elasticity to resist surface tension, leading to extensive bead and droplet formation. The images of LMW-20% (Figure 5. 3a) clearly showed thin fibres interspersed with spherical beads, while LMW-30% and LMW-40% (Figure 5. 3b and c) exhibited fewer beads but still displayed irregular fibre diameters and discontinuities. Quantitative analysis (Figure 5. 5a) confirmed this instability: the mean fibre diameter increased from 118 ± 35 nm at 20% to 188 ± 95 nm at 40%, accompanied by bead distribution suggesting that the jet oscillated frequently between electrospray and true electrospinning regimes. Correspondingly, the pore size distribution (Figure 5. 4b) showed a gradual upward shift but remained heterogeneous, consistent with the irregular spacing observed in SEM. These results indicated that even at high concentrations, LMW PCL lacked the molecular chain length required to form an interconnected entanglement network. Bead defects persisted throughout, severely limiting the scaffolds' structural integrity. Such discontinuities are undesirable in tissue engineering because they lead to uneven stress distribution and disrupted cell attachment, often resulting in poor proliferation and migration on the scaffold surface [208].

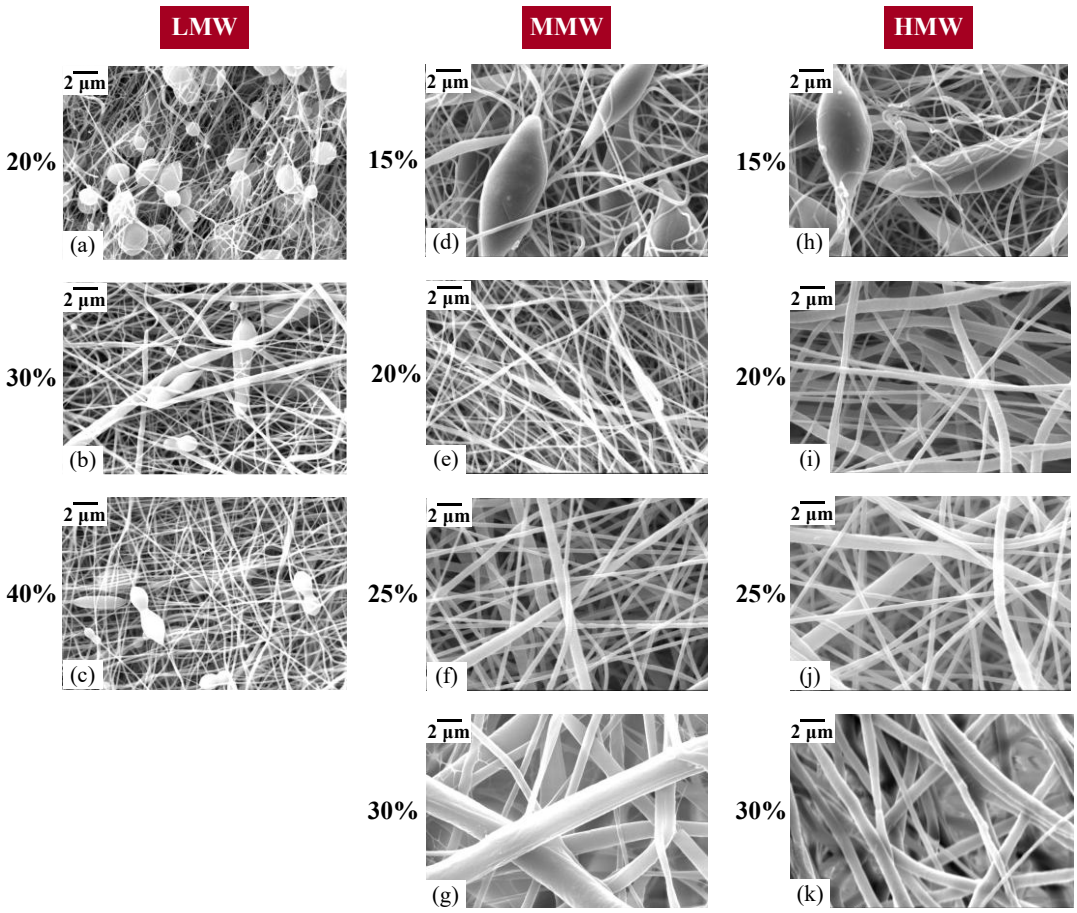

Figure 5. 3: SEM images of electrospun PCL nanofibre scaffolds prepared at various concentrations (flow rate, 1.5ml/h).

The situation improved markedly for MMW and HMW PCL. At 15%, both still displayed bead-on-string morphologies (Figure 5. 3d and h), which corresponded to the onset of chain overlap but insufficient viscosity for a fully stable jet. When the concentration increased to 20%, the fibres became smooth, continuous, and uniform across the field of view (Figure 5. 3e and i). As depicted in Figure 5. 4c and e, fibre diameter increased with rising PCL concentration. The average fibre diameters increased from 202 ± 46 nm (MMW-15%-1.5) and 182 ± 39 nm (HMW-15%-1.5) to 470 ± 209 nm and 594 ± 313 nm, respectively, when the concentration was raised to 25%. The SEM images also revealed well-defined inter-fibre voids and uniform pore networks, which were ideal for supporting cell infiltration and nutrient transport. Further increasing the concentration to 30% introduced adverse effects. Both MMW-30%-1.5 and HMW-30%-1.5 samples (Figure 5. 3g and k) exhibited noticeably thicker fibres with occasional fusion at cross-points and reduced inter-fibre spacing. The surfaces appeared smoother and denser, lacking the open porous texture observed at 20–25%.

Statistical results (Figure 5. 5c) confirmed that porosity decreased sharply by nearly 10% as the concentration increased from 25% to 30%. This densification can be attributed to two coupled factors. First, as viscosity increased, jet stretching was hindered, leading to large, slow-moving fibres that compactly deposit on the collector. Second, at high polymer concentrations, solvent evaporation becomes kinetically limited. As the solvent evaporates from the fibre surface, a polymer-rich outer layer forms rapidly. This layer can behave as a semi-solid "crust" that hinders further solvent diffusion from the fibre core to the surface, thereby reducing the effective evaporation rate. Such crust formation during solvent removal has been well documented in thin polymer films and is associated with diffusion-limited drying processes [209]. The slightly glossy or off-white background visible in these SEM micrographs provided visual evidence of incomplete drying and partial fibre coalescence. As successive fibre layers accumulated, residual solvent within the underlying layer softened the deposited mat, further reducing pore interconnectivity. Such morphological compaction and residual solvent entrapment are detrimental to cell culture applications because they limit the diffusion of oxygen and nutrients through the scaffold thickness [210]. Given the resulting reduction in porosity and poor solvent removal, 30% PCL solutions were unsuitable for fabricating electrospun scaffolds for tissue engineering applications.

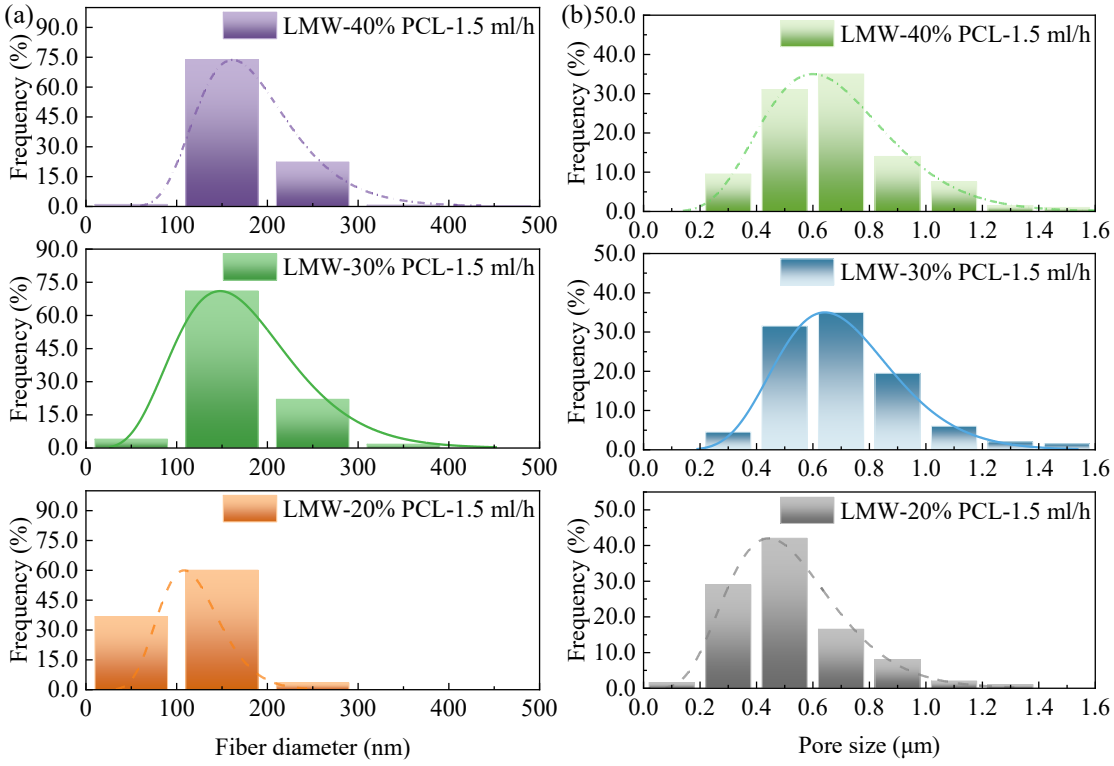

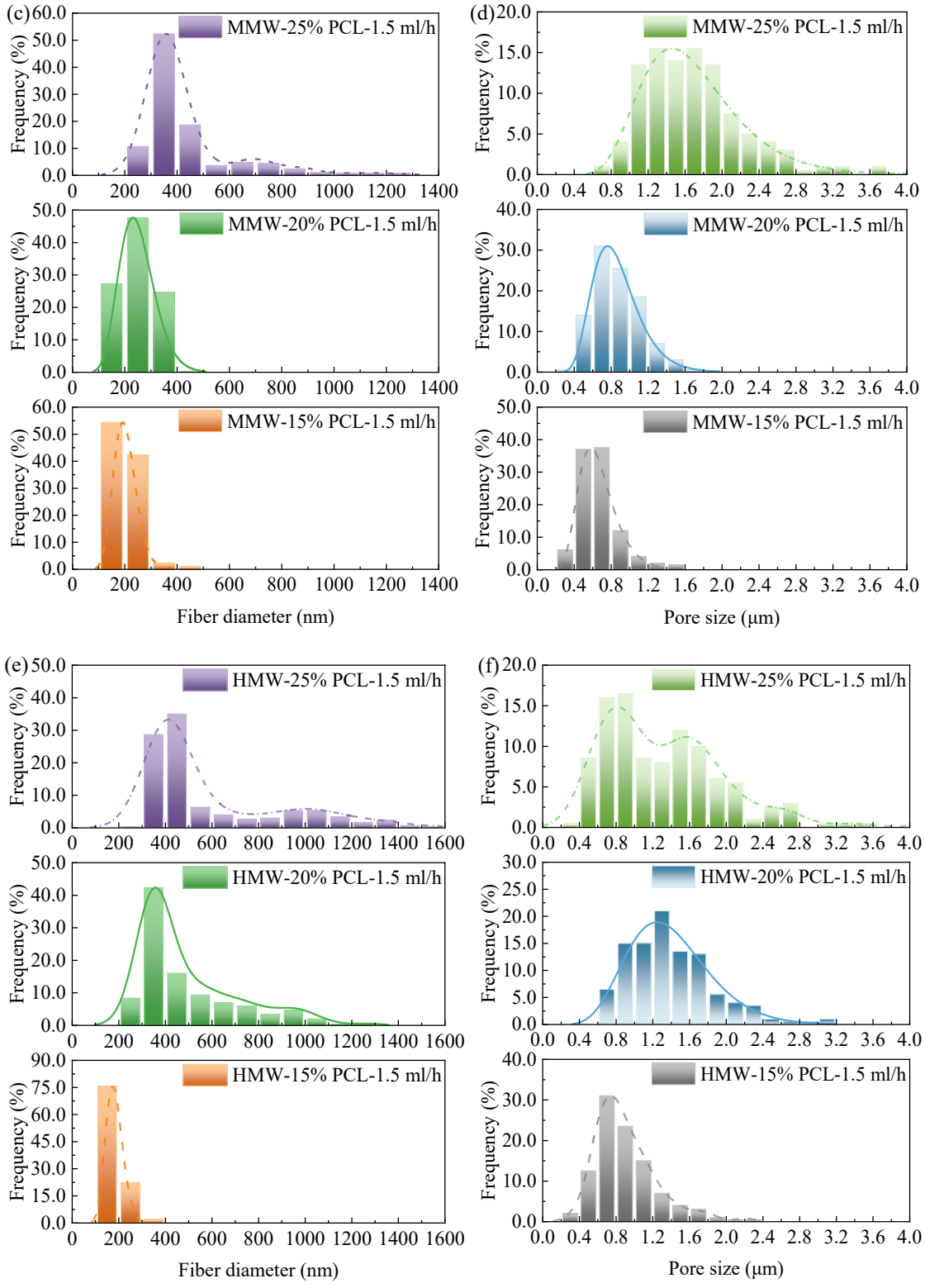

Figure 5. 4: Distributions of fibre diameters ((a), (c), (e)) and pore sizes ((b), (d), (f)) of PCL scaffolds fabricated with different concentrations and MWs (flow rate of 1.5 ml/h).

The quantitative results in Figure 5. 5 identified MMW-25%-1.5 as the most balanced formulation among the tested samples. It combined a moderate fibre diameter (470 ± 209 nm) with the largest average pore size (1.7 ± 0.6 μm) and a porosity of 58.38 ± 2.68%, representing a structure that was

open enough for cell penetration yet mechanically coherent. In comparison, HMW-20%-1.5 exhibited slightly smaller pores (1.4 ± 0.5 μm) but higher overall porosity (60.26 ± 1.54%), suggesting that higher molecular weight polymers reach optimal spinnability at slightly lower concentrations due to their inherently greater chain entanglement. When the HMW PCL concentration was further increased to 25%, the porosity decreased and the fibre packing became denser, confirming that over-entanglement can restrict fibre thinning. Since pore size and porosity are key parameters influencing cell adhesion, migration, and nutrient diffusion, scaffolds with larger, more open structures are generally more favourable for tissue regeneration [211]. Electrospun scaffolds with limited pore size and low porosity have been shown to hinder cell infiltration and tissue ingrowth [203].

Taken together, Figure 5. 3-Figure 5. 5 clearly demonstrated the dual control of fibre morphology by molecular weight and concentration. Both parameters governed solution viscosity, which, in turn, determined the stability of the electrospinning jet and the resulting scaffold architecture. For tissue engineering, achieving the right balance between fibre diameter and porosity is essential. Fragile fibres may form dense mats that restrict cell infiltration, whereas overly thick fibres reduce surface area and impair initial cell adhesion. The scaffolds fabricated from MMW-25%-1.5 and HMW-20%-1.5 achieved the most desirable microstructure, providing an interconnected pore network suitable for fibroblast proliferation and migration. These two compositions were therefore selected for subsequent wettability and biocompatibility assessments described in Sections 5.3.3 and 5.3.4.

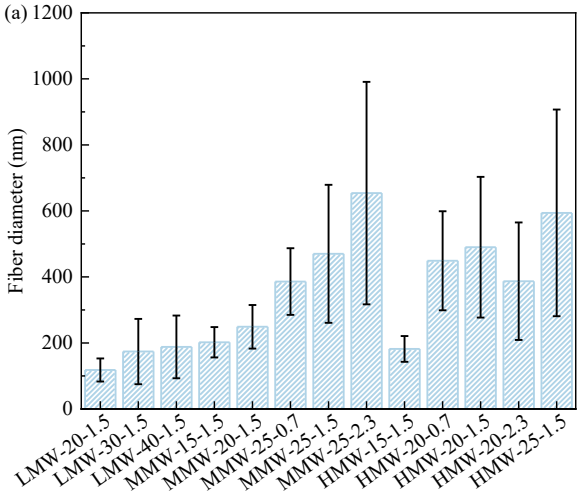

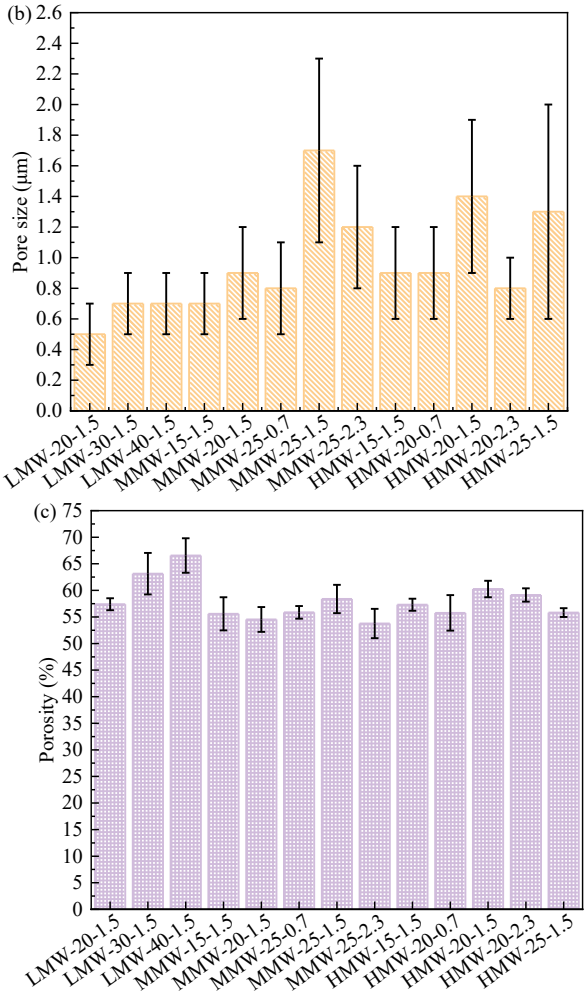

Figure 5. 5: Average fibre diameters, pore sizes, and porosities of PCL scaffolds fabricated under different conditions.

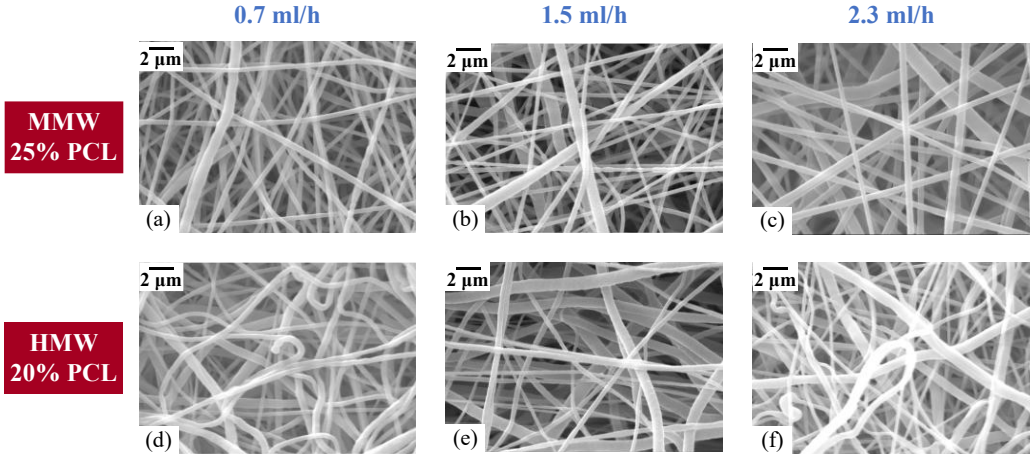

Figure 5. 6: Morphology of MMW-25% and HMW-20% PCL scaffolds fabricated with different flow rates.

Figure 5. 6 and Figure 5. 7 illustrated the influence of flow rate on the morphology of electrospun scaffolds fabricated from the two optimal formulations identified earlier (MMW-25% and HMW-20%). All other spinning parameters were kept constant so that the observed differences could be

attributed solely to changes in flow rate. As shown in Figure 5. 6, both materials exhibited the most uniform and porous fibre networks at a moderate flow rate of 1.5 mL/h. When the flow rate was reduced to 0.7 mL/h, the deposited fibres appeared thinner and more densely packed, with shallow, discontinuous pores. At the opposite extreme, 2.3 mL/h produced an irregular surface with partially fused fibres, suggesting incomplete solvent evaporation. These contrasting features clearly indicated that fibre morphology and porosity were sensitive to the polymer solution feed rate.

Quantitative data in Figure 5. 7 confirmed these visual observations. Among the tested conditions, MMW-25%-1.5 and HMW-20%-1.5 yielded the most favourable scaffold morphologies, as evidenced by uniform fibre formation and well-distributed pores (Figure 5. 6b and e). For MMW-25%, the average pore size increased from 0.8 ± 0.3 μm at 0.7 mL/h to 1.7 ± 0.6 μm at 1.5 mL/h, before decreasing to 1.2 ± 0.4 μm at 2.3 mL/h. In terms of porosity (Figure 5. 5c), MMW-25%-1.5 achieved a significantly higher value of 58.4 ± 2.7%, outperforming both lower and higher flow rate conditions. The same trend was observed in the HMW-20% series, where 1.5 mL/h produced the most open structure, with a pore size of 1.4 ± 0.5 μm and a porosity of 60.26 ± 1.54%. At both lower and higher flow rates, porosity dropped noticeably, accompanied by a denser fibre arrangement. These results suggested that an intermediate flow rate allowed a balance between polymer supply and solvent evaporation, producing scaffolds with high interconnectivity and uniform fibre distribution.

This behaviour can be explained by the dynamic balance among three competing factors: the volume of solution delivered, the rate of solvent evaporation, and the stretching capacity of the electrospinning jet. At low flow rates, the polymer supply is insufficient to maintain a stable Taylor cone, which refers to the conical meniscus formed at the spinneret tip when electrostatic forces overcome the surface tension of the polymer solution, enabling the ejection of a charged jet [212]. This instability leads to intermittent jet formation and the production of overly thin fibres that pack tightly upon deposition. Such dense fibre stacking decreases effective pore area and overall porosity. In contrast, when the flow rate is too high, the incoming jet carries excess solvent that cannot fully evaporate during its travel from the spinneret to the collector. As a result, the fibres reach the collector in a semi-liquid state and fuse at contact points, forming compact regions and reducing pore connectivity. The intermediate value of 1.5 mL/h provided a compromise between these two extremes.

It supplied enough polymer to form a continuous jet while still allowing sufficient solvent removal, resulting in smooth fibres and open pores. This explanation is consistent with previous findings on the importance of maintaining balanced mass flux and drying kinetics in electrospinning [213, 214].

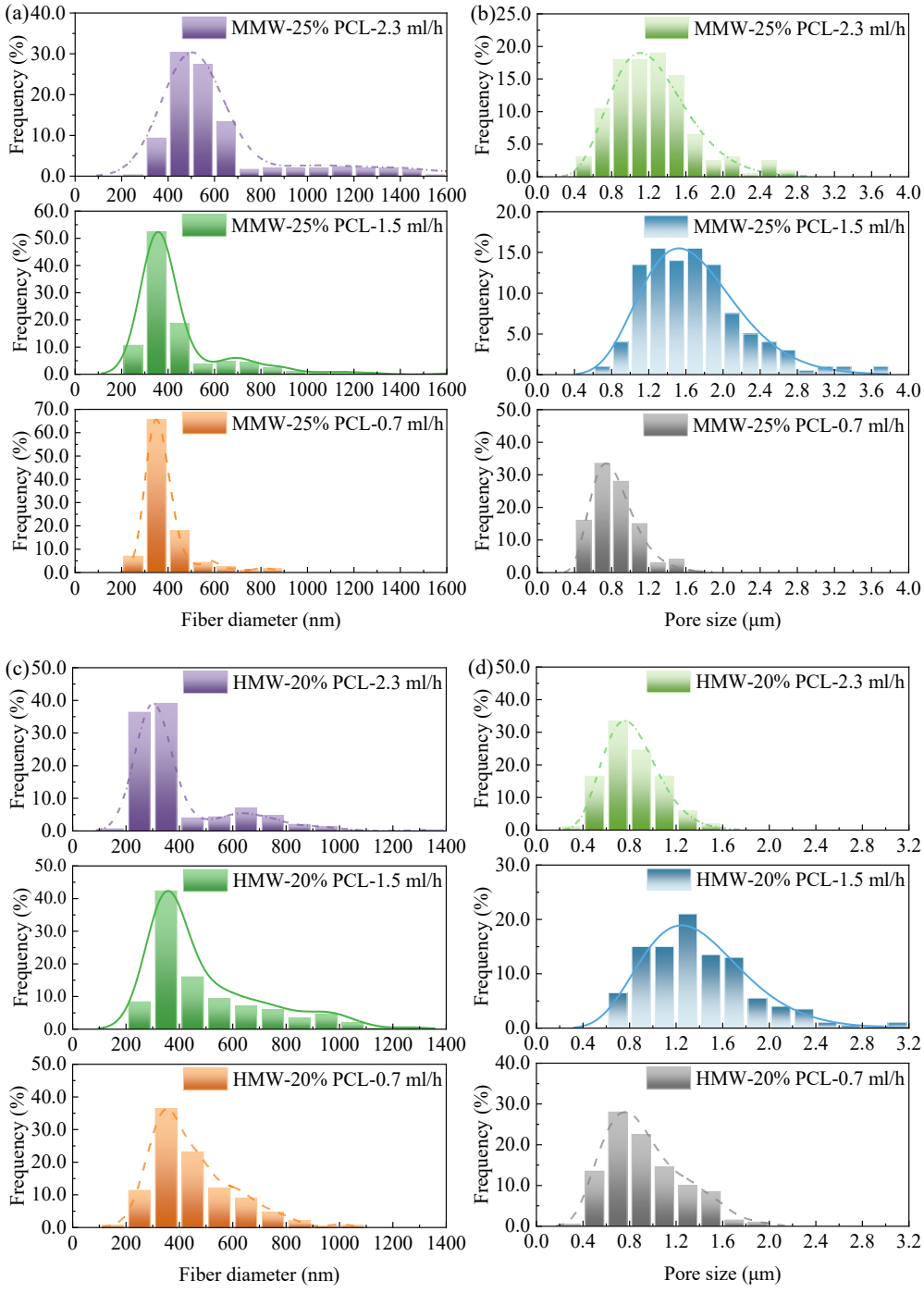

Figure 5. 7: Distributions of fibre diameters ((a), (c)) and pore sizes ((b), (d)) of MMW-25% and HMW-20% PCL scaffolds fabricated from different batches with different flow rates.

The flow-rate optimisation complemented the earlier findings on molecular weight and concentration. In summary, low-concentration solutions or those based on LMW PCL tended to produce a mixture

of fibres and beads due to insufficient chain entanglement and low viscosity. Increasing either concentration or molecular weight enhanced chain entanglement and viscoelasticity, enabling the electrospinning process to overcome surface tension and generate uniform, bead-free fibres. Once the concentration and molecular weight were tuned into the optimal range (as with MMW-25% and HMW-20%), the flow rate became the key factor determining fibre uniformity and scaffold architecture. A moderate flow rate was critical for achieving smooth, continuous fibre formation and a porous scaffold structure. Both excessively low and high flow rates resulted in dense surface morphologies, either due to fibre thinning or incomplete solvent evaporation. The selected conditions (MMW-25%-1.5 and HMW-20%-1.5) thus represent an optimal combination that consistently produces uniform, bead-free fibres with interconnected pores and balanced porosity around 60%. Such structural characteristics are essential for tissue engineering scaffolds because they facilitate nutrient transport and provide sufficient space for cell proliferation and migration. These two formulations were therefore chosen for subsequent evaluations of surface wettability and biocompatibility in the following sections.

5.3.3 Hydrophobicity of the scaffolds

WCA measurements were performed to evaluate the surface wettability of the electrospun PCL scaffolds, as the degree of hydrophilicity or hydrophobicity strongly influences nutrient diffusion, protein adsorption, and cell adhesion behaviour. As shown in Figure 5. 8a–c, the contact angles of scaffolds fabricated from LMW, MMW, and HMW PCL varied with concentration and flow rate, and the comparative results were summarised in Figure 5. 8d. A clear dependence on polymer chain characteristics was observed: LMW scaffolds showed relatively low contact angles that increased sharply with concentration, whereas MMW and HMW scaffolds remained highly hydrophobic under all tested conditions.

For LMW PCL, increasing the solution concentration from 20% to 40% increased the water contact angle (WCA) from 74 ± 10 ° to 115 ± 5 °, representing an absolute increase of approximately 41 °, consistent with enhanced surface hydrophobicity. This increase correlated with the morphological changes seen in Figure 5. 3 and Figure 5. 4, thicker fibres and a smoother surface at higher concentrations. The increase in fibre diameter and the decrease in surface roughness resulted in a less

wettable surface. The pronounced hydrophobicity was shown in dense LMW-40% scaffolds. In contrast, scaffolds electrospun from MMW and HMW PCL exhibited contact angles consistently above 110 ° across all spinning parameters. These values confirmed the intrinsic hydrophobic nature of PCL and suggested that neither molecular weight, concentration, nor flow rate altered the hydrophobicity of the as-spun fibres. Minor variations observed between samples can be attributed to differences in fibre packing and local surface roughness.

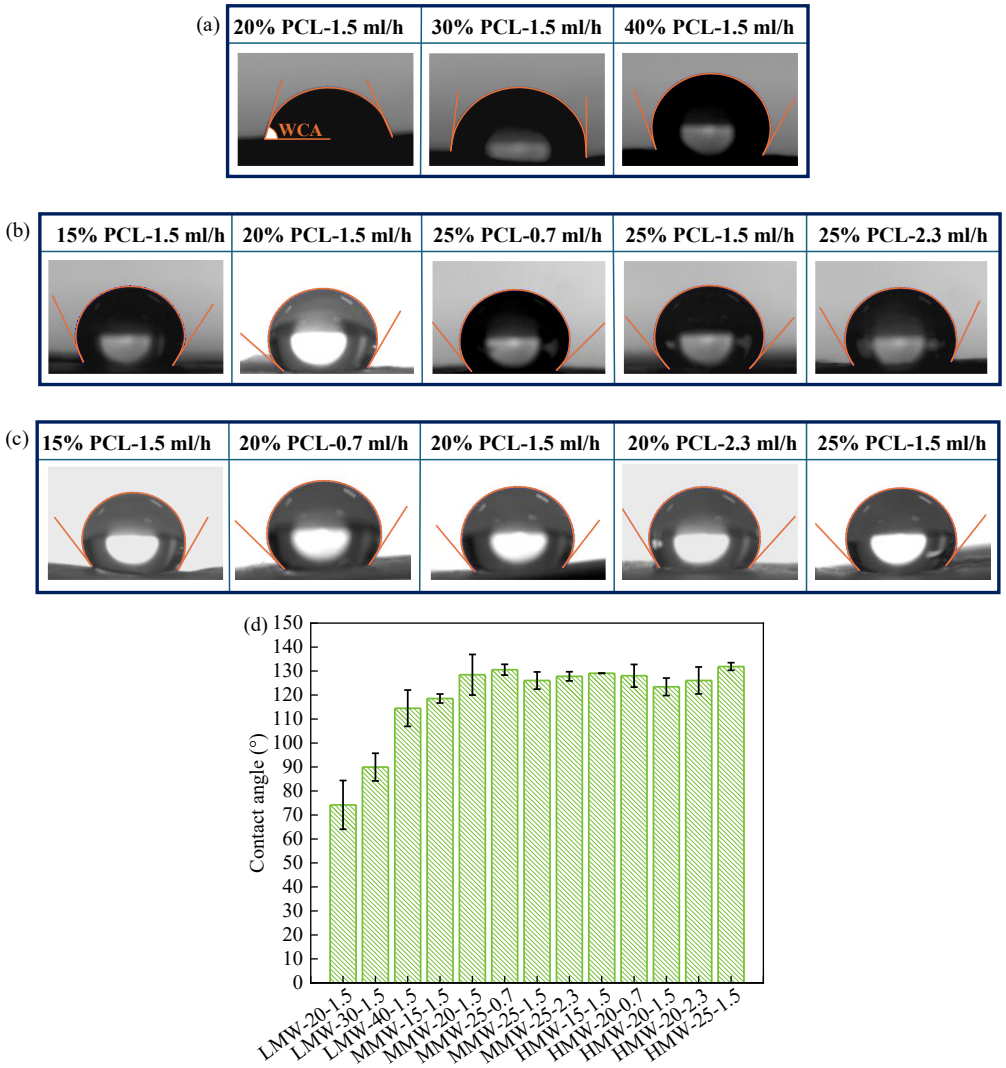

Figure 5. 8: Contact angles of PCL scaffolds fabricated from LMW (a), MMW (b), and HMW (c) with different concentrations and flow rates. Data comparison chart (d).

In general, a contact angle greater than 90 ° denotes a hydrophobic surface that resists water spreading and limits the infiltration of aqueous media into the scaffold. While such surfaces may slow initial wetting, they can also hinder protein adsorption and subsequent cell attachment. By contrast, moderately hydrophilic surfaces (contact angles below 90 °) are known to promote fluid penetration and support cell–material interactions. Prior studies have shown that surface wettability

plays a critical role in regulating cell adhesion, spreading, and proliferation, with moderately hydrophilic surfaces providing more favourable conditions for cellular attachment than strongly hydrophobic ones [215]. Although the MMW-25%-1.5 and HMW-20%-1.5 scaffolds were identified as optimal from a structural perspective, exhibiting uniform fibres, interconnected pores, and high porosity, their strong hydrophobicity represented a limitation for direct biological application.

The results of Figure 5. 8 thus highlighted an essential trade-off in scaffold design: the processing conditions that yielded ideal morphology and mechanical stability did not necessarily provide sufficient hydrophilicity for cell adhesion. Improving the hydrophilicity of electrospun PCL scaffolds is therefore a necessary step before biological use. Common strategies include plasma treatment [216], alkaline hydrolysis [217], or surface coating with bioactive polymers [218]. These approaches can introduce polar functional groups onto the PCL surface, significantly lowering the contact angle and enhancing cell–material interactions.

Although the Section 5 focused on pure PCL scaffolds, the systematic investigation of their processing–structure–property relationships provided an essential foundation for future work on composite scaffolds. Since reports on the use of unmodified PCL alone in tissue engineering remain limited, understanding the detailed correlations between processing parameters, fibre architecture, and resultant scaffold properties is crucial. These insights in Section 5 not only clarified the intrinsic behaviour of PCL but also offered a mechanistic basis for interpreting and optimising the performance of PCL-based composite scaffolds in future studies.

5.3.4 In vitro biocompatibility

The primary aim of fabricating electrospun 3D scaffolds is to mimic the structural and functional characteristics of the native ECM, thereby providing a suitable physical framework for cellular attachment, proliferation, and migration. Among the fabricated samples, the HMW-20%-1.5 PCL scaffold was selected for cell culture studies due to its optimal morphology and porosity, which support nutrient diffusion and facilitate cell infiltration. Its balanced fibre diameter and interconnected pore network were expected to create a microenvironment capable of sustaining long-term cell growth while maintaining adequate mechanical stability. The average pore size of the electrospun scaffolds was approximately 1.5–2 μm, with an overall porosity of around 60%.

Although this pore size is smaller than the typical diameter of L929 fibroblasts (approximately 10–20 µm), electrospun nanofibrous scaffolds primarily support cell attachment and surface spreading rather than full-cell penetration through individual pores. Cells interact with the fibrous network by extending filopodia along and between fibres, enabling migration across the scaffold surface. Meanwhile, the interconnected pore structure and moderate porosity facilitate oxygen and nutrient diffusion throughout the scaffold thickness. Therefore, while the pore dimensions do not permit bulk cellular infiltration, they provide a microenvironment conducive to cell adhesion, proliferation, and metabolic exchange.

The proliferation of L929 fibroblast cells on this scaffold was evaluated using the MTT assay after 1, 3, and 7 days of incubation, with the results presented in Figure 5. 9. A gradual increase in cell viability was observed over time for both the PCL scaffolds and the tissue culture plate (TCP) control, confirming that the material did not exert cytotoxic effects and could support cell survival. Although overall metabolic activity on PCL was lower than on TCP, the positive growth trend across all time points indicated that fibroblasts adhered to and proliferated on the scaffold surface. The difference in proliferation rates is mainly due to surface wettability. As demonstrated in Figure 5. 8, the electrospun PCL scaffolds exhibited contact angles above 110 °, indicating a hydrophobic surface that limited protein adsorption and the initial cell-anchoring phase. In contrast, the hydrophilic nature of the 2D TCP substrate promoted rapid wetting and stable integrin-mediated adhesion, explaining its higher apparent viability values.

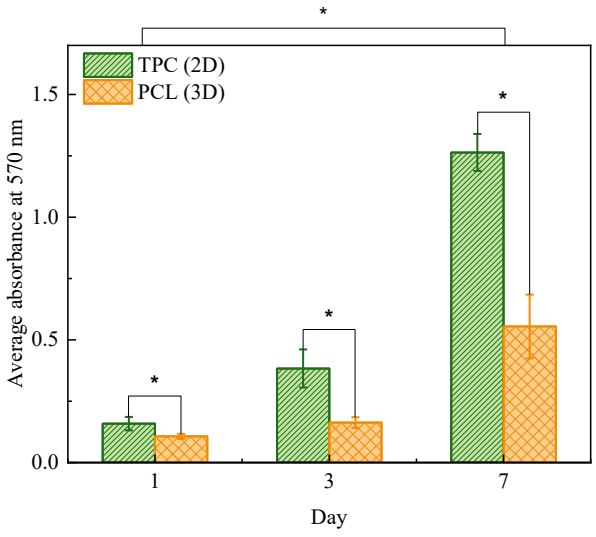

Figure 5. 9: Proliferation results of L929 cells on the TCP (2D control) and PCL nanofibrous scaffold (3D) after 1, 3, and 7 days from the MTT tests (P* < 0.05).

In addition to the quantitative MTT results, a distinct colour change was observed in the PCL scaffolds during the assay: the samples developed purple even in the absence of cells when exposed to PBS, cell culture medium, or MTT reagents. This phenomenon suggested possible interactions between the polymer surface and assay components. One plausible explanation was the absorption of formazan crystals or medium constituents within the scaffold's porous network, which can intensify the apparent colour and influence the accuracy of colourimetric readings. Therefore, while the overall increasing trend confirmed biocompatibility, the absolute absorbance values obtained from the MTT assay should be interpreted cautiously.

Taken together, the results confirmed that the electrospun HMW-20%-1.5 PCL scaffold supported fibroblast viability and proliferation over one week, demonstrating good cytocompatibility in vitro. Nevertheless, the relatively low wettability and the potential interference with colourimetric reagents highlighted intrinsic limitations of pristine PCL surfaces. Future work should consider complementary cell-viability assays, such as Live/Dead staining or Alamar Blue, to more accurately quantify cell activity on PCL scaffolds.

It was hypothesised that chemical interactions between PCL and the reagents used in the MTT assay might compromise the test's accuracy. A careful review of the literature revealed no published studies that explicitly describe or explain such interactions in PCL. To examine this possibility, a set of six blank control experiments was designed to isolate the contribution of each component involved in the assay. The experimental conditions were as follows: (1) pure PCL scaffold, (2) PCL with PBS, (3) PCL with culture medium, (4) PCL with PBS + MTT, (5) PCL with medium + MTT, and (6) PCL with MTT alone. All samples were incubated for three hours under standard culture conditions and subsequently air-dried at room temperature.

As shown in Figure 5. 10a, a pronounced purple colouration developed in all samples exposed to the MTT reagent, regardless of whether PBS or culture medium was present. In contrast, no colour change was observed in samples without MTT exposure. This finding provided clear evidence that PCL interacted directly with the MTT reagent rather than with the medium components. Such a direct reaction implied that the polymer itself or reactive species associated with its surface may participate in non-enzymatic reduction of MTT, generating coloured products even in the absence of viable cells.

To investigate the nature of this interaction, FTIR spectroscopy was employed to analyse potential molecular changes in the scaffold after exposure to the different treatments. The spectra in Figure 5. 10b showed that all samples retained the characteristic absorption bands of PCL, consistent with previous studies [199, 219]. However, scaffolds treated with MTT displayed noticeable variations in peak intensity at several key positions: CH_2 stretching vibrations at 2940 and 2860 cm^{-1}, ester carbonyl stretching at 1725 cm^{-1}, CH_3 deformation bands at 1466 and 1368 cm^{-1}, and C–O–C and C–O stretching vibrations at 1294, 1171, and 1104 cm^{-1}. An additional band appeared near 730 cm^{-1}, corresponding to NH bending, which may be attributed to MTT residues or weak interactions between the polymer backbone and the reagent's aromatic amine groups. These spectral changes suggested that reactive radicals or surface groups in PCL may interact with the MTT, partially reducing or consuming MTT molecules.

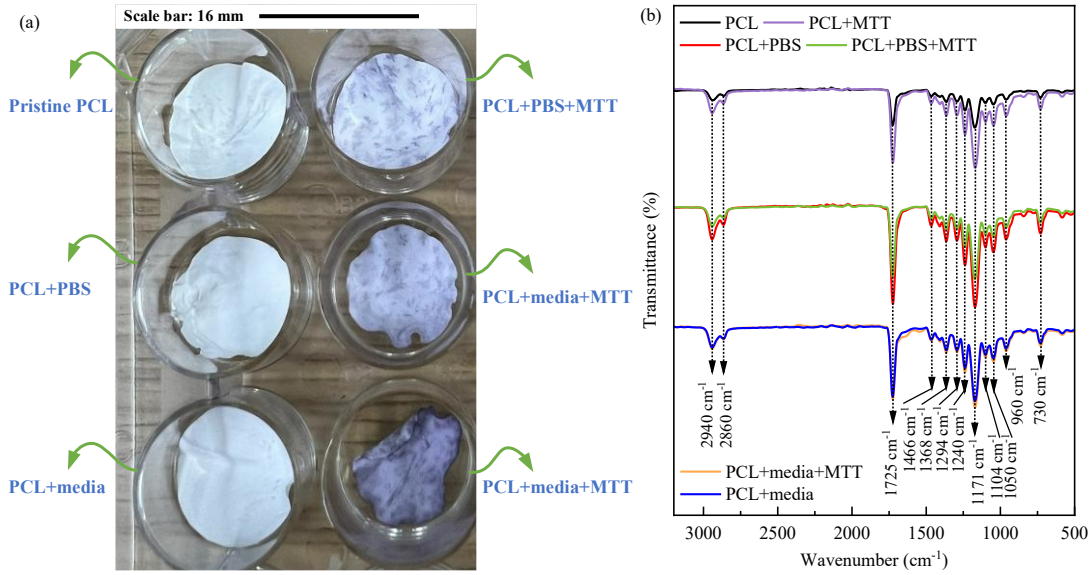

Figure 5. 10: Pristine PCL scaffold and PCL scaffolds treated by different solutions (a) and the comparison of FTIR spectra of PCL scaffolds treated by different solutions (b).

Because the MTT assay relies on enzymatic reduction of MTT to formazan by mitochondrial dehydrogenases in viable cells, any non-specific consumption of the reagent by the scaffold material would lead to underestimation of actual cell viability. Notably, when comparing 3D PCL scaffolds to 2D culture surfaces, the larger surface area and porosity of PCL mats increased the likelihood of reagent absorption. The observed colour change and FTIR evidence thus indicated that pristine PCL can chemically interfere with MTT, potentially biasing quantitative results and limiting the reliability of this method for assessing cell proliferation on PCL scaffolds.

To overcome this limitation and gain a more accurate understanding of cell–scaffold interactions, complementary imaging approaches were employed. SEM and confocal fluorescence microscopy were used to visualise cell adhesion, spreading, and morphology directly on the scaffold surface. These observations provided valuable confirmation of cell viability, independent of colourimetric interference, and helped establish a more comprehensive assessment of the biological performance of electrospun PCL scaffolds.

To assess the adhesion and proliferation behaviour of fibroblast cells on the electrospun scaffolds, SEM imaging was performed on the HMW-20%-1.5 PCL samples after 3 and 7 days of culture. As shown in Figure 5. 11, the low-magnification image (scale bar: 40 µm) revealed that, by day 3, L929 cells were already uniformly distributed across the scaffold surface, forming a continuous layer that followed the underlying fibre contours. At higher magnification (scale bar: 3 µm), the cells displayed elongated shapes with numerous filopodia and lamellipodia extending along and between adjacent fibres. These pseudopodial extensions created multiple anchoring points, suggesting active cytoskeletal engagement with the nanofibrous matrix and stable adhesion.

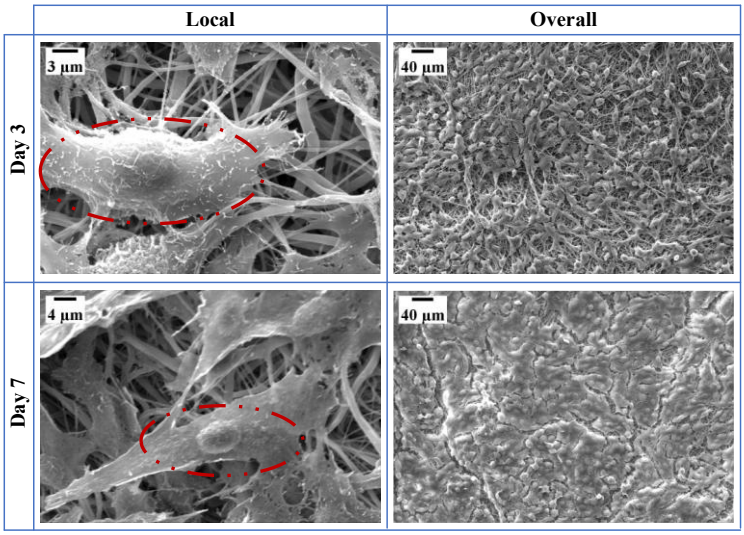

Figure 5. 11: SEM images of L929 cells cultured for 3 and 7 days on the HMW-20%-1.5 PCL scaffold.

After 7 days of culture, the extent of cellular coverage increased markedly. The scaffold surface appeared almost filled with fibroblasts, with individual cell boundaries no longer clearly visible. The cells exhibited a plump, well-spread morphology with flattened centres and radiating edges, an appearance often described as “fried-egg-like”, which is characteristic of healthy, metabolically active fibroblasts [220, 221]. This morphology, combined with the dense and continuous layer

observed, indicated that the PCL scaffold not only supported initial cell attachment but also facilitated proliferation and lateral migration over time. The close association between cells and fibres also implied that the nanoscale roughness and 3D porosity of the scaffold provided topographical cues conducive to cytoskeletal organisation and cell spreading.

To further visualise cellular distribution and morphology, confocal fluorescence microscopy was performed on the same scaffolds. L929 cells were stained with DAPI (blue) to label nuclei and with Phalloidin-iFluor 488 (green) to highlight filamentous actin (F-actin) within the cytoskeleton. The fluorescence micrographs shown in Figure 5. 12 corroborated the SEM observations. After 3 days, discrete cells with well-defined nuclei and emerging actin filaments were clearly visible across the scaffold surface, with cell nuclei stained blue and actin filaments stained green. By day 7, the fluorescence signal intensified substantially, reflecting higher cell density and the development of interconnected cytoskeletal networks spanning multiple fibres. The cells appeared to bridge neighbouring filaments, forming a continuous tissue-like layer with evenly distributed nuclei. Such extensive actin organisation indicated strong adhesion and mechanical integration with the underlying PCL matrix.

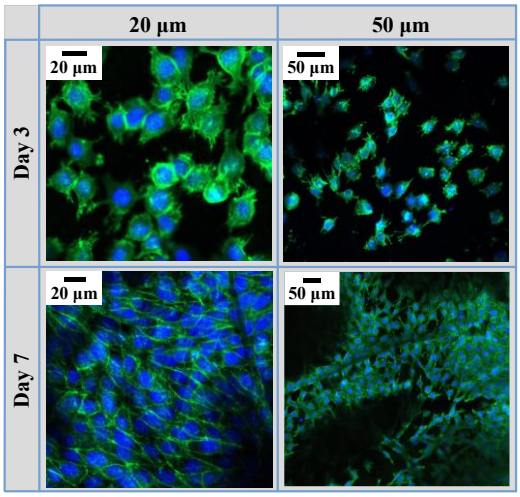

Figure 5. 12: Fluorescent microscopic images of L292 cells seeded on HMW-20%-1.5 PCL scaffolds stained with DAPI (blue, nuclei) and Phalloidin-iFluor 488 reagents (green, cytoskeleton).

The SEM and confocal microscopy results demonstrated that the electrospun HMW-20%-1.5 PCL scaffold provided a favourable microenvironment for fibroblast attachment, spreading, and proliferation. Despite its intrinsic hydrophobicity, the interconnected pores and nanoscale topography promoted sufficient cell adhesion and growth. These findings confirmed the cytocompatibility of the optimised PCL scaffold and highlighted its potential for tissue-engineering applications, providing

3D cellular support and guidance.

5.3.5. Perspective on modification of PCL scaffolds

Despite encouraging biocompatibility results, the intrinsic hydrophobicity of PCL remains a key limitation for its use in tissue engineering. Numerous studies have demonstrated that surfaces with moderate hydrophilicity promote faster wetting and liquid infiltration throughout porous scaffolds [27, 44, 47, 59, 69, 106]. Improved wettability allows culture media to spread more evenly, enabling cells to penetrate deeper into the structure and establish firm attachment at earlier stages of growth. This enhanced cell–material interaction not only supports higher proliferation rates but also accelerates tissue integration and more efficient regeneration, ultimately reducing overall healing time.

Composite scaffolds composed of PCL and a selected biomass-based hydrophilic polymer have received significant attention. These added polymers are expected to adjust the composite's hydrophilicity, favouring cell adhesion and further proliferation. Furthermore, materials derived from biomass are attractive because biomass is one of the largest sustainable energy sources worldwide and has attracted significant attention for its availability, renewability, and carbon neutrality [222, 223]. García et al. [224] fabricated composite scaffolds by electrospinning a mixture of PCL and starch, then combined with 5 wt.% CaO nanoparticles derived from eggshells. The PCL/Starch/CaO scaffolds showed improved hydrophilicity and degradation, evidenced by 3500% water absorption over 7 days and 60% mass loss. The in vivo and in vitro experiments verified the superior biomineralisation, biological performance, and biocompatibility. Rashtchian et al. [104] produced CNC (cellulose nanocrystals)-incorporated PCL-PVA/CaAlg (calcium alginate) nanofibres by biaxial electrospinning technique. They found that CNC-incorporated and CaAlg-crosslinked samples showed higher hydrophilicity. Additionally, PCL/CaAlg-CNC showed higher cell viability (> 90%) and enhanced cell coverage, making it a good candidate for biological applications. Unal et al. [225] fabricated PCL/Gel/BCNC (bacterial cellulose nanocrystal) nanofibrous composite scaffolds via electrospinning to mimic the ECM of glioblastoma (GBM) cells. PCL/Gel/BCNC showed better cell adhesion than the PCL/Gel control group. GBM cells spread on the PCL/Gel/BCNC surface and inside the scaffold, attributed to the suitable fibre diameter (259 ± 225

nm) and pore size. Tolba et al. [226] prepared the PCL electrospun nanofibrous scaffolds functionalized with CIMD (cellulose-bearing imidazolium tosylate) and SA (sodium alginate). The addition of CIMD and SA contributed to the antibacterial effect and the in vitro response of hMSCs, respectively.

To simulate the natural ECM of skin, Rad and the co-workers [227] produced PCL/Zein/GA (gum Arabic) scaffolds. PCL, GA, and Zein played roles in improving mechanical properties, enhancing hydrophilicity, and moderating the degradation behaviour of composite scaffolds, respectively. PCL/Zein/GA scaffolds exhibited high hydrophilicity, favourable porosity (around 80%), and appropriate tensile strength (1.36-3 MPa) and elongation (19.13-44.06%), which were desirable for mimicking skin. Therefore, PCL/Zein/GA illustrated good proliferation and adhesion of L929 cells. Kamalipooya et al. [230] prepared electrospun PCL/cellulose acetate (CA)-based nanofibrous scaffolds integrated with CeO_2-CSNPs (chitosan nanoparticles encapsulated with cerium oxide nanoparticles) by electrospraying. The PCL/CA/CeO_2-CSNPs electrospun scaffolds displayed significantly high antibacterial properties against S. aureus (< 58.59 μg/mL), antioxidant activity up to 89.59%, cell migration rate up to 90.3% after 2 days, and repair rate of diabetic wounds up to 95.47% after 15 days.

Table 5. 2 summarises the components, process parameters, morphology, and improvements of biomass-incorporated PCL composite scaffolds. Plenty of evidence shows that incorporating biomass-based polymers into PCL is a promising approach for fabricating nanofibre scaffolds for cell growth. For example, Rad et al. [107] fabricated composite scaffolds combining PCL with zein and gum Arabic to better mimic the ECM architecture while improving scaffolds' biocompatibility and mechanical performance compared to pure PCL scaffolds. Cellulose-based polymers are natural polymers that are the main component of biomass [212-220]. Cellulose is a linear polymer formed by the basic units of glucose connected via β-1,4 glycosidic bonds, which have excellent biocompatibility, biodegradability, mechanical properties, chemical stability, and low cytotoxicity. In recent decades, cellulose-based polymers have been widely researched for various cell types in tissue engineering applications. Furthermore, to improve cellulose solubility, a series of cellulose derivatives, such as cellulose acetate and ethyl cellulose [43, 229], are often prepared by esterifying or etherifying cellulose hydroxyl groups with other functional groups.

Table 5. 2: Biomass-incorporated PCL composite scaffolds: components, process parameters, morphology, and improvements achieved

Material	CONC[a]	Cell	Process parameter				Morphology		Improvement	Reference
			Voltage (kV)	FR (ml/h)	Distance (cm)	Inner needle diameter (mm)	Avg. fibre diameter (nm)	Avg. pore size (μm)		
PCL Starch CaO	15% w/v 15% w/v 5 wt.%	Preosteoblastic M3T3-E1	20	1.0	15	0.60	1200	—	• Enhanced hydrophilicity (3500% water absorption) and degradation (60% mass loss) over 7 days. • Superior biomineralisation and biocompatibility.	[220]
Crosslink PCL CaAlg CNC	19% w/v 3% w/v 1% w/w	Fibroblast NIH/3T3	12	0.1	16	0.51	216 ± 89	—	• Enhanced hydrophilicity. • Superior cell viability and coverage.	[104]
PCL Gel BCNC	15 wt.% 15 wt.% 0.5 wt.%	GBM U251 MG	29	0.4	13	0.84	259 ± 225	—	• Promoted cell migration due to optimal pore size. • Excellent cytocompatibility • Promising 3D platform for cell proliferation.	[225]
PCL CIMD SA	15 wt.% 15 wt.% 0.2% w/v	hMSCs SCC034	17	—	15	0.69	834 ± 378	—	• Antibacterial effect and in vitro response of hMSCs cells.	[226]
PCL Zein GA	20% w/v 15% w/v 6% w/v	Fibroblast L929	18	0.2	15	0.33	449 ± 242	4.6 ± 5.1	• Enhanced mechanical strength, hydrophilicity, and controlled degradation.	[227]

									• Supporting L929 cell growth and adhesion.	
PCL Zein GA C.officinalis	20% w/v 15% w/v 6% w/v	Fibroblast L929	18	0.2	15	0.33	405 ± 384	3.7 ± 3.6	• Enhanced hydrophilicity controlled tensile strength and flexibility. • Promoted cell proliferation and imparted antibacterial properties.	[107]
PCL CNC	16% 1%	—	17	0.9	16	—	288 ± 57	—	• Increased modulus and tensile strength by 47% and 46%, respectively. • Enhanced biodegradation versus pure PCL.	[228]
ECL PCL Gel ZEO ZnO	12.5% w/v 30% w/w 3% w/w	Penicillium notatum (PTCC5014) Aspergillus niger (PTCC5012)	16	1	15	0.51	381 ± 13	—	• Balanced mechanical, antioxidant, thermal, and antimicrobial properties with good biocompatibility.	[229]
PCL CA CeO_2-CSNPs	12 wt.% 12 wt.% 0.1 wt.%	—	20	0.5	14	—	75.34	—	• Potent antibacterial, antioxidant, and wound healing properties with rapid cell migration.	[230]

In addition, post-processing treatments, such as plasma [216] or alkaline activation [217], and biofunctional coatings [218], can also significantly alter the surface energy and biological behaviour of electrospun PCL scaffolds. Understanding how these strategies influence morphology, mechanical stability, and cell response is crucial for tailoring materials to specific clinical requirements. This insight provides a practical framework for selecting appropriate processing parameters and modification methods to enhance the biological performance of PCL-based scaffolds for future tissue-engineering applications.

5.4 Conclusions

This section systematically demonstrates that optimising electrospinning parameters, particularly the molecular weight and solution concentration of PCL, is essential for tailoring scaffold morphology and improving biocompatibility. Under optimised conditions, medium- and high-molecular-weight PCL solutions produced bead-free nanofibrous scaffolds with desirable features, including fibre diameters of 470–490 nm, pore sizes of 1.4-1.7 μm, and porosity greater than 58%. These structures significantly enhanced L929 fibroblast adhesion, proliferation, and spreading in vitro. An unexpected colourimetric response observed between PCL scaffolds and MTT reagents highlighted a key methodological issue in viability testing, which should be carefully addressed in future studies. Despite the promising morphological and biological performance, the hydrophobic nature of PCL remains a limitation for effective cell infiltration. Strategies such as surface modification or blending with hydrophilic, natural polymers may offer a practical route to improving scaffold–cell interactions.

CHAPTER 6

6 Multilayer PCL-based membranes for oily water treatment

Abstract

This section reports the fabrication of sandwich-structured PCL/PMMA@PCL/PCL electrospun membranes with PCL outer layers and a PMMA@PCL middle layer, where "@" denotes the physical blending of PMMA and PCL, designed to enhance mechanical strength and separation efficiency for oil-in-water emulsion treatment. To improve surface wettability, the membranes were treated with ethanol, introducing physically adsorbed hydroxyl groups without altering the chemical structure. A cold-pressing process was employed to increase membrane compactness, thereby enhancing mechanical performance. Morphological and structural characterisation confirmed the successful formation of the layered architecture, with reduced fibre diameter attributed to axial stretching under compressive force. Compared with single-layer PCL membranes, the multilayer structure exhibited a more balanced combination of mechanical robustness and separation performance. The Sandwich-1 membrane exhibited high oil rejection rates (~95%) and satisfactory mechanical properties in short-term filtration tests, indicating its suitability for water treatment applications. Although the flux recovery ratio remained above 90%, it was somewhat limited by basic DI water rinsing, which was insufficient to remove trapped oil droplets entirely. Long-term filtration further revealed a gradual decline in flux, attributed to membrane compaction and partial pore blockage. These findings highlighted the potential of structural and physical surface modifications for developing high-performance membranes, suggesting that future optimisation should focus on more effective antifouling and cleaning strategies to improve long-term operational stability.

6.1 Introduction

Water pollution remains a persistent global challenge, critically endangering human populations and aquatic ecosystems [231]. The level of water pollution and the corresponding health problems are increasing rapidly due to anthropogenic activities, including rapid population growth, unchecked industrialisation, and sprawling urbanisation [232]. As projected, global demand for freshwater will rise by 35% by 2050, a trend poised to strain already further-compromised water resources and amplify environmental degradation [233]. Oily wastewater is a major contributor to water contamination [234]. Various oily wastewaters are widely generated across industrial processes, including produced water from oil and gas extraction, wastewater from metal cutting and grinding operations, emulsified effluents from metallurgical rolling, and water mixed with oil during extraction, storage, and transportation. Without proper treatments, these effluents would eventually enter rivers, lakes, and oceans via surface runoff, posing significant threats to aquatic organisms such as fish, algae, and coral, and gradually disrupting the entire marine ecosystem.

Oily wastewater typically exists as either immiscible oil/water mixtures or oil/water emulsions. The immiscible oil/water system is relatively easy to separate based on its physical differences. The separation of oil/water emulsions is much more difficult because surfactants stabilise the oil and disperse it as small droplets in water. Various chemical (electrocoagulation and demulsification), physical (centrifugation, skimming, and air flotation), and biological (biodegradation) approaches have been used to address oil-contaminated wastewater [235]. However, these conventional approaches exhibit inherent limitations, including low separation efficiency, high energy consumption, operational and processing complexity, and the risk of secondary pollution [236]. Those critical shortcomings would hinder their practical implementation in real-world water remediation. Thus, developing efficient, environmentally friendly, and cost-effective separation techniques is imperative.

Membrane filtration emerges as a strategically viable solution to address these challenges, combining high separation efficiency, energy conservation, operational simplicity, and a significantly reduced risk of secondary pollution [237]. Among the various membrane fabrication approaches, the electrospun nanofibrous membrane is considered a cutting-edge membrane technology with a simple

fabrication process, a large specific surface area, high porosity, and controllable physicochemical properties (porosity, morphology, and hydrophilicity) [150, 238]. Various polymers have been electrospun into nanofibrous membranes and utilised in water treatment applications, including PCL [159], Poly(methyl methacrylate) (PMMA) [239], Poly(butylene succinate) (PBS) [240], Poly(lactic acid) (PLA) [241], and Poly(vinylidene fluoride) (PVDF) [198], etc. PCL electrospun membranes have been widely used in water treatment, due to their favourable mechanical properties (flexibility and plasticity), nontoxicity, biocompatibility, and biodegradability [234]. The electrospun PMMA fibrous membranes are fluffy and intractable, resulting in good compressive strength but low tensile strength [242]. Therefore, its applications in water treatment are limited due to fibre breaking. Polymer blending is attracting increasing attention owing to its ability to incorporate properties from multiple components and offset the disadvantages of individual polymers [243]. Simões and the coauthor [244] prepared core-sheath fibres combining PMMA and PCL using a coaxial electrospinning system. Compared to the pure PMMA fibres, the thermal stability and mechanical properties were improved in the PMMA-PCL core-sheath fibres. Son et al. [245] fabricated PCL/PMMA electrospun biopolymer composites with different ratios. They found that the average fibre diameter of PCL/PMMA increased with increasing PMMA ratio.

The principle of membrane separation is that when emulsion passes through the membrane under the action of transmembrane pressure, oil droplets that are larger than the pore sizes of the membrane are trapped on the surface of the membrane, forming a filter cake, while the water droplets that are smaller than the membrane pore sizes pass through the membrane to achieve the purpose of filtration [246]. To reject oil droplets, membranes should be hydrophilic; otherwise, severe fouling and pore blockage pose significant challenges for hydrophobic membranes, reducing flux and lifetime [247]. However, both PCL and PMMA are hydrophobic; therefore, improving the hydrophilicity is imperative for the PCL/PMMA composite membranes to mitigate fouling.

Hydrophilicity can be achieved by plasma treatment [247], blending with hydrophilic polymers [20], solvent-soaking treatment (group substitution) [249], etc. Plasma surface treatment has the disadvantages of being expensive, complex in process, and resulting in product instability [250]. Regarding blending with hydrophilic polymers, phase separation is a common issue that impairs the electrospinning process [160]. The hydrophilic components are likely to be washed off during

filtration without cross-linking. In addition, the fibre morphology may be altered due to the addition of new polymers. Compared to the techniques mentioned above, solvent treatment is an efficient, simple, and cost-effective technique to improve the hydrophilicity of membrane materials [251]. Ethanol, as a solvent rich in hydroxy groups, can be a promising candidate for treating membranes by introducing a large number of hydrophilic hydroxyl groups to membrane surfaces. Xu et al. [252] reported that hydrophilic groups, such as hydroxyl groups, could be introduced onto the surface of PVDF membranes via ethanol treatment, thereby enhancing the membrane's hydrophilicity. However, there are limited reports on the use of ethanol to improve the hydrophilicity of PCL-based membranes for water filtration applications.

Sandwich-like membranes offer distinct advantages for water treatment. Their multi-layer structure can effectively disperse mechanical stress, thereby prolonging service life [253]. The assembly of multiple layers also results in a more intricate pore distribution, which enhances the rejection of oil droplets. Additionally, incorporating functional materials, such as TiO_2 and ZnO (for photocatalysis) [176] or Ag (for antibacterial properties) [254], into specific layers enables multifunctional integration, allowing for simultaneous filtration, degradation, and sterilisation within a single system.

This section fabricated sandwich-structured PCL/PMMA@PCL/PCL electrospun membranes for oil/water separation, employing mechanical pressing (9.81 MPa) to enhance layer integration and ethanol treatment to improve hydrophilicity. A pressurised crossflow filtration system was utilised to evaluate performance, overcoming limitations of conventional dead-end setups. The influence of PMMA content on solution rheology, morphology, mechanical strength, and filtration efficiency was systematically analysed. Membranes were characterised via WCAs (pre-/post-ethanol treatment), SEM (surface/cross-section), and mechanical testing. Filtration efficacy was assessed through flux, flux decline rate (FDR), flux recovery rate (FRR), and oil rejection rates, elucidating structure-performance relationships for optimised separation and antifouling capabilities.

6.2 Preparation of the electrospun membranes

The fabrication process of the sandwich-like electrospun membranes is illustrated in Figure 6. 1c. Before electrospinning, 2.5 mL of Solution A and 5 mL of Solution B were separately loaded into syringes fitted with 26 G spinnerets (inner diameter of 0.25 mm). The electrospinning voltage was

supplied by a high-voltage source (Series ES, Gamma High Voltage, USA) connected to a low-voltage safety switch unit. The polymer jets were ejected from the spinneret tips toward a vertically mounted collector covered with aluminium foil. The KDS 100 Legacy Single Syringe Infusion Pump (KD Scientific, USA) fed the solutions to the spinneret tips at controlled flow rates.

The sandwich-like fibrous membranes shown in Figure 6. 1d were fabricated by sequential electrospinning, in which Solution A (2.5 mL) was first electrospun to form the bottom PCL layer, followed by Solution B (5 mL) to create the functional middle layer (Mid-1 or Mid-2, depending on composition). Finally, another 2.5 mL of Solution A was added to produce the top PCL layer. The resulting structure thus comprised two outer PCL layers and an intermediate central layer. For comparison, membranes electrospun solely from 10 mL of Solution A were prepared as the single-layer control group.

The electrospinning parameters were kept constant across all solutions, with a voltage of 15 kV, a flow rate of 1.5 mL/h, and a spinneret-to-collector distance of 15 cm, to ensure consistent fibre formation conditions. All membranes were collected on aluminium foil and peeled off after drying overnight at room temperature. The fabricated membranes and their corresponding compositions are summarised in Table 6. 1, which also indicates the layer configuration of each structure. Sandwich-type membranes differed from Mid-type membranes by incorporating an additional middle layer that modified overall thickness and porous characteristics.

Prior to the filtration experiments, all membranes were compressed using a cold-pressing machine (Specac AtlasTM) under a load of 10 tons at room temperature to eliminate fluffiness caused by PMMA fibres. The membranes were clamped between two square plates measuring 10 cm × 10 cm, ensuring even load distribution. The applied load of 10 tons corresponded to a pressure of approximately 9.81 MPa.

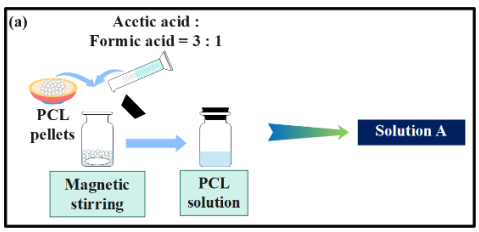

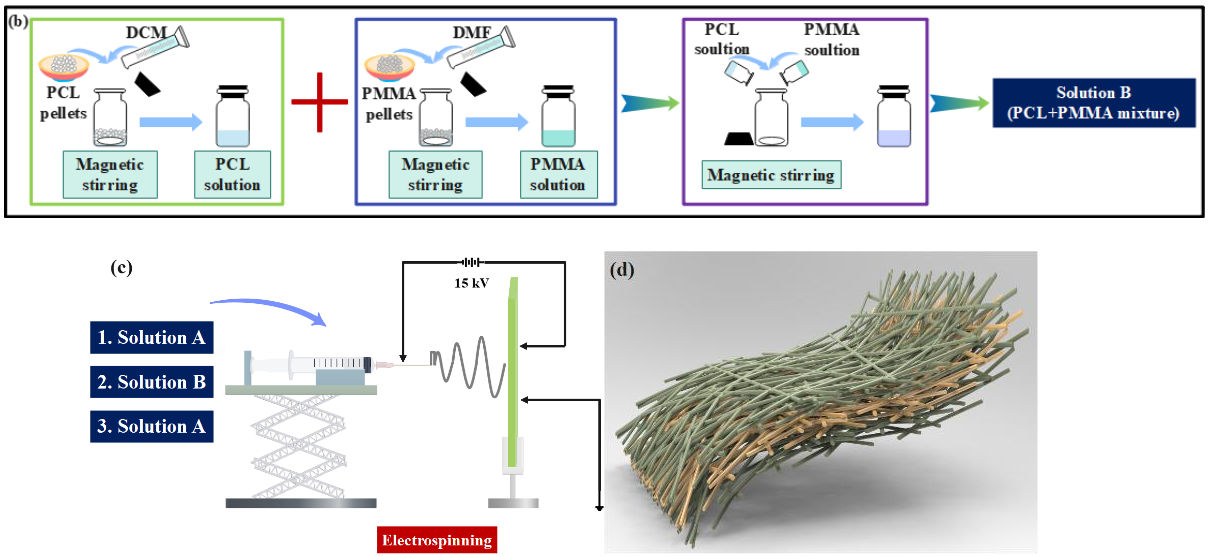

Figure 6. 1: Schematic illustration of the preparation processes for Solution A (a) and Solution B (b); the electrospinning setup for fabricating the PCL/PMMA@PCL/PCL nanofibrous membrane (c); and the structure of the sandwich-like PCL/PMMA@PCL/PCL nanofibrous membrane (d).

Table 6. 1: Summary of fabricated membranes involved in this work.

Sample	Treatment
20% PCL (Solution A)	Without ethanol treatment
30% PMMA (Solution B)	
Mid-1 (20%PCL/30%PMMA = 1:1, Solution B_1)	
Mid-2 (20%PCL/30%PMMA = 1:2, Solution B_2)	
Sandwich-1 (Sandwich-like structure composed of PCL outer layers and a Mid-1 middle layer)	
Sandwich-2 (Sandwich-like structure composed of PCL outer layers and a Mid-2 middle layer)	
20% PCL	With ethanol treatment
Sandwich-1	
Sandwich-2	

6.3 Results and discussion

6.3.1 Viscosity

The viscosity of PCL solutions with different molecular weights and concentrations was determined

using a rotational viscometer, as described in Section 4.5.1. Figure 6. 2 compares the viscosities of 20% PCL (in DCM), 30% PMMA (in DMF), and their two mixed solutions, designated as Solution B_1 and B_2. The results showed a pronounced difference in rheological behaviour among the samples. Pure PCL exhibited a viscosity of 2.198 ± 0.146 Pa·s, nearly an order of magnitude higher than that of PMMA (0.270 ± 0.055 Pa·s). In contrast, both blended solutions displayed viscosity values close to that of PMMA, 0.239 ± 0.030 Pa·s for Solution B_1 and 0.258 ± 0.040 Pa·s for Solution B_2, indicating a substantial decrease relative to pure PCL. This reduction represented an apparent *viscosity-lowering effect*, or a negative deviation from the expected average, suggesting that mixing the two polymers altered molecular interactions within the solution rather than simply combining their individual behaviours.

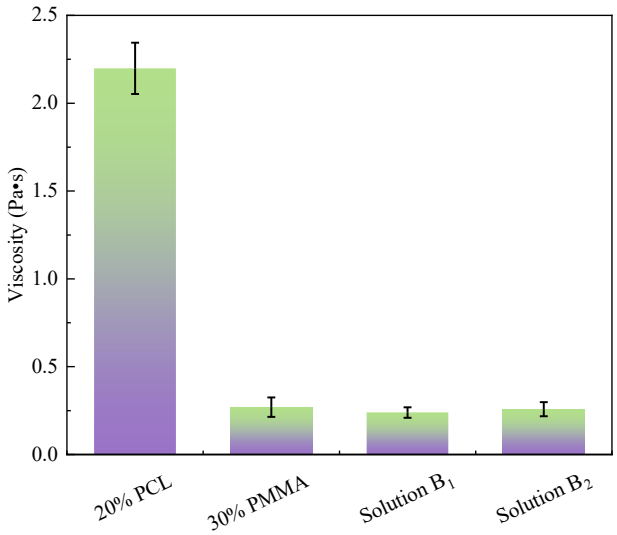

Figure 6. 2: Viscosity of 20% PCL (dissolved in DCM), 30% PMMA, and their two mixtures, Solution B_1 and B_2, respectively.

The observed decrease in viscosity can be explained by differences in polymer–solvent affinity and the resulting chain conformation. DMF is known to be a strong solvent for PMMA, promoting extensive solvation and chain expansion, whereas DCM provides relatively poor solvation for PCL, leading to compact coil structures [255]. When the two systems were mixed, the DMF fraction introduced by the PMMA solution can improve the overall solvent quality, increasing PCL chain mobility and reducing inter-chain friction. At the same time, partial miscibility between PMMA and PCL may lead to rearrangement of polymer segments, weakening the entanglement network. As a result, the overall viscosity of the mixed solutions decreased.

Another contributing factor may be the disruption of PCL's pseudo-plastic (shear-thinning) behaviour

by the presence of PMMA chains. The more rigid PMMA backbone interferes with the cooperative chain alignment typical of PCL, thereby lowering the effective viscosity [257]. Similar viscosity-reducing effects have been reported in other polymer blends, where incompatible or weakly interacting chains restrict the entanglement network, thereby promoting lower viscosity [256].

From a processing standpoint, this viscosity reduction has essential implications for electrospinning. Lower viscosity generally decreases the degree of chain entanglement within the jet, which can influence fibre uniformity, diameter distribution, and the likelihood of bead formation. These morphological effects are examined in detail in Section 6.3.4, where the relationship between solution viscosity and fibre structure is further analysed. Overall, the results presented in Figure 6. 2 demonstrated that incorporating PMMA into the PCL solution significantly altered solution dynamics, producing a more fluid mixture that may affect the resulting fibre morphology.

6.3.2 Combined FTIR-DSC analysis

The FTIR and DSC characterisations were conducted following the procedures described in Section 4.7.1. Figure 6. 3a compares the FTIR spectra of the membranes, which display characteristic absorption bands consistent with those reported in previous studies [199]. All samples exhibited the typical vibrational features of ester-based polymers, including peaks at 2940 cm^{-1} (CH_2 stretching), 1725 cm^{-1} (C=O stretching of ester groups), 1466 cm^{-1} (asymmetric deformation of CH_3), 1368 cm^{-1} (symmetric wagging of CH_3), 1240 cm^{-1} (CH_3 vibrations), 1104 cm^{-1} (asymmetric and symmetric stretching of C–O), 1050 cm^{-1} (C–O stretching and CH_2 rocking), and 960 cm^{-1} (symmetric C–O–C stretching). No new absorption bands were detected, indicating that no new covalent bonds were formed during processing. However, minor peak shifts were observed in the Mid-1 and Mid-2 systems relative to the PCL-dominant membranes (PCL, Sandwich-1, and Sandwich-2), particularly in the bands at 1466, 1171 (asymmetric and symmetric C–O stretching), 960, and 730 (CH_2 rocking) cm^{-1}. In addition, the characteristic band at 1294 cm^{-1} (asymmetric and symmetric C–O–C stretching) became significantly weakened or indistinct in the blended systems. These spectral changes, although subtle, suggest the presence of local chain interactions and partial mixing between PCL and PMMA.

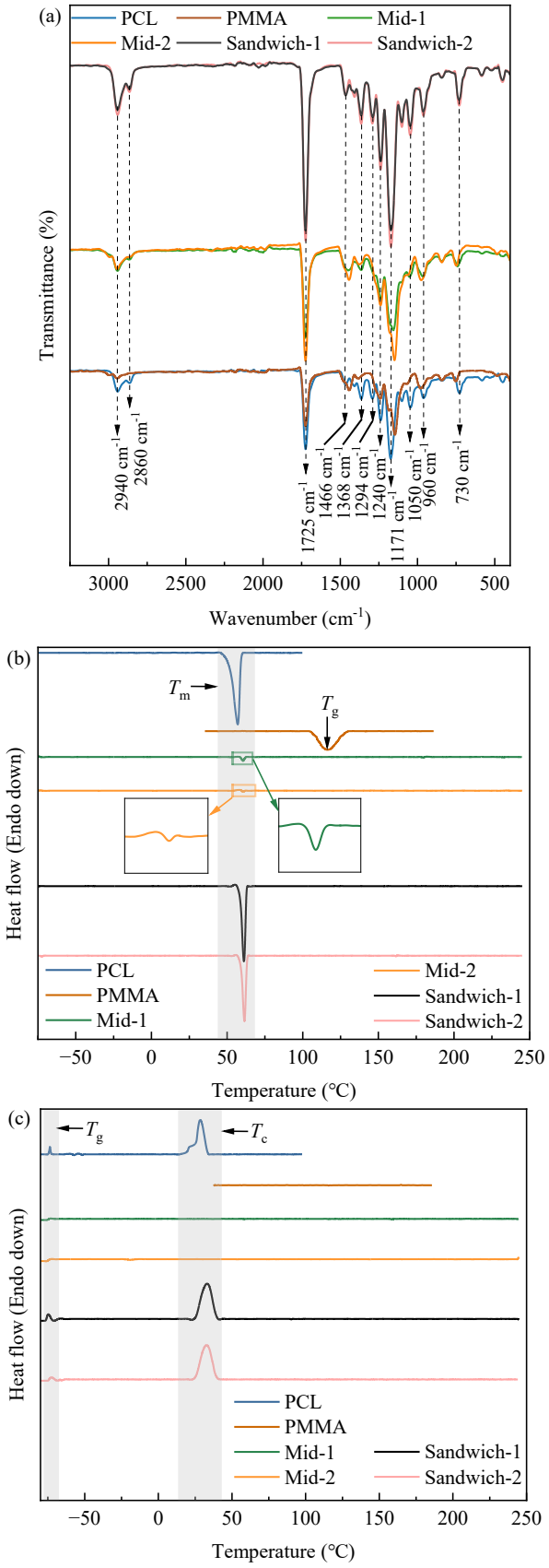

Figure 6. 3: FTIR spectra (a), DSC thermograms from the second heating run (b), and the first cooling run (c) of the fabricated membrane samples.

The thermal behaviour of the membranes, as presented in the DSC thermograms in Figure 6. 3b and

6.3c, further supported the FTIR findings. The first heating scan was used to eliminate the prior thermal history and remove residual stresses or solvent effects. The first cooling scan recorded the crystallisation behaviour of the molten sample as it cooled. In contrast, the second heating scan captured the intrinsic thermal transitions of the polymer, including the melting temperature (T_m), crystallisation temperature (T_c), and glass transition temperature (T_g) after baseline correction. This standard heat–cool–heat cycle is routinely used in polymer DSC measurements to eliminate the effects of previous thermal history and obtain reproducible intrinsic transition temperatures. As a semi-crystalline polymer, PCL exhibits distinct melting and crystallisation peaks, typically at T_m (55–65 °C) and T_c (30–40 °C), together with a low T_g (–65 to –60 °C). By contrast, PMMA, being amorphous, shows only a T_g in the range of 100–105 °C [200, 201]. These expected values in the peaks of the individual polymer samples confirm the reliability of the measurements.

However, notable differences emerged in the blended systems. In Mid-1 and Mid-2, the T_m peak intensity decreased markedly, and both T_c and T_g became less distinct in the cooling scan. These changes indicate reduced crystallinity and restricted chain mobility, consistent with local interfacial interactions between PCL and PMMA. It should be noted that thermal softening during the first heating cycle may promote limited interfacial interdiffusion; therefore, the second heating scan reflects the thermal behaviour after this potential rearrangement. In contrast, the Sandwich-1 and Sandwich-2 membranes, which contained PCL as the dominant phase, retained well-defined T_m, T_c, and T_g peaks close to those of pure PCL. This similarity indicated that the PCL layers primarily governed the thermal behaviour of the sandwich membranes, while the PMMA middle layer exerted only a limited influence on the composite's overall crystallinity.

Overall, the combined FTIR and DSC analyses support the presence of local interfacial interactions and partial mixing between PCL and PMMA.

6.3.3 Hydrophilicity

The WCA of the fabricated membranes, both before and after ethanol treatment, together with comparative data, are shown in Figure 6. 4a–c. Before ethanol treatment, all membranes displayed distinctly hydrophobic characteristics, with WCAs exceeding 100 °. Among the tested samples, the PMMA membrane exhibited the highest WCA of 127.7 ± 2.5 °, followed by the PCL membrane at

111.3 ± 3.1 °. The difference in these values reflected the intrinsic surface properties of the polymers: PMMA has lower surface polarity than PCL, which accounts for its higher hydrophobicity. In mixed and multilayer membranes in which PCL was incorporated into the PMMA matrix, the WCA decreased relative to pure PMMA, suggesting that PCL contributed to slightly higher surface polarity and improved wettability.

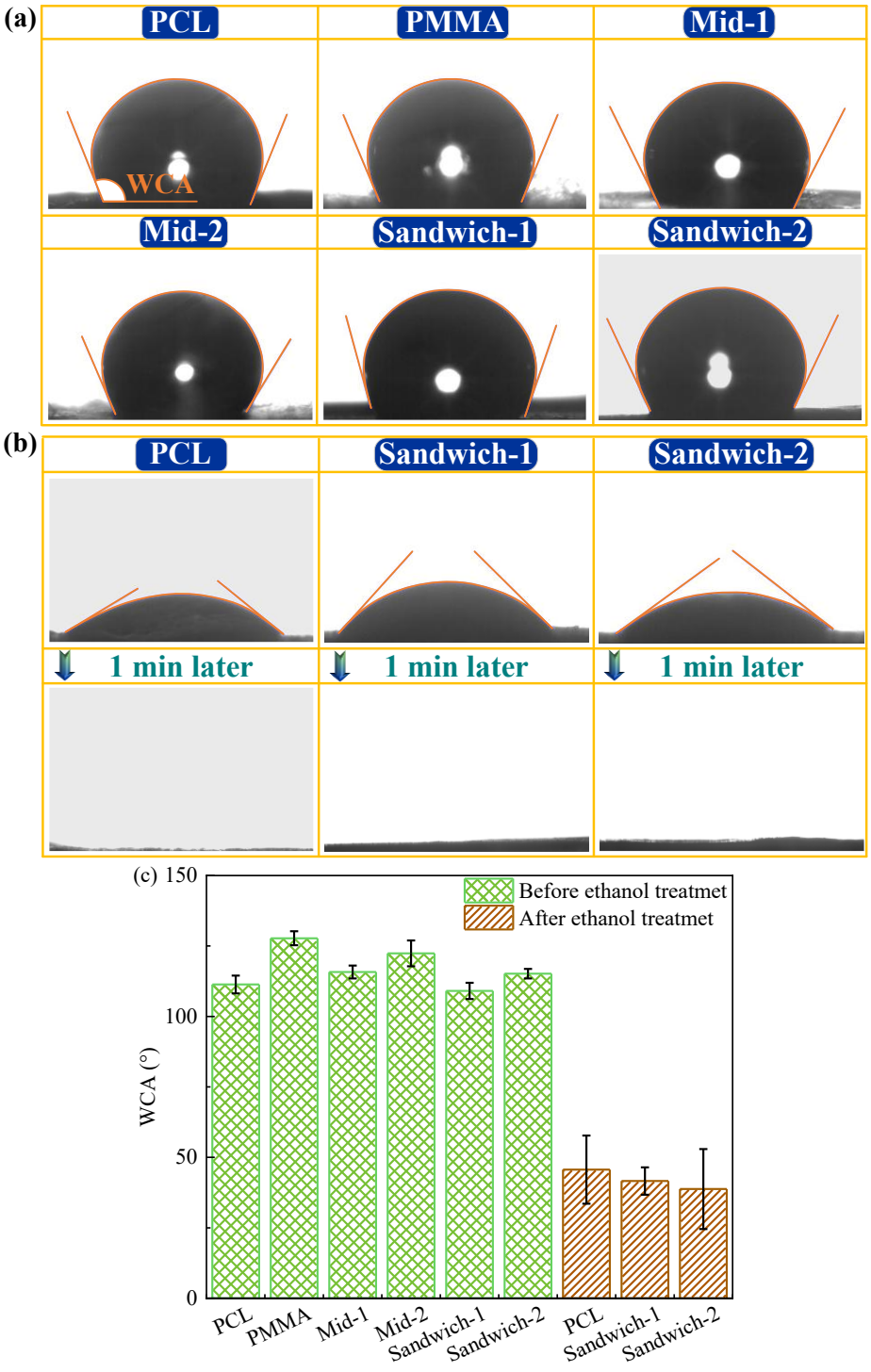

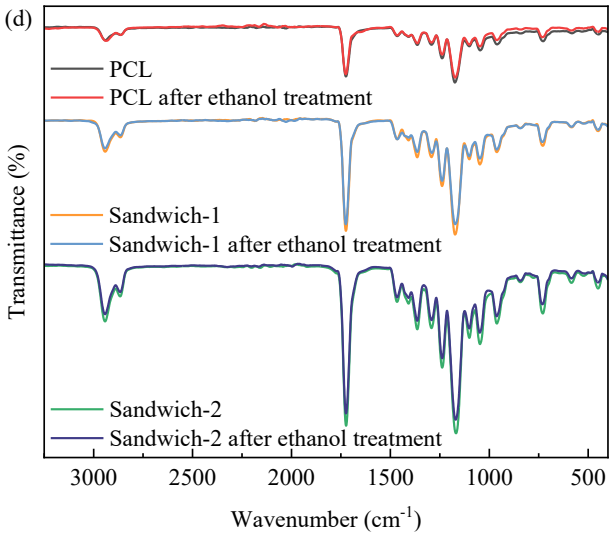

Figure 6. 4: WCA measurements of the fabricated membranes before (a) and after (b) ethanol treatment; (c) comparative WCA values; and (d) FTIR spectra of membranes before and after ethanol treatment.

After ethanol treatment, a dramatic change in surface behaviour was observed. The WCA of both the control group (PCL) and the sandwich-like membranes (PCL/PMMA@PCL/PCL) dropped below 50 °, and the deposited water droplets were fully absorbed into the membranes within one minute. This rapid water uptake demonstrated that ethanol treatment effectively transformed the membrane surface from hydrophobic to hydrophilic. Enhanced hydrophilicity played a vital role in oily water separation, as it promoted water permeation through the membrane, reduced oil adhesion to the surface, and mitigated fouling caused by oil film or cake formation. The results in Figure 6. 4 therefore, confirmed that ethanol treatment was a simple yet highly effective method for temporarily improving membrane wettability.

However, it is worth noting that the hydrophilicity enhancement caused by ethanol treatment is temporary. When the ethanol-treated membranes were dried and re-examined, their WCAs gradually returned to values comparable to those of the untreated samples. To clarify whether the treatment induced any chemical modifications, the FTIR spectra of ethanol-treated and pristine membranes were compared (Figure 6. 4d). The two spectra showed identical characteristic peaks, with no new bands or peak shifts, indicating that the ethanol treatment did not alter the chemical structure of the polymers. This finding implied that the observed improvement in hydrophilicity arose primarily from physical effects, specifically the temporary adsorption of hydroxyl groups or residual ethanol molecules onto the membrane surface.

Previous studies support this interpretation. Ethanol has been reported to transiently increase membrane hydrophilicity by forming hydrophilic groups or weakly associating with polar sites on the polymer surface [202, 252]. Once the solvent evaporates, these interactions disappear, and the surface reverts to its native hydrophobic state. Zhao et al. [258] also noted this reversible phenomenon, showing that ethanol-treated membranes regained their original WCA values after complete drying. Therefore, ethanol can be regarded as a convenient short-term modifier that provides immediate, but temporary, enhancement of surface hydrophilicity. For practical use, the membranes should be kept immersed in DI to retain their wettability or re-treated with ethanol before filtration experiments to ensure optimal water permeability and antifouling performance.

6.3.4 Morphology

SEM analysis was carried out to examine the morphology and fibre distribution of the electrospun membranes. Representative micrographs of the PMMA, Mid-1, and Mid-2 samples are presented in Figure 6. 5. The PMMA membrane showed the largest average fibre diameter of 1918 ± 638 nm, forming thick, uneven fibre diameters with a loosely entangled arrangement. When PCL was incorporated into the spinning solution, the average fibre diameter gradually decreased. The Mid-2 and Mid-1 composites exhibited mean diameters of 1883 ± 586 nm and 1427 ± 567 nm, respectively. This gradual reduction in fibre diameter is consistent with the viscosity data reported in Figure 6. 2, where the addition of PMMA led to lower solution viscosity. A decrease in viscosity typically reduced polymer chain entanglement during electrospinning, resulting in thinner fibres. The correspondence between the rheological and morphological results confirmed that solution viscosity was a key factor influencing fibre size and uniformity.

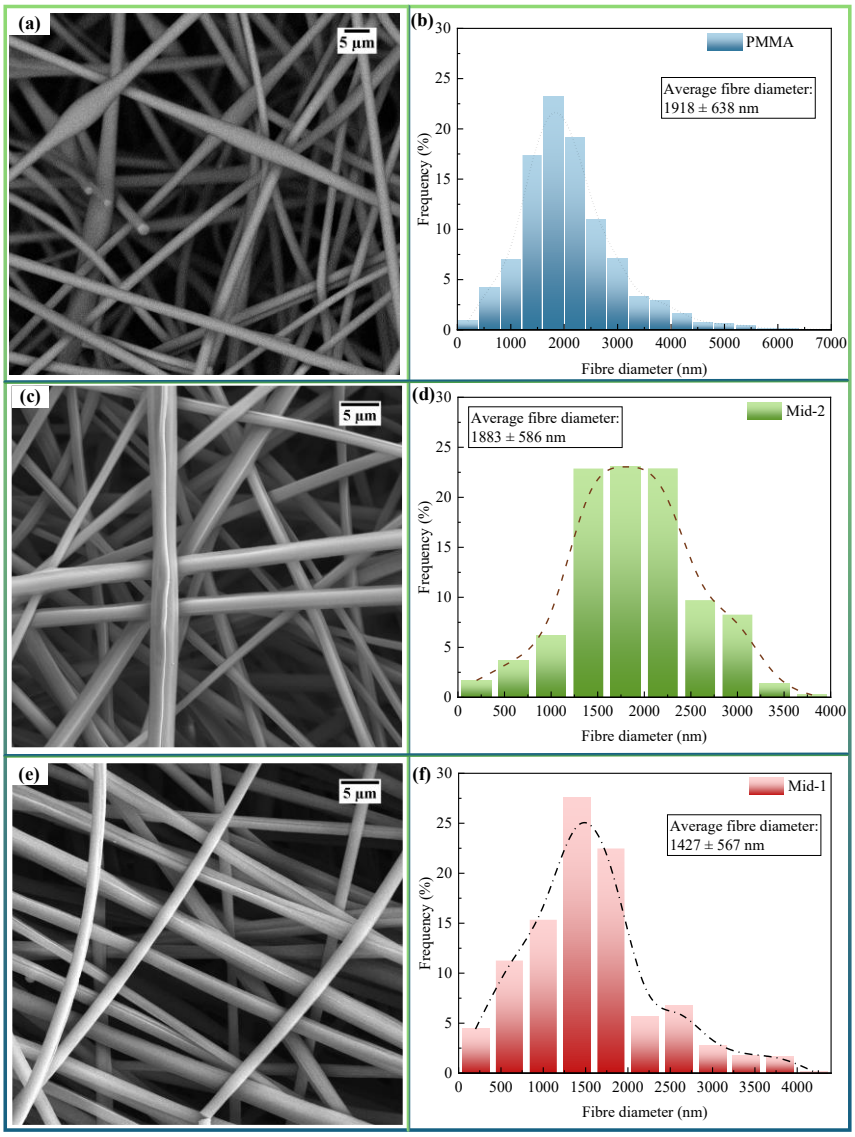

Figure 6. 5: SEM images (a, c, e) and corresponding fibre diameter distributions with average fibre diameters for PMMA (b), Mid-2 (d), and Mid-1 (f) membranes.

In addition to differences in fibre diameter, all PMMA, Mid-1, and Mid-2 membranes exhibited a fluffy, fragile surface texture. This was evident from visual inspection under ambient conditions, where even gentle handling results in observable fibre deformation or detachment, indicating poor structural integrity [242]. This fragility is likely attributed to several physicochemical and mechanical factors. First, PMMA is an inherently brittle polymer; its molecular chains fracture easily under stress and show minor plastic deformation before breaking [259]. Second, the relatively high glass transition temperature of PMMA (around 105 °C) restricts chain mobility at room temperature, limiting the ability of fibres to deform or recover when external forces are applied [260]. Third, the intrinsic rigidity of PMMA chains results in limited fibre flexibility and poor inter-fibre packing,

which gives the membrane a loose, fluffy appearance. Finally, the weak adhesion between adjacent fibres prevents efficient load transfer throughout the network, further reducing mechanical strength and making the membranes prone to surface cracking or delamination during handling [212, 261].

Because of these material limitations, the PMMA-rich membranes (PMMA, Mid-1, and Mid-2) are unsuitable for practical filtration. Their brittleness and low cohesive strength would make them unstable under the pressure and shear conditions encountered during oily water separation. Consequently, subsequent investigations focused on the structural and functional evaluation of the specifically PCL, Sandwich-1, and Sandwich-2 membranes, which possessed greater flexibility and better mechanical robustness. These membranes were further examined to assess their potential for effective oil/water separation performance.

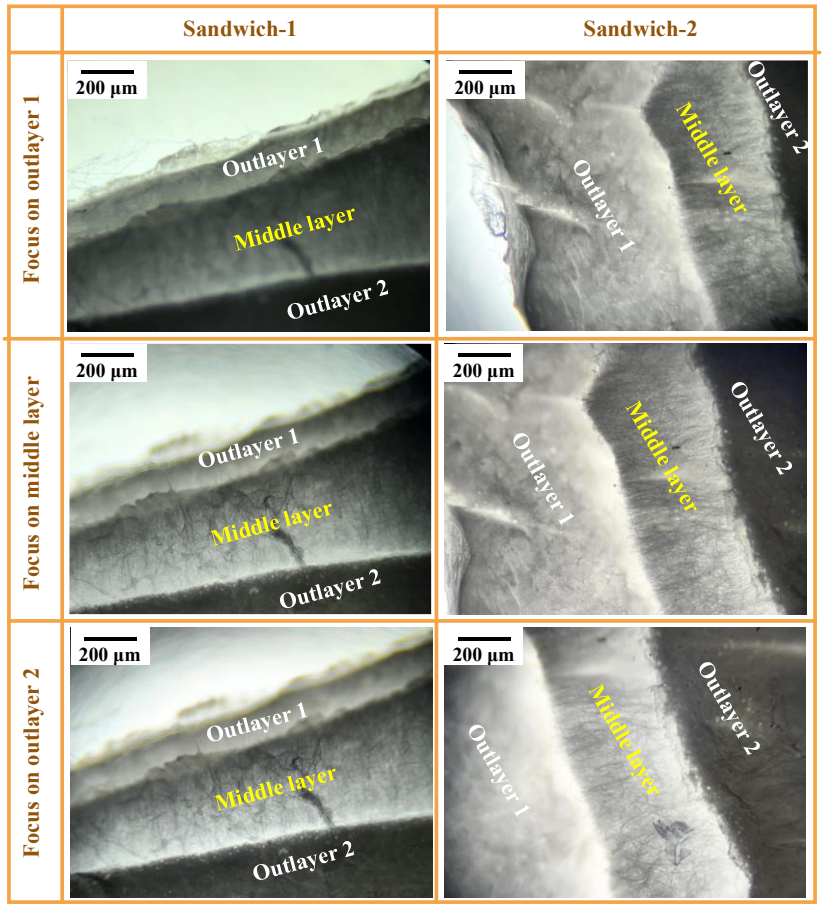

Figure 6. 6: Microscope images showing the sandwich structure of pressed sandwich-1 and sandwich-2 membranes.

Microscope images of the cold-pressed Sandwich-1 and Sandwich-2 membranes (Figure 6. 6) clearly confirmed the formation of a well-defined sandwich-like configuration, consisting of distinct outer and inner layers. The outer layers were composed of electrospun PCL, while the middle layer was

composed of the respective PCL/PMMA composite. The three layers were closely integrated after cold-pressing, with no visible delamination or interfacial gaps. The detailed cold-pressing procedure, including the applied pressure (9.81 MPa) and pressing duration, is described in Section 4.4.2.

It should be noted that the microstructural differences between the Mid-1 and Mid-2 layers have already been characterised in Figure 6. 5. Figure 6. 6 is therefore presented to verify the successful assembly of the multilayer sandwich-like configuration in both membranes after the cold-pressing process. Both Sandwich-1 and Sandwich-2 exhibited similar three-layer architectures consisting of two PCL outer layers and a central composite middle layer, with no visible delamination or interfacial gaps. This observation verified the structural integrity of multilayer architecture, which was essential for ensuring mechanical stability and consistent filtration behaviour during operation.

Figure 6. 7 presents the SEM micrographs of both pressed and unpressed membranes, together with their fibre diameter distributions and average values for the PCL, Sandwich-1, and Sandwich-2 membranes. All membranes exhibited smooth, continuous, and randomly oriented nanofibres free of beads or defects, indicating that the electrospinning process produced high-quality fibrous mats. Because the external surfaces of all three membranes consisted entirely of PCL, their surface morphologies were similar: a uniform, porous network of interconnected nanofibres. The measured average fibre diameters of the unpressed samples were 201 ± 92 nm for pure PCL, 202 ± 84 nm for Sandwich-1, and 213 ± 113 nm for Sandwich-2, showing negligible variation among them. This similarity further confirmed that the outer PCL layers dominated the composite membranes' surface features.

After cold pressing, noticeable morphological changes occurred. The fibres in all membranes became more compact and closely packed, with a visible reduction in apparent diameter. The average diameters decrease to 175 ± 40 nm (PCL), 175 ± 38 nm (Sandwich-1), and 179 ± 56 nm (Sandwich-2). The pressed samples displayed denser textures, suggesting that the applied perpendicular pressure effectively compressed the membrane structure. Visually, the cold-pressed fibres in SEM images appeared slightly flattened and thinner compared with their pristine counterparts, supporting the quantitative findings.

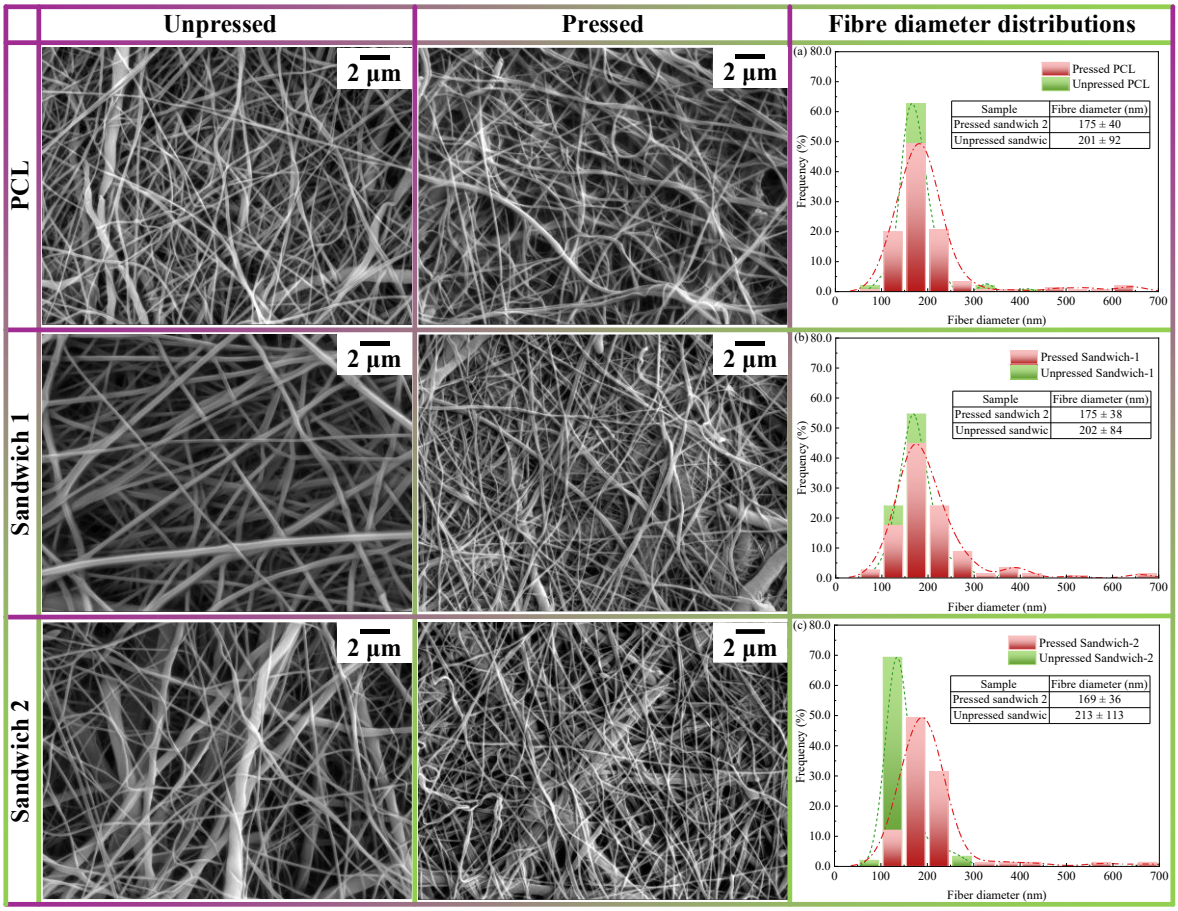

Figure 6. 7: SEM images of pressed and unpressed membranes and fibre diameter distributions with average fibre diameters for the PCL, Sandwich-1, and Sandwich-2 membranes.

This reduction in fibre diameter can be attributed to mechanical deformation induced by the cold-pressing process. The perpendicular force exerted during pressing generated both transverse compression and axial tensile stress along individual fibres. Under this stress field, the fibres were subjected to fibre flattening or axial stretching. Axial stretching generated tensile stress along the fibre length, resulting in fibre elongation and a reduction in fibre diameter. The combination of axial stretching and local fibre rearrangement resulted in a more compact fibrous network with a higher packing density. Similar stretch-induced diameter reduction behaviour has been reported previously in electrospun membranes subjected to mechanical compaction [262].

Therefore, based on morphological evidence and diameter measurements, the decrease in fibre diameter after pressing can be explained by the axial stretching effect produced under the applied perpendicular pressure. This process not only reduced fibre size but also enhanced fibre–fibre contact and network cohesion, thereby improving the overall mechanical integrity and stability of the membranes. These changes were expected to influence the subsequent mechanical performance and

separation behaviour examined in the following sections.

It should be noted that pressing the sandwich-like PCL/PMMA@PCL/PCL membranes is an essential step to ensure structural stability. In the unpressed state, the individual layers adhered only loosely, and the interfaces between the PCL and PCL/PMMA layers could easily separate, especially during handling or filtration. This separation made the multilayer structure unstable and unsuitable for practical use. The pressing process effectively eliminated this issue. Since PCL is a thermoplastic polymer with inherent flexibility and ductility at room temperature, it can undergo slight deformation under pressure without fracturing. The combination of PCL's ductility and the applied high compressive force of 9.81 MPa promoted physical bonding and inter-fibre entanglement across the interfaces, resulting in strong adhesion between layers. As a result, the pressed membranes behaved as nearly unified structures at the macroscopic scale, exhibiting improved dimensional stability and mechanical integrity.

For this reason, only the pressed PCL, Sandwich-1, and Sandwich-2 membranes were selected for subsequent characterisation and oil/water separation testing. Their porosity and pore structure were evaluated to assess how the multilayer configuration influences internal architecture. Volumetric porosity and average pore radius are calculated according to Eqs. (1) and (2), and the results are summarised in Table 6. 2. The membrane thickness followed the order PCL < Sandwich-1 < Sandwich-2. The pure PCL membrane exhibited the highest volumetric porosity (35.15 ± 12.35%) and the largest average pore radius (0.610 ± 0.293 μm), indicating a more open structure with a greater number of interconnected pores per unit volume.

In contrast, the multilayer membranes exhibited slightly reduced porosity and smaller pore sizes, which can be attributed to compaction induced by pressing and to the additional middle layer in the sandwich configuration. The thicknesses of Sandwich-1 (0.171 ± 0.038 mm) and Sandwich-2 (0.171 ± 0.025 mm) were approximately double that of the single-layer PCL membrane (0.086 ± 0.058 mm). The increased thickness and more compact structure were expected to influence both the mechanical strength and the permeability characteristics of the membranes. Specifically, while the denser configuration may enhance tensile strength and resistance to deformation under pressure, it could also result in slightly lower flux during filtration.

Table 6. 2: Properties of the fabricated membranes regarding thickness, volumetric porosity, average fibre diameter, and pore radius.

Sample	Thickness (δ, mm)	Volumetric porosity (ε, %)	Average fibre diameter (d, nm)	Average pore radius (r, μm)
PCL	0.086 ± 0.058	35.15 ± 12.35	175 ± 40	0.610 ± 0.293
Sandwich-1	0.171 ± 0.038	30.75 ± 10.06	175 ± 38	0.522 ± 0.247
Sandwich-2	0.171 ± 0.025	29.66 ± 2.04	169 ± 36	0.456 ± 0.116

6.3.5 Mechanical properties

The stress–strain curves of the electrospun membranes are presented in Figure 6. 8. The corresponding tensile strength, elongation at break, and Young's modulus are summarised in Table 6. 3. The mechanical testing procedure, including specimen geometry (dog-bone-shaped samples, 6 × 15 mm) and testing conditions (crosshead speed of 0.05 mm/s), followed the method described in Section 4.7.2.

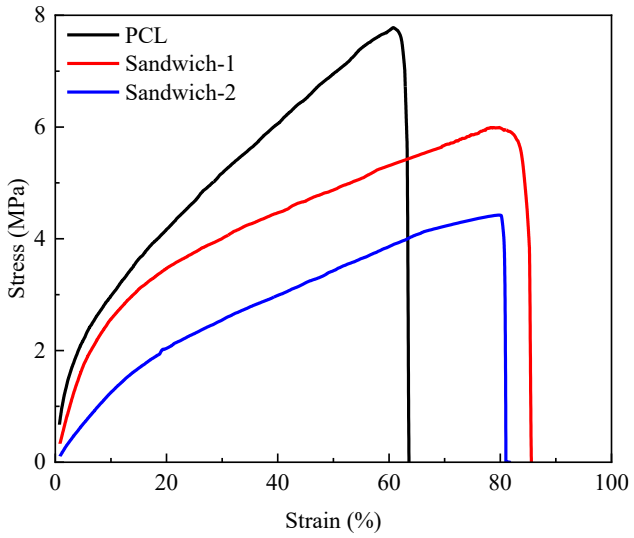

Figure 6. 8: Stress-strain curves for fabricated electrospun membranes.

The pure PCL membrane exhibited the highest tensile strength of 7.74 ± 0.02 MPa, demonstrating its superior mechanical robustness among all samples. When PMMA was introduced into the structure to form the sandwich-like membranes, the tensile strength decreased progressively, reaching 4.36 ± 0.18 MPa for the Sandwich-2 membrane. This decline indicated that the inclusion of the PMMA middle layer slightly reduced the composite's overall load-bearing capacity, most likely

because PMMA was a brittle polymer with limited chain flexibility. Its incorporation reduced inter-fibre cohesion and disrupted the continuous load network provided by the PCL matrix.

In contrast, the elongation at break showed the opposite trend, increasing from 60.75 ± 0.62% for the pure PCL membrane to 80.28 ± 0.11% for Sandwich-2. As discussed in Section 6.3.4, the slightly greater thickness of the sandwich structures may help distribute tensile stress more evenly through the membrane during deformation, reducing the likelihood of premature fracture. The multi-layer configuration could also provide a small degree of buffering at the interfaces, allowing the membrane to extend marginally more before failure. These effects together may explain the modest increase in elongation at break observed for the sandwich membranes compared with pure PCL.

The calculated Young's modulus values followed the order PCL > Sandwich-1 > Sandwich-2, consistent with the observed tensile strength trend. This progressive reduction in modulus reflected a decrease in stiffness as the PMMA content increases, again due to the intrinsic brittleness and lower inter-fibre bonding strength of PMMA compared to PCL. Overall, the mechanical properties of the PCL-based membranes developed in this section are comparable to those reported for similar electrospun PCL systems in previous literature (Table 6. 3). Although the incorporation of PMMA slightly compromised tensile strength, the resulting sandwich-like membranes still exhibited sufficient strength and elasticity to meet the mechanical requirements for practical water treatment applications. The mechanical results suggested that the membranes can maintain their fibrous structure during operation, providing a stable basis for subsequent separation testing.

6.3.6 Short-term multi-cycle oil/water emulsion separation experiment

Short-term multi-cycle oil/water emulsion separation experiments were conducted according to the procedure described in Section 4.4.2 to evaluate the filtration performance and stability of the PCL-based membranes. The variation in DI water flux over 60 minutes is shown in Figure 6. 9a. All membranes exhibited a gradual, modest decline in flux during the test. Specifically, the DI water flux decreased by 3.75%, 12.15%, and 26.64% for the pure PCL, Sandwich-1, and Sandwich-2 membranes, respectively. This behaviour is common in pressure-driven filtration and can be attributed to gradual membrane compaction and minor pore blockage under sustained load.

Table 6. 3: Comparison of the mechanical properties and separation performance of PCL-based electrospun membranes from this section with those reported for other electrospun membranes.

Samples	Filtered solutions	Facilities	Mechanical properties			Rejection rate (%)	FDR (%)	FRR (%)	Reference
			Tensile strength (MPa)	Elongation at break (%)	Young's modulus (MPa)				
PCL	n-hexadecane/water emulsion	Pressure -driven	7.74 ± 0.02	60.75 ± 0.62	9.13 ± 0.02	85.67 ± 1.49	36.43 ± 1.56	92.06 ± 0.61	This work
Sandwich-1			5.99 ± 0.01	79.00 ± 0.46	5.25 ± 0.05	95.58 ± 1.16	37.09 ± 1.84	90.09 ± 0.45	
Sandwich-2			4.36 ± 0.18	80.28 ± 0.11	4.53 ± 0.01	95.89 ± 0.87	42.16 ± 3.21	90.31 ± 1.14	
SKL-incorporated PCL	n-hexadecane/water emulsion	Gravity-driven	—	—	6.96 ± 0.17	97.5	79	98	[159]
PCL/Tween 80	hexadecane/water emulsion	Gravity-driven	6.59 ± 1.67	130 ± 21	—	99	—	—	[160]
Chitosan/PCL	Hexane/water emulsion	Gravity-driven	8.2	97 ± 11	—	99.9	—	—	[162]
PAN/PU-TA	n-hexane/water emulsion	Gravity-driven	6.42 ± 0.50	132.52 ± 14.72	—	95.44	—	—	[265]
PA6(3)T	Dodecane or motor oil	Pressure -driven	—	—	—	~50	—	~80	[266]
PAN			—	—	—	~80	—	~75	

PEF/PLA	Medium-chain triglyceride oil/water emulsion	Pressure -driven	1.53	~ 60	~ 0.11	95.45	—	98.65	[267]
MPNs coated PSf	n-hexane/water emulsion	Pressure -driven	—	—	—	97.5	—	96.4	[268]
PVAc-coated N6/SiO_2	Machine oil/water emulsion	Pressure -driven	23.3	—	—	~99	—	85	[269]
PMMA/PCL	Light mineral oil/water emulsion	—	0.95 ± 0.15	31.7 ± 7.9	20. 9 ± 2.5	—	—	—	[270]

Note: PAN/PU-TA, polyacrylonitrile/polyurethane-tannic acid; PA6(3)T, Poly(trimethyl hexamethylene terephthalamide); PAN, Polyacrylonitrile; PEF/PLA, Poly(ethylene furanoate)/poly(lactic acid); MPNs coated PSf, Metal-phenolic network coated polysulfone; PVAc-coated N6/SiO_2, Polyvinyl acetate-coated nylon 6/Silica.

During filtration, the membranes were clamped tightly between the upper and lower parts of the filtration cell to ensure leak-free operation, uniform pressure distribution, consistent mechanical support, and accurate flux measurement. This setup was necessary to maintain membrane integrity, ensure consistent filtration conditions, and prevent bypass or leakage, both of which could significantly impact experimental accuracy and distort flux measurements. However, sustained compression over time can lead to slight structural deformation or "creep compaction," which reduces the adequate pore size and thereby increases flow resistance. This structural densification explains the observed slow decline in flux over time [263]. Moreover, even though DI water contains no visible contaminants, trace amounts of dissolved organic residues or fine particulates may accumulate within the pores, contributing to membrane pore blockage and further flux reduction [264].

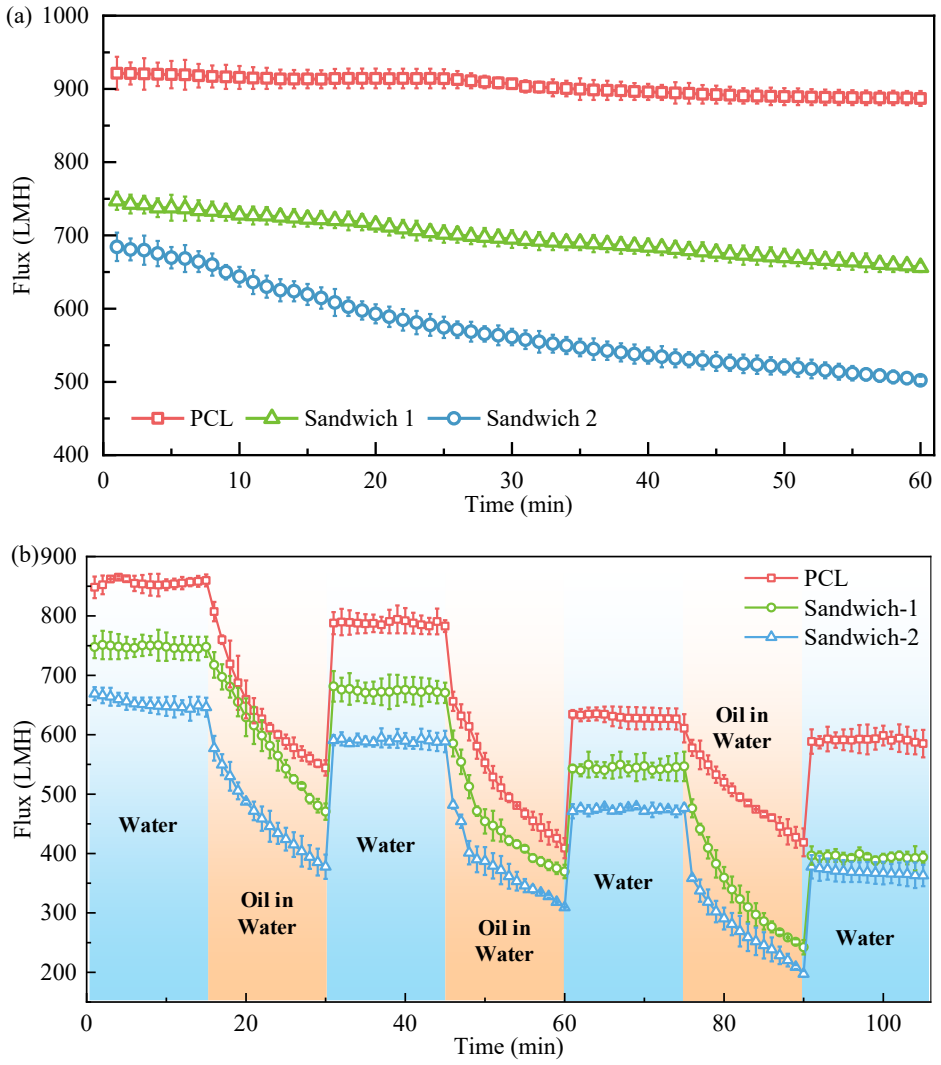

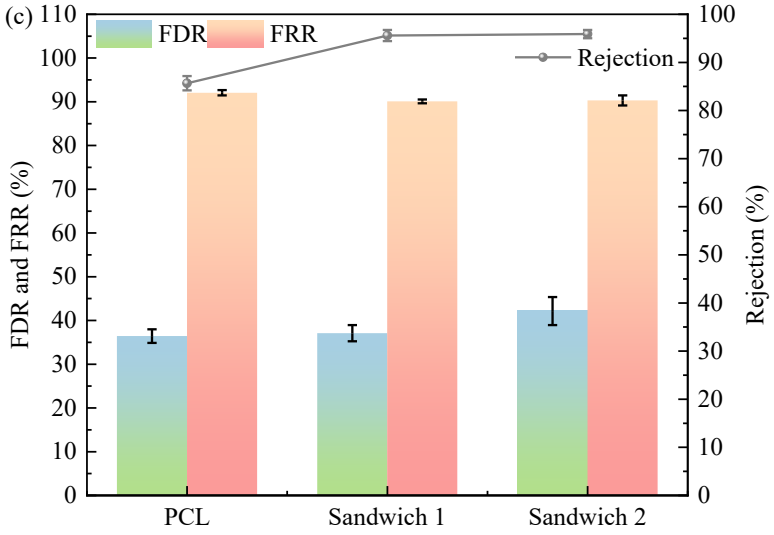

Figure 6. 9: (a) DI water flux over 60 minutes, (b) flux variation of membranes over three cycles of oil/water emulsion, (c) FDR, FRR, and oil rejection of membranes after filtration of oil/water emulsions in short-term multi-cycle filtration experiments.

Among the three membranes, Sandwich-2 showed the most significant flux decline (26.64%), consistent with its greater thickness, lower porosity, and smaller average pore size. These structural characteristics made it more prone to compaction and clogging under pressure. In contrast, the pure PCL membrane, with its thinner, more porous structure, showed only a slight 3.75% decrease in flux, maintaining relatively stable permeability throughout the test period.

The flux variations across three cycles of oil/water emulsion separation are shown in Figure 6. 9b. In each cycle, the flux dropped rapidly when switching from DI water to the oil/water emulsion due to the introduction of oil droplets and residual surfactant, which immediately increased flow resistance. Although a simple rinse with distilled water partially restored the flux, a gradual decline persisted after each cycle. This reduction can be attributed to the accumulation of tiny oil droplets trapped within membrane pores, which could not be wholly removed by simple rinsing. Over time, these trapped droplets formed partial blockages that restricted effective flow channels.

When comparing membrane performance, the PCL membrane maintained the highest relative flux, followed by Sandwich-1, while Sandwich-2 exhibited the lowest flux. The lower permeability of Sandwich-2 was consistent with its lower porosity (29.66 ± 2.04%) and smaller pore radius (0.456 ± 0.116 μm), which provided fewer, narrower pathways for water permeation. Consequently, under identical operating conditions, its flux was the lowest among the three.

The FDR, FRR, and oil rejection values calculated using Eqs. (4–6) are summarised in Figure 6. 9c.

The FDR values followed the order: PCL (36.4 ± 1.56%) < Sandwich-1 (37.1 ± 1.84%) < Sandwich-2 (42.2 ± 3.21%). The increase in FDR corresponded to a decrease in porosity and pore size, as lower porosity and smaller pore sizes made it easier for tiny oil droplets to embed in the membrane, thereby intensifying pore blockage and causing a decline in flux. Despite these variations, all membranes exhibited high FRRs of approximately 90% after simple DI water rinsing, indicating that most fouling was reversible and that the membranes exhibited good short-term antifouling performance. This suggested that all three membranes exhibited decent short-term oil antifouling properties, which can be attributed to their lipophobic and hydrophilic characteristics, consistent with the WCA results in Section 6.3.3.

The PCL, Sandwich-1, and Sandwich-2 membranes exhibited oil rejection values of 85.67 ± 1.49%, 95.58 ± 1.16%, and 95.89 ± 0.87%, respectively. The PCL membrane, with the highest porosity (35.15 ± 12.35%) and the largest pore size (0.610 ± 0.293 μm), exhibited unsatisfactory oil rejection, indicating it was ineffective at separating oil from water despite its higher flux. Conversely, the Sandwich-like membranes effectively blocked the passage of oil droplets while maintaining good water permeability, resulting in much higher separation efficiency.

Among all tested samples, Sandwich-1 achieved the best overall balance of performance. It maintained a relatively high flux, exhibited strong antifouling characteristics (high FRR), and completed oil rejection above 95% during the short-term multi-cycle filtration experiment. The pure PCL membrane, although offering the highest initial flux, performed poorly in oil rejection, whereas Sandwich-2 suffered from limited permeability due to its dense structure. Therefore, the Sandwich-1 membrane demonstrated the most favourable combination of permeability, antifouling behaviour, and separation efficiency, making it the most suitable candidate for short-term oily water treatment applications.

The separation performance and mechanical properties of the electrospun membranes developed in this section were compared with those of previously reported membranes, as summarised in Table 6. 3. The fabricated sandwich-structured membranes demonstrated oil rejection rates of approximately 95% and mechanical strength values comparable to those found in the literature, indicating that the present fabrication strategy successfully achieved both structural robustness and high separation efficiency. This section provided a relatively comprehensive evaluation of membrane performance,

encompassing both mechanical and filtration aspects. In contrast, many earlier studies have focused primarily on either mechanical durability or separation behaviour [266, 268, 270]. Such narrowly scoped investigations can lead to incomplete or unbalanced assessments of overall membrane suitability for practical use.

Although the FRR values obtained in this work exceeded 90%, they were slightly lower than those reported by Mizan et al. [159], Juraij et al. [267], and Obaid et al. [268]. The difference is mainly attributed to the cleaning procedure used after each separation cycle. In this section, only a simple rinse with DI water was applied between cycles, which may not be sufficient to remove oil droplets trapped within the membrane pores completely. Other researchers have reported higher FRR values by employing more advanced cleaning techniques, such as alkaline washing with NaOH solutions to dissolve residual grease, UV-assisted photocatalytic cleaning using TiO_2-based membranes, or mechanical back-flushing with specialised systems [180]. These approaches help to recover flux more effectively and extend membrane lifespan. However, these procedures are not implemented in the present work due to laboratory constraints and equipment availability. Future studies will incorporate these cleaning methods to further enhance the reusability and long-term stability of the fabricated membranes.

Figure 6. 10a shows the size distribution of oil droplets in the prepared oil/water emulsions, as measured by DLS. The results indicated that 74.59% of the droplets had diameters greater than the average value of 1.376 μm. Given the mean pore sizes of the membranes (0.610 ± 0.293 μm of PCL, 0.522 ± 0.247 μm of Sandwich-1, and 0.456 ± 0.116 μm for Sandwich-2), it is clear that all three membranes possess pore sizes substantially smaller than the predominant droplet sizes. This size disparity is essential for effective physical separation, as it allows the membranes to retain oil droplets at the surface while permitting water to pass through under applied pressure.

Figure 6. 10b further illustrated this phenomenon using confocal and optical microscopy images, as well as digital photographs of the emulsions before and after filtration. The initial emulsion appeared cloudy and milky, typical of a stable oil/water emulsion with fine dispersed droplets. After filtration, the permeate collected from the sandwich-like membranes became visibly clear and transparent, demonstrating efficient removal of oil droplets. The confocal images confirmed these observations: numerous oil droplets were visible in the feed emulsion, whereas none were detected in the permeate

after filtration through Sandwich-1 and Sandwich-2 membranes. In contrast, a small number of oil droplets remained in the permeate after filtration through the PCL membrane, consistent with the oil rejection results. This correlation between microscopic observations and quantitative separation data reinforced the conclusion that the single-layer PCL membrane was less effective for oil/water separation, whereas multilayer sandwich configurations performed better.

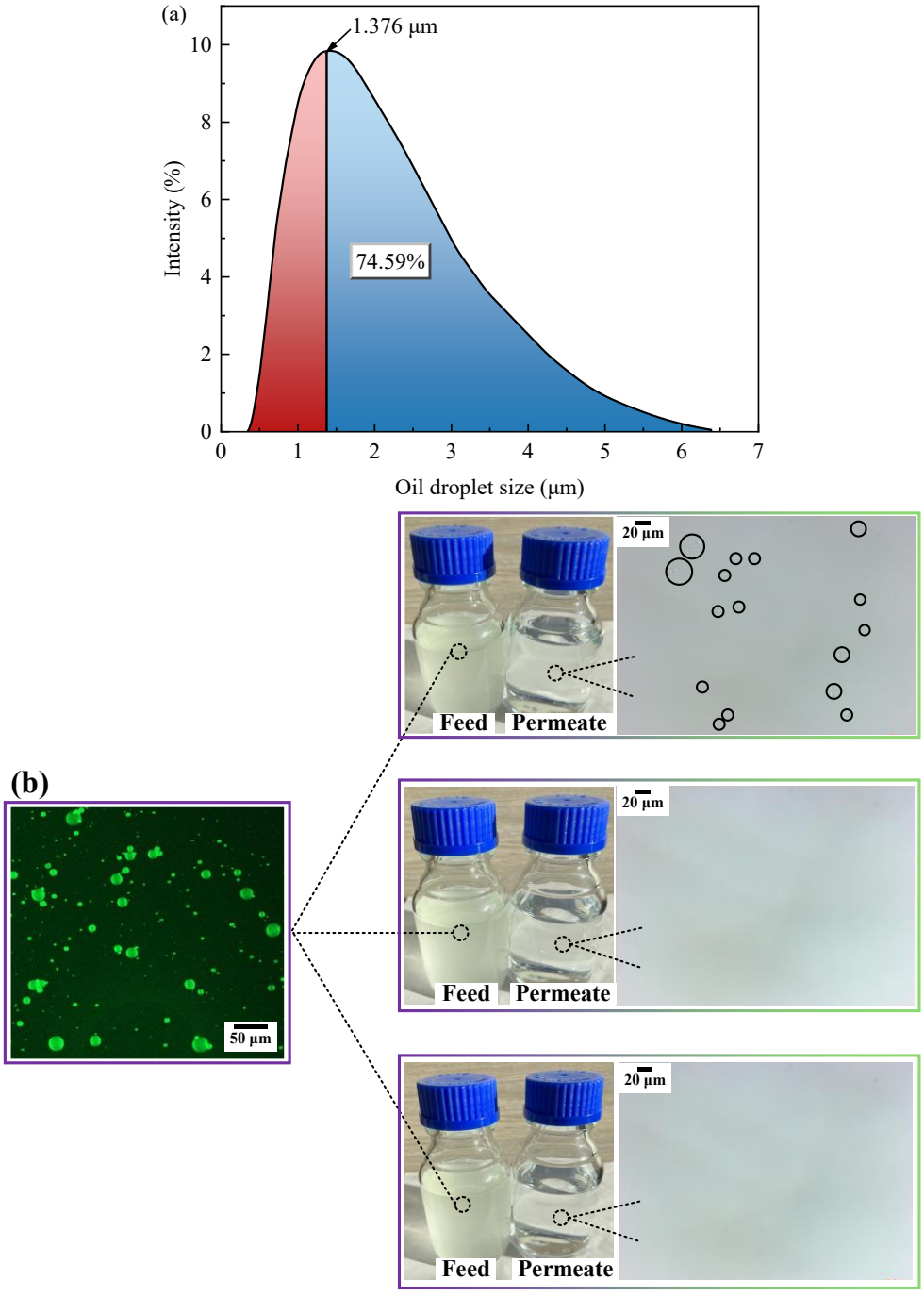

Figure 6. 10: (a) Size distribution of oil droplets in oil/water emulsions, and (b) confocal and optical microscope images, along with digital photos of the oil/water emulsions before and after filtration through the fabricated membranes.

These findings confirmed that the sandwich-like electrospun membranes achieved a favourable balance between mechanical integrity, separation efficiency, and short-term reusability. Their well-controlled pore structure and layered design enabled efficient rejection of oil droplets while maintaining stable flux in the short term, highlighting their potential for practical oily wastewater treatment.

6.3.7 Long-Term Oil/Water Emulsion Filtration Experiment

Long-term oil/water emulsion separation experiments were conducted to evaluate the filtration stability and fouling resistance of the electrospun membranes during extended operation, following the procedure detailed in Section 4.7.5. The variation of flux with time is presented in Figure 6. 11a. A sharp decline in flux was observed during the first 10 minutes after switching from DI water to the oil/water emulsion, which was consistent with the behaviour observed in the short-term multi-cycle tests (see Figure 6. 9b). This initial drop corresponded to the rapid accumulation of oil droplets on the membrane surface, leading to the formation of a thin fouling layer. As filtration proceeded, the flux gradually decreased over the next 50 minutes due to the progressive blockage of surface pores and internal channels by retained oil droplets and emulsified residues.

After 60 minutes of continuous filtration, the recorded fluxes were 94.5 LMH for the PCL membrane, 71.1 LMH for Sandwich-1, and 66.7 LMH for Sandwich-2. The overall flux hierarchy remained consistent with that observed in short-term experiments, PCL > Sandwich-1 > Sandwich-2, reflecting the influence of membrane thickness, porosity, and pore size on permeability. The pure PCL membrane, with its thinner structure and larger pores, maintained the highest flux, whereas the thicker, denser sandwich membranes exhibited lower permeation rates.

Figure 6. 11b summarises the FDR and FRR values for all membranes. The FDR stabilised at around 90% for the duration of the test, suggesting that the degree of fouling remained under constant long-term pressure operation. In contrast, the FRR gradually decreased to approximately 73%, indicating partial irreversibility of fouling over time. The combination of high FDR and reduced FRR suggested that long-term exposure to the emulsion resulted in more persistent pore blockage and compaction than short-term operation. These results implied that, while the membranes maintained structural integrity, the simple DI water rinsing was limited. As noted earlier, employing more advanced

cleaning protocols could improve flux recovery and extend the operational lifetime of the membranes [180].

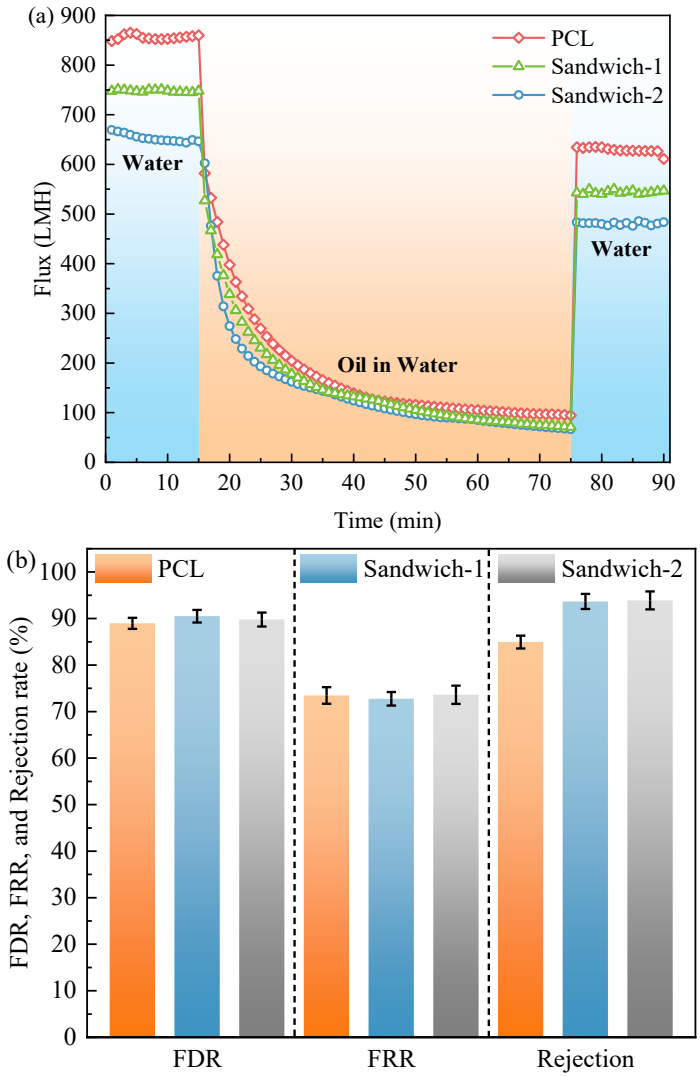

Figure 6. 11: Flux (a) and FDR, FRR, and oil rejection rate (b) during long-term oil/water emulsion separation experiments using the fabricated membranes.

In terms of separation efficiency, the oil rejection rates followed the order PCL (84.95 ± 1.38%) < Sandwich-1 (93.67 ± 1.62%) < Sandwich-2 (93.88 ± 1.93%), consistent with the short-term results. The relatively low rejection of the PCL membrane could be explained by its larger pore size (0.610 ± 0.293 μm), which allowed fine oil droplets to pass through. Both Sandwich-1 and Sandwich-2 exhibited significantly higher rejection efficiencies (>93%), confirming that the introduction of the PMMA middle layer and the resulting denser pore structure effectively enhanced oil retention.

In terms of overall performance, Sandwich-1 continued to exhibit the most balanced characteristics among the tested membranes. It combined high oil rejection with moderate flux and stable antifouling

behaviour, outperforming the pure PCL membrane, which suffered from lower rejection, and the Sandwich-2 membrane, which was limited by lower flux. The consistent short-term and long-term results demonstrated that the Sandwich-1 configuration provided a more balanced and favourable performance, making it a strong candidate for practical oily wastewater treatment.

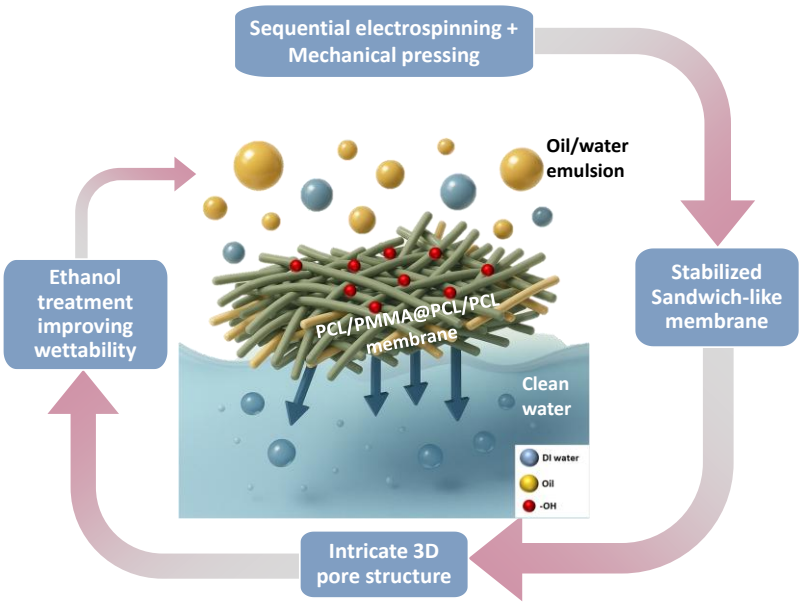

Figure 6. 12: Schematic diagram of the sequential electrospinning and post-treatment processes enhancing the oil/water separation performance of sandwich-like membranes.

Figure 6. 12 illustrates the overall mechanism by which the sequential electrospinning and post-treatment processes enhance the oil/water separation performance of the sandwich-like membranes. Sequential electrospinning followed by mechanical pressing formed a stabilised PCL/PMMA@PCL/PCL sandwich structure with an intricate 3D pore network, providing both mechanical robustness and interconnected pathways for selective separation. Subsequent ethanol treatment further improved the membrane's surface wettability by introducing temporary –OH groups, thereby promoting hydrophilicity, facilitating water permeation, and repelling oil droplets. These combined structural and interfacial modifications allowed clean water to pass through while retaining oil, thereby achieving stable and high-performance separation behaviour.

6.4 Conclusion

In this section, sandwich-like electrospun membranes composed of PCL and PMMA were successfully fabricated and systematically evaluated for oil/water emulsion separation. The

combination of ethanol surface treatment and cold-pressing enhanced membrane hydrophilicity and mechanical integrity. The hydrophilicity induced by ethanol was due to physical adsorption of hydroxyl groups, as confirmed by FTIR-DSC, with a temporary effect that diminished after drying. The cold-pressing process resulted in denser membrane structures and reduced fibre diameters, both of which were attributed to axial stretching during pressing. The fabricated membranes exhibited high oil rejection rates (~95%) and satisfactory mechanical properties, indicating their suitability for water treatment applications. Long-term filtration tests revealed that flux decline was associated with membrane compaction and partial pore blockage. Although the FRR remained above 90%, it was limited by the simple DI water rinsing protocol, which was insufficient to entirely remove trapped oil droplets. This section provides a thorough characterisation of sandwich-structured electrospun membranes, highlighting their advantages and identifying current limitations. Future research may focus on integrating more advanced cleaning strategies to enhance long-term antifouling performance and ensure membrane reusability in practical applications. In addition, incorporating functional additives with photocatalytic or antibacterial properties may further expand the membranes' application potential.

CHAPTER 7

7 Integrated image processing-ANN for Electrospun Fibre Prediction

Abstract

Electrospun nanofibrous membranes are widely used in biomedical, filtration, and energy-related applications, where fibre diameter plays a key role in determining membrane morphology and performance. However, conventional manual measurement of fibre diameters from SEM images is inefficient and subject to human error. In this section, two image-processing tools, DiameterJ and SIMPoly, were compared for fibre-diameter analysis to improve efficiency, accuracy, and consistency. DiameterJ was selected for its higher measurement accuracy and support for batch processing. Using DiameterJ, 144 datasets were collected and used to train an ANN model with four electrospinning parameters (molecular weight, solution concentration, flow rate, and tip-to-collector distance) as inputs. The ANN model showed high predictive accuracy, with correlation coefficients exceeding 0.97 and prediction errors below 4%. A RSM model was also developed for comparison; however, it showed limited predictive accuracy in unseen conditions, with prediction errors reaching up to 28.57%. The ANN model exhibited superior reliability and generalisability. IRI and contour plots indicated that molecular weight and concentration had the most significant effects on fibre diameter. Overall, combining image processing with machine learning offers a promising strategy for the design and optimisation of PCL electrospun fibrous materials and holds potential for broader applications in related fields.

7.1 Introduction

In recent decades, electrospun nanofibrous materials have attracted extensive attention due to their unique advantages, including versatile fabrication methods, broad material selection, high porosity, large specific surface area, and excellent mechanical properties. Consequently, these materials exhibit promising applications in various fields, including tissue engineering [271], filtration [272], flexible sensors [273], electrode materials [274], and packaging materials [275]. In these applications, the morphology of nanofibres, particularly fibre diameter, significantly influences membrane porosity and mechanical properties, thereby affecting the overall performance of nanofibrous membranes [32]. Fibre diameter is primarily determined by solution characteristics (e.g., molecular weight and concentration) and processing parameters (e.g., flow rate and tip-to-collector distance) [276]. Therefore, developing precise and efficient analytical tools to characterise fibre morphology is crucial for elucidating structure-performance relationships and optimising fabrication parameters. Given that electrospun fibres typically range in diameter from the nanoscale to the microscale, SEM remains the most widely used and effective technique for detailed morphological analysis.

Traditional fibre diameter measurement commonly relies on manual analysis of SEM images using the line tool in ImageJ/Fiji, followed by basic statistical processing [33]. However, manual methods are prone to subjective bias due to limited human sampling, and they exhibit low throughput and time inefficiency [34]. Automated computational tools that quantitatively analyse SEM images offer enhanced objectivity and efficiency [277]. For instance, Hotaling et al. [35] developed "DiameterJ", an open-access ImageJ/Fiji plugin that automates fibre diameter analysis, achieving approximately 10-fold speed improvement and generating at least 100-fold more data points (3,000-12,000 measurements within 10 seconds) compared to manual measurement (25 measurements in 100 seconds), without compromising accuracy. DiameterJ can also provide additional data, such as fibre orientation, diameter distribution histograms, porosity, and pore area. Similarly, Murphy et al. [36] presented Semiautomated Image Measurements of Polymers (SIMPoly), an open-access MATLAB programme for fibre diameter measurement from SEM images. SIMPoly demonstrated accurate, rapid measurement capabilities validated through synthetic images and electrospun PLGA fibre samples. Götz et al. [37] introduced the General Image Fibre Tool (GIFT), which employs a strategy involving Sobel edge extraction, image binarisation, multi-angle rotation, linear morphological

opening operations, and edge spacing measurement. Although GIFT offers superior accuracy in fibre-diameter measurements, its complexity and heavy reliance on parameter optimisation pose a higher barrier to entry-level users.

The morphology of electrospun fibres is governed by the interplay of multiple processing parameters, making it difficult to establish direct correlations that accurately predict fibre diameters [38]. Traditional experimental approaches often require extensive trials to disentangle these complex relationships, resulting in considerable time and cost [39]. To address this challenge, researchers aim to optimise the fabrication process and enable the targeted production of fibres with desired properties for various industrial applications. ANNs, a class of machine learning models, offer a promising solution by establishing a fitted, nonlinear structural model (black-box model) between multiple input features and continuous output variables [40]. An ANN typically comprises an input layer, one or more hidden layers, and an output layer [278]. Each neuron in the network receives input signals, applies a set of weights and biases, and transmits the processed signals to subsequent layers. These weights and biases are iteratively updated during training to minimise prediction error [279]. Activation functions are used in the hidden and output layers to introduce nonlinearity and improve model performance. For model development, the dataset is typically partitioned into training, validation, and testing subsets [280]. The training set is used to learn the input-output mapping; the validation set aids hyperparameter tuning (e.g., learning rate, regularisation); and the testing set evaluates the model's generalisation ability on unseen data [281].

ANN models have been widely applied to predict fibre diameters and optimise electrospinning parameters. Samadian et al. [282] employed an ANN to investigate the effects of solution concentration, tip-to-collector distance, and applied voltage on the diameters of electrospun PAN fibres. Their model achieved a high coefficient of determination (R^2 = 0.994) with strong predictive accuracy, revealing that fibre diameter increased with concentration and voltage but decreased with distance. Premasudha et al. [283] trained an ANN to predict the diameters of electrospun Hylon VII starch nanofibres based on the concentration, feed rate, voltage, and spinning distance. The model achieved average errors of only 0.05% on the training dataset and 2.6% on the test dataset. Ma et al. [284] also developed an ANN model to guide the production of PAN nanofibres, identifying solution concentration and voltage as dominant factors influencing fibre diameter. Their model reached an R^2

of 0.990, further confirming the reliability of ANN predictions. Compared with conventional trial-and-error methods, ANN models can process large datasets and capture complex nonlinear relationships between processing variables and fibre morphologies. This significantly reduces experimental workload, time, and material waste [41]. Their adaptive learning capability also makes them suitable for dynamic systems such as electrospinning [279]. Previous studies have developed ANN models for predicting electrospun fibre diameters in various systems with extensive manually measured datasets. However, these studies generally relied on data collected by humans, which may limit consistency and scalability. In contrast, this section integrates validated automated image-processing tools (DiameterJ and SIMPoly) with ANN modelling to enable objective, high-throughput data generation and morphological prediction.

RSM is also a widely used approach for modelling and predicting response variables while minimising the number of required experiments. Unlike ANNs, RSM establishes explicit mathematical relationships, typically in the form of quadratic polynomial regression models, between input variables and the response, thereby offering clear quantitative interpretability. Khatti et al. [279] developed an RSM model to investigate the effects of four factors, including polymer concentration, applied voltage, tip-to-collector distance, and the PCL-to-Gel ratio, on the diameters of composite PCL/Gel electrospun fibres. The model accurately predicted fibre diameters and identified concentration as the most influential parameter. In a subsequent study, Khatti et al. [286] applied RSM to predict the diameters of electrospun PCL fibres, demonstrating the model's effectiveness in guiding the fabrication of fibres with desired diameters.

Based on these insights, this section aimed to develop both ANN and RSM models to predict fibre diameters under various electrospinning conditions. PCL electrospun membranes were used as the model system to investigate how key electrospinning parameters influence fibre diameters, with the ultimate goal of enabling intelligent optimisation and predictive control. To enhance the accuracy, efficiency, and objectivity of data analysis, automated image-processing tools (DiameterJ and SIMPoly) were employed to extract large datasets of fibre diameters from SEM images. Unlike previous ANN-based studies that relied mainly on manual measurements, this approach integrated validated image analysis into the modelling framework, enabling more consistent and high-throughput data generation. A large dataset of fibre diameter measurements was used to train both

ANN and RSM models. Their predictive performance was evaluated by comparing prediction errors, and the more accurate model was identified accordingly. Furthermore, the index of relative importance (IRI) and contour map analyses were performed to reveal the influence of different electrospinning parameters on PCL fibre diameters. This integration of image processing analysis with ANN modelling offers a robust, intelligent framework for characterising and optimising the morphology of electrospun membranes. It provides a data-driven foundation for process design and quality control in practical applications.

7.2 Electrospinning Experimental Dataset

Pure PCL electrospun membranes were selected as the model system. A schematic illustration of the electrospinning setup was presented in Figure 5. 1. Four key processing parameters were systematically investigated: molecular weight (38600–96700 g/mol), solution concentration (15–40% w/v), flow rate (0.7–2.3 mL/h), and tip-to-collector distance (11–19 cm). These parameters were selected because they were widely recognised as the dominant factors governing fibre formation and morphology in electrospinning. Molecular weight and concentration directly determine the viscosity and entanglement density of the polymer solution, while flow rate and tip-to-collector distance affect the jet stretching, solvent evaporation, and deposition behaviour. These four parameters together represent the most influential and controllable variables determining the resulting fibre diameter and membrane uniformity.

The PCL nanofibrous membranes used in this chapter were fabricated following the electrospinning procedure described in Section 4.2. Briefly, PCL of different molecular weights was dissolved in an acetic acid–formic acid solvent mixture (3:1 v/v) at various concentrations, and the resulting solutions were electrospun under ambient conditions using a constant voltage of 15 kV, a controlled flow rate, and a fixed tip-to-collector distance. All membranes were collected on a vertical copper collector and dried under ambient conditions. In total, 144 membrane samples were designed and fabricated by systematically varying the selected electrospinning parameters. This ensures that the ANN was trained on a diverse parameter space that can represent different electrospinning regimes. The resulting membranes were characterised using SEM to examine their morphological features.

7.3 Construction of ANN models

ANN modelling was conducted using the ANN Toolbox in MATLAB. The MLP network, BP algorithm, and Levenberg–Marquardt optimisation method were selected to construct the ANN model for predicting fibre diameters. Based on the 144 datasets collected, a single hidden layer with 10 neurons was applied following Kolmogorov's theorem, which indicated that a single hidden layer could theoretically approximate [288]. Several researchers have employed single-layer hidden architectures and verified the predictive performance of their established ANN models [282, 284, 287, 289]. The fibre diameter of PCL was designated as the output variable. At the same time, four electrospinning parameters (polymer molecular weight, solution concentration, feed flow rate, and tip-to-collector distance) were selected as input variables. A schematic representation of the proposed ANN model is presented in Figure 7. 1. The activation functions used were the hyperbolic tangent sigmoid function for the hidden layer and a linear function for the output layer, as shown in Eqs. (7) and (8).

$$tanh(x) = \frac{e^{x} - e^{-x}}{e^{x} + e^{-x}} \tag{7}$$

$$g(x) = x \tag{8}$$

where x denotes the input to each layer, and $tanh(x)$ and $g(x)$ represent the activation functions used in the hidden layer and output layer, respectively.

This configuration of activation functions corresponds to the default setting in MATLAB's Neural Network Toolbox for regression-type ANN models. It has been widely validated in electrospinning and materials modelling studies [290, 291]. According to the MathWorks documentation, "Feed-forward neural networks often have one or more hidden layers of sigmoid neurons followed by an output layer of linear neurons. The linear output layer is most often used for function fitting (or nonlinear regression) problems." [292].

The tangent sigmoid function was particularly suitable because the four electrospinning input variables were normalised prior to training, and their relationship with the fibre diameter was strongly nonlinear. The symmetric output range of the *tanh* function (–1 to 1) helps the network capture these

nonlinear dependencies efficiently and ensures smooth gradient propagation during learning. The linear activation in the output layer allows the model to predict unbounded continuous outputs that directly correspond to experimentally measured fibre diameters, which is appropriate for regression problems involving physical quantities.

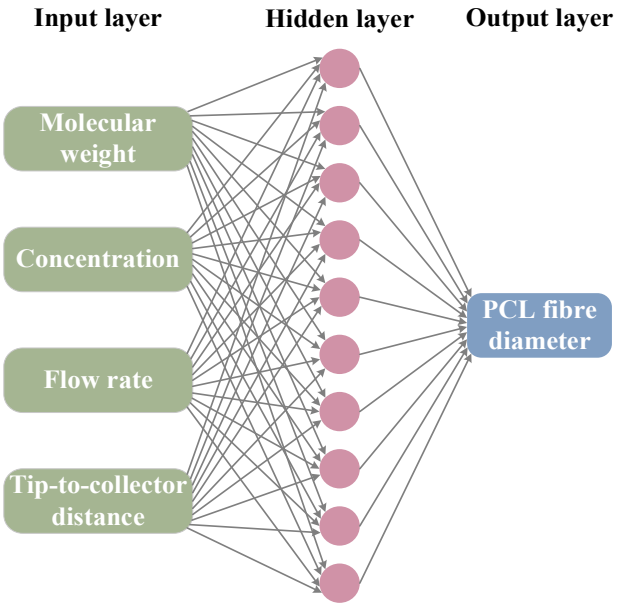

Figure 7. 1: Constructed schematic diagram of the ANN model.

The use of a nonlinear model is essential because fibre formation in electrospinning depends on multiple interacting parameters that simultaneously affect the viscosity, surface tension, and charge density of the polymer jet. These factors interact in a coupled and nonlinear manner to determine jet stability, stretching, and solvent evaporation, ultimately influencing fibre diameter. Therefore, an ANN with nonlinear activation provides a more accurate and physically meaningful mapping than linear regression models, which cannot capture such multivariate interactions. Despite having only one hidden layer, the network remained nonlinear due to the activation function, enabling the approximation of complex input–output relationships with a reliable balance between accuracy and computational efficiency.

Each dataset entry contained four input variables (molecular weight, solution concentration, flow rate, and tip-to-collector distance) and one output variable (average fibre diameter). All input variables and the output variable were preprocessed before ANN fitting using the built-in processing functions in MATLAB's Neural Network Toolbox. For each input and output variable, MATLAB automatically removed constant rows and applied min–max scaling through the "mapminmax"

function to rescale the data to approximately [–1, 1] before training [293]. During prediction, the toolbox internally applies the inverse transformation of "mapminmax", so that the network outputs are returned in the original physical units (i.e., fibre diameter in nm) [292]. A total of 140 samples were randomly divided into training, validation, and test subsets at 70%:15%:15%.

In addition, 4 samples were reserved as an independent hold-out set and were not used during network training or hyperparameter optimisation. The purpose of this small external set was to provide an additional, unbiased check of the ANN model's generalisation ability on completely unseen data. The exact number of samples in a hold-out set is not fixed; a small number is sufficient as long as they are excluded from the entire training/validation/testing pipeline. This practice is commonly adopted in machine-learning-based modelling to avoid overly optimistic performance estimates and to verify the robustness of the trained model on new input conditions [294, 295].

The model performance was evaluated using mean squared error (MSE) and the coefficient of determination (R^2), as defined in Eqs. (9) and (10).

$$\mathrm{MSE} = \frac{\sum_{i=1}^{n} \left(y_i - \hat{y}_i \right)^2}{n} \tag{9}$$

$$R^2 = \frac{\sum_{i=1}^{n} \left(\hat{y}_i - \bar{y}_i \right)^2}{\sum_{i=1}^{n} \left(y_i - \bar{y}_i \right)^2} \tag{10}$$

where y_i, $\hat{y}_i$, and $\bar{y}_i$ denote actual values, predicted outputs, and the mean of the actual fibre diameters, respectively, and n is the number of samples. Lower MSE and a higher R^2 identify the optimal ANN model. These metrics serve as essential criteria for evaluating how accurately the predicted outputs represent the actual results.

The dataset covered a broad range of fibre diameters (approximately 100–1200 nm) generated under systematically varied electrospinning parameters, ensuring adequate statistical diversity for model training. To control model complexity and reduce the risk of overfitting, early stopping and validation monitoring were implemented during training. Model convergence and error distributions were subsequently examined to verify that the training and testing errors remained

comparable. In addition, the ANN was trained with five different random weight initialisations to assess stability, and the resulting R^2 values varied by ± 0.02, confirming consistent predictive performance across multiple runs. A detailed description of the network convergence behaviour for stabilisation and the associated learning curves is provided in Figure 7. 5 in Section 7.5.2.

The IRI was introduced to quantitatively evaluate the contribution or significance of each input variable, thereby enabling the ranking of their relative influence [296-298]. Among various approaches, Garson's algorithm is one of the most commonly used methods in ANN models for estimating the importance of input variables [299]. It is based on the distribution of absolute weights in the hidden layer [300]. The formulation of the Garson algorithm was presented in Eq. (11).

$$\mathrm{IRI}_a = \frac{\sum_b \left| w_{ab} \times w_{bc} \right|}{\sum_{a'} \sum_b \left| w_{a'b} \times w_{bc} \right|} \tag{11}$$

where a denotes the number of input variables, b the number of neurons in the hidden layer (b = 10 in this work), c the number of neurons in the output layer (typically c = 1), a' traversal over all input variables, and $a'b$ all connection paths from the input layer to the hidden layer.

7.4 Construction of RSM models

RSM coupled with a Central Composite Design (CCD) was employed to develop a multiple-regression model describing the relationship between electrospinning parameters and fibre diameters. Consistent with the ANN approach, four electrospinning parameters (polymer molecular weight, solution concentration, flow rate, and tip-to-collector distance) were defined as the model factors, and fibre diameter was set as the response variable. A total of 140 experimental datasets were imported into Design-Expert (v13) using the Custom Design – Blank Spreadsheet function.

Based on the CCD structure, an RSM analysis was conducted, and a quadratic polynomial model was established to describe the combined effects of the four factors on fibre diameter. The significance of the main, interaction, and quadratic terms was evaluated using Analysis of Variance (ANOVA), which assesses statistical significance through each term's F-value and corresponding p-value. Following standard RSM practice, a term is considered statistically significant when its p-value is < 0.05, with larger F-values indicating a greater contribution relative to the experimental

error [301, 302]. Only significant terms are retained in the final regression model, while insignificant terms are removed. The fitted regression equation derived from this procedure is presented and discussed in Section 7.5.3. The remaining 4 datasets, which were excluded from model construction, were used as an independent hold-out set to further validate the RSM model's predictive accuracy.

Additionally, the model's explanatory and predictive capabilities were quantified using the adjusted and predicted coefficients of determination (R^2). The "lack-of-fit" (LOF) test was also examined to determine whether the fitted model adequately represented the experimental data. A model is considered adequate when the p-value of LOF exceeds 0.05, indicating that the unexplained variation is not statistically greater than the pure experimental error. Conversely, a significant LOF ($p < 0.05$) would suggest that the model is underfitted and fails to capture the proper relationship between the factors and the response. Overall, ANOVA provides a systematic framework for optimising model structure, eliminating insignificant terms, and establishing response models with reliable predictive performance.

Since the input factors have different units and scales, coded values were used to normalise the corresponding variables, as described in Eq. (12):

$$x = \frac{X - X_{\text{center}}}{(X_{\text{high}} - X_{\text{low}})/2} \tag{12}$$

where X is the actual value of the factor, X_{center} is the central (median) value, and X_{high} and X_{low} are the maximum and minimum values of the factor, respectively.

7.5 Results and discussion

7.5.1 Comparing the performance of image processing methods

Before developing and evaluating the ANN and RSM predictive models, it was necessary to verify the accuracy and consistency of the fibre-diameter measurements used as input data. As introduced in Section 4.8, three image-processing approaches (manual measurement, the DiameterJ ImageJ plugin, and the SIMPoly MATLAB programme) were considered for extracting fibre diameters from SEM images. To assess the accuracy and reliability of these methods, a commercial 53-gauge steel wire with a certified diameter of 16.7 ± 0.1 μm was used as a benchmark sample. Owing to its stable,

uniform, and circular cross-section, this wire provided an ideal reference for evaluating measurement consistency across the three techniques.

Manual measurements were first performed. As shown in Figure 7. 2, a total of 150 filament segments were randomly selected (Figure 7. 2a), and each measurement was taken perpendicular to the filament centreline to minimise geometric error. The resulting frequency distribution of measured diameters displayed a narrow, symmetric Gaussian profile (Figure 7. 2b). The manually measured average diameter was 16.91 ± 1.40 µm, as summarised in Table 7. 1.

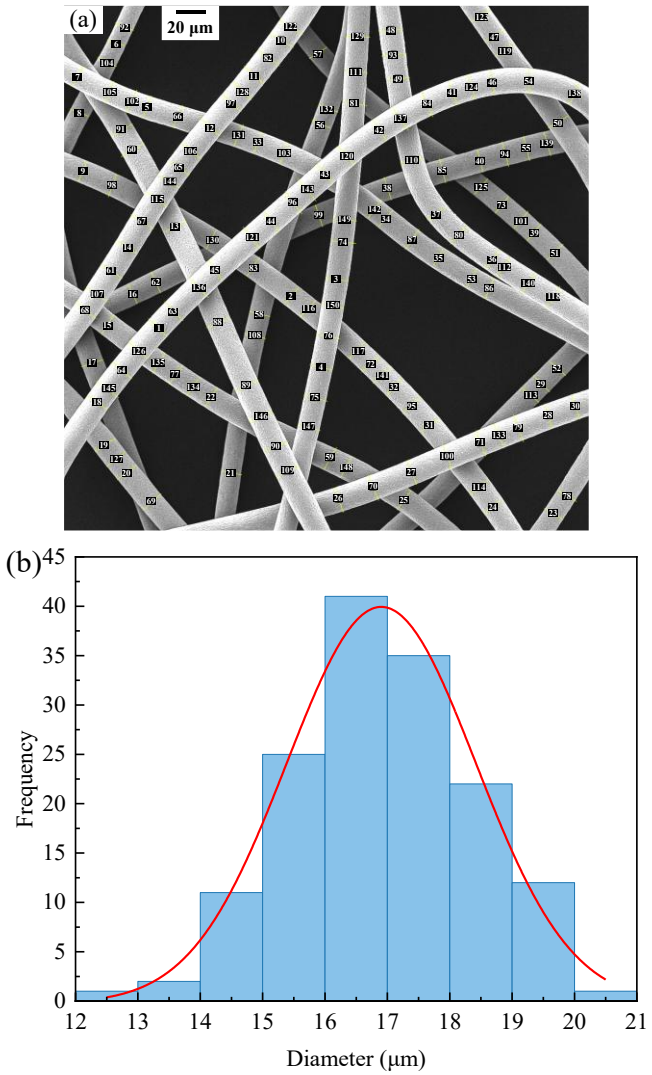

Figure 7. 2: Manual measurement (a) and corresponding diameter frequency distribution and Gaussian fitting (b) of the benchmark.

The same image was subsequently processed using DiameterJ, which used automatic thresholding and fibre skeletonisation. As illustrated in Figure 7. 3a, fifteen different thresholding algorithms were applied to segment the SEM image. Among them, the segmentation that most accurately preserved

the filament morphology relative to the original image was selected for subsequent operations, including axial thinning, Euclidean distance transformation, and pore-structure analysis (Figure 7. 3b). The resulting diameter frequency distribution and Gaussian fitting (Figure 7. 3c) demonstrated a well-defined, unimodal distribution. As reported in Table 7. 1, the average diameter obtained using DiameterJ was 16.70 μm with a standard deviation of 1.39 μm, corresponding to a relative error of 0% compared with the benchmark diameter (16.7 ± 0.1 μm). This near-perfect agreement confirmed the high accuracy and reliability of DiameterJ for automated fibre diameter measurement. The combination of multiple thresholding algorithms and morphology-based refinement allowed the programme to effectively capture filament boundaries and minimise user bias, offering strong reproducibility for large-scale fibre analysis.

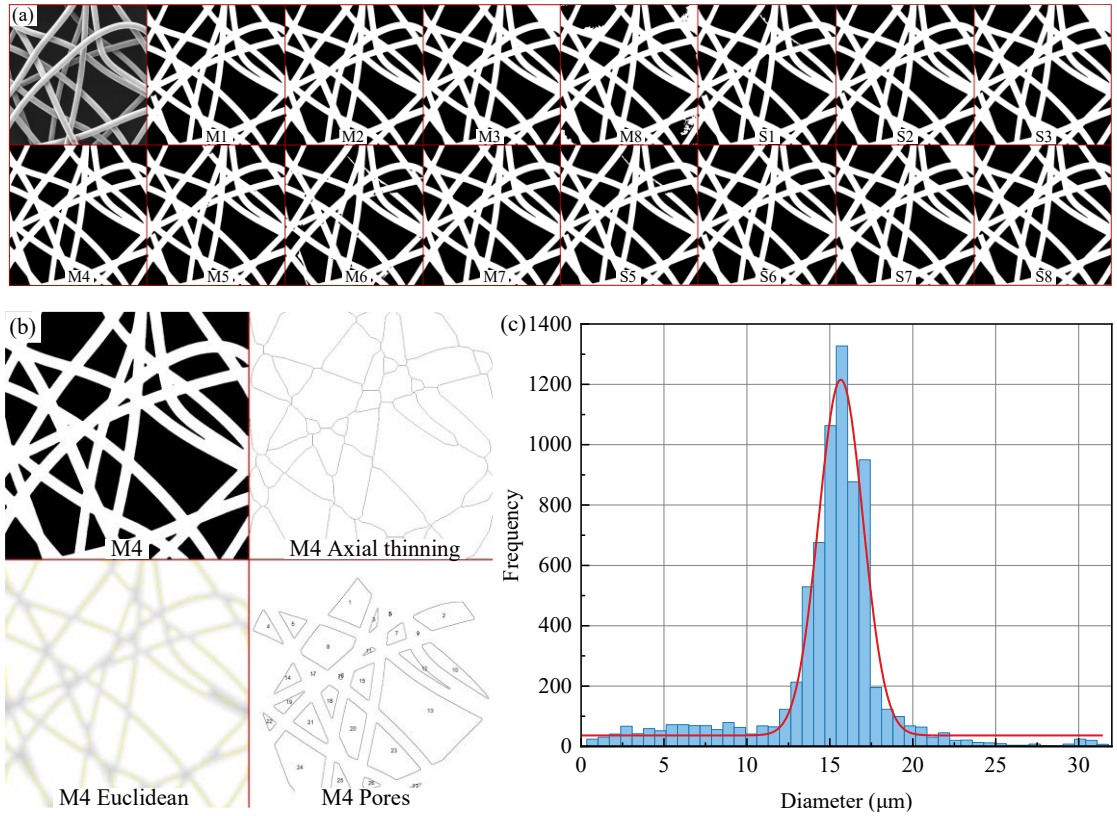

Figure 7. 3: Image processing of the SEM image of the benchmark using DiameterJ: (a) segmentation results obtained with different thresholding methods, (b) further processing of the optimal segmentation (M4), and (c) corresponding diameter frequency distribution. (M and S denote the mask image and the skeleton image, respectively.)

The SIMPoly programme adopted a different analytical approach, only employing a global threshold for image segmentation (Figure 7. 4a). A visual overlay was used to verify that the extracted fibre skeleton aligned accurately with the filament centreline (Figure 7. 4 b). A colour-coded diameter map

was then generated to display local variations in fibre diameter along the filament axis (Figure 7. 4c). The corresponding diameter distribution and Gaussian fitting (Figure 7. 4d) yielded an average diameter of 16.67 μm with a standard deviation of 1.07 μm, producing a relative error of only 0.18% compared with the benchmark.

Table 7. 1: Comparison of measured diameters and relative error of the benchmark using three image processing methods.

Methods	Measured average diameter of benchmark (μm)	Standard deviation (μm)	Relative error
Manual measurement	16.91	1.40	1.26%
DiameterJ	16.70	1.39	0%
SIMPoly	16.67	1.07	0.18%

It is important to emphasise that manual diameter measurement, although straightforward, presents several inherent drawbacks that can compromise both accuracy and efficiency. These limitations include (a) the subjective selection of filament segments by the operator, which can introduce user bias; (b) the restricted number of data points that can reasonably be collected, limiting statistical reliability; and (c) the time-consuming nature of manual measurement, which makes it unsuitable for large datasets or high-throughput analyses. The manually measured diameter of the benchmark sample (16.91 ± 1.40 μm) showed a slight deviation from the nominal diameter (16.7 ± 0.1 μm), corresponding to a higher relative error of 1.26%, indicating reduced precision compared with automated approaches. These results highlight that manual measurement, while proper for verification, lacks the objectivity, reproducibility, and efficiency required for high-throughput systematic quantitative analysis.

In contrast, both DiameterJ and SIMPoly provide more objective, reliable, and efficient means of measuring fibre diameters. Their automated workflows eliminate the subjective element of manual selection and allow a much larger number of measurements to be performed in a fraction of the time, significantly improving statistical robustness. Among the two, DiameterJ offers particular advantages. It supports multiple thresholding algorithms for image segmentation and allows flexible adjustment of processing parameters, enabling accurate analysis across a wide variety of SEM image types without extensive manual intervention. The plugin's batch-processing capability also makes it

especially suitable for high-throughput image analysis. Moreover, DiameterJ includes an integrated set of analytical tools capable of quantifying not only fibre diameter but also fibre orientation, pore size, and porosity, which are valuable parameters for comprehensive characterisation of fibrous membranes.

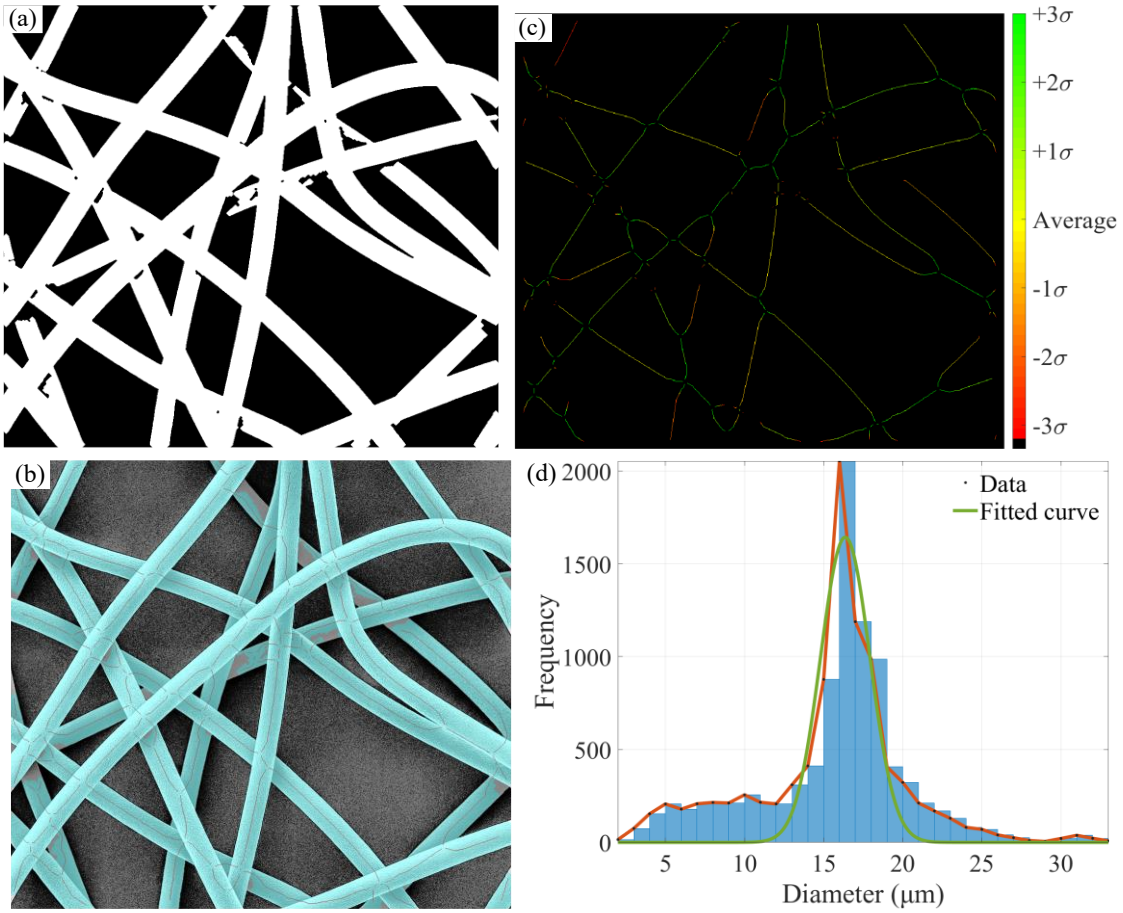

Figure 7. 4: Image processing of the SEM image of the benchmark using SIMPoly: (a) segmentation result, (b) segmentation overlay with centerlines extraction, (c) colour-coded diameter map along the centerlines, and (d) corresponding diameter frequency distribution.

It should be noted that the steel-wire benchmark was used solely to validate the fibre-diameter measurement capability of DiameterJ. The steel wire has a uniform and well-defined diameter, making it suitable for assessing whether the two programmes can accurately extract single-fibre diameters from SEM images. While DiameterJ also includes algorithms for estimating pore-structure characteristics, these outputs are not reliable for electrospun membranes. This is because the input imaging condition makes such calculations inherently inaccurate. The benchmark steel wire represents a simple, single-layer structure with clearly defined openings, whereas electrospun membranes consist of a randomly deposited, multilayered 3D fibre network. SEM, however, provides

only a 2D projection of this complex 3D architecture. As a result, the pore-structure values derived from DiameterJ inevitably reflect only a flattened, partial view of the membrane and therefore do not represent the actual porosity or pore connectivity of the scaffold. For this reason, pore-structure outputs from DiameterJ were not used in this work. The analysis focused exclusively on fibre diameter, which remained the most measurable and meaningful morphological parameter influencing membrane uniformity, mechanical behaviour, and filtration performance.

By comparison, the SIMPoly programme uses a simpler algorithm, applying a single global threshold for segmentation and processing each image separately. While this approach produced highly accurate diameter measurements, its limited adaptability and lack of batch-processing capability made it less suitable for large-scale studies involving numerous SEM images acquired under varying conditions. Given these considerations, the DiameterJ plugin was selected as the primary analytical tool for this research. It was subsequently applied to SEM images of electrospun PCL membranes fabricated under different experimental conditions for fibre-diameter measurement. A total of 144 samples were processed and analysed, providing a comprehensive database of fibre diameter distributions. These data were then used as input to the ANN model developed in the following sections, enabling quantitative prediction of fibre diameters from process parameters while significantly reducing experimental cost and time.

7.5.2 Performance of the ANN model

The architecture of the ANN used is shown in Figure 7. 1. The network was trained using the Levenberg–Marquardt backpropagation algorithm, implemented through the “trainlm” function in MATLAB’s Neural Network Toolbox. This algorithm is widely used for training feed-forward neural networks because it provides fast convergence and high accuracy for nonlinear regression problems [286, 303, 304]. To construct and validate the model, the dataset was randomly divided into three subsets: training, validation, and testing. Specifically, 70% of the data (n = 98) was allocated for training, during which the model iteratively adjusted the weights and biases to minimise prediction errors and capture the underlying nonlinear relationships between the experimental input parameters and the measured fibre diameters (output).

Throughout the training process, model performance was continuously monitored to fine-tune

hyperparameters and determine the most effective network configuration. To prevent overfitting and ensure that the trained model generalised well to new data, 15% of the dataset (n = 21) was reserved for validation. Once training and validation were complete, the remaining 15% (n = 21) served as an independent test set to evaluate the model's predictive capability on previously unseen data.

The evolution of the training state is illustrated in Figure 7. 5a. The training gradient, which guided the weight update process, decreased steadily from approximately 10^6 at the beginning of training to 232.47 by epoch 17, demonstrating a continuous reduction in the error-surface slope and indicating evident progress toward convergence. The damping parameter Mu, a stabilising factor in the Levenberg–Marquardt algorithm, initially increased as the algorithm adjusted the search step, but subsequently stabilised at 10 by epoch 17, indicating that the Levenberg–Marquardt optimisation had reached a stable update regime. The validation failure count (Val fail) increased gradually and reached six at epoch 17, at which point early stopping was triggered. This confirmed that the model was halted at the epoch corresponding to the minimum validation error, preventing overfitting and ensuring that the selected network state generalised well. Overall, the combined trends, including monotonic gradient reduction, stabilisation of Mu, and controlled validation-failure behaviour, indicated that the training process converged efficiently and produced a stable, generalisable ANN model.

The MSE evolution in Figure 7. 5b reflected the progressive reduction in prediction error during training. In MATLAB's Neural Network Toolbox, the MSE is computed as the mean of the squared differences between the target and predicted fibre diameters. Because the fibre diameters spanned a wide range from 100 to 1200 nm, initial prediction errors can also be significant. For example, if the early network output deviated from the target by several hundred nanometres, the squared error may readily reach magnitudes of 10^5–10^6. This explains the high MSE values observed in the early epochs of Figure 7. 5b. As training progressed, the MSE for the training, validation, and test sets decreased rapidly and stabilised at lower values. The best validation performance occurred at epoch 11, where the validation MSE reached 958.97, corresponding to an average squared error of less than 31 nm in root-mean-square terms. The convergence of all training, validation, and test curves to comparably low MSE values demonstrated that the ANN successfully captured the nonlinear relationship between the electrospinning parameters and the fibre diameter without overfitting. The error

histogram in Figure 7. 5c illustrates the distribution of prediction errors across the training, validation, and test subsets. Most of the error values were concentrated near zero (marked by the orange line), indicating a good model fit, i.e., the model predictions were highly consistent with the experimental data.

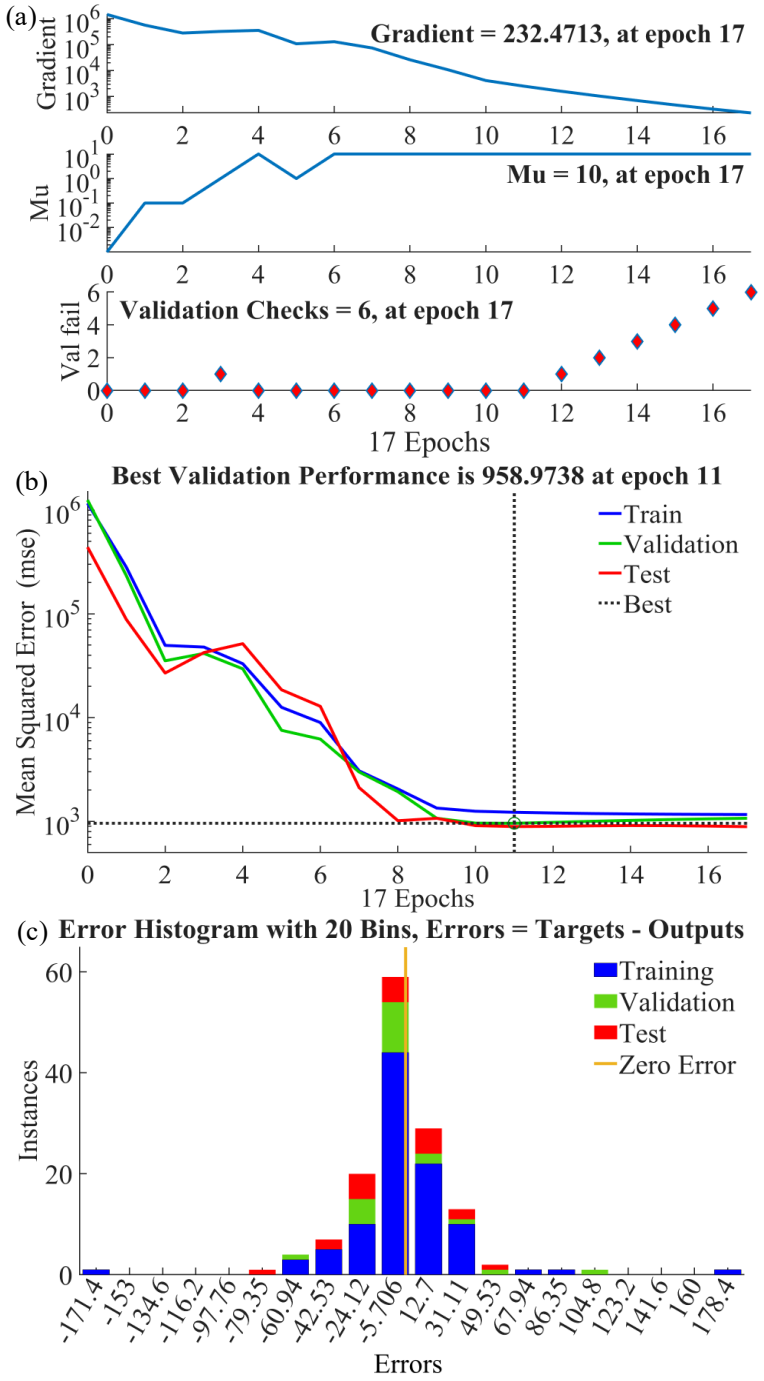

Figure 7. 5: Training state plot (a), MSE plot (b), and error histogram (c) for training, validation, and test sets in the established ANN model.

The overall correlation between the predicted and experimentally measured fibre diameters is presented in Figure 7. 6. In all subplots, the x-axis represents the actual fibre diameters obtained from

SEM images analysed using DiameterJ, and the y-axis represents the corresponding ANN-predicted diameters. Across the training, validation, and test sets (Figure 7. 6a–c), most data points clustered closely around the $y = x$ parity line, indicating strong agreement between predictions and experimental measurements. It should be noted that the fitted regression lines shown in Figure 7. 6 represent linear relationships between predicted and actual values, rather than any internal functional mapping between the input variables and the ANN output. Thus, these lines were used solely as diagnostic tools to assess prediction accuracy and potential systematic bias, and did not reflect the ANN's underlying nonlinear structure. The high R^2 (0.980 for training, 0.984 for validation, and 0.977 for testing) confirmed the excellent predictive capability and generalisation performance of the ANN model.

Nevertheless, several systematic features are evident and warrant discussion. First, the fitted regression lines deviated slightly from the ideal parity line ($\hat{y} = 0.97x + 11$ for training, $\hat{y} = 0.87x + 40$ for validation, $\hat{y} = 1.10x - 15$ for test), indicating mild systematic bias in different subsets. Specifically, deviations were most pronounced in the large-diameter range (>800 nm), where the distribution of a small number of samples made this region intrinsically more difficult for the network to learn with uniform accuracy. In contrast, the lower-diameter region (50–600 nm), where the majority of data were concentrated, exhibited very tight clustering around the parity line with minimal deviation. Importantly, the magnitude of the observed deviations was small relative to the whole experimental diameter range of 100–1200 nm, and the fitted lines remained closely aligned with the parity line across all subsets. Overall, these results indicated that although deviations appeared in sparsely sampled regions of the parameter space, the ANN model successfully captured the dominant nonlinear relationships between the electrospinning parameters and fibre diameter. The consistently high R^2 values across all subsets and the strong alignment between predicted and target values demonstrated strong predictive accuracy and generalisation capability of the developed model.

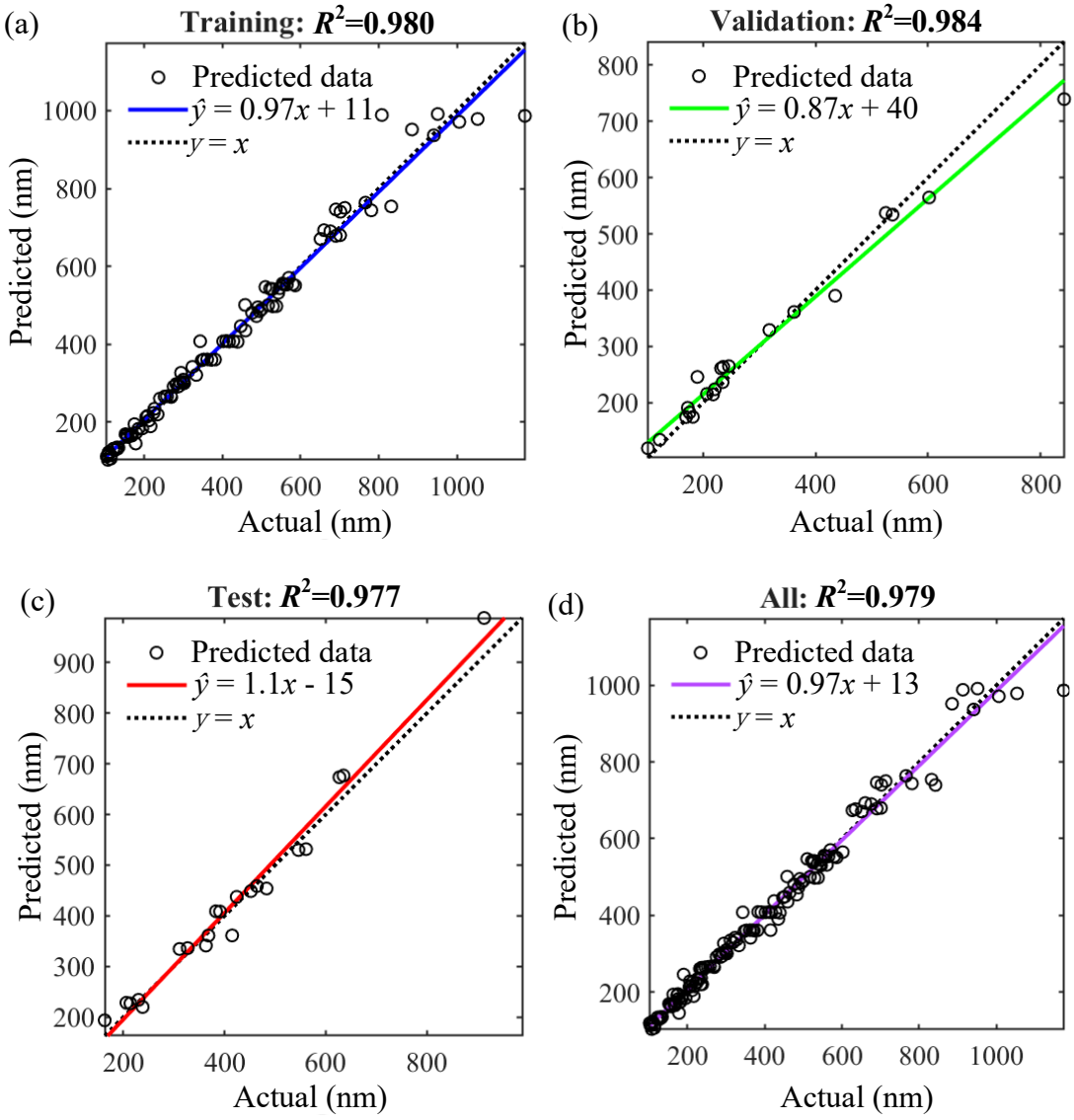

Figure 7. 6: ANN regression analysis of the predicted versus actual values for the training (a), validation (b), testing (c), and overall (d) datasets.

7.5.3 Statistical results obtained by RSM

Multiple regression analysis within the RSM framework was carried out to establish a mathematical relationship between the electrospinning parameters and the resulting fibre diameters. A CCD was adopted because its second-order polynomial structure provides an appropriate model form for capturing linear, interaction, and squared effects among the processing parameters, as is well established in response surface methodology [301, 305]. The general form of a second-order polynomial is expressed in Eq. (13):

$$y = \beta_0 + \sum_{i=1}^{k} \beta_i x_i + \sum_{i=1}^{k} \beta_{ii} x_i^2 + \sum_{i<j} \beta_{ij} x_i x_j \tag{13}$$

where x_i represents the coded input variables, and y denotes the predicted response. In this formulation, β_0 is the intercept, β_i the linear coefficients, β_{ii} the quadratic coefficients, and β_{ij} the interaction coefficients. The indices i and j range from 1 to k, where k is the number of factors in the experimental design, and the constraint $i < j$ ensures that each interaction term is represented only once.

Based on this CCD structure, a quadratic model was fitted to the experimental data, and ANOVA was subsequently used to determine which linear, interaction, and squared terms were statistically significant. Details on the ANOVA method used are provided in Section 7.4. The ANOVA results are summarised in Table 7. 2. The analysis indicated that factors *A* (molecular weight), *B* (concentration), *C* (flow rate), and their interaction or squared terms *AB*, *BC*, $A^{2,}$ and B^2 exhibited statistically significant effects ($P < 0.05$). Non-significant terms ($P > 0.05$) were removed to improve model simplicity and predictive stability. The regression coefficients were obtained from the coded quadratic model generated by Design-Expert software (v13), which uses least-squares regression internally to estimate the model parameters [306]. Substituting the significant terms into the general quadratic form yielded the final regression model shown in Eq. (14), which represents the best-fitting quadratic surface within the investigated design space to describe the predicted PCL fibre diameter:

$$\begin{aligned} y = {} & 351.16 + 351.64A + 337.79B + 108.92C \\ & + 323.71AB + 95.26BC + 119.18A^2 + 118.80B^2 \end{aligned} \tag{14}$$

where y denotes the predicted PCL fibre diameter, and A, B, and C represent the coded values of molecular weight, concentration, and flow rate, respectively.

The overall regression model was statistically significant ($P < 0.0001$), indicating that it accounted for the majority of the observed variability in fibre diameter. The lack-of-fit test was non-significant ($P = 0.0960$), indicating that the fitted model adequately represented the experimental data. The adjusted R^2 (0.957) and the predicted R^2 (0.949) were both high and closely aligned, demonstrating strong internal consistency and robust predictive performance within the experimental range.

Table 7. 2: ANOVA results for the response surface quadratic model based on the $\log_{10}$-transformed PCL fibre diameters.

Source	Sum of square	*df*	Mean square	F-value	P-value
Model	7.194E+06	14	5.138E+05	228.75	< 0.0001*
A	2.395E+06	1	2.395E+06	1066.09	< 0.0001*
B	6.839E+05	1	6.839E+05	304.46	< 0.0001*
C	49836.69	1	49836.69	22.19	< 0.0001*
D	18.82	1	18.82	0.0084	0.9272**
AB	5.043E+05	1	5.043E+05	224.50	< 0.0001*
AC	2076.76	1	2076.76	0.9246	0.3381**
AD	14.13	1	14.13	0.0063	0.9369**
BC	21862.20	1	21862.20	9.73	0.0022*
BD	4.67	1	4.67	0.0021	0.9637**
CD	19.34	1	19.34	0.0086	0.9262**
A^2	1.654E+05	1	1.654E+05	73.64	< 0.0001*
B^2	53198.41	1	53198.41	23.68	< 0.0001*
C^2	523.26	1	523.26	0.2330	0.6302**
D^2	268.90	1	268.90	0.1197	0.7299**
Lack of Fit	2.890E+05	125	2312.01	3.84	0.0960**
Pure Error	3007.00	5	601.40		

Note: *, significant at 95% confidence interval; **, not significant at 95% confidence; *A*, *B*, *C*, and *D* represent the coded values of molecular weight, concentration, flow rate, and tip-to-collector distance, respectively.

According to the final quadratic regression model (Eq. (14)), the predicted fibre diameters were obtained by substituting the corresponding coded input variables and subsequently compared with the actual experimental measurements. The RSM regression analysis is presented in Figure 7. 7. As with the ANN analysis, the linear regression line shown in Figure 7. 7 represented a post-hoc diagnostic relationship between predicted and actual fibre diameters and should not be interpreted as

part of the quadratic RSM model itself. Its purpose was solely to assess prediction accuracy and potential systematic bias. The fitted regression line was $\hat{y} = 0.96x + 15$, which deviated from the ideal $y = x$ line and showed a visibly wider spread of data points. In contrast to the ANN-based regression results in Figure 7. 6(d), where predictions clustered tightly around the parity line, the RSM model exhibited substantial dispersion across the full range of fibre diameters. This indicated that the quadratic polynomial model was less capable of capturing the nonlinear and coupled effects of the electrospinning parameters, resulting in lower predictive accuracy than the ANN approach.

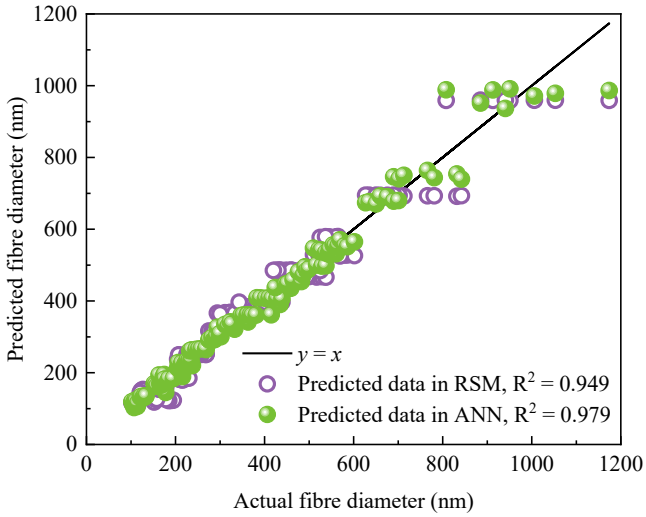

Figure 7. 7: Comparison of predicted vs. actual fibre diameters for the RSM and ANN models.

To further evaluate the predictive capability of the trained ANN model, 4 samples were reserved as an independent hold-out test set and were not used during network training or hyperparameter optimisation (see Section 7.3). The predicted fibre diameters and corresponding percentage errors for both the ANN and RSM models are summarised in Table 7. 3. For the ANN model, all prediction errors were below 4%, demonstrating consistent and reliable predictive performance within the experimental design space. This high level of predictive accuracy enabled the ANN to serve as an efficient tool for pre-evaluating fibre-diameter outcomes before conducting actual electrospinning experiments.

For comparison, the same hold-out datasets are evaluated using the RSM model through Eq. (14), and the resulting predictions and associated errors are also presented in Table 7. 3. The RSM model produced higher prediction errors, with the maximum deviation reaching 28.57%. The most significant discrepancy, observed at a molecular weight of 38600 g/mol, reflected the limited capacity

of a quadratic polynomial to investigate the complex, nonlinear, and coupled relationships among the electrospinning parameters. Because a quadratic RSM model (Eq. (14)) can only represent second-order curvature, it lacked the capacity to capture the strongly nonlinear and coupled behaviour of the electrospinning process, particularly in regions where the response surface departed from the central design domain. Consequently, its predictive accuracy was limited. Within the operating domain examined, the ANN therefore provided markedly superior predictive performance. Such predictive capability offered practical value, enabling more efficient planning of electrospinning experiments and reducing unnecessary material consumption.

Table 7. 3: Comparison of predicted and actual fibre diameters with associated errors in ANN and RSM models.

Molecular weight (g/mol)	Concentration (wt. %)	Flow rate (mL/h)	Distance (cm)	Actual diameter (nm)	Predict diameter (nm)		Error	
					ANN	RSM	ANN	RSM
38600	20	1.2	17.62	119	116	153	2.52%	28.57%
83700	20	1.5	17.99	301	312	316	3.65%	4.98%
83700	30	1.7	17.59	753	760	693	0.93%	7.97%
96700	25	1.6	15.68	641	659	694	2.81%	8.27%

Although the RSM model was statistically significant according to ANOVA, this significance merely confirmed a good fit to the existing dataset and did not guarantee predictive accuracy for unseen conditions. The frequent assumption that statistical significance equates to strong predictive power can therefore be misleading in practical applications of RSM [307]. In contrast, the trained ANN model demonstrated not only excellent agreement with the training data but also superior generalisation ability when applied to new parameter combinations [285, 286, 308]. All ANN predictions exhibited errors below 4%, confirming its robustness and adaptability to nonlinear parameter interactions.

In summary, while both RSM and ANN can model the relationship between electrospinning parameters and fibre diameter, the ANN model provided a more flexible and accurate predictive framework. Its data-driven learning capability enabled it to capture complex, nonlinear dependencies

that the polynomial-based RSM cannot fully describe. Consequently, the ANN approach proved to be a more reliable and efficient tool for optimising electrospinning processes and predicting fibre morphology across diverse operating conditions.

7.5.4 Relative importance of electrospun parameters on fibre diameter

The IRI values were calculated using Eq. (11) based on Garson's algorithm. The corresponding relative contributions of each electrospinning parameter are presented in Figure 7. 8. Previous studies have applied ANN models to predict electrospun fibre diameters, typically relying on manually measured datasets [279, 282-285]. In contrast, this section employed an automated, standardised image-processing workflow (DiameterJ) to directly obtain fibre diameter measurements from SEM images. It is important to note that this automation is not intended to enhance the ANN's predictive performance, but rather to reduce operator-dependent variability and ensure consistent data quality across the entire experimental domain. Both the ANN and RSM models were trained and evaluated on the same automatically extracted dataset; the superior performance of the ANN reflected its stronger ability to capture nonlinear parameter interactions, rather than any advantage arising from automated measurement tools. The resulting dataset was more comprehensive and internally consistent than manually generated datasets, providing a solid foundation for robust model training and for reliably assessing parameter significance through the IRI method.

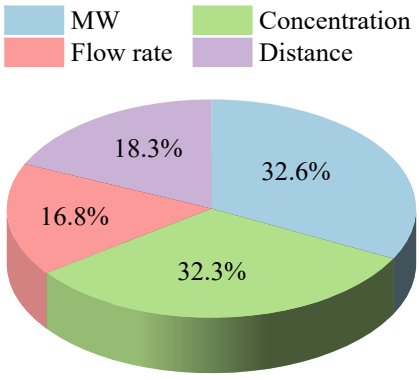

Figure 7. 8: IRI of electrospun parameters on fibre diameters.

The parameter importance derived from the ANN analysis aligned closely with the known physical behaviour of electrospinning, confirming the validity and reliability of the proposed modelling framework. Among the four studied input parameters, molecular weight and solution concentration exhibited the highest IRI values of 32.6% and 32.3%, respectively, which were approximately twice

those of flow rate and collector distance. The overall ranking of parameter influence on fibre diameter followed the order: Molecular weight ≈ Concentration > Collector distance ≈ Flow rate.

This ranking highlighted that molecular weight and concentration exerted dominant control over fibre formation, while flow rate and distance played secondary roles. This observation is entirely consistent with the physical mechanisms governing electrospinning. In particular, molecular weight and concentration determine the viscosity and degree of chain entanglement in the polymer solution, which are two critical factors controlling jet stability, elongation, and solidification. When viscosity and entanglement are insufficient, bead formation occurs; when excessive, jet stretching is hindered, resulting in thicker fibres. In contrast, flow rate and collector distance primarily influence process dynamics; flow rate affects the supply rate of polymer solution and jet volume, whereas collector distance governs the flight path and evaporation time.

Looking ahead, the current model could be further refined by incorporating additional electrospinning variables, such as applied voltage, ambient humidity, temperature, and solvent composition. Expanding the set of input parameters would enrich the model's representation of the underlying process–structure relationships and enable the ANN to learn a broader range of fibre formation behaviours, thereby improving robustness and generalisation capability. Future work should also expand the experimental dataset, as a larger number of samples is required to reliably train neural networks with higher-dimensional input spaces.

To further visualise the combined effects of different electrospinning parameters on fibre diameter, contour plots were generated based on the trained ANN predictions (Figure 7. 9). The colour gradients represented the predicted fibre diameters, where warmer colours indicated thicker fibres and cooler colours corresponded to finer ones. Figure 7. 9a illustrates the combined influence of polymer molecular weight and solution concentration. Both parameters showed similar trends: fibre diameter increased with increasing molecular weight or concentration, even when the other parameter was held constant. This can be attributed to the fact that higher polymer molecular weight and concentration lead to increased solution viscosity and stronger molecular entanglements, which restrict jet stretching during electrospinning and result in thicker fibres [309, 310].

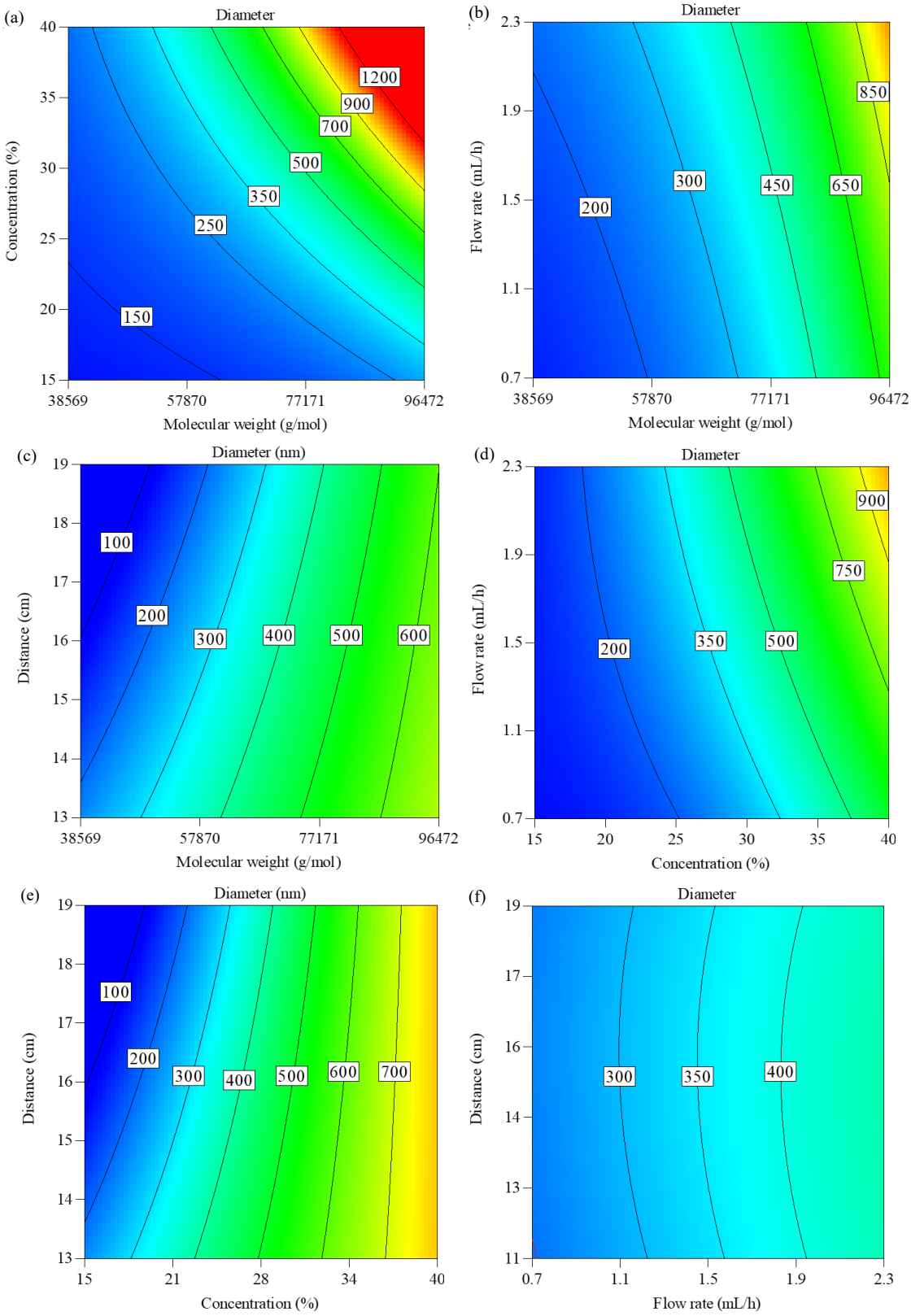

Figure 7. 9: Contour plots showing the ANN-predicted effect of electrospinning parameters on fibre diameter: molecular weight vs. concentration (a), molecular weight vs. flow rate (b), molecular weight vs. distance (c), concentration vs. flow rate (d), concentration vs. distance (e), flow rate vs. distance (f).

Figure 7. 9b and d display the effects of flow rate in relation to molecular weight and concentration,

respectively. Although flow rate had a comparatively minor impact, higher values promoted greater volumetric extrusion of polymer solution, leading to slightly thicker fibres due to limited stretching time before solidification [311, 312]. The influence of collector distance, shown in Figure 7. 9c and e, followed the opposite trend: as the tip-to-collector distance increased, the extended flight path allowed more time for jet stretching and solvent evaporation, typically resulting in thinner fibres [313]. Finally, Figure 7. 9f presents the combined influence of flow rate and collector distance. The nearly uniform colour distribution across the plot indicated minimal interaction between the two parameters, corroborating the IRI analysis, which ranked both as less influential.

7.6 Conclusion

In this section, an integrated approach combining image processing techniques with ANN modelling was developed to enable efficient and accurate prediction of electrospun PCL fibre diameters. Automated analysis tools (DiameterJ and SIMPoly) were evaluated against manual measurements using a benchmark SEM image, with DiameterJ selected for its superior accuracy and high-throughput capability. DiameterJ was subsequently used to extract 144 datasets from SEM images of electrospun PCL membranes prepared under systematically varied experimental parameters. These datasets were used to train a feedforward ANN model that demonstrated excellent predictive performance, with R^2 values exceeding 0.97 and prediction errors below 4% in unseen conditions. In contrast, the RSM model, though statistically significant, showed limited predictive accuracy for unseen conditions, with errors up to 28.57%. The improved predictive performance of the ANN model was closely linked to the way the training data were obtained. By integrating automated image analysis (DiameterJ) into the workflow, the model was trained on a larger, more consistent dataset than those typically used in previous studies that relied on manual measurements. The trained ANN model enables users to predict fibre diameters under various fabrication conditions before electrospinning, thereby significantly reducing experimental time and material consumption. The IRI analysis revealed that molecular weight and solution concentration were the most influential parameters affecting fibre diameter. Contour maps further illustrated the interactive effects of these parameters on fibre morphology, confirming their dominant role in fibre formation. This section highlights the strength of integrating advanced image processing with machine learning to enable data-driven design and optimisation of electrospun materials, offering a broadly applicable

framework for morphological prediction in fibre-based manufacturing.

Future work will focus on expanding the model by incorporating additional electrospinning parameters and larger datasets to further enhance its predictive accuracy and generalisation capability across different polymer systems. Beyond the current PCL framework, the proposed approach can be extended to other electrospun materials used in biomedical scaffolds, filtration membranes, and energy devices, where rapid and reliable morphology prediction is crucial for performance optimisation. Strengthening such application-oriented developments will facilitate the translation of this methodology from laboratory-scale research to practical process design and manufacturing.

CHAPTER 8

8 Conclusions and perspectives

PCL-based membranes have been comprehensively investigated throughout this thesis as a versatile and sustainable material platform. Owing to their biodegradability, biocompatibility, non-toxicity, and tunable porosity, PCL membranes exhibit great potential across seemingly distinct but intrinsically connected fields, including tissue engineering and water treatment. In the biological domain, electrospun PCL nanofibrous scaffolds were designed to mimic the extracellular matrix, providing favourable microenvironments for fibroblast adhesion, proliferation, and tissue regeneration. In contrast, in the environmental domain, the same electrospinning strategy was extended to construct multilayered or surface-functionalised PCL membranes that achieve high oil/water separation efficiency, excellent reusability, and improved environmental safety. These two applications, though targeting different end uses, share a common structural rationale: the optimisation of pore interconnectivity, surface wettability, and mechanical integrity to regulate mass transport and interfacial interactions.

Beyond experimental design, this thesis further integrated automated image-processing algorithms and ANN modelling to quantitatively link electrospinning parameters, fibre morphology, and functional performance. By extracting large-scale diameter data from SEM images and using the ANN for predictive analysis, a robust parameter–structure–performance relationship was established. This intelligent framework not only reduced human bias and experimental workload but also enabled data-driven optimisation of membrane fabrication. The cross-disciplinary convergence of biomedical applications, environmental engineering, and intelligent modelling thus forms a unified narrative for this research, demonstrating how a polymer system can be engineered through both experimental and

computational strategies to address challenges ranging from cellular regeneration to sustainable water purification.

In this section, the significant findings are summarised and critically discussed, highlighting how integrating materials design, experimental validation, and intelligent modelling contributes to a broader understanding of structure–function relationships in PCL-based membranes. Future perspectives are then proposed to guide the further translation of these findings toward advanced multifunctional membrane systems and sustainable manufacturing strategies.

8.1 Conclusions

This thesis systematically investigated the design, fabrication, and functional optimisation of electrospun PCL membranes across biological and environmental applications. By integrating experimental characterisation with data-driven modelling, a comprehensive understanding of the structure–property–performance relationships governing PCL-based systems was achieved. The work collectively demonstrates that rational control over electrospinning parameters enables precise modulation of fibre morphology, which in turn determines the cell culture and oil/water separation efficiency of the resulting membranes. The incorporation of automated image analysis and ANN further advanced this understanding, providing predictive capability and quantitative insight into parameter sensitivity. The outcomes of Chapters 5–7 are summarised below to highlight how each objective contributed to this overarching framework.

Chapter 5, addressing Objective 2, investigated the structure–property relationships of electrospun PCL scaffolds, focusing on how fabrication parameters affect nanofibre morphology and cellular responses. A systematic analysis revealed that optimising key electrospinning parameters, particularly PCL molecular weight and solution concentration, is critical for controlling scaffold structure and improving biocompatibility. Under optimal conditions, medium- and high-molecular-weight PCL solutions produced bead-free nanofibres with desirable diameters, significantly enhancing cell adhesion, proliferation, and spreading. Furthermore, GPC analysis revealed notable discrepancies between the nominal and actual molecular weights of commercial PCL, emphasising the need for careful material characterisation. Despite the favourable morphological outcomes, the intrinsic hydrophobicity of PCL remained a barrier to effective cell infiltration. This limitation

highlights the importance of post-processing strategies, such as surface modification or blending with biomass-derived hydrophilic polymers, to improve scaffold–cell interactions.

Chapter 6, addressing Objective 3, focused on the design, fabrication, and performance evaluation of PCL-based multilayer membranes for oily wastewater separation. Electrospun sandwich-structured membranes composed of PCL and PMMA were successfully fabricated and post-treated to enhance mechanical integrity and wettability. Ethanol immersion and cold-pressing improved surface hydrophilicity, promoted tighter fibre packing, and reduced fibre diameter, attributed to axial fibre stretching during compression. PMMA incorporation lowered solution viscosity, contributing to finer fibre formation. The resulting membranes achieved high oil rejection rates (~95%) and demonstrated satisfactory mechanical strength. Long-term filtration tests showed a decline in flux due to membrane compaction and partial pore blockage. Moreover, the FRR was limited by the simplicity of the DI water rinsing protocol, which could not entirely remove adhered oil droplets. These results emphasise the need for improved cleaning protocols or antifouling strategies to ensure membrane durability and reusability in practical settings.

Chapter 7, addressing Objective 4, developed an integrated, data-driven workflow combining automated image analysis with ANN modelling to predict fibre diameters under diverse electrospinning conditions. Comparative evaluation of image analysis tools confirmed the superior performance and throughput of DiameterJ over manual measurement and SIMPoly for fibre diameter extraction from SEM images. The extracted data were used to train a feedforward ANN model, which achieved excellent predictive accuracy, with R^2 values exceeding 0.97 and prediction errors below 4% on unseen data. The IRI and contour map analyses identified molecular weight and solution concentration as the most influential parameters governing fibre diameter, aligning well with the experimental findings reported in Chapter 5. This section demonstrates the effectiveness of integrating advanced image processing with machine learning to enable predictive control and optimisation of electrospun fibre morphology. The proposed framework is scalable, transferable, and broadly applicable across fibre-based manufacturing systems.

8.2 Perspectives

8.2.1 Perspectives in tissue engineering

While substantial challenges remain, PCL-based scaffolds hold great promise across a broad spectrum of tissue engineering applications due to their tunable physicochemical properties, structural versatility, and biocompatibility. Ongoing advancements in materials science, fabrication technologies, and translational strategies are expected to drive the development of next-generation scaffolds with enhanced functionality, thereby improving patient outcomes in regenerative medicine worldwide.

To facilitate clinical translation, several critical barriers must be addressed through coordinated, interdisciplinary research. Future work should prioritise integrating multiscale structural features and mechanical performance by combining complementary fabrication methods, such as electrospinning and 3D printing. In parallel, computational approaches, including ML and high-throughput screening, can support the rational design of scaffold compositions and architectures tailored to specific tissue types. Enhancing sustainability and scalability also remains a key goal, requiring the adoption of green solvents and cost-effective, industrially viable production processes. Moreover, the establishment of standardised evaluation protocols, covering mechanical integrity, degradation kinetics, and biocompatibility, is essential for regulatory approval and clinical deployment. Achieving these objectives will require close collaboration among materials scientists, biomedical engineers, and clinicians to ensure that scaffold design aligns with practical clinical needs and translational feasibility.

8.2.2 Perspectives in oil/water separation

Although significant progress has been made in developing PCL-based membranes for oil/water separation, several challenges remain to be addressed for practical application. Long-term performance under complex, dynamic wastewater conditions, such as fluctuations in temperature, salinity, and pH, warrants further investigation. Mechanical stability and resistance to fouling and fatigue during extended operation are critical to reliability. Recyclability is also a significant concern, as many membranes experience irreversible fouling and structural degradation during regeneration.

Developing environmentally benign, non-destructive cleaning strategies will be essential to improving reusability. In terms of production, the scalability of fabrication remains limited. The advancement of scalable methods, such as roll-to-roll electrospinning and extrusion-based 3D printing, is expected to improve production efficiency.

Additionally, although PCL is inherently biodegradable, the frequent use of toxic solvents during membrane fabrication raises concerns regarding environmental sustainability. Exploring green processing technologies and bio-based additives may help mitigate these impacts. Integrating additional functionalities, such as photocatalytic or antibacterial properties, could further enhance membrane versatility in treating complex oily wastewater containing surfactants, dyes, or biological contaminants. Emerging tools such as ML and HTS offer new opportunities to accelerate membrane design and performance optimisation, but remain underutilised. Addressing these issues is crucial for transitioning PCL-based membranes from laboratory research to practical oil/water separation applications.

Bibliography

[1] Liao Y, Loh CH, Tian M, Wang R, Fane AG. Progress in electrospun polymeric nanofibrous membranes for water treatment: fabrication, modification and applications. Prog Polym Sci 2018;77:69-94. https://doi.org/10.1016/j.progpolymsci.2017.10.003.

[2] Barnes CP, Sell SA, Boland ED, Simpson DG, Bowlin GL. Nanofiber technology: designing the next generation of tissue engineering scaffolds. Adv Drug Deliv Rev 2007;59(14):1413-33. https://doi.org/10.1016/j.addr.2007.04.022.

[3] World Health Organization. Standards and recommendations for burns care in mass casualty incidents, https://www.who.int/publications/i/item/9789240100237; 2024 [accessed 25 June 2025].

[4] World Health Organization. Fragility fractures, https://www.who.int/news-room/fact-sheets/detail/fragility-fractures; 2024 [accessed 25 June 2025].

[5] Chouhan D, Dey N, Bhardwaj N, Mandal BB. Emerging and innovative approaches for wound healing and skin regeneration: current status and advances. Biomaterials 2019;216:119267. https://doi.org/10.1016/j.biomaterials.2019.119267.

[6] Zhang L, Graham N, Li GB, Yu WZ. Divergent accumulation of membrane biofouling by slight elevation of nitrogen and phosphorus in drinking water treatment: performances and mechanisms. Water Res 2022;222:118898. https://doi.org/10.1016/j.watres.2022.118898.

[7] Cesur S, Oktar FN, Ekren N, Kilic O, Alkaya DB, Seyhan SA, et al. Preparation and characterization of electrospun polylactic acid/sodium alginate/orange oyster shell composite nanofiber for biomedical application. J Aust Ceram Soc 2020;56(2):533-43. https://doi.org/10.1007/s41779-019-00363-1.

[8] Hanumantharao SN, Rao S. Multi-functional electrospun nanofibers from polymer blends for scaffold tissue engineering. Fibers 2019;7(7):66. https://doi.org/10.3390/fib7070066.

[9] Kahrizi M, Gonzales RR, Kong LX, Matsuyama H, Lu P, Lin JY, et al. Significant roles of substrate properties in forward osmosis membrane performance: A review. Desalination 2022;528:115615. https://doi.org/10.1016/j.desal.2022.115615.

[10] Govindan R, Gu FL, Karthi S, Girija EK. Effect of phosphate glass reinforcement on the mechanical and biological properties of freeze-dried gelatin composite scaffolds for bone tissue engineering applications. Mater Today Commun 2020;22:100765. https://doi.org/10.1016/j.mtcomm.2019.100765.

[11] Pavan Kalyan BG, Kumar L. 3D Printing: Applications in tissue engineering, medical devices, and drug delivery. Aaps Pharmscitech 2022;23:92. https://doi.org/10.1208/s12249-022-02242-8.

[12] Valentine DL, Fisher GB, Bagby SC, Nelson RK, Reddy CM, Sylva SP, et al. Fallout plume of submerged oil from deepwater horizon. Proc Natl Acad Sci U S A 2014;111(45):15906-11. https://doi.org/10.1073/pnas.1414873111.

[13] Joye SB. Deepwater horizon, 5 years on. Science 2015;349(6248):592-3. https://doi.org/10.1126/science.aab4133.

[14] Ge J, Ye YD, Yao HB, Zhu X, Wang X, Wu L, et al. Pumping through porous hydrophobic/oleophilic materials: an alternative technology for oil spill remediation. Angew Chem Int Edit 2014;53(14):3612-6. https://doi.org/10.1002/anie.201310151.

[15] Miguel SP, Figueira DR, Simões D, Ribeiro MP, Coutinho P, Ferreira P, et al. Electrospun polymeric nanofibres as wound dressings: A review. Colloid Surface B 2018;169(1):60-71. https://doi.org/10.1016/j.colsurfb.2018.05.011.

[16] Jiang YC, Jiang L, Huang A, Wang XF, Li Q, Turng LS. Electrospun polycaprolactone/gelatin composites with enhanced cell–matrix interactions as blood vessel endothelial layer scaffolds. Mat Sci Eng C-Mater 2017;71:901-8. https://doi.org/10.1016/j.msec.2016.10.083.

[17] Bazgir M, Zhang W, Zhang XM, Elies J, Saeinasab M, Coates P, et al. Degradation and characterisation of electrospun polycaprolactone (PCL) and poly(lactic-co-glycolic acid) (PLGA) scaffolds for vascular tissue engineering. Materials 2021;14(17):4773. https://doi.org/10.3390/ma14174773.

[18] Peng SJ, Jin GR, Li LL, Li K, Srinivasan M, Ramakrishna S, et al. Multi-functional electrospun nanofibres for advances in tissue regeneration, energy conversion & storage, and water treatment. Chem Soc Rev 2016;45(5):1225-41. https://doi.org/10.1039/C5CS00777A.

[19] Rezaei V, Mirzaei E, Taghizadeh SM, Berenjian A, Ebrahiminezhad A. Nano iron oxide-PCL composite as an improved soft tissue scaffold. Processes 2021;9(9):1559. https://doi.org/10.3390/pr9091559.

[20] Kim H, Hwangbo H, Koo YW, Kim GH. Fabrication of mechanically reinforced gelatin/hydroxyapatite bio-composite scaffolds by core/shell nozzle printing for bone tissue engineering. Int J Mol Sci 2020;21(9):3401. https://doi.org/10.3390/ijms21093401.

[21] Ho CMB, Mishra A, Lin PTP, Ng SH, Yeong WY, Kim YJ, et al. 3D printed polycaprolactone carbon nanotube composite scaffolds for cardiac tissue engineering. Macromol Biosci 2017;17(4):1600250. https://doi.org/10.1002/mabi.201600250.

[22] Meng D, Hou YH, Kurniawan D, Weng RJ, Chiang WH, Wang WG. 3D-printed graphene and graphene quantum dot-reinforced polycaprolactone scaffolds for bone-tissue engineering. Acs Appl Nano Mater 2024;7(1):1245-56. https://doi.org/10.1021/acsanm.3c05225.

[23] Arunagiri V, Prasannan A, Udomsin J, Lai JY, Wang CF, Hong PD, et al. Facile fabrication of eco-friendly polycaprolactone (PCL)/Poly-D, L-Lactic acid (PDLLA) modified melamine sorbent for oil-spill cleaning and water/oil (W/O) emulsion separation. Sep Purif Technol 2021;259:118081. https://doi.org/10.1016/j.seppur.2020.118081.

[24] Han G, Oh SJ, Yeo SJ, Lee JK, Lim H. Eco-friendly polycaprolactone-bound diatomite filter for the removal of metal ions and micro/nanoplastics from water. Sci Total Environ 2023;905:166956. https://doi.org/10.1016/j.scitotenv.2023.166956.

[25] Liao Y, Loh CH, Tian M, Wang R, Fane AG. Progress in electrospun polymeric nanofibrous membranes for water treatment: Fabrication, modification and applications. Prog Polym Sci 2018;77: 69-94. https://doi.org/10.1016/j.progpolymsci.2017.10.003.

[26] Ntrivala MA, Pitsavas AC, Lazaridou K, Baziakou Z, Karavasili D, Papadimitriou M, et al. Polycaprolactone (PCL): the biodegradable polyester shaping the future of materials – a review on synthesis, properties, biodegradation, applications and future perspectives. Eur Polym J 2025;234:114033. https://doi.org/10.1016/j.eurpolymj.2025.114033.

[27] Azari A, Golchin A, Mahmoodinia Maymand M, Mansouri F, Ardeshirylajimi A. Electrospun polycaprolactone nanofibers: Current research and applications in biomedical application. Adv Pharm Bull. 2022;12(4):658-672. https://doi.org/10.34172/apb.2022.070.

[28] Eskandarinia A, Kefayat A, Agheb M, Rafienia M, Amini Baghbadorani M, Navid S, et al. A novel bilayer wound dressing composed of a dense polyurethane/propolis membrane and a biodegradable polycaprolactone/gelatin nanofibrous scaffold. Sci Rep 2020;10(1):3063. https://doi.org/10.1038/s41598-020-59931-2.

[29] Zhang GH, Wang PP, Zhang XX, Xiang CH, Li LL. Preparation of hierarchically structured PCL superhydrophobic membrane via alternate electrospinning/electrospraying techniques. J Polym Sci B Polym Phys 2019;57(8):421-30. https://doi.org/10.1002/polb.24795.

[30] Allaf RM, Futian M. Solid-state blending for the preparation of porous eco-friendly PCL membranes: Potential for filtration applications. J Plast Film Sheeting 2023;39(4):375-98. https://doi.org/10.1177/87560879231186427.

[31] Saleh HM, Albukhaty S, Sulaiman GM, Abomughaid MM. Design, preparation, and characterization of polycaprolactone–chitosan nanofibers via electrospinning techniques for efficient methylene blue removal from aqueous solutions. J Compos Sci 2024;8(2):68. https://doi.org/10.3390/jcs8020068.

[32] Naghibzadeh M, Adabi M, Rahmani HR, Mirali M, Adabi M. Evaluation of the effective forcespinning parameters controlling polyvinyl alcohol nanofibers diameter using artificial neural network. Adv Polym Technol 2018;37(6):1608-17. https://10.1002/adv.21817.

[33] Schindelin J, Arganda-Carreras I, Frise E, Kaynig V, Longair M, Pietzsch T, et al. Fiji: an open-source platform for biological-image analysis. Nat Methods 2012;9(7):676-82. https://10.1038/nmeth.2019.

[34] Stanger JJ, Tucker N, Buunk N, Truong YB. A comparison of automated and manual techniques for measurement of electrospun fibre diameter. Polym Test 2014;40:4-12. https://10.1016/j.polymertesting.2014.08.002.

[35] Hotaling NA, Bharti K, Kriel H, Simon CGJ. DiameterJ: a validated open source nanofiber diameter measurement tool. Biomaterials 2015;61:327-38. https://10.1016/j.biomaterials.2015.05.015.

[36] Murphy R, Turcott A, Banuelos L, Dowey E, Goodwin B, Cardinal KO. SIMPoly: a matlab-based image analysis tool to measure electrospun polymer scaffold fiber diameter. Tissue Eng Part C Methods 2020;26(12):628-36. https://10.1089/ten.TEC.2020.0304.

[37] Götz A, Senz V, Schmidt W, Huling J, Grabow N, Illner S. General image fiber tool: a concept for automated evaluation of fiber diameters in SEM images. Measurement 2021;177:109265. https://10.1016/j.measurement.2021.109265.

[38] Zhou HL, Shi ZR, Wan X, Fang HL, Yu DG, Chen XH, et al. The relationships between process parameters and polymeric nanofibers fabricated using a modified coaxial electrospinning. Nanomaterials 2019;9(6):843. https://10.3390/nano9060843.

[39] Chomachayi MD, Solouk A, Mirzadeh H. Electrospun silk-based nanofibrous scaffolds: fiber diameter and oxygen transfer. Prog Biomater 2016;5:71-80. https://10.1007/s40204-016-0046-6.

[40] Vatankhah E, Semnani D, Prabhakaran MP, Tadayon M, Razavi S, Ramakrishna S. Artificial neural network for modeling the elastic modulus of electrospun polycaprolactone/gelatin scaffolds. Acta Biomater 2014;10(2):709-21. https://10.1016/j.actbio.2013.09.015.

[41] Wang FJ, Elbadawi M, Tsilova SL, Gaisford S, Basit AW, Parhizkar M. Machine learning to empower electrohydrodynamic processing. Mater Sci Eng C Mater Biol Appl 2022;132:112553. https://10.1016/j.msec.2021.112553.

[42] Aydogdu MO, Ekren N, Suleymanoglu M, Erdem-Kuruca S, Lin CC, Bulbul E, et al. Novel electrospun polycaprolactone/graphene oxide/Fe_3O_4 nanocomposites for biomedical applications. Colloid Surface B 2018;172:718-27. https://doi.org/10.1016/j.colsurfb.2018.09.035.

[43] Ramos DM, Abdulmalik S, Arul MR, Rudraiah S, Laurencin CT, Mazzocca AD, et al. Insulin immobilized PCL-cellulose acetate micro-nanostructured fibrous scaffolds for tendon tissue engineering. Polym Advan Technol 2019;30(5):1205-15. https://doi.org/10.1002/pat.4553.

[44] Sawadkar P, Mohanakrishnan J, Rajasekar P, Rahmani B, Kohli N, Bozec L, et al. A synergistic relationship between polycaprolactone and natural polymers enhances the physical properties and biological activity of scaffolds. Acs Appl Mater Inter 2020;12(12):13587-97. https://doi.org/10.1021/acsami.9b19715.

[45] Yoshida M, Turner PR, Ali MA, Cabral JD. Three-dimensional melt-electrowritten polycaprolactone/chitosan scaffolds enhance mesenchymal stem cell behavior. Acs Appl Bio Mater 2021;4(2):1319-29. https://doi.org/10.1021/acsabm.0c01213.

[46] Shahverdi M, Seifi S, Akbari A, Mohammadi K, Shamloo A, Movahhedy MR. Melt electrowriting of PLA, PCL, and composite PLA/PCL scaffolds for tissue engineering application. Sci Rep 2022;12:19935. https://doi.org/10.1038/s41598-022-24275-6.

[47] Ghalia MA, Alhanish A. Mechanical and biodegradability of porous PCL/PEG copolymer-reinforced cellulose nanofibers for soft tissue engineering applications. Med Eng Phys 2023;120:104055. https://doi.org/10.1016/j.medengphy.2023.104055.

[48] Manhas N, Balasubramanian K, Prajith P, Rule P, Nimje S. PCL/PVA nanoencapsulated reinforcing fillers of steam exploded/autoclaved cellulose nanofibrils for tissue engineering applications. RSC Adv 2015;5:23999-24008. https://doi.org/10.1039/C4RA17191H.

[49] Bhattarai DP, Aguilar LE, Park CH, Kim CS. A review on properties of natural and synthetic based electrospun fibrous materials for bone tissue engineering. Membranes 2018;8(3):62. https://doi.org/10.3390/membranes8030062.

[50] Gharibshahian M, Salehi M, Beheshtizadeh N, Kamalabadi-Farahani M, Atashi A, Nourbakhsh MS, et al. Recent advances on 3D-printed PCL-based composite scaffolds for bone tissue engineering. Front Bioeng Biotechnol 2023;11:1168504. https://doi.org/10.3389/fbioe.2023.1168504.

[51] Fereshteh Z. 7 - Freeze-drying technologies for 3D scaffold engineering. In: Deng Y, Kuiper J, editors. Functional 3D tissue engineering scaffolds, Oxford: Woodhead Publishing; 2018, pp. 151-74.

[52] Zeinali R, del Valle LJ, Torras J, Puiggali J. Recent progress on biodegradable tissue engineering scaffolds prepared by thermally-induced phase separation (TIPS). Int J Mol Sci 2021;22(7):3504. https://doi.org/10.3390/ijms22073504.

[53] Xue JJ, Wu T, Dai YQ, Xia YN. Electrospinning and electrospun nanofibers: Methods, materials, and applications. Chem Rev 2019;119(8):5298-415. https://doi.org/10.1021/acs.chemrev.8b00593.

[54] Gao HC, Yang YQ, Akampumuza O, Hou J, Zhang HN, Qin XH. A low filtration resistance three-dimensional composite membrane fabricated via free surface electrospinning for

effective $PM_{2.5}$ capture. Environ Sci-Nano 2017;4:864-75. https://doi.org/10.1039/C6EN00696E.

[55] Surucu S, Turkoglu Sasmazel H. Development of core-shell coaxially electrospun composite PCL/chitosan scaffolds. Int J Biol Macromol 2016;92:321-8. https://doi.org/10.1016/j.ijbiomac.2016.07.013.

[56] Hassanajili S, Karami-Pour A, Oryan A, Talaei-Khozani T. Preparation and characterization of PLA/PCL/HA composite scaffolds using indirect 3D printing for bone tissue engineering. Mat Sci Eng C-Mater 2019;104:109960. https://doi.org/10.1016/j.msec.2019.109960.

[57] Chung JJ, Im H, Kim SH, Park JW, Jung YM. Toward biomimetic scaffolds for tissue engineering: 3D printing techniques in regenerative medicine. Front Bioeng Biotechnol 2020;8:586406. https://doi.org/10.3389/fbioe.2020.586406.

[58] Vyas C, Zhang J, Øvrebø Ø, Huang BY, Roberts I, Setty M, et al. 3D printing of silk microparticle reinforced polycaprolactone scaffolds for tissue engineering applications. Mat Sci Eng C-Mater 2021;118:111433. https://doi.org/10.1016/j.msec.2020.111433.

[59] Mader M, Jérôme V, Freitag R, Agarwal S, Greiner A. Ultraporous, compressible, wettable polylactide/polycaprolactone sponges for tissue engineering. Biomacromolecules 2018;19(5):1663-73. https://doi.org/10.1021/acs.biomac.8b00434.

[60] Zhang WC, Ullah I, Shi L, Zhang Y, Ou H, Zhou JG, et al. Fabrication and characterization of porous polycaprolactone scaffold via extrusion-based cryogenic 3D printing for tissue engineering. Mater Design 2019;180:107946. https://doi.org/10.1016/j.matdes.2019.107946.

[61] Jing X, Mi HY, Cordie T, Salick M, Peng XF, Turng LS. Fabrication of porous poly(ε-caprolactone) scaffolds containing chitosan nanofibers by combining extrusion foaming, leaching, and freeze-drying methods. Ind Eng Chem Res 2014;53(46):17909-18. https://doi.org/10.1021/ie5034073.

[62] Tüzün-Antepli B, Elçin AE, Elçin YM. Construction of micro-grooved PCL/nanohydroxyapatite membranes by non-solvent induced phase separation method and its evaluation for use as a substrate for human periodontal ligament fibroblasts. Chem Eng Sci 2022;248:117120. https://doi.org/10.1016/j.ces.2021.117120.

[63] Kim SI, Kim NE, Park SJ, Choi JH, Lee YH, Jeon G, et al. Characterization of non-solvent- and thermal-induced phase separation applied polycaprolactone/demineralized bone matrix scaffold for bone tissue engineering. In Vitro Models 2022;1:197-207. https://doi.org/10.1007/s44164-022-00018-9.

[64] Bouyer D. Chapter 3 - Polymeric membranes prepared by vapor-induced phase separation process (VIPS). In: Tavajohi N, Khayet M, editors. Polymeric membrane formation by phase inversion, Amsterdam: Elsevier; 2024. pp. 83-123.

[65] Pervin R, Ghosh P, Basavaraj MG. Tailoring pore distribution in polymer films via evaporation induced phase separation. RSC Adv 2019;9:15593-605. https://doi.org/10.1039/C9RA01331H.

[66] Huang HY, Fan FY, Shen YK, Wang CH, Huang YZ, Chern MJ, et al. 3D poly-ε-caprolactone/graphene porous scaffolds for bone tissue engineering. Colloid Surface A 2020;606:125393. https://doi.org/10.1016/j.colsurfa.2020.125393.

[67] Matson T, Gootee J, Snider C, Brockman J, Grant D, Grant SA. Electrospun PCL, gold nanoparticles, and soy lecithin composite material for tissue engineering applications. J Biomater Appl 2018;33(7):979-88. https://doi.org/10.1177/0885328218815807.

[68] Joshi MK, Tiwari AP, Pant HR, Shrestha BK, Kim HJ, Park CH, et al. In situ generation of

cellulose nanocrystals in polycaprolactone nanofibers: Effects on crystallinity, mechanical strength, biocompatibility, and biomimetic mineralization. Acs Appl Mater Inter 2015;7(35):19672-83. https://doi.org/10.1021/acsami.5b04682.

[69] Coverdale BDM, Gough JE, Sampson WW, Hoyland JA. Use of lecithin to control fiber morphology in electrospun poly (ε-caprolactone) scaffolds for improved tissue engineering applications. J Biomed Mater Res A 2017;105(10):2865-74. https://doi.org/10.1002/jbm.a.36139.

[70] Patel DK, Seo YR, Dutta SD, Lim KT. Enhanced osteogenesis of mesenchymal stem cells on electrospun cellulose nanocrystals/poly(ε-caprolactone) nanofibers on graphene oxide substrates. RSC Adv 2019;9:36040-9. https://doi.org/10.1039/C9RA06260B.

[71] Qi HF, Ye ZH, Ren HL, Chen NN, Zeng QY, Wu XL, et al. Bioactivity assessment of PLLA/PCL/HAP electrospun nanofibrous scaffolds for bone tissue engineering. Life Sci 2016;148:139-44. https://doi.org/10.1016/j.lfs.2016.02.040.

[72] Heydari Z, Mohebbi-Kalhori D, Afarani MS. Engineered electrospun polycaprolactone (PCL)/octacalcium phosphate (OCP) scaffold for bone tissue engineering. Mat Sci Eng C-Mater 2017;81:127-32. https://doi.org/10.1016/j.msec.2017.07.041.

[73] Felice B, Sánchez MA, Socci MC, Sappia LD, Gómezc MI, Cruz MK, et al. Controlled degradability of PCL-ZnO nanofibrous scaffolds for bone tissue engineering and their antibacterial activity. Mat Sci Eng C-Mater 2018;93:724-38. https://doi.org/10.1016/j.msec.2018.08.009.

[74] Tohidlou H, Shafiei SS, Abbasi S, Asadi-Eydivand M, Fathi-Roudsari M. Amine-functionalized single-walled carbon nanotube/polycaprolactone electrospun scaffold for bone tissue engineering: in vitro study. Fiber Polym 2019;20:1869-82. https://doi.org/10.1007/s12221-019-1262-1.

[75] Maharjan B, Kaliannagounder VK, Jang SR, Awasthi GP, Bhattarai DP, Choukrani G, et al. In-situ polymerized polypyrrole nanoparticles immobilized poly(ε-caprolactone) electrospun conductive scaffolds for bone tissue engineering. Mat Sci Eng C-Mater 2020;114:111056. https://doi.org/10.1016/j.msec.2020.111056.

[76] Suryavanshi A, Khanna K, Sindhu KR, Bellare J, Srivastava R. Magnesium oxide nanoparticle-loaded polycaprolactone composite electrospun fiber scaffolds for bone–soft tissue engineering applications: in-vitro and in-vivo evaluation. Biomed Mater 2017;12:55011. https://doi.org/10.1088/1748-605X/aa792b.

[77] Jiao ZW, Luo B, Xiang SY, Ma HP, Yu Y, Yang WM. 3D printing of HA / PCL composite tissue engineering scaffolds. Adv Ind Eng Poly Res 2019;2(4):196-202. https://doi.org/10.1016/j.aiepr.2019.09.003.

[78] Moghaddaszadeh A, Seddiqi H, Najmoddin N, Ravasjani SA, Klein-Nulend J. Biomimetic 3D-printed PCL scaffold containing a high concentration carbonated-nanohydroxyapatite with immobilized-collagen for bone tissue engineering: enhanced bioactivity and physicomechanical characteristics. Biomed Mater 2021;16:065029. https://doi.org/10.1088/1748-605X/ac3147.

[79] Liu DH, Nie W, Li DJ, Wang WZ, Zheng LX, Zhang JT, et al. 3D printed PCL/SrHA scaffold for enhanced bone regeneration. Chem Eng J 2019;362:269-79. https://doi.org/10.1016/j.cej.2019.01.015.

[80] Lin YH, Chiu YC, Shen YF, Wu YHA, Shie MY. Bioactive calcium silicate/poly-ε-

caprolactone composite scaffolds 3D printed under mild conditions for bone tissue engineering. J Mater Sci: Mater Med 2018;29:11. https://doi.org/10.1007/s10856-017-6020-6.

[81] Dong QS, Zhang M, Zhou XX, Shao Y, Li JY, Wang LM, et al. 3D-printed Mg-incorporated PCL-based scaffolds: A promising approach for bone healing. Mat Sci Eng C-Mater 2021;129:112372. https://doi.org/10.1016/j.msec.2021.112372.

[82] Yu YX, Hua S, Yang MK, Fu ZZ, Teng SS, Niu KR, et al. Fabrication and characterization of electrospinning/3D printing bone tissue engineering scaffold. RSC Adv 2016;6:110557-65. https://doi.org/10.1039/C6RA17718B.

[83] Cakmak AM, Unal S, Sahin A, Oktar FN, Sengor M, Ekren N, et al. 3D printed polycaprolactone/gelatin/bacterial cellulose/hydroxyapatite composite scaffold for bone tissue engineering. Polymers 2020;12(9):1962. https://doi.org/10.3390/polym12091962.

[84] Patrício T, Domingos M, Gloria A, Bártolo P. Characterisation of PCL and PCL/PLA scaffolds for tissue engineering. Procedia CIRP 2013;5:110-4. https://doi.org/10.1016/j.procir.2013.01.022.

[85] Park SA, Lee SJ, Seok JM, Lee JH, Kim WD, Kwon IK. Fabrication of 3D printed PCL/PEG polyblend scaffold using rapid prototyping system for bone tissue engineering application. J Bionic Eng 2018;15:435-42. https://doi.org/10.1007/s42235-018-0034-8.

[86] Park SA, Lee SH, Kim WD. Fabrication of porous polycaprolactone/hydroxyapatite (PCL/HA) blend scaffolds using a 3D plotting system for bone tissue engineering. Bioproc Biosyst Eng 2011;34:505-13. https://doi.org/10.1007/s00449-010-0499-2.

[87] Wang WG, Junior JRP, Nalesso PRL, Musson D, Cornish J, Mendonca F, et al. Engineered 3D printed poly(ε-caprolactone)/graphene scaffolds for bone tissue engineering. Mat Sci Eng C-Mater 2019;100:759-70. https://doi.org/10.1016/j.msec.2019.03.047.

[88] Radhakrishnan S, Nagarajan S, Belaid H, Farha C, Iatsunskyi I, Coy E, et al. Fabrication of 3D printed antimicrobial polycaprolactone scaffolds for tissue engineering applications. Mat Sci Eng C-Mater 2021;118:111525. https://doi.org/10.1016/j.msec.2020.111525.

[89] Wibowo A, Vyas C, Cooper G, Qulub F, Suratman R, Mahyuddin AI, et al. 3D printing of polycaprolactone-polyaniline electroactive scaffolds for bone tissue engineering. Materials 2020;13(3):512. https://doi.org/10.3390/ma13030512.

[90] Li Y, Li Q, Li HM, Xu X, Fu XM, Pan JJ, et al. An effective dual-factor modified 3D-printed PCL scaffold for bone defect repair. J Biomed Mater Res B 2020;108B:2167-79. https://doi.org/10.1002/jbm.b.34555.

[91] Safari B, Aghanejad A, Kadkhoda J, Aghazade M, Roshangar L, Davaran S. Biofunctional phosphorylated magnetic scaffold for bone tissue engineering. Colloid Surface B 2022;211:112284. https://doi.org/10.1016/j.colsurfb.2021.112284.

[92] Ehterami A, Abbaszadeh-Goudarzi G, Haghi-Daredeh S, Niyakan M, Alizadeh M, Jafarisani M, et al. Bone tissue engineering using 3-D polycaprolactone/gelatin nanofibrous scaffold containing berberine: In vivo and in vitro study. Polym Advan Technol 2022;33(2):672-81. https://doi.org/10.1002/pat.5549.

[93] Malikmammadov E, Tanir TE, Kiziltay A, Hasirci N. Preparation and characterization of poly(ε-caprolactone) scaffolds modified with cell-loaded fibrin gel. Int J Biol Macromol 2019;125:683-9. https://doi.org/10.1016/j.ijbiomac.2018.12.036.

[94] Mahdipour Ganji S, Tehranchi M, Ehterami A, Semyari H, Taleghani F, Habibzadeh M, et al. Bone tissue engineering via application of a PCL/Gelatin/Nanoclay/Hesperetin 3D

nanocomposite scaffold. J Drug Deliv Sci Tec 2022;76:103704. https://doi.org/10.1016/j.jddst.2022.103704.

[95] Wu F, Wei J, Liu CS, O'Neill B, Ngothai Y. Fabrication and properties of porous scaffold of zein/PCL biocomposite for bone tissue engineering. Compos Part B-Eng 2012;43(5):2192-7. https://doi.org/10.1016/j.compositesb.2012.02.040.

[96] Taherkhani S, Moztarzadeh F. Fabrication of a poly(ε-caprolactone)/starch nanocomposite scaffold with a solvent-casting/salt-leaching technique for bone tissue engineering applications. J Appl Polym Sci 2016;133(23):43523. https://doi.org/10.1002/app.43523.

[97] Song Y, Choi JH, Tumursukh NE, Kim NE, Jeon GY, Kim SE, et al. Macro- and microporous polycaprolactone/duck's feet collagen scaffold fabricated by combining facile phase separation and particulate leaching techniques to enhance osteogenesis for bone tissue engineering. J Biomat Sci-Polym E 2022;33(8):1025-42. https://doi.org/10.1080/09205063.2022.2036933.

[98] Thi Hiep N, Chan Khon H, Dai Hai N, Byong-Taek L, Van Toi V, Thanh Hung L. Biocompatibility of PCL/PLGA-BCP porous scaffold for bone tissue engineering applications. J Biomat Sci-Polym E 2017;28(9):864-78. https://doi.org/10.1080/09205063.2017.1311821.

[99] Nahanmoghadam A, Asemani M, Goodarzi V, Ebrahimi-Barough S. Design and fabrication of bone tissue scaffolds based on PCL/PHBV containing hydroxyapatite nanoparticles: dual-leaching technique. J Biomed Mater Res 2021;109:981–93. https://doi.org/10.1002/jbm.a.37087.

[100] Dziadek M, Pawlik J, Menaszek E, Stodolak-Zych E, Cholewa-Kowalska K. Effect of the preparation methods on architecture, crystallinity, hydrolytic degradation, bioactivity, and biocompatibility of PCL/bioglass composite scaffolds. J Biomed Mater Res B 2015;103(8):1580-93. https://doi.org/10.1002/jbm.b.33350.

[101] Yang DL, Faraz F, Wang JX, Radacsi N. Combination of 3D printing and electrospinning techniques for biofabrication. Adv Mater Technol 2022;7(7):2101309. https://doi.org/10.1002/admt.202101309.

[102] Feng YQ, Jupei Z, Dong ZH, Tang L. Characterization, biocompatibility, and optimization of electrospun SF/PCL composite nanofiber films. Rev Adv Mater Sci 2023;62(1):20220333. https://doi.org/10.1515/rams-2022-0333.

[103] Chandika P, Oh GW, Heo SY, Kim SC, Kim TH, Kim MS, et al. Electrospun porous bilayer nano-fibrous fish collagen/PCL bio-composite scaffolds with covalently cross-linked chitooligosaccharides for full-thickness wound-healing applications. Mat Sci Eng C-Mater 2021;121:111871. https://doi.org/10.1016/j.msec.2021.111871.

[104] Rashtchian M, Hivechi A, Bahrami SH, Milan PB, Simorgh S. Fabricating alginate/poly(caprolactone) nanofibers with enhanced bio-mechanical properties via cellulose nanocrystal incorporation. Carbohyd Polym 2020;233:115873. https://doi.org/10.1016/j.carbpol.2020.115873.

[105] Sadeghianmaryan A, Karimi Y, Naghieh S, Alizadeh Sardroud H, Gorji M, Chen XB. Electrospinning of scaffolds from the polycaprolactone/polyurethane composite with graphene oxide for skin tissue engineering. Appl Biochem Biotech 2020;191:567-78. https://doi.org/10.1007/s12010-019-03192-x.

[106] Unalan I, Slavik B, Buettner A, Goldmann WH, Frank G, Boccaccini AR. Physical and antibacterial properties of peppermint essential oil loaded poly (ε-caprolactone) (PCL) electrospun fiber mats for wound healing. Front Bioeng Biotechnol 2019;7:346.

https://doi.org/10.3389/fbioe.2019.00346.
[107] Rad ZP, Mokhtari J, Abbasi M. *Calendula officinalis* extract/PCL/Zein/Gum arabic nanofibrous bio-composite scaffolds via suspension, two-nozzle and multilayer electrospinning for skin tissue engineering. Int J Biol Macromol 2019;135:530-43. https://doi.org/10.1016/j.ijbiomac.2019.05.204.
[108] Baghersad S, Hivechi A, Bahrami SH, Milan PB, Siegel RA, Amoupour M. Optimal Aloe vera encapsulated PCL/Gel nanofiber design for skin substitute application and the evaluation of its in vivo implantation. J Drug Deliv Sci Tec 2022;74:103536. https://doi.org/10.1016/j.jddst.2022.103536.
[109] Sharahi M, Hivechi A, Bahrami SH, Hemmatinejad N, Milan PB. Co-electrospinning of lignocellulosic nanoparticles synthesized from walnut shells with poly(caprolactone) and gelatin for tissue engineering applications. Cellulose 2021;28:4943–57. https://doi.org/10.1007/s10570-021-03709-w.
[110] Rahmani Del Bakhshayesh A, Mostafavi E, Alizadeh E, Asadi N, Akbarzadeh A, Davaran S. Fabrication of three-dimensional scaffolds based on nano-biomimetic collagen hybrid constructs for skin tissue engineering. Acs Omega 2018;3(8):8605-11. https://doi.org/10.1021/acsomega.8b01219.
[111] Fereshteh Z, Fathi M, Bagri A, Boccaccini AR. Preparation and characterization of aligned porous PCL/zein scaffolds as drug delivery systems via improved unidirectional freeze-drying method. Mat Sci Eng C-Mater 2016;68:613-22. https://doi.org/10.1016/j.msec.2016.06.009.
[112] Salerno A, Domingo C, Saurina J. PCL foamed scaffolds loaded with 5-fluorouracil anti-cancer drug prepared by an eco-friendly route. Mat Sci Eng C-Mater 2017;75:1191-7. https://doi.org/10.1016/j.msec.2017.03.011.
[113] Hakim RS, Maghsoud Z, Halabian R. Fabrication and evaluation of polycaprolactone/olive oil scaffolds by phase inversion for tissue engineering. Eur Polym J 2021;150:110394. https://doi.org/10.1016/j.eurpolymj.2021.110394.
[114] Wu YY, Ding XT, Wang YW, Ouyang DF. Harnessing the power of machine learning into tissue engineering: current progress and future prospects. Burns Trauma 2024;12:tkae053. https://doi.org/10.1093/burnst/tkae053.
[115] Foroughi AH, Valeri C, Razavi MJ. A review of computational optimization of bone scaffold architecture: methods, challenges, and perspectives. Prog Biomed Eng 2025;7:012003. https://doi.org/10.1088/2516-1091/ad879a.
[116] Al-Kharusi G, Dunne NJ, Little S, Levingstone TJ. The role of machine learning and design of experiments in the advancement of biomaterial and tissue engineering research. Bioengineering 2022;9(10):561. https://doi.org/10.3390/bioengineering9100561.
[117] Bagherpour R, Bagherpour G, Mohammadi P. Application of artificial intelligence in tissue engineering. Tissue Eng Part B Rev 2025;31(1):31-43. https://doi.org/10.1089/ten.teb.2024.0022.
[118] Guo JL, Januszyk M, Longaker MT. Machine learning in tissue engineering. Tissue Eng Part A 2023;29(1-2):2-19. https://doi.org/10.1089/ten.tea.2022.0128.
[119] Shi QS, Song F, Zhou XC, Chen XY, Cao JQ, Na J, et al. Early predicting osteogenic differentiation of mesenchymal stem cells based on deep learning within one day. Ann Biomed Eng 2024;52(6):1706-18. https://doi.org/10.1007/s10439-024-03483-3.
[120] Zhang C, Li YS, Jiang B, Wang RG, Liu YL, Jia LY. Mechanical properties prediction of

composite laminate with FEA and machine learning coupled method. Compos Struct 2022;299:116086. https://doi.org/10.1016/j.compstruct.2022.116086.

[121] Omigbodun FT, Oladapo BI. AI-optimized lattice structures for biomechanics scaffold design. Biomimetics 2025;10(2):88. https://doi.org/10.3390/biomimetics10020088.

[122] Hernandez Korner ME, Lamban MP, Albajez JA, Santolaria J, Ng Corrales LC, Royo J. Cost model framework for pieces additively manufactured in fused deposition modeling for low to medium batches. 3D Print Addit Manuf 2024;11(1):287-98. https://doi.org/10.1089/3dp.2022.0044.

[123] Yang Q, Chen L, Shen XY, Tan ZQ. Preparation of polycaprolactone tissue engineering scaffolds by improved solvent casting/particulate leaching method. J Macromol Sci B 2006;45(6):1171-81. https://doi.org/10.1080/00222340600976783.

[124] Dong XB, Lu D, Harris TAL, Escobar IC. Polymers and solvents used in membrane fabrication: A review focusing on sustainable membrane development. Membranes 2021;11(5):309. https://doi.org/10.3390/membranes11050309.

[125] Zhu JY, Hou JW, Zhang YT, Tian MM, He T, Liu JD, et al. Polymeric antimicrobial membranes enabled by nanomaterials for water treatment. J Membr Sci 2018;550:173-97. https://doi.org/10.1016/j.memsci.2017.12.071.

[126] Rajapaksha PP, Power A, Chandra S, Chapman J. Graphene, electrospun membranes and granular activated carbon for eliminating heavy metals, pesticides and bacteria in water and wastewater treatment processes. Analyst 2018;143(23):5629-45. https://doi.org/10.1039/C8AN00922H.

[127] Marković D, Milovanović S, Radovanović Ž, Zizovic I, Šaponjić Z, Radetić M. Floating photocatalyst based on poly(ε-caprolactone) foam and TiO_2 nanoparticles for removal of textile dyes. Fiber Polym 2018;19(6):1219-27. https://doi.org/10.1007/s12221-018-8148-5.

[128] Agarwal S, Greiner A, Wendorff JH. Functional materials by electrospinning of polymers. Prog Polym Sci 2013;38(6):963-91. https://doi.org/10.1016/j.progpolymsci.2013.02.001.

[129] Hu MY, Chiao YH, Fu WM, Zhang PF, Fang S, Guan KC, et al. One-step phase separation and mineralization fabrication of membranes for oily wastewater treatment. ACS Appl Mater Interfaces 2024;16(29):38723-32. https://doi.org/10.1021/acsami.4c07067.

[130] Tijing LD, Dizon JRC, Ibrahim I, Nisay ARN, Shon HK, Advincula RC. 3D printing for membrane separation, desalination and water treatment. Appl Mater Today 2020;18:100486. https://doi.org/10.1016/j.apmt.2019.100486.

[131] Han L, Shen LG, Lin HJ, Huang ZY, Xu YC, Li RJ, et al. 3D printing titanium dioxide-acrylonitrile-butadiene-styrene (TiO_2-ABS) composite membrane for efficient oil/water separation. Chemosphere 2023;315:137791. https://doi.org/10.1016/j.chemosphere.2023.137791.

[132] Wu BL, Lo IMC. Surface functional group engineering of CeO_2 particles for enhanced phosphate adsorption. Environ Sci Technol 2020;54(7):4601-8. https://doi.org/10.1021/acs.est.9b06812.

[133] Zhang J, Wang Y, Yu J, Wang QY, Khattak KN, Yang XP. Determination of pyrethroids in water samples by dispersive solid-phase extraction coupled with high-performance liquid chromatography. Water Environ Res 2022;94(11):e10813. https://doi.org/10.1002/wer.10813.

[134] Wang QQ, Jia XL, Jin MC, Guo RJ, Niu BL, Yan H, et al. A magnetically recyclable carboxyl-functionalized chitosan composite for efficiently removing methyl orange from wastewater:

Isotherm, kinetics, thermodynamic, and adsorption mechanism. Int J Biol Macromol 2023;253:126631. https://doi.org/10.1016/j.ijbiomac.2023.126631.
[135] Yan H, Wu H, Li K, Wang YW, Tao X, Yang H, et al. Influence of the surface structure of graphene oxide on the adsorption of aromatic organic compounds from water. ACS Appl Mater Interfaces 2015;7(12):6690-7. https://doi.org/10.1021/acsami.5b00053.
[136] Noah NM. Current status and advancement of nanomaterials within polymeric membranes for water purification. ACS Appl Nano Mater 2024;7(16):18610-25. https://doi.org/10.1021/acsanm.3c04110.
[137] Ren J, Liu Z, Guo SJ, Li JF, Cheng FQ. Progresses of hydrophilic/hydrophobic composite membranes in membrane distillation for enhanced treatment of industrial wastewater. Chem Ind Eng Prog 2021;40(11):6347-57. https://doi.org/10.16085/j.issn.1000-6613.2020-2389.
[138] Gao CM, Chen HY, Liu SH, Chen JC, Xing YQ, Ji SF, et al. Bimetallic polyphenol networks structure modified polyethersulfone membrane with hydrophilic and anti-fouling properties based on reverse thermally induced phase separation method. Chemosphere 2022;288:132537. https://doi.org/10.1016/j.chemosphere.2021.132537.
[139] Zhang ML, Yang Y, An XQ, Hou LA. A critical review of g-C_3N_4-based photocatalytic membrane for water purification. Chem Eng J 2021;412:128663. https://doi.org/10.1016/j.cej.2021.128663.
[140] Koe WS, Lee JW, Chong WC, Pang YL, Sim LC. An overview of photocatalytic degradation: photocatalysts, mechanisms, and development of photocatalytic membrane. Environ Sci Pollut Res Int 2020;27(3):2522-65. https://doi.org/10.1007/s11356-019-07193-5.
[141] Ghosh S, Kouamé NA, Ramos L, Remita S, Dazzi A, Deniset-Besseau A, et al. Conducting polymer nanostructures for photocatalysis under visible light. Nat Mater 2015;14(5):505-11. https://doi.org/10.1038/nmat4220.
[142] Wang J, Licciardello N, Sgarzi M, Cuniberti G. Multifunctional polymer-based nanocomposites for synergistic adsorption and photocatalytic degradation of mixed pollutants in water. Nanoscale Adv 2024;6(6):1653-60. https://doi.org/10.1039/D3NA00931A.
[143] Yu YL, Yu YT, Wu HY, Shi J, Morikawa H, Zhu CH. A trimode self-cleaning composite membrane with an eco-friendly substrate for energy-saving wastewater recycling. Adv Fiber Mater 2024;6(5):1495-508. https://doi.org/10.1007/s42765-024-00430-8.
[144] Jiang SC, Liu HC, Zhang X, Ren YJ, Cui XX, Song XF. Synthesis of PCL-branched P(MMA-co-HEMA) to toughen electrospun PLLA fiber membrane. Polym Adv Technol 2018;29(1):442-50. https://doi.org/10.1002/pat.4133.
[145] Li SC, Lee BK. Highly efficient separation of water-in-oil emulsion using electrospun helicoidal polymer strips. Sep Purif Technol 2024;330:125405. https://doi.org/10.1016/j.seppur.2023.125405.
[146] Maio A, Gammino M, Gulino EF, Megna B, Fara P, Scaffaro R. Rapid one-step fabrication of graphene oxide-decorated polycaprolactone three-dimensional templates for water treatment. ACS Appl Polym Mater 2020;2(11):4993-5005. https://doi.org/10.1021/acsapm.0c00852.
[147] Eom J, Kwak Y, Nam C. Electrospinning fabrication of magnetic nanoparticles-embedded polycaprolactone (PCL) sorbent with enhanced sorption capacity and recovery speed for spilled oil removal. Chemosphere 2022;303:135063. https://doi.org/10.1016/j.chemosphere.2022.135063.
[148] He NN, Li LL, Chen JQ, Zhang JH, Liang C. Extraordinary superhydrophobic

polycaprolactone-based composite membrane with an alternated micro-nano hierarchical structure as an eco-friendly oil/water separator. ACS Appl Mater Interfaces 2021;13(20):24117-29. https://doi.org/10.1021/acsami.1c03019.

[149] Pagno V, Módenes AN, Dragunski DC, Fiorentin-Ferrari LD, Caetano J, Guellis C, et al. Heat treatment of polymeric PBAT/PCL membranes containing activated carbon from Brazil nutshell biomass obtained by electrospinning and applied in drug removal. J Environ Chem Eng 2020;8(5):104159. https://doi.org/10.1016/j.jece.2020.104159.

[150] Wang FQ, Liu KX, Xi YN, Li ZX. One-step electrospinning PCL/ph-LPSQ nanofibrous membrane with excellent self-cleaning and oil-water separation performance. Polymer 2022;249:124858. https://doi.org/10.1016/j.polymer.2022.124858.

[151] Li WL, Zong YK, Liu Q, Sun Y, Li ZR, Wang HP, et al. A highly stretchable and biodegradable superamphiphobic fluorinated polycaprolactone nanofibrous membrane for antifouling. Prog Org Coat 2020;147:105776. https://doi.org/10.1016/j.porgcoat.2020.105776.

[152] Zhang XX, Zhao J, Ma L, Shi XJ, Li LL. Biomimetic preparation of a polycaprolactone membrane with a hierarchical structure as a highly efficient oil–water separator. J Mater Chem A 2019;7(42):24532-42. https://doi.org/10.1039/C9TA08660A.

[153] Zhang GH, Wang PP, Zhang XX, Xiang CH, Li LL. The preparation of PCL/MSO/SiO_2 hierarchical superhydrophobic mats for oil-water separation by one-step method. Eur Polym J 2019;116:386-93. https://doi.org/10.1016/j.eurpolymj.2019.04.011.

[154] Li BF, Qi B, Han J, Yang C, Qian XW, Jiao TF. Preparation and separation performance of biomimetic polycaprolactone/graphene oxide composite membrane. Colloid Surface A 2024;693:134088. https://doi.org/10.1016/j.colsurfa.2024.134088.

[155] Nanni F, Lamastra FR, Pisa F, Gusmano G. Synthesis and characterization of poly(ε-caprolactone) reinforced with aligned hybrid electrospun PMMA/nano-Al_2O_3 fibre mats by film stacking. J Mater Sci 2011;46(18):6124-30. https://doi.org/10.1007/s10853-011-5577-6.

[156] Lamastra FR, Puglia D, Monti M, Vella A, Peponi L, Kenny JM, et al. Poly(ε-caprolactone) reinforced with fibres of Poly(methyl methacrylate) loaded with multiwall carbon nanotubes or graphene nanoplatelets. Chem Eng J 2012;195-196:140-8. https://doi.org/10.1016/j.cej.2012.04.078.

[157] Hani A, Haikal RR, El-Mehalmey WA, Safwat Y, Alkordi MH. Durable and recyclable MOF@polycaprolactone mixed-matrix membranes with hierarchical porosity for wastewater treatment. Nanoscale 2023;15(48):19617-28. https://doi.org/10.1039/D3NR04044E.

[158] Hasanin MS, El Fray M, Al-Qabandi OA, Bassyouni M, Almutlaq N, Zhou QH, et al. Tailored biopolymer films based on cellulose acetate and cobalt ferrite nanoparticles: Dye adsorption and antimicrobial activity. Carbohydr Polym Tech 2025;9:100716. https://doi.org/10.1016/j.carpta.2025.100716.

[159] Mizan MMH, Gurave PM, Rastgar M, Rahimpour A, Srivastava RK, Sadrzadeh M. “Biomass to membrane”: sulfonated kraft lignin/PCL superhydrophilic electrospun membrane for gravity-driven oil-in-water emulsion separation. ACS Appl Mater Interfaces 2023;15(35):41961-76. https://doi.org/10.1021/acsami.3c09964.

[160] Panatdasirisuk W, Liao ZW, Vongsetskul T, Yang S. Separation of oil-in-water emulsions using hydrophilic electrospun membranes with anisotropic pores. Langmuir 2017;33(23):5872-8. https://doi.org/10.1021/acs.langmuir.7b01138.

[161] Li BF, Qi B, Han J, Qian XW, Yang C, Cai SM. Separation of oil–water emulsion by

biomimetic polycaprolactone tannic acid hydrophilic modified membranes. Fuel 2025;386:134242. https://doi.org/10.1016/j.fuel.2024.134242.

[162] Doan HN, Vo PP, Baggio A, Negoro M, Kinashi K, Fuse Y, et al. Environmentally friendly chitosan-modified polycaprolactone nanofiber/nanonet membrane for controllable oil/water separation. ACS Appl Polym Mater 2021;3(8):3891-901. https://doi.org/10.1021/acsapm.1c00463.

[163] Palacios Hinestroza H, Urena-Saborio H, Zurita F, Guerrero de Leon AA, Sundaram G, Sulbaran-Rangel B. Nanocellulose and polycaprolactone nanospun composite membranes and their potential for the removal of pollutants from water. Molecules 2020;25(3):683. https://doi.org/10.3390/molecules25030683.

[164] Sadeghi A, Mousavi SM, Saljoughi E, Kiani S. Biodegradable membrane based on polycaprolactone/polybutylene succinate: Characterization and performance evaluation in wastewater treatment. J Appl Polym Sci 2021;138(18):50332. https://doi.org/10.1002/app.50332.

[165] Mizan MMH, Rastgar M, Sultana H, Karami P, Sadrzadeh M. Green polycaprolactone/sulfonated kraft lignin phase inversion membrane for dye/salt separation. J Membr Sci 2024;702:122806. https://doi.org/10.1016/j.memsci.2024.122806.

[166] Manholi S, Athiyanathil S. Poly (ε-caprolactone)-based porous membranes for filtration applications—effect of solvents on precipitation kinetics, performance, and morphology. J Appl Polym Sci 2022;139(10):51720. https://doi.org/10.1002/app.51720.

[167] Nivedita S, Joseph S. Performance of polycaprolactone/TiO_2 composite membrane for the effective treatment of dairy effluents. Water Sci Technol 2021;83(10):2477-85. https://doi.org/10.2166/wst.2021.143.

[168] Sepehri E, Mousavi SM, Saljoughi E, Bahreini M, Doaei M, Kiani S. Enhancing anti-biofouling property by incorporating graphene oxide-silver nanocomposite into polycaprolactone membrane for ultrafiltration application. J Chem Technol Biotechnol 2023;98(10):2517-31. https://doi.org/10.1002/jctb.7478.

[169] Geravand MHA, Saljoughi E, Mousavi SM, Kiani S. Biodegradable polycaprolactone/MXene nanocomposite nanofiltration membranes for the treatment of dye solutions. J Taiwan Inst Chem E 2021;128:124-39. https://doi.org/10.1016/j.jtice.2021.08.048.

[170] Dong YQ, Zhang HS, Liu X, Luo XZ, Wang YQ, Zhang Q. Quaternization and degradation of block copolymer templates for UF and ED membranes via non-solvent induced and solvent evaporation induced phase separation. J Membr Sci 2024;710:123156. https://doi.org/10.1016/j.memsci.2024.123156.

[171] Benhacine F, Lounis FM, Hadj-Hamou AS, Toumi DA, Ferroukhi AC. Polycaprolactone-zinc oxide biocomposite membranes for wastewater treatment by ultrafiltration process: Synthesis, characterization and removal of inorganic pollutants. J Environ Chem Eng 2024;12(6):114698. https://doi.org/10.1016/j.jece.2024.114698.

[172] Benhacine F, Abdellaoui N, Arous O, Hadj-Hamou AS. Behaviours of poly(ε-caprolactone)/silver-montmorillonite nanocomposite in membrane ultrafiltration for wastewater treatment. Environ Technol 2018;41(16):2049-60. https://doi.org/10.1080/09593330.2018.1555283.

[173] Chandran AM, Tayal E, Mural PKS. Polycaprolactone-blended cellulose acetate thin-film composite membrane for dairy waste treatment using forward osmosis. Environ Sci Pollut R

2022;29(57):86418-26. https://doi.org/10.1007/s11356-022-20813-x.

[174] Peng H, Jiang JX, Liu YF, Wang X, Li WW, Zheng GF. Surfaced-modified TiO_2 nanofibers with enhanced photodegradation under visible light. Chem Res Chin Univ 2022;38(6):1475-81. https://doi.org/10.1007/s40242-022-2056-3.

[175] Cordoba A, Guernelli M, Montalti M, Saldías C, Focarete ML, Leiva A. Nanofibers of chitosan-polycaprolactone blends as active support for photocatalytic nanoparticles: Outstanding role of chitosan in the degradation of an organic dye in water. Int J Biol Macromol 2023;253:127111. https://doi.org/10.1016/j.ijbiomac.2023.127111.

[176] Morante N, Viscusi G, Gorrasi G, Monzillo K, Sannino D. Immobilization of solar light-active photocatalyst Cr-TiO_2 into the polyurethane/polycaprolactone electrospun membrane for the photocatalytic oxidation of Acid Orange 7. J Water Process Eng 2025;69:106529. https://doi.org/10.1016/j.jwpe.2024.106529.

[177] Korina E, Stoilova O, Manolova N, Rashkov I. Polymer fibers with magnetic core decorated with titanium dioxide prospective for photocatalytic water treatment. J Environ Chem Eng 2018;6(2):2075-84. https://doi.org/10.1016/j.jece.2018.03.016.

[178] Wang YH, Huang J, Zhang Y, Zhang SW, Li LL, Pang X. The design of PAN-based Janus membrane with adjustable asymmetric wettability in wastewater purification. Materials 2024;17(2):417. https://doi.org/10.3390/ma17020417.

[179] Tu H, Li D, Yi Y, Liu R, Wu Y, Dong XY, et al. Incorporation of rectorite into porous polycaprolactone/TiO_2 nanofibrous mats for enhancing photocatalysis properties towards organic dye pollution. Compos Commun 2019;15:58-63. https://doi.org/10.1016/j.coco.2019.06.006.

[180] Halanur Mruthunjayappa M, Shachar C, Imbar A, Menashe OA, Mamane H. Cellulose acetate and polycaprolactone based photoactive ultrafiltration membrane: A novel approach with UV-switchable photocatalytic activity. Sep Purif Technol 2024;329:125102. https://doi.org/10.1016/j.seppur.2023.125102.

[181] Karthik P, Ravichandran S, Prakash N, Mukkannan A, Rajesh J. Evaluation of ZnO infused CA/PCL nanocomposites using potential wastewater treatment and invitro anticancer activity. Water Cycle 2024;5:121-30. https://doi.org/10.1016/j.watcyc.2024.03.002.

[182] Sasikala V, Karthik P, Ravichandran S, Prakash N, Rajesh J, Mukkannan A. Effective removal of organic dyes using novel $MnWO_4$ incorporated CA/PCL nanocomposite membranes. Surf Interfaces 2023;40:103008. https://doi.org/10.1016/j.surfin.2023.103008.

[183] Jayachitra R, Lincy V, Prasannan A, Jebaranjitham JN, Sangaraju S, Hong PD. Tailored fabrication of biodegradable polymer/ Fe_3O_4 doped WO_3 nano star-based porous membrane with enhanced photo fentonic activity for environmental remediation. Environ Res 2024;248:118262. https://doi.org/10.1016/j.envres.2024.118262.

[184] Yao L, Sun C, Lin H, Li G, Lian Z, Song R, et al. Enhancement of AFB_1 removal efficiency via adsorption/photocatalysis synergy using surface-modified electrospun PCL-g-C_3N_4/CQDs membranes. Biomolecules 2023;13(3):550. https://doi.org/10.3390/biom13030550.

[185] Padmanabhan NT, Sabin C, Unni Krishnan H, Hrithik M, Mythili U, Jayaraj MK, et al. Analysing the efficacy of TiO_2/g-C_3N_4 nanohybrid electrospun membranes for visible-light photocatalytic water purification. Chem Phys Lett 2024;854:141547. https://doi.org/10.1016/j.cplett.2024.141547.

[186] Scaffaro R, Gammino M. 3D wet-electrospun “branch leaf” graphene oxide polycaprolactone

fibers structure for enhancing oil-water separation treatment performance in a multi-scale design. Sustain Mater Technol 2025;43:e01200. https://doi.org/10.1016/j.susmat.2024.e01200.

[187] Ismail N, Essalhi M, Tavajohi N. Chapter 13 - Sustainability in membrane production. In: Tavajohi N, Khayet M, editors. Polymeric Membrane Formation by Phase Inversion. Elsevier; 2024. pp. 421-33. https://doi.org/10.1016/B978-0-323-95628-4.00016-1.

[188] Razali M, Kim JF, Attfield M, Budd PM, Drioli E, Lee YM, et al. Sustainable wastewater treatment and recycling in membrane manufacturing. Green Chem 2015;17(12):5196-205. https://doi.org/10.1039/C5GC01937K.

[189] Bhunia SK, Ushavipinachandran V, Rajendran S. 16 - Degradation of emergent pollutants using visible light-triggered photocatalysts. In: Nayak AK, Sahu NK, editors. Nanostructured Materials for Visible Light Photocatalysis. Elsevier; 2022. pp. 433-65. https://doi.org/10.1016/B978-0-12-823018-3.00004-X.

[190] Johnston BD, Scown TM, Moger J, Cumberland SA, Baalousha M, Linge K, et al. Bioavailability of nanoscale metal oxides TiO_2, CeO_2, and ZnO to fish. Environ Sci Technol 2010;44(3):1144-51. https://doi.org/10.1021/es901971a.

[191] Song YK, Hong SH, Jang M, Han GM, Jung SW, Shim WJ. Combined effects of UV exposure duration and mechanical abrasion on microplastic fragmentation by polymer type. Environ Sci Technol 2017;51(8):4368-76. https://doi.org/10.1021/acs.est.6b06155.

[192] Xie WC, Li T, Tiraferri A, Drioli E, Figoli A, Crittenden JC, et al. Toward the next generation of sustainable membranes from green chemistry principles. ACS Sustainable Chem Eng 2021;9(1):50-75. https://doi.org/10.1021/acssuschemeng.0c07119.

[193] Hoseini S, Zhang GY, Polke D, Surjana A, Wagner L, Schmitz C. "Coatings Intelligence: Data-driven Automation for Chemistry 4.0," 2024 IEEE 7th International Conference on Industrial Cyber-Physical Systems (ICPS), St. Louis, MO, USA, 2024, pp. 1-6. https://doi.org/10.1109/ICPS59941.2024.10640053.

[194] Kazi MK, Varghese S, Sarker N, Aich N, Gadhamshetty V. Advancing PFAS remediation through physics-based modeling of 2D materials: Recent progress, challenges, and opportunities. Ind Eng Chem Res 2025;64(4):1894-906. https://doi.org/10.1021/acs.iecr.4c03715.

[195] Jacobs R, Mayeshiba T, Afflerbach B, Miles L, Williams M, Turner M, et al. The Materials Simulation Toolkit for Machine learning (MAST-ML): An automated open source toolkit to accelerate data-driven materials research. Comp Mater Sci 2020;176:109544. https://doi.org/10.1016/j.commatsci.2020.109544.

[196] Lowe M, Qin RW, Mao XW. A review on machine learning, artificial intelligence, and smart technology in water treatment and monitoring. Water 2022;14(9):1384. https://doi.org/10.3390/w14091384.

[197] Sankar N, Joseph S. Effect of unmodified and modified montmorillonite on the properties of PCL based ultrafiltration membrane for water treatment applications. J Water Process Eng 2018;21:61-8. https://doi.org/10.1016/j.jwpe.2017.12.002.

[198] Gopi S, Kargl R, Kleinschek KS, Pius A, Thomas S. Chitin nanowhisker – inspired electrospun PVDF membrane for enhanced oil-water separation. J Environ Manage 2018;228:249-59. https://doi.org/10.1016/j.jenvman.2018.09.039.

[199] Peidavosi N, Azami M, Beheshtizadeh N, Ramazani Saadatabadi A. Piezoelectric conductive electrospun nanocomposite PCL/polyaniline/barium titanate scaffold for tissue engineering

applications. Sci Rep 2022;12(1):20813-28. https://doi.org/10.1038/s41598-022-25332-w.
[200] Koesdjojo MT, Nammoonnoy J, Wu YY, Frederick RT, Remcho VT. Cost-efficient fabrication techniques for microchips and interconnects enabled by polycaprolactone. J Micromech Microeng 2012;22:115030. http://dx.doi.org/10.1088/0960-1317/22/11/115030.
[201] Shin HS, Lee H, Jun CH, Jung YM, Kim SB. Transition temperatures and molecular structures of poly(methyl methacrylate) thin films by principal component analysis: comparison of isotactic and syndiotactic poly(methyl methacrylate). Vib Spectrosc 2005;37(1):69-76. https://doi.org/10.1016/j.vibspec.2004.06.005.
[202] Du JR, Peldszus S, Huck PM, Feng XS. Modification of membrane surfaces via microswelling for fouling control in drinking water treatment. J Membrane Sci 2015;475:488-95. https://doi.org/10.1016/j.memsci.2014.10.040.
[203] Zamani F, Amani TM, Abbasi A. Fabrication of PCL nanofibrous scaffold with tuned porosity for neural cell culture. Prog Biomater 2021;2:151-60. https://doi.org/10.1016/j.msec.2020.110913.
[204] Mwiiri FK, Daniels R. Influence of PVA molecular weight and concentration on electrospinnability of birch bark extract-loaded nanofibrous scaffolds intended for enhanced wound healing. Molecules 2020;20:4799. https://doi.org/10.3390/molecules25204799.
[205] Zhao Q, Evans CM. Effect of molecular weight on viscosity scaling and ion transport in linear polymerised ionic liquids. Macromolecules 2021;7:3395-404. https://doi.org/10.1021/acs.macromol.0c02801.
[206] Moreira A, Lawson D, Onyekuru L, Dziemidowicz K, Angkawinitwong U, Costa PF, et al. Protein encapsulation by electrospinning and electrospraying. J Controlled Release 2021:329;1172-97. https://doi.org/10.1016/j.jconrel.2020.10.046.
[207] Park BK, Um IC. Effect of molecular weight on electrospinning performance of regenerated silk. Int J Biol Macromol 2018;106:1166-72. https://doi.org/10.1016/j.ijbiomac.2017.08.115.
[208] Fong H, Chun I, Reneker DH. Beaded nanofibers formed during electrospinning. Polymer 1999;40:4585-92. https://doi.org/10.1016/S0032-3861(99)00068-3.
[209] de Gennes PG. Solvent evaporation of spin cast films: “crust” effects. Eur Phys J E 2002;7:31-4. https://doi.org/10.1140/epje/i200101169.
[210] Bancroft WD, Davis HL. Raoult's Law, J Phys Chem 1929;33:361-70. https://doi.org/10.1021/j150297a004.
[211] Samourides A, Browning L, Hearnden V, Chen BQ. The effect of porous structure on the cell proliferation, tissue ingrowth and angiogenic properties of poly(glycerol sebacate urethane) scaffolds. Mater Sci Eng C 2020;108:110384. https://doi.org/10.1016/j.msec.2019.110384.
[212] Reneker DH, Yarin AL. Electrospinning jets and polymer nanofibers. Polymer 2008;49(10): 2387-425. https://doi.org/10.1016/j.polymer.2008.02.002.
[213] Cadafalch GG, Smulders V, Veldhuis SA, Wieringa P, Moroni L, Boukamp BA, et al. Influence of solution properties and process parameters on the formation and morphology of YSZ and NiO ceramic nanofibers by electrospinning. Nanomaterials 2017;7:16. https://doi.org/10.3390/nano7010016.
[214] O'Connor RA, Cahill PA, McGuinness GB. Effect of electrospinning parameters on the mechanical and morphological characteristics of small diameter PCL tissue engineered blood vessel scaffolds having distinct micro and nano fibre populations – A DOE approach. Polym Test 2021;96:107119. https://doi.org/10.1016/j.polymertesting.2021.107119.

[215] Gilarska A, Lewandowska-Lancucka J, Horak W, Nowakowska M. Collagen/chitosan/hyaluronic acid – based injectable hydrogels for tissue engineering applications – design, physicochemical and biological characterization. Colloid Surface B 2018;70:152-62. https://doi.org/10.1016/j.colsurfb.2018.06.004.

[216] Jacobs T, Morent R, Geyter ND, Dubruel P, Leys C. Plasma surface modification of biomedical polymers: Influence on cell-material interaction. Plasma Chem. Plasma Process 2012;32:1039–73. https://doi.org/10.1007/s11090-012-9394-8.

[217] Nam YS, Yoon JJ, Lee JG, Park TG. Adhesion behaviours of hepatocytes cultured onto biodegradable polymer surface modified by alkali hydrolysis process. J Biomat Sci-Polym E 1999;10(11):1145-58. https://doi.org/10.1163/156856299X00801.

[218] Harnett EM, Alderman J, Wood T. The surface energy of various biomaterials coated with adhesion molecules used in cell culture. Colloid Surface B 2007;55:90-7. https://doi.org/10.1016/j.colsurfb.2006.11.021.

[219] Janarthanan G, Kim IG, Chung E, Noh I. Comparative studies on thin polycaprolactone-tricalcium phosphate composite scaffolds and its interaction with mesenchymal stem cells. Biomater Res 2019;23:1. https://doi.org/10.1186/s40824-018-0153-7.

[220] AA Mamun, CX Shao, PW Geng, SH Wang, J Xiao. Recent advances in molecular mechanisms of skin wound healing and its treatments. Front Immunol 2024;15:1395479. https://doi.org/10.3389/fimmu.2024.1395479.

[221] E Bruder, J Hofmeister, C Aslanidis, J Hammer, L Bubendorf, et al. Ultrastructural and molecular analysis in fatal neonatal interstitial pneumonia caused by a novel ABCA3 mutation. Modern Pathol 2007;20:1009-18. https://doi.org/10.1038/modpathol.3800928.

[222] YE Li. Sustainable biomass materials for biomedical applications. Acs Biomater Sci Eng 2019;5:2079-92. https://doi.org/10.1021/acsbiomaterials.8b01634.

[223] N Kasoju, A Sunilkumar. Convergence of tissue engineering and sustainable development goals. Biotechnol Sustain Mater 2024;1:20. https://doi.org/10.1186/s44316-024-00021-y.

[224] G. García, V. Moreno-Serna, M. Saavedra, A. Cordoba, D. Canales, A. Alfaro, A. Guzmán-Soria, P. Orihuela, S. Zapata, C.D. Grande-Tovar, C.H. Valencia-Llano, P.A. Zapata, Electrospun scaffolds based on a PCL/starch blend reinforced with CaO nanoparticles for bone tissue engineering, Int J Biol Macromol 273 (2024) 132891. https://doi.org/10.1016/j.ijbiomac.2024.132891.

[225] S. Unal, S. Arslan, B. Karademir Yilmaz, D. Kazan, F.N. Oktar, O. Gunduz. Glioblastoma cell adhesion properties through bacterial cellulose nanocrystals in polycaprolactone/gelatin electrospun nanofibers. Carbohyd Polym 233 (2020) 115820. https://doi.org/10.1016/j.carbpol.2019.115820.

[226] E. Tolba, A. Salama, A.K. Saleh, I. Cruz-Maya, V. Guarino, Sodium alginate- and cationic cellulose-functionalized polycaprolactone nanofibers for in vitro and antibacterial applications, Moleculee 28 (2023) 7305. https://doi.org/10.3390/molecules28217305.

[227] Z. Pedram Rad, J. Mokhtari, M. Abbasi, Fabrication and characterisation of PCL/zein/gum arabic electrospun nanocomposite scaffold for skin tissue engineering, Mat Sci Eng C-Mater 93 (2018) 356-366. https://doi.org/10.1016/j.msec.2018.08.010.

[228] A. Hivechi, S.H. Bahrami, R.A. Siegel, Drug release and biodegradability of electrospun cellulose nanocrystal reinforced polycaprolactone, Mat Sci Eng C-Mater 94 (2019) 929-937. https://doi.org/10.1016/j.msec.2018.10.037.

[229] S. Beikzadeh, S.M. Hosseini, V. Mofid, S. Ramezani, M. Ghorbani, A. Ehsani, A.M. Mortazavian, Electrospun ethyl cellulose/poly caprolactone/gelatin nanofibers: The investigation of mechanical, antioxidant, and antifungal properties for food packaging, Int J Biol Macromol 191 (2021) 457-464. https://doi.org/10.1016/j.ijbiomac.2021.09.065.

[230] S. Kamalipooya, S. Fahimirad, H. Abtahi, M. Golmohammadi, M. Satari, M. Dadashpour, D. Nasrabadi, Diabetic wound healing function of PCL/cellulose acetate nanofiber engineered with chitosan/cerium oxide nanoparticles, Int J Pharmaceut 653 (2024) 123880. https://doi.org/10.1016/j.ijpharm.2024.123880.

[231] Amoatey P, Baawain MS. Effects of pollution on freshwater aquatic organisms. Water Environ Res 2019;91:1272-87. https://doi.org/10.1002/wer.1221.

[232] Meijide FJ, Da Cuña RH, Prieto JP, Dorelle LS, Babay PA, Lo Nostro FL. Effects of waterborne exposure to the antidepressant fluoxetine on swimming, shoaling and anxiety behaviours of the mosquitofish Gambusia holbrooki. Ecotoxicol Environ Saf 2018;163:646-55. https://doi.org/10.1016/j.ecoenv.2018.07.085.

[233] Ahmed FE, Lalia BS, Hashaikeh R. A review on electrospinning for membrane fabrication: challenges and applications. Desalination 2015;356:15-30. https://doi.org/10.1016/j.desal.2014.09.033.

[234] Su RL, Li SM, Wu WL, Song C, Liu GQ, Yu Y. Recent progress in electrospun nanofibrous membranes for oil/water separation. Sep Purif Technol 2021;256:117790. https://doi.org/10.1016/j.seppur.2020.117790.

[235] Shamaei L, Khorshidi B, Perdicakis B, Sadrzadeh M. Treatment of oil sands produced water using combined electrocoagulation and chemical coagulation techniques. Sci Total Environ 2018;645:560-72. https://doi.org/10.1016/j.scitotenv.2018.06.387.

[236] Wu JX, Zhang J, Kang YL, Wu G, Chen SC, Wang YZ. Reusable and recyclable superhydrophilic electrospun nanofibrous membranes with in situ co-cross-linked polymer–chitin nanowhisker network for robust oil-in-water emulsion separation. ACS Sustain Chem Eng 2018;6(2):1753-62. https://doi.org/10.1021/acssuschemeng.7b03102.

[237] Ying T, Su JF, Jiang YJ, Ke QF, Xu H. A pre-wetting induced superhydrophilic/superlipophilic micro-patterned electrospun membrane with self-cleaning property for on-demand emulsified oily wastewater separation. J Hazard Mater 2020;384:121475. https://doi.org/10.1016/j.jhazmat.2019.121475.

[238] Yan XH, Xiao X, Au C, Mathur S, Huang LJ, Wang YX, et al. Electrospinning nanofibers and nanomembranes for oil/water separation. J Mater Chem a Mater 2021;9(38):21659-84. https://doi.org/10.1039/D1TA05873H.

[239] Omidvar A, Masoumi S, Monsefi M, Jafarzadeh Y, Nasiri M, Hazrati H. PVC/PMMA blend ultrafiltration membranes for oil-in-water emulsion separation. Polym Bull 2023;80(8):9275-95. https://doi.org/10.1007/s00289-022-04514-6.

[240] Bang J, Park S, Hwang SW, Oh JK, Yeo H, Jin HJ, et al. Biodegradable and hydrophobic nanofibrous membranes produced by solution blow spinning for efficient oil/water separation. Chemosphere 2023;312:137240. https://doi.org/10.1016/j.chemosphere.2022.137240.

[241] Liu LJ, Yuan WZ. A hierarchical functionalized biodegradable PLA electrospun nanofibrous membrane with superhydrophobicity and antibacterial properties for oil/water separation. New J Chem 2018;42(21):17615-24. https://doi.org/10.1039/C8NJ03112F.

[242] Munj HR, Tomasko DL. Polycaprolactone–polymethyl methacrylate electrospun blends for

biomedical applications. Polym Sci 2017;59:695-707. https://doi.org/10.1134/S0965545X17050121.

[243] Seah MQ, Chua SF, Ang WL, Lau WJ, Mansourizadeh A, Thamaraiselvan C. Advancements in polymeric membranes for challenging water filtration environments: A comprehensive review. J Environ Chem Eng 2024;12(3):112628. https://doi.org/10.1016/j.jece.2024.112628.

[244] Simões MCR, Cragg SM, Barbu E, De Sousa FB. The potential of electrospun poly(methyl methacrylate)/polycaprolactone core–sheath fibers for drug delivery applications. J Mater Sci 2019;54(7):5712-25. https://doi.org/10.1007/s10853-018-03261-2.

[245] Son SR, Linh NB, Yang HM, Lee BT. In vitro and in vivo evaluation of electrospun PCL/PMMA fibrous scaffolds for bone regeneration. Sci Technol Adv Mater 2013;14(1):15009. https://doi.org/10.1088/1468-6996/14/1/015009.

[246] Shalaby MS, Sołowski G, Abbas W. Recent aspects in membrane separation for oil/water emulsion. Adv Mater Interfaces 2021;8(20):2100448. https://doi.org/10.1002/admi.202100448.

[247] Ge DT, Yang LL, Wang CB, Lee E, Zhang YQ, Yang S. A multi-functional oil–water separator from a selectively pre-wetted superamphiphobic paper. Chem Commun 2015;51(28):6149-52. https://doi.org/10.1039/C4CC09813G.

[248] Yi Y, Tu H, Zhou X, Liu R, Wu Y, Li D, et al. Acrylic acid-grafted pre-plasma nanofibers for efficient removal of oil pollution from aquatic environment. J Hazard Mater 2019;371:165-74. https://doi.org/10.1016/j.jhazmat.2019.02.085.

[249] Hua D, Chung TS. Polyelectrolyte functionalized lamellar graphene oxide membranes on polypropylene support for organic solvent nanofiltration. Carbon 2017;122:604-13. https://doi.org/10.1016/j.carbon.2017.07.011.

[250] Van der Bruggen B. Chemical modification of polyethersulfone nanofiltration membranes: A review. J Appl Polym Sci 2009;114(1):630-42. https://doi.org/10.1002/app.30578.

[251] Meng JX, Zhang J, Shen X, Xie J, Liao QY, He F, et al. Bio-inspired surface engineering of hydrophobic membranes with nano-structured hydrogel toward viscous oil-in-water emulsion separation. Chem Eng J 2023;473:145519. https://doi.org/10.1016/j.cej.2023.145519.

[252] Xu ZT, Ma GX, Rana D, Matsuura T, Lan CQ. Modification of exterior and intraporous surfaces of polyvinylidene fluoride membranes using KOH/water/alcohol ternary: Effects of wettability, polarity, and OH^- activity. React Funct Polym 2025;208:106147. https://doi.org/10.1016/j.reactfunctpolym.2024.106147.

[253] Bao SW, Zhang XY, Zhang L, Ning X, Niu HT, Zhou H. Sandwich-structured nanofiber membranes with dual-directional water-transport ability for high-efficiency water harvesting. ACS Appl Polym Mater 2024;6(6):3294-302. https://doi.org/10.1021/acsapm.3c03123.

[254] Zhan JJ, Zhang W, Wang M, Guan WW, Yan XH, Zhang QS, et al. Fabrication, characterization and antibacterial properties of ZnO nanoparticles decorated electrospun polyacrylonitrile nanofibers membranes. Mater Today Commun 2022;32:103958. https://doi.org/10.1016/j.mtcomm.2022.103958.

[255] Cheng D, Chen TF, Cao W. Study on the viscoelastic behaviors of PMMA. J Phys: Conf Ser 2020;1637:012120. https://dx.doi.org/10.1088/1742-6596/1637/1/012120.

[256] Robin C, Lorthioir C, Amiel C, Fall A, Ovarlez G, Cœur CL. Unexpected rheological behavior of concentrated poly(methacrylic acid) aqueous solutions. Macromolecules 2017;50(2):700-10. http://dx.doi.org/10.1021/acs.macromol.6b01552.

[257] Liu K, Kiran E. Miscibility, viscosity and density of poly (ε-caprolactone) in acetone + CO_2 binary fluid mixtures. J Supercrit Fluids 2006;39(2):192-200. https://doi.org/10.1016/j.supflu.2006.03.026.

[258] Zhao YY, Yuan QP. Effect of membrane pretreatment on performance of solvent resistant nanofiltration membranes in methanol solutions. J Membrane Sci 2006;280(1-2):195-201. https://doi.org/10.1016/j.memsci.2006.01.026.

[259] Fujimoto K, Tang ZY, Shinoda W, Okazaki S. All-atom molecular dynamics study of impact fracture of glassy polymers. I: Molecular mechanism of brittleness of PMMA and ductility of PC. Polymer 2019;178:121570. https://doi.org/10.1016/j.polymer.2019.121570.

[260] Lin CT, Kuo SW, Huang CF, Chang FC. Glass transition temperature enhancement of PMMA through copolymerization with PMAAM and PTCM mediated by hydrogen bonding. Polymer 2010;51(4):883-9. https://doi.org/10.1016/j.polymer.2009.12.039.

[261] Nauman S, Lubineau G, Alharbi HF. Post Processing Strategies for the Enhancement of Mechanical Properties of ENMs (Electrospun Nanofibrous Membranes): A Review. Membranes 2021;11(1):39. https://doi.org/10.3390/membranes11010039.

[262] Madurantakam PA, Rodriguez IA, Garg K, McCool JM, Moon PC, Bowlin GL. Compression of multilayered composite electrospun ccaffolds: A novel strategy to rapidly enhance mechanical properties and three dimensionality of bone scaffolds. Adv Mater Sci Eng 2013;7:561273. https://doi.org/10.1155/2013/561273.

[263] Stade S, Kallioinen M, Tuuva T, Mänttäri M. Compaction and its effect on retention of ultrafiltration membranes at different temperatures. Sep Purif Technol 2015;151:211-7. https://doi.org/10.1016/j.seppur.2015.07.034.

[264] Bibi W, Asif M, Rabbi J. Investigation of membrane fouling in vacuum membrane distillation (VMD) using blocking filtration laws. Eng Proc 2021;12(1):82. https://doi.org/10.3390/engproc2021012082.

[265] Fang SK, Li HR, Feng SD, Wang PX, Yu Y, Zhang H, et al. TA modified PAN/PU nanofiber membrane with excellent strength for oil/water separation. Fiber Polym 2024;25:47-58. https://doi.org/10.1007/s12221-023-00418-y.

[266] Song C, Rutledge GC. Electrospun polyimide fiber membranes for separation of oil-in-water emulsions. Sep Purif Technol 2021;270:118825. https://doi.org/10.1016/j.seppur.2021.118825.

[267] Juraij K, Niroula A, Greish Y, Mural PKS, Nazir A, Iqbal MZ. Sustainable, antifouling poly (ethylene furanoate)/ poly (lactic acid) (PEF/PLA) blend electrospun nanofibrous membranes for switchable premix emulsification/demulsification. J Membrane Sci 2025;717:123622. https://doi.org/10.1016/j.memsci.2024.123622.

[268] Obaid M, Mohamed HO, Alayande AB, Kang Y, Ghaffour N, Kim IS. Facile fabrication of superhydrophilic and underwater superoleophobic nanofiber membranes for highly efficient separation of oil-in-water emulsion. Sep Purif Technol 2021;272:118954. https://doi.org/10.1016/j.seppur.2021.118954.

[269] Shahidul Islam Md, McCutcheon JR, Saifur Rahaman Md. A high flux polyvinyl acetate-coated electrospun nylon 6/SiO_2 composite microfiltration membrane for the separation of oil-in-water emulsion with improved antifouling performance. J Membrane Sci 2017;537:297-309. https://doi.org/10.1016/j.memsci.2017.05.019.

[270] Barroso-Solares S, Pinto J, Nannia G, Fragoulia D, Athanassiou A. Enhanced oil removal from water in oil stable emulsions using electrospun nanocomposite fiber mats. RSC Adv

2018;8:7641-50. https://doi.org/10.1039/C7RA12646H.
[271] Yan BM, Zhang YW, Li ZX, Zhou PH, Mao YJ. Electrospun nanofibrous membrane for biomedical application. Sn Appl Sci 2022;4:172. https://doi.org/10.1007/s42452-022-05056-2.
[272] Huang LW, Arena JT, Manickam SS, Jiang XQ, Willis BG, McCutcheon JR. Improved mechanical properties and hydrophilicity of electrospun nanofiber membranes for filtration applications by dopamine modification. J Membrane Sci 2014;460:241-9. https://doi.org/10.1016/j.memsci.2014.01.045.
[273] Wang XH, Yue XY, Zhang LZ, Han X, Hong JH. Graphene-decorated polyurethane nanofiber membrane flexible sensor with different fiber orientation. Sensor Actuat A-Phys 2024;376:115628. https://doi.org/10.1016/j.sna.2024.115628.
[274] Leote RJB, Beregoi M, Enculescu I, Diculescu VC. Metallized electrospun polymeric fibers for electrochemical sensors and actuators. Curr Opin Electroche 2022;34:101024. https://doi.org/10.1016/j.coelec.2022.101024.
[275] Bhavesh B, Moucham BG, Diksha Y, Sachin K, Pravin GI. Nano-electrospun membranes: Green solutions for diverse industrial needs. J Hazard Mater Adv 2023;12:100373. https://doi.org/10.1016/j.hazadv.2023.100373.
[276] Chinnappan BA, Krishnaswamy M, Xu HZ, Hoque ME. Electrospinning of biomedical nanofibers/nanomembranes: effects of process parameters. Polymers 2022;14(18):3719. https://10.3390/polym14183719.
[277] Eekhoff JD, Lake SP. Three-dimensional computation of fibre orientation, diameter and branching in segmented image stacks of fibrous networks. J R Soc Interface 2020;17(169):20200371. https://10.1098/rsif.2020.0371.
[278] Agatonovic-Kustrin S, Beresford R. Basic concepts of artificial neural network (ANN) modeling and its application in pharmaceutical research. J Pharm Biomed Anal 2000;22(5):717-27. https://10.1016/s0731-7085(99)00272-1.
[279] Khatti T, Naderi-Manesh H, Kalantar SM. Prediction of diameter in blended nanofibers of polycaprolactone-gelatin using ANN and RSM. Fiber Polym 2017;18(12):2368-78. https://10.1007/s12221-017-7631-8.
[280] Xu Y, Goodacre R. On splitting training and validation set: a comparative study of cross-validation, bootstrap and systematic sampling for estimating the generalization performance of supervised learning. J Anal Test 2018;2(3):249-62. https://10.1007/s41664-018-0068-2.
[281] Kurani A, Doshi P, Vakharia A, Shah M. A comprehensive comparative study of artificial neural network (ANN) and support vector machines (SVM) on stock forecasting. Annals of Data Science 2023;10(1):183-208. https://10.1007/s40745-021-00344-x.
[282] Samadian H, Zakariaee SS, Faridi-Majidi R. Evaluation of effective needleless electrospinning parameters controlling polyacrylonitrile nanofibers diameter via modeling artificial neural networks. J Text Inst 2019;110(4):477-86. https://10.1080/00405000.2018.1532781.
[283] Premasudha M, Bhumi Reddy SR, Lee YJ, Panigrahi BB, Cho KK, Nagireddy Gari SR. Using artificial neural networks to model and interpret electrospun polysaccharide (Hylon VII starch) nanofiber diameter. J Appl Polym Sci 2021;138(11):e50014. https://10.1002/app.50014.
[284] Ma M, Zhou HC, Gao SH, Li N, Guo WJ, Dai Z. Analysis and prediction of electrospun nanofiber diameter based on artificial neural network. Polymers 2023;15(13):2813. https://10.3390/polym15132813.
[285] Pervez MN, Yeo WS, Mishu MMR, Talukder ME, Roy H, Islam MS, et al. Electrospun

nanofiber membrane diameter prediction using a combined response surface methodology and machine learning approach. Sci Rep 2023;13(1):9679. https://10.1038/s41598-023-36431-7.

[286] Khatti T, Naderi-Manesh H, Kalantar SM. Application of ANN and RSM techniques for modeling electrospinning process of polycaprolactone. Neural Comput Appl 2019;31(1):239-48. https://10.1007/s00521-017-2996-6.

[287] Pham BT, Nguyen MD, Bui KT, Prakash I, Chapi K, Bui DT. A novel artificial intelligence approach based on multi-layer perceptron neural network and biogeography-based optimization for predicting coefficient of consolidation of soil. Catena 2019;173:302-11. https://10.1016/j.catena.2018.10.004.

[288] Hornik K, Stinchcombe M, White H. Multilayer feedforward networks are universal approximators. Neural Netw 1989;2(5):359-66. https://10.1016/0893-6080(89)90020-8.

[289] Seifollahi S, Yearwood J, Ofoghi B. Novel weighting in single hidden layer feedforward neural networks for data classification. Comput Math Appl 2012;64(2):128-36. https://10.1016/j.camwa.2012.01.042.

[290] Soyer MA, Tüzün N, Karakaş Ö, Berto F. An investigation of artificial neural network structure and its effects on the estimation of the low-cycle fatigue parameters of various steels. Fatigue Fract Eng M 2023;46(8):2929-48. https://doi.org/10.1111/ffe.14054.

[291] Igwe KC, Oyedum OD, Aibinu AM, Ajewole MO, Moses AS. Application of artificial neural network modeling techniques to signal strength computation. Heliyon 2021;7(3):e06047. https://doi.org/10.1016/j.heliyon.2021.e06047.

[292] MathWorks. Fit Data with a Neural Network. Deep Learning Toolbox Documentation, https://www.mathworks.com/help/deeplearning/gs/fit-data-with-a-neural-network.html; 2024 [accessed 2025 Nov 11].

[293] MathWorks. mapminmax: Min-Max Normalization Function. Deep Learning Toolbox Documentation, https://www.mathworks.com/help/deeplearning/ref/mapminmax.html; 2024 [accessed 2025 Nov 11].

[294] Gütlein M, Helma C, Karwath A, Kramer S. A Large-Scale Empirical Evaluation of Cross-Validation and External Test Set Validation in (Q)SAR. Mol Inform 2013;32:516-28. https://doi.org/10.1002/minf.201200134.

[295] Levman J, Jennings M, Kabaria P, Rouse E, Nangaku M, Berger D, et al. Hold-out validation for the assessment of stability and reliability of multivariable regression demonstrated with magnetic resonance imaging of patients with schizophrenia. Int J Dev Neurosci 2021;81(7):655–62. https://doi.org/10.1002/jdn.10144.

[296] Reddy NS, Panigrahi BB, Ho CM, Kim JH, Lee CS. Artificial neural network modeling on the relative importance of alloying elements and heat treatment temperature to the stability of α and β phase in titanium alloys. Comput Mater Sci 2015;107:175-83. https://10.1016/j.commatsci.2015.05.026.

[297] Sadan MK, Ahn H, Chauhan GS, Reddy NS. Quantitative estimation of poly(methyl methacrylate) nano-fiber membrane diameter by artificial neural networks. Eur Polym J 2016;74:91-100. https://10.1016/j.eurpolymj.2015.11.014.

[298] Li CL, Narayana PL, Reddy NS, Choi SW, Yeom JT, Hong JK, et al. Modeling hot deformation behavior of low-cost Ti-2Al-9.2Mo-2Fe beta titanium alloy using a deep neural network. J Mater Sci Technol 2019;35(5):907-16. https://10.1016/j.jmst.2018.11.018.

[299] Luíza Da Costa N, Dias De Lima M, Barbosa R. Evaluation of feature selection methods based

on artificial neural network weights. Expert Syst Appl 2021;168:114312. https://10.1016/j.eswa.2020.114312.

[300] Cai J, Zheng P, Qaisar M, Luo T. Prediction and quantifying parameter importance in simultaneous anaerobic sulfide and nitrate removal process using artificial neural network. Environ Sci Pollut Res Int 2015;22(11):8272-9. https://10.1007/s11356-014-3976-3.

[301] Montgomery DC. Design and analysis of experiments. 9th ed. Hoboken (NJ): John Wiley & Sons; 2017.

[302] Myers RH, Montgomery DC, Anderson-Cook CM. Response surface methodology: process and product optimization using designed experiments. 4th ed. Hoboken (NJ): John Wiley & Sons; 2016.

[303] Hagan MT, Menhaj MB. Training feedforward networks with the Marquardt algorithm. IEEE Trans Neural Netw 1994;5(6):989-93. https://doi.org/10.1109/72.329697.

[304] Kalantary S, Jahani A, Pourbabakia R, Beigzadeh Z. Application of ANN modeling techniques in the prediction of the diameter of PCL/gelatin nanofibers in environmental and medical studies. RSC Adv 2019;9:24858. https://doi.org/10.1039/C9RA04927D.

[305] Box GEP, Wilson KB. On the Experimental Attainment of Optimum Conditions. In: Kotz S, Johnson NL, editors. Breakthroughs in Statistics. Springer Series in Statistics. Springer, New York; 1992. pp. 270–310. https://doi.org/10.1007/978-1-4612-4380-9_23.

[306] Stat-Ease Inc. General Sequence of Analysis: ANOVA Output, https://www.statease.com/docs/v23.1/contents/analysis/anova-output/; 2023 [accessed 16 November 2025].

[307] Chi GY, Hu SQ, Yang YH, Chen T. Response surface methodology with prediction uncertainty: A multi-objective optimisation approach. Chem Eng Res Des 2012;90(9):1235-44. https://doi.org/10.1016/j.cherd.2011.12.012.

[308] Abdel-Fattah MK, Abd-Elmabod SK, Zhang ZH, Merwad A-RMA. Exploring the applicability of regression models and artificial neural networks for calculating reference evapotranspiration in arid regions. Sustainability 2023;15(21):15494. https://doi.org/10.3390/su152115494.

[309] Dobrynin AV, Sayko R, Colby RH. Viscosity of polymer solutions and molecular weight characterization. ACS Macro Lett 2023;12(6):773-9. https://10.1021/acsmacrolett.3c00219.

[310] Hayahara T, Takao S. Relationship between polymer concentration and molecular weight in the viscosity behavior of concentrated solution. Colloid Polym Sci 1968;225(2):106-11. https://10.1007/BF02086182.

[311] Zargham S, Bazgir S, Tavakoli A, Rashidi AS, Damerchely R. The effect of flow rate on morphology and deposition area of electrospun nylon 6 nanofiber. J Eng Fiber Fabr 2012;7(4):42-9. https://10.1177/155892501200700414.

[312] Kalluri L, Satpathy M, Duan YY. Effect of electrospinning parameters on the fiber diameter and morphology of PLGA nanofibers. Dent Oral Biol Craniofacial Res 2021;4(2). https://10.31487/j.dobcr.2021.02.04.

[313] Xie Y, Fang Q, Zhao H, Li Y, Lin ZH, Chen JX. Effects of six processing parameters on the size of PCL fibers prepared by melt electrospinning writing. Micromachines-Basel 2023;14(7):1437. https://10.3390/mi14071437.